A NEW NUMERICAL OPTIMIZATION METHOD BASED ON TAYLOR SERIES FOR CHALLENGING TRAJECTORY OPTIMIZATION PROBLEMS

BY

CHRISTOPHER SCOTT MARTIN

DISSERTATION

Submitted in partial fulfillment of the requirements
for the degree of Doctor of Philosophy in Aerospace Engineering
in the Graduate College of the
University of Illinois at Urbana-Champaign, 2011

Urbana, Illinois

Doctoral Committee:

Professor Bruce A. Conway, Chair
Professor John E. Prussing
Professor Victoria L. Coverstone
Assistant Professor Anil N. Hirani

Abstract

New methods to solve trajectory optimization problems are devised. The methods use direct transcription to convert the continuous optimal control problem into a parameter optimization problem that can be solved with non-linear programming. In direct transcription the system equations must be converted into algebraic constraints. Existing methods use only zeroth and first order derivatives of the system equations to formulate these constraints. The techniques of automatic differentiation allow the computation of the derivatives of the state equations to arbitrary order in reasonable time. The new methods devised use these higher-order derivatives to form the constraints.

To investigate the performance of the new methods they are tested on a series of progressively more challenging optimal control problems, culminating in the capstone problem. This capstone problem is a low-thrust Earth-Moon transfer that uses the interesting dynamics of the circular restricted three body problem (CR3BP), in particular the stable and unstable manifolds of a halo orbit about the interior L_1 Lagrange point in the Earth-Moon system.

To Rebecca.

Acknowledgments

First and foremost I'd like to thank my PhD. research adviser Dr. Bruce Conway, his patient guidance and attention to detail have made this research and document what it is today. He truly deserves all the teaching awards he has received. I'd also like to thank my doctoral committee Dr. Victoria Coverstone, Dr. Anil Hirani and in particular Dr. John Prussing. Dr. Prussing's classes piqued my interest in the topic of optimization and his help on optimal control questions helped my research greatly.

Many thanks go to my fellow students who have made my time in Illinois an enjoyable one. The discussions about trajectory optimization I had with Jacob Englander, Brad Wall, Alex Ghosh and Predipto Ghosh were not just enjoyable but productive as well. To my fellow Aussies Joshua Cantone and Manu Sharma, it was always great to hear a familiar accent. To the lads of the Cricket Club of Illinois (CCI) and the Flatlanders Rugby Club, it was great to be able to play the commonwealth sports in the heart of the United States. Also thanks go to my short-term cubicle mates, Greg Williamson and Ben Pomeroy, I was sorry to leave you guys but I couldn't pass up the corner office.

Lastly I'd like to thank my wife Rebecca who was marooned in Champaign long after she graduated. She provided much support, both emotional and technical. She tirelessly read though my earlier drafts, correcting my grammar, which at times can be unconventional.

Table of Contents

List of Tables

List of Figures

Chapter 1

Introduction

1.1 Earth-Moon Transfer and Three Body Dynamics

In this work we determine an optimal transfer from the Earth to the Moon. Many variations of this problem have been solved using different numerical methods in various coordinate systems; multiple two-body[1] (patched-conics), the three-body (Earth-Moon-Spacecraft)[2–4] and the four body (Earth-Moon-Sun-Spacecraft).[5–7] We will seek a trajectory that takes advantage of the efficiency of low-thrust engines and the interesting dynamics of the circular restricted three body system to construct a trajectory that requires minimal propellant mass but that also has a reasonable time of flight.

The circular restricted three body system (CR3BP) describes the motion of a massless particle in the presence of two massive primaries in a reference frame that rotates with the primaries. There exist five equilibrium points in the CR3BP, known as Lagrange points: the three collinear points along the line of the two primaries and the two equilateral points that form a equilateral triangle with the two primaries. It is the collinear points that are of the most interest and in particular the L_1 point between the two primaries and the L_2 point on the far side of the smaller primary. There also exist periodic solutions to the CR3BP that orbit about the Lagrange points. Since Poincaré[8] there has been much work on finding periodic solutions to the three body problem. Richardson[9] constructed 1st and 3rd order analytic approximations by linearizing the equations of motion about the L_1 and L_2 points. Higher-order approximations were computed by Gomez and Mancote.[10] Various others methods have been employed; generating functions,[11] Fourier analysis[12] and multiple shooting.[13] In this work the periodic orbit generation problem is instead formulated as an optimal control problem.

There also exist tubes in phase space known as invariant manifolds that are asymptotic to these periodic orbits. That is, if a body is on the stable manifold of a periodic orbit its trajectory will take it along the manifold until eventually it reaches the periodic orbit. Similarly the trajectory of a body perturbed from a periodic orbit will follow the unstable manifold. It is these invariant manifolds that are the exit and entry points (in phase space) to the periodic orbits .

In the last 20 years there has been much study of the gravitational three body system, in particular how to exploit its special dynamics, such as periodic orbits and their invariant manifolds, to create low energy transfers. The Hiten spacecraft[5,14] (1991) was the first mission to use a low energy transfer devised using the dynamics of the CR3BP. The intersection of the stable and unstable manifolds of various periodic orbits in various three body systems can be used to create trajectories that are capable of traveling vast distances around the solar system for almost no fuel expenditure. These trajectories traverse the so-called "Interplanetary Super Highway" (IPS).[15] Low energy trajectories that travel from the Earth to the Moon[14] or that tour the Jovian moons[16–18] have been constructed.

Several recent missions have targeted periodic orbits directly for their advantageous properties. For example, a periodic orbit about the Earth-Sun L_2 Lagrange point minimizes solar radiation, allowing the extremely low temperatures required for missions such as Herschel[19] and Planck[20] to be reached and maintained. The Genesis mission used a periodic orbit about the Earth-Sun L_2 Lagrange point in order to maximize the incidence of solar wind.[21]

In this work a low-thrust transfer from the Earth to the Moon is constructed using the dynamics of the Earth-Moon three body system. The transfer will be split into two phases. The first phase of the transfer is a thrust arc to intersect the stable manifold, followed by a coast along the stable manifold until the spacecraft enters a periodic orbit about L_1. The second phase is a departure from the periodic orbit and a coast along the unstable manifold (i.e. the manifold departing L_1) towards the moon followed by a thrust arc to transfer into a low lunar orbit. In general, there is no guarantee that the combination of two individually optimal trajectories is optimal. However, in this case the periodic orbit can be considered as a parking orbit which can be traversed with no cost, effectively decoupling the Earth-Halo transfer from the Halo-Moon transfer. We will use the framework of optimal control to construct this optimal trajectory.

1.2 Optimal Control

In an optimal control problem the dynamic system is described by a system of differential equations. The goal is then to minimize a cost functional subject to path constraints on the states and controls. The optimal control for this dynamical system can be determined using direct or indirect methods. Indirect methods introduce adjoint variables and use the calculus of variations or the maximum principle to determine necessary conditions that must be satisfied by an optimal solution.[22] The determination of the controls from the necessary conditions generally results in a two point boundary value problem (TPBVP). Unfortunately analytic solutions only exist for a small subset of simple optimal control problems, therefore a numerical shooting method is usually applied to solve the TPBVP.[23] However, while these indirect methods allow very accurate computation of the optimal solution, the region of convergence can

be small and therefore an accurate initial guess of the states and adjoints is required. Direct methods, in which the optimal control problem is converted into a nonlinear programming problem (NLP) also require an initial guess but are more robust. That is, they will converge to a solution satisfying the system governing equations and terminal conditions from a poor initial guess of the optimal solution. They do not explicitly use the necessary conditions and therefore do not require the addition of adjoint variables. Without adjoint variables the direct formulation of the problem is significantly smaller than the corresponding indirect formulation, which is partly responsible for the improved robustness.

We will consider the direct transcription method for solving optimal control problems, where the continuous optimal control problem is transcribed into a discrete parameter optimization problem and solved using non-linear programming techniques. In direct transcription each state and control (if there are any) is discretized, so that the trajectory is wholly described by the states and controls on a mesh of a finite number of nodes. These values, along with any event variables such as time of flight etc, are collected into a parameter vector. This parameter vector now completely describes the trajectory. The infinite dimensional continuous optimal control problem is now a finite dimensional parameter optimization problem. However, additional steps must be taken to ensure that the trajectory described by values in the parameter vector is valid, i.e. that it satisfies the system governing equations. This is achieved by converting the system governing equations into algebraic constraints. There are many existing methods for performing this conversion; they fall into two basic categories, collocation methods and shooting methods.

In collocation methods such as Hermite-Simpson[24] and Gauss-Lobatto[25] the state within a segment is approximated by a polynomial in time. The constraint is then to match the derivative of the polynomial and the derivative from the governing equations at the chosen collocation points. The Gauss pseudospectral methods use orthogonal collocation at the Legendre-Gauss (LG),[26] Legendre-Gauss-Radau (LGR),[27] or Legendre-Gauss-Lobatto (LGL)[28] points and use global Chebyshev[29] or Legendre[28] polynomials as the state and control estimates to achieve faster convergence.[30]

For shooting methods the state is propagated, either from one segment boundary to the other, or from both boundaries to an interior match point. The constraint is then the difference between the state estimates at this match point. The state can be propagated using a finite number of integration steps as in Runge-Kutta Multiple Shooting,[31] or using explicit numerical integration as in the Sims-Flanagan[32] method.

The Earth-Moon transfer considered here is a complicated trajectory. Due to the low power of the engine, many revolutions of the Earth, resembling a spiral, are needed in order to escape the Earth. Similarly the capture spiral at the Moon involves many revolutions. It was found that a fine mesh was required to ensure that satisfaction of the algebraic

constraints implies the satisfaction of the system governing equations. Since the size of the NLP parameter vector is directly related to the number of nodes in the mesh, this resulted in a large NLP parameter vector that adversely affects the convergence and runtime of the NLP solver. If the size of this NLP vector could be reduced a significant saving in computation time could be potentially achieved. One way to reduce the size of this NLP vector is to reduce the number of nodes in the mesh. To achieve this without sacrificing accuracy requires methods with higher-order accuracy.

1.3 New Methods for Formulating the Constraints

All of the methods cited above for converting the system equations into algebraic constraints, direct or indirect, collocation or shooting, use only first order derivative information about the states, which is all that is available directly from the system governing equations. This thesis will investigate whether more efficient alternative methods for formulating the constraints can be developed if this limitation is removed, i.e. higher-order derivative information of states is available.

The techniques of automatic differentiation[33] enable straightforward computation of the higher derivatives of the states by breaking up the equations into their elementary operations and repeatedly applying the chain rule. Angel and Jorba[34] used automatic differentiation to numerically solve initial value ordinary differential equations to very high accuracy by using the Taylor series expansion (computed to high order) to step the solution forward in time. In this work the Taylor series expansion is used to form constraints that are analogous to the shooting constraints described previously.

For the collocation methods described in the previous section (1.2) a polynomial estimate of the states within a segment is generated using the states and their derivatives at the segment boundaries and perhaps some interior points. The order of interpolating polynomial is limited by the number of nodes used in its formulation; derivative information (zeroth and first) at two nodes is required to fit a cubic polynomial, three nodes for a quintic polynomial, etc. The state values at each node must be stored as NLP parameters. However, if the higher-order state derivatives are computed, interpolating polynomials of higher degree can be used without a corresponding increase in the size of the NLP parameter vector. In this work a higher-order collocation scheme is developed using automatic differentiation.

1.4 Thesis Organization

Chapter 2 presents the general form of an optimal control problem and will describe some existing numerical solution methods. In particular, direct transcription with Runge-Kutta Multiple Shooting and Gauss-Lobatto 5^{th} order

Collocation. Two new alternative methods for converting the system equations into nonlinear constraints are developed; the Taylor series multiple shooting and higher-order collocation. Automatic differentiation is introduced as a method for computing the higher-order state derivatives that both methods require. These methods also require the higher-order derivatives of the control variables. Several methods are explored for specifying the control variables such that their derivatives are easily calculated. A mesh refinement scheme is developed that evenly distributes the numerical errors.

In Chapter 3 the effectiveness of the new methods is demonstrated by solving a series of progressively more difficult optimal control problems and comparing the results with those obtained using an efficient existing method; the Runge-Kutta Multiple Shooting method.

Chapter 4 consists of the capstone problem, a low-thrust Earth-Moon transfer via the L_1 interior Lagrange point, solved using both the conventional Runge-Kutta multiple shooting method and the new Taylor series multiple shooting method. Chapter 5 will contain some final discussion of results and the conclusions drawn from the preliminary work using these new methods. Finally, avenues for future investigation, including ways to improve the method, will be discussed in Chapter 6.

Chapter 2

Numerical Solution Methods

2.1 Discretization

Consider the optimal control problem with the following system governing equations:

$$\dot{\mathbf{x}}(t) = \mathbf{f}(\mathbf{x}(t), \mathbf{u}(t), t), \mathrm{t}_0 \leq \mathrm{t} \leq \mathrm{t}_\mathrm{f} \tag{2.1}$$

and the objective function:

$$J = \Phi(\mathbf{x}(t_f), t_f) + \int_{t_0}^{t_f} L(\mathbf{x}(t), \mathbf{u}(t), t)dt \tag{2.2}$$

which is subject to the path constraints:

$$\mathbf{g}(\mathbf{x}, \mathbf{u}, t) \leq 0, t_0 \leq t \leq t_f \tag{2.3}$$

and the terminal constraints:

$$\Psi(\mathbf{x}(t_f), t_f) = 0 \tag{2.4}$$

The method used to solve the optimal control problems in this work is the method of direct transcription with non-linear programming.[25] There exist a set of analytic necessary conditions for the problem of (2.1)-(2.4)[22] that introduce the adjoint variables (or co-states). The optimal control problem then becomes a two point boundary value problem (TPBVP) with the size of the phase space doubled (states, co-states), this is the *indirect* solution. Unfortunately analytical solutions only exist for a small, simple subset of problems, so in general the TPBVP must be solved numerically. This is difficult using traditional single (or multiple) shooting methods for solving boundary value problems as the co-state equations can be very sensitive. Therefore a good initial guess for the values of the co-states is required. However, the co-states lack a physical basis making it difficult to produce this initial guess. This TPBVP can be solved using direct transcription and non-linear programming using the methods outlined in this chapter. However, the problem can also be solved *directly* by ignoring the co-states and allowing the control variables themselves to be optimization parameters. This reduces the reliance on the sensitive co-state equations and removes the need for an initial guess of the co-states. Direct methods are generally much more robust, that is, they will converge to a solution

satisfying the system governing equations and terminal conditions from a poor initial guess of the optimal solution. However, they do not explicitly use the necessary conditions and therefore there is no guarantee of optimality. In this work we will solve the optimal control problems using direct methods and where possible solve the indirect problem to provide a check of the solution.

In direct transcription with non-linear programming each state and control (if there are any) is discretized. An example for the history of a state variable is shown in the cartoon of Figure 2.1. The control time history is described in a similar way, such that the controls are specified at the system nodes and sometimes also at interior points.

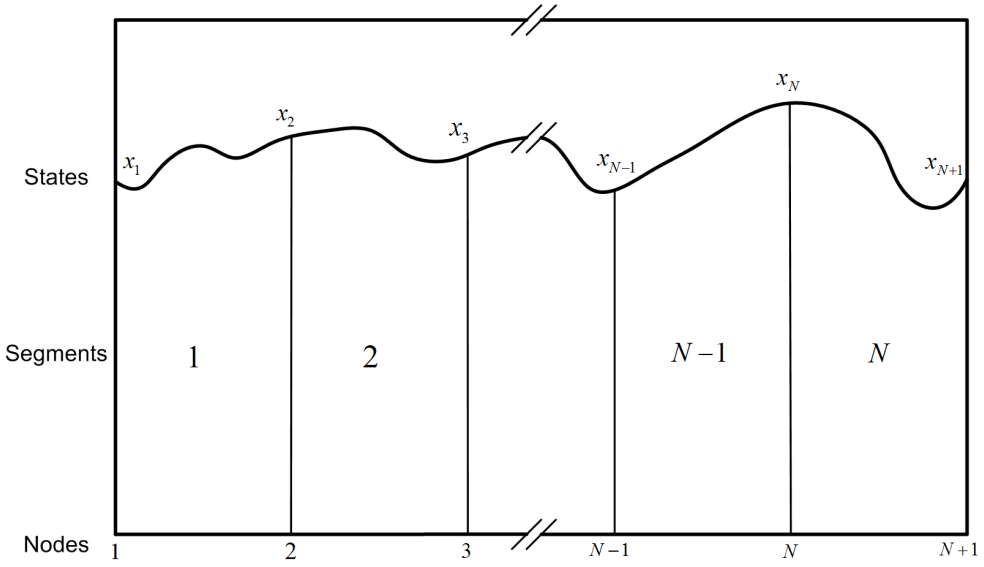

Figure 2.1: Illustration of the discretization of the continuous system.

The trajectory is now wholly defined by the state variables, $\mathbf{x}$, and the control variables, $\mathbf{u}$, defined at (N+1) nodes and possibly at some interior points.

The state parameters $\mathbf{x}$, control parameters $\mathbf{u}$, and the event variables $\mathbf{E}$ are collected into a single vector $\mathbf{P}$. Event variables are extra parameters required to describe the trajectory such as time of flight, engine burn times, departure date, etc.

$$\mathbf{P} = [\mathbf{Z}, \mathbf{E}] \tag{2.5}$$

where:

$$\mathbf{Z} = [\mathbf{x}_1, ...\mathbf{x}_{N+1}, \mathbf{u}_1, ..., \mathbf{u}_{N+1}]$$

The nonlinear programming (NLP) problem is then to minimize a discrete objective function $\Gamma(P)$ subject to:

$$\mathbf{b}_L \leq \left\{ \begin{array}{c} \mathbf{P} \\ A\mathbf{P} \\ C(\mathbf{P}) \end{array} \right\} \leq \mathbf{b}_U \tag{2.6}$$

where $A\mathbf{P}$ is a vector of linear constraints defined by the matrix A, and $C(\mathbf{P})$ is a vector of non-linear constraints. Virtually all of the non-linear constraints are implicit integration constraints used to ensure that the equations of motion are satisfied, as shown in Ref. 8.[35] $\mathbf{b}_L$ and $\mathbf{b}_U$ are the lower and upper bounds respectively on the states and constraints. The problem of minimizing $\Gamma(P)$ subject to (2.6) is a discretized form of the problem (2.1)-(2.4).

2.2 Nonlinear Constraints

2.2.1 Existing Methods

There are many existing methods for enforcing the system governing equations by transcribing them into algebraic constraints. These methods fall into two general categories: collocation methods and shooting methods. For collocation methods such as the Hermite-Simpson,[24] the Gauss-Lobatto[25] and the Pseudospectral methods,[36] the state histories within a segment are approximated by a polynomial. The state estimate given by the polynomial is used in the system equations to compute the state derivatives. The defects become the difference between this derivative and the derivative of the polynomial at certain collocation points. The location of these collocation points and the degree of the polynomial state estimate is the main difference between the various collocation methods. When these defects have been driven to zero the trajectory is said to satisfy the governing equations.

In the shooting method the states are propagated using numerical integration from one (or both) end/s of the segment to either the other end of the segment or an interior match point. The numerical integration can be explicit (Sims-Flanagan[32]) or it can consist of a finite number of integration steps (Runge-Kutta Multiple-Shooting[31]). The defect is either the difference in the the two state estimates at the match point, in the case of shooting from both ends, or the difference between the state estimate and the state stored in the parameters vector, as is the case for forward shooting.

In this work we will formulate new methods to formulate collocation and shooting style constraints by the using the higher-order derivatives of the states and controls. These higher-order derivatives will be calculated using automatic differentiation.

Collocation

Collocation is possibly the earliest method for converting a continuous optimal control problem into a constrained parameter optimization problem. Dickmanns and Wells[24] applied collocation to the indirect (calculus of variations) problem using a 3rd degree Hermite polynomial to approximate the states and co-states. Hargraves and Paris[37] applied collocation to the direct problem using linearly interpolated control variables. Herman and Conway[25] introduced higher-order (5th degree) polynomials. The higher-order collocation method developed in this thesis is an extension of these methods, so collocation and in particular the 5th order Gauss-Lobatto method of Herman and Conway will be described in more detail here.

For each interval the time history of each state variable is approximated over the interval by a polynomial. Herman and Conway[25] found that the accuracy and computational efficiency of direct collocation using 5th degree polynomial trajectory approximations was superior to approximations using polynomials of lower degree. Six conditions are required to uniquely define the approximating quintic polynomial over the segment. The values of the states at the segment boundary nodes $(i, i+1)$ are defined and the derivatives can be calculated from the system equation $\dot{\mathbf{x}} = \mathbf{f}(\mathbf{x}, \mathbf{u}, t)$ providing four conditions $(\mathbf{x}_i, \mathbf{f}_i, \mathbf{x}_{i+1}, \mathbf{f}_{i+1})$. That is, the approximating polynomial must evaluate to $\mathbf{x}_i$ at the left side node and its slope must correspond to $\mathbf{f}_i = \mathbf{f}(\mathbf{x}_i)$ there. At the right side node the polynomial must evaluate to $\mathbf{x}_{i+1}$ and its slope must be $\mathbf{f}_{i+1}$. The remaining two conditions are defined by adding a node at the center of the segment with corresponding state $\mathbf{x}_c$ and time rate of change $\dot{\mathbf{x}}_c = \mathbf{f}(\mathbf{x}_c, \mathbf{u}_c, t_c)$, where $\mathbf{u}_c$, the control at the center point, and $\mathbf{x}_c$ are free parameters.

These six conditions determine a quintic polynomial satisfying the governing equations at the left and right nodes and at the center of the segment as shown in the cartoon of Figure 2.2. An additional constraint is imposed that the derivative of the quintic polynomial be equal to the derivative calculated from the system equations at two interior collocation points.

The collocation points (t_1, t_2) are selected to minimize the error in the polynomial estimation of the state.[25] For a 5th degree Gauss-Lobatto polynomial the collocation points are located at

$$\begin{aligned} t_1 &= t_c - \sqrt{\frac{3}{7}}\frac{1}{2}\Delta t_i \\ t_2 &= t_c + \sqrt{\frac{3}{7}}\frac{1}{2}\Delta t_i \end{aligned} \tag{2.7}$$

where Δt_i is the width of the i^{th} time segment, i.e. $\Delta t_i = t_{i+1} - t_i$.

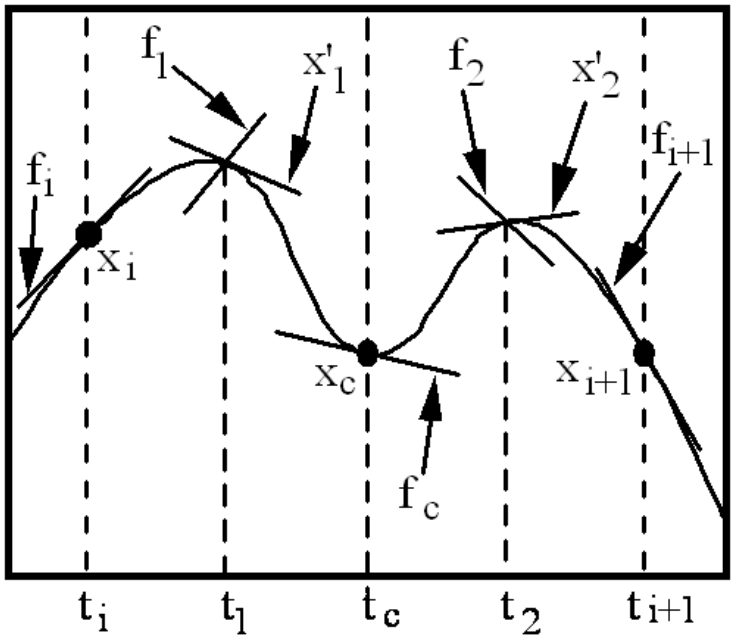

Figure 2.2: Illustration of the Gauss-Lobatto quintic polynomial.

The states at the collocation points in segment i are obtained from the polynomial evaluated at times t_1 and t_2:

$$\mathbf{x}_1 = \frac{1}{686}\left\{\begin{array}{l}\left(39\sqrt{21}+231\right)\mathbf{x}_i + 224 + \left(-39\sqrt{21}+231\right)\mathbf{x}_{i+1} \\ +\Delta t_i\left[\left(3\sqrt{21}+21\right)\mathbf{f}_i - 16\sqrt{21}\mathbf{f}_c + \left(3\sqrt{21}-21\right)\mathbf{f}_{i+1}\right]\end{array}\right\} \tag{2.8}$$

$$\mathbf{x}_2 = \frac{1}{686}\left\{\begin{array}{l}\left(-39\sqrt{21}+231\right)\mathbf{x}_i + 224 + \left(39\sqrt{21}+231\right)\mathbf{x}_{i+1} \\ +\Delta t_i\left[\left(-3\sqrt{21}+21\right)\mathbf{f}_i + 16\sqrt{21}\mathbf{f}_c + \left(-3\sqrt{21}-21\right)\mathbf{f}_{i+1}\right]\end{array}\right\} \tag{2.9}$$

where $\mathbf{f}_i = \mathbf{f}(\mathbf{x}_i, \mathbf{u}_i, t_i)$, $\mathbf{f}_c = \mathbf{f}(\mathbf{x}_c, \mathbf{u}_c, t_c)$ and $\mathbf{f}_{i+1} = \mathbf{f}(\mathbf{x}_{i+1}, \mathbf{u}_{i+1}, t_{i+1})$. The system constraints are then:

$$\mathbf{C}_{5,1}(\mathbf{x}_i, \mathbf{x}_{i+1}) = \frac{1}{360}\left\{\begin{array}{l}\left(32\sqrt{21}+180\right)\mathbf{x}_i - 64\sqrt{21}\mathbf{x}_c + \left(32\sqrt{21}-180\right)\mathbf{x}_{i+1} \\ \Delta t_i\left[\left(9+\sqrt{21}\right)\mathbf{f}_i + 98\mathbf{f}_1 + 64\mathbf{f}_c + \left(9-\sqrt{21}\right)\mathbf{f}_{i+1}\right]\end{array}\right\} = 0 \tag{2.10}$$

$$\mathbf{C}_{5,2}(\mathbf{x}_i, \mathbf{x}_{i+1}) = \frac{1}{360}\left\{\begin{array}{l}\left(-32\sqrt{21}+180\right)\mathbf{x}_i + 64\sqrt{21}\mathbf{x}_c + \left(-32\sqrt{21}-180\right)\mathbf{x}_{i+1} \\ \Delta t_i\left[\left(9-\sqrt{21}\right)\mathbf{f}_i + 64\mathbf{f}_c + 98\mathbf{f}_2 + \left(9+\sqrt{21}\right)\mathbf{f}_{i+1}\right]\end{array}\right\} = 0 \tag{2.11}$$

where $\mathbf{f}_1 = \mathbf{f}(\mathbf{x}_1, \mathbf{u}_1, t_1)$, $\mathbf{f}_2 = \mathbf{f}(\mathbf{x}_2, \mathbf{u}_2, t_2)$. Note that the values of the controls at collocation points t_1 and t_2 must be specified. This then adds two more control parameters per segment per control.

Runge-Kutta Multiple Shooting

The Runge-Kutta Multiple Shooting method was used as a comparison for the test problems solved in Chapters 3 and 4. The Taylor series shooting constraints developed in this thesis will build on ideas from the Runge-Kutta Multiple Shooting approach, therefore it will be explained in more detail.

In the Runge-Kutta Multiple Shooting method[35] the states are adjusted so that when the state at one boundary of the segment is integrated forward in time over the segment it is equal to the state at the other boundary. The states are propagated forward using an explicit Runge-Kutta four-stage integration formula.

$$\begin{aligned} y_i^1 &= x_{i-1} + \tfrac{h}{2} f\left(x_{i-1}, u_{i-1}\right) \\ y_i^2 &= x_{i-1} + \tfrac{h}{2} f\left(y_i^1, v_i\right) \\ y_i^3 &= x_{i-1} + h f\left(y_i^2, v_i\right) \\ y_i^4 &= x_{i-1} + \tfrac{h}{6}\left[f\left(x_{i-1}, u_{i-1}\right) + 2f\left(y_i^1, v_i\right) + 2f\left(y_i^2, v_i\right) + f\left(y_i^3, u_i\right)\right] \end{aligned} \tag{2.12}$$

The nonlinear constraint is then:

$$y_i^4 - x_i = 0 \tag{2.13}$$

In order to economize on the number of nonlinear constraints and the number of state variables in the parameter vector $\mathbf{P}$, multiple Runge-Kutta steps are taken for each segment; 3 steps are shown in Figure 2.3. The choice of the number of steps is arbitrary but 3 steps has been shown to work well in the past.[31] That is, steps (2.12) and (2.13) are taken three times as the integration proceeds from t_{i-1} to t_i.

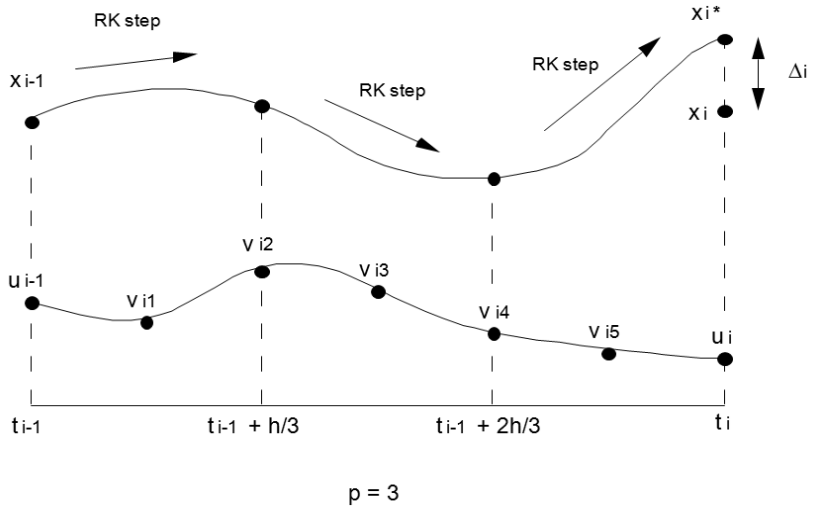

Figure 2.3: Illustration of the Runge-Kutta Parallel Shooting constraints.

2.2.2 Alternative Constraints

The Runge-Kutta integration scheme has a $O(h^5)$ local error, therefore many segments are required to accurately model complicated trajectories such as the Earth-Moon transfer. This problem is not unique to the Runge-Kutta method; the direct collocation, pseudospectral and Sims Flanagan methods all suffer from this problem. This greatly affects computation time, because, while the parameter vector for the NLP solver and the vector of nonlinear constraints grow only linearly with the number of segments, the Jacobian and the Hessian grow with the square of the number of segments and therefore become very large quickly. This is known as the "Curse of Dimensionality". It is, therefore, desirable to be able to describe the trajectory using as few NLP parameters as possible.

Reducing the number of segments would enable problems to be solved much more quickly, or allow larger problems to be tractable in reasonable computation time. In order to use fewer segments while retaining the necessary accuracy, a more accurate integration scheme (shooting) or polynomial approximation (collocation) is required.

Taylor Series Multiple Shooting

To find a higher-order shooting method we will return to perhaps the oldest method for solving ODEs: the Taylor method. The state at node $i+1$ is approximated by the first M terms of the Taylor expansion about node i:

$$\begin{aligned}\mathbf{x}\left(t_{i+1}\right) =&\mathbf{x}\left(t_i\right)+\dot{\mathbf{x}}\left(t_i\right)\left(t_{i+1}-t_i\right)+\frac{\ddot{\mathbf{x}}\left(t_i\right)}{2!}\left(t_{i+1}-t_i\right)^2+\ldots \\ &\frac{\mathbf{x}^{(3)}\left(t_i\right)}{3!}\left(t_{i+1}-t_i\right)^3+\ldots+\frac{\mathbf{x}^{(M)}\left(t_i\right)}{M!}\left(t_{i+1}-t_i\right)^M\end{aligned} \tag{2.14}$$

Substituting the system equations:

$$\dot{\mathbf{x}}=\mathbf{f}\left(\mathbf{x},\mathbf{u},t\right) \tag{2.15}$$

yields:

$$\begin{aligned}\mathbf{x}\left(t_{i+1}\right) =&\mathbf{x}\left(t_i\right)+\mathbf{f}\left(\mathbf{x}_i,\mathbf{u}_i,t_i\right)\left(t_{i+1}-t_i\right)+\frac{\mathbf{f}^{(1)}\left(\mathbf{x}_i,\mathbf{u}_i,t_i\right)}{2!}\left(t_{i+1}-t_i\right)^2+\ldots \\ &\frac{\mathbf{f}^{(2)}\left(\mathbf{x}_i,\mathbf{u}_i,t_i\right)}{3!}\left(t_{i+1}-t_i\right)^3+\ldots+\frac{\mathbf{f}^{(M-1)}\left(\mathbf{x}_i,\mathbf{u}_i,t_i\right)}{M!}\left(t_{i+1}-t_i\right)^M\end{aligned} \tag{2.16}$$

The difficulty with this formulation is that it requires knowledge of the first $M-1$ derivatives of the system equations with respect to time. The derivatives can be found using the rules of automatic differentiation[34] combined with the system equations. Since the derivatives of the control variables are not described by the state equations they must be supplied. More precisely, the control must be specified in such a way that the derivatives can be readily calculated. Methods for parameterizing controls are discussed in Section 2.4.

Taylor Series multiple shooting resembles Runge-Kutta multiple shooting except that the states are estimated using the Taylor series expansion (2.16). Each Taylor step propagates the states forward for a portion ($\frac{1}{p}$) of the time interval, where p is the number of subsegments within each subsegment. Once p steps have been completed there is an estimate ($\mathbf{y}_i^p$) for the state at the right boundary of the segment:

$$\begin{aligned}
\mathbf{y}_i^1 &= \mathbf{x}_{i-1} + \mathbf{f}\left(\mathbf{x}_i, \mathbf{u}_i, t_{i-1}\right)\Delta t + \frac{\mathbf{f}^{(1)}(\mathbf{x}_i,\mathbf{u}_i,t_{i-1})}{2!}\Delta t^2 \\
&\quad + \frac{\mathbf{f}^{(2)}(\mathbf{x}_i,\mathbf{u}_i,t_{i-1})}{3!}\Delta t^3 + \ldots + \frac{\mathbf{f}^{(M-1)}(\mathbf{x}_i,\mathbf{u}_i,t_{i-1})}{M!}\Delta t^M \\
\mathbf{y}_i^2 &= \mathbf{y}_i^1 + \mathbf{f}\left(\mathbf{y}_i^1, \mathbf{u}_i, t_{i-1} + \Delta t\right)\Delta t + \frac{\mathbf{f}^{(1)}\left(\mathbf{y}_i^1,\mathbf{u}_i,t_{i-1}+\Delta t\right)}{2!}\Delta t^2 \\
&\quad + \frac{\mathbf{f}^{(2)}\left(\mathbf{y}_i^1,\mathbf{u}_i,t_{i-1}+\Delta t\right)}{3!}\Delta t^3 + \ldots + \frac{\mathbf{f}^{(M-1)}\left(\mathbf{y}_i^1,\mathbf{u}_i,t_{i-1}+\Delta t\right)}{M!}\Delta t^M \\
&\vdots \quad \vdots \\
\mathbf{y}_i^p &= \mathbf{y}_i^{p-1} + \mathbf{f}\left(\mathbf{y}_i^{p-1}, \mathbf{u}_i, t_{i-1} + (p-1)\,\Delta t\right)\Delta t \\
&\quad + \frac{\mathbf{f}^{(1)}\left(\mathbf{y}_i^{p-1},\mathbf{u}_i,t_{i-1}+(p-1)\Delta t\right)}{2!}\Delta t^2 \\
&\quad + \frac{\mathbf{f}^{(2)}\left(\mathbf{y}_i^{p-1},\mathbf{u}_i,t_{i-1}+(p-1)\Delta t\right)}{3!}\Delta t^3 + \ldots \\
&\quad + \frac{\mathbf{f}^{(M-1)}\left(\mathbf{y}_i^{p-1},\mathbf{u}_i,t_{i-1}+(p-1)\Delta t\right)}{M!}\Delta t^M
\end{aligned} \tag{2.17}$$

where:

$$\Delta t = \frac{t_i - t_{i-1}}{p} \tag{2.18}$$

The nonlinear constraint is then simply;

$$\mathbf{y}_i^p - \mathbf{x_i} = \mathbf{0} \tag{2.19}$$

which is analogous to the constraint in the Runge-Kutta multiple shooting method (2.13). The number of subsegments in each segment is an adjustable parameter.

The Taylor series approximation is only valid if the control has indefinitely many continuous derivatives. Hence, subsegment boundaries must be placed at locations where the control does not have M continuous derivatives, such as spline knots. The control derivatives are then continuous over the time interval of the Taylor step. The Taylor series for the state vector is truncated to M terms where M is determined by the accuracy required.

Higher-order Collocation

In collocation methods each state within a segment is approximated by a polynomial whose coefficients are determined by the values of the states and the first derivatives at certain points. The degree of the polynomial interpolant differs depending on the method. For Hermite-Simpson collocation a cubic polynomial is fitted so that four pieces of data are required to uniquely determine the polynomial fit, the values of the state and its derivative at each seg-

ment boundary. The more accurate, higher-order, Gauss-Lobatto method[25] described in Section 2.2.1 uses a quintic polynomial which requires two additional pieces of data over those required for the cubic polynomial. As a result of this a node must be added at the mid-point of the segment. If only the first-derivatives of the states are known, then any increase in the order of the polynomial requires the addition of extra nodes, however, if the higher derivatives of the states are known at the segment boundaries, say to order M, then a polynomial of up to degree $2M-1$ can be fitted without the addition of any nodes. This allows more accurate polynomial approximations to be fitted without a corresponding increase in the number of state variables in the NLP vector.

An example of this polynomial fit is shown in Figure 2.4. There are now two estimates of the state derivative at the collocation point t_c; the derivative of the polynomial ($p'(t_c)$) and the value of the system governing equations evaluated using the state estimate given by the polynomial, the control at time t_c and time t_c itself. The defect is then the difference between these two estimates, if this defect is driven to zero the equations of motion are satisfied. The collocation constraints are then:

$$p'_x(t_c) - f(p_x(t_c), u(t_c), t_c) = 0 \tag{2.20}$$

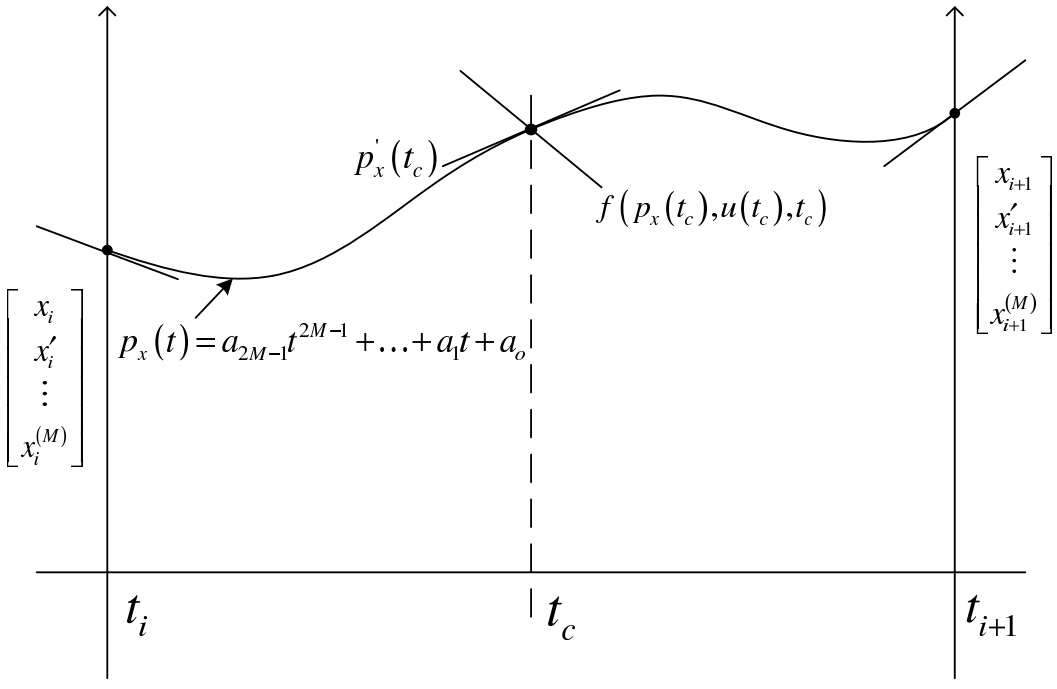

Figure 2.4: Collocation using higher-order derivatives.

2.3 Automatic Differentiation

Both the Taylor series multiple shooting (equation (2.17)) and the higher-order collocation (cf. Figure 2.4) require knowledge of the first $(M-1)$ derivatives of the system equations $f(x,u,t)$. Computing these derivatives is not a trivial task. There are several methods available to compute the higher-order derivatives of the state equations.

The equations of motion can be differentiated analytically. While tedious to do by hand, the process can be streamlined with the aid of a symbolic math program such as Matlab or Mathematica. However, the expressions for the higher derivatives of state equations quickly become very complicated even for relatively simple equations of motion, making the programming of these equations unwieldy.

The higher-order derivatives could be computed using finite differences. Finite difference formulas for higher-order derivatives can be constructed from the formulas for lower-order derivatives. The formulas for higher-order derivatives (> 3) quickly become very large and complicated. The finite difference methods also have limited accuracy as the step-size must be small to limit truncation error, but these small step-sizes introduce subtraction cancelation errors.

The subtraction cancellation errors can be removed by using complex step differentiation[38] which removes the subtraction from the finite difference equation by taking a step into the complex plane. The method for computing the first derivative of Martins, Sturdza and Alonso[38] was extended to higher derivatives by Lantoine and Russell[39] using multicomplex numbers. However, a multicomplex number of order n containing 2^n terms is required to compute the n^{th} derivative, making this method inefficient for higher-order derivatives.

The method used in this work is automatic differentiation; in particular the method proposed by Jorba and Zou.[34] The equations are decomposed into their individual operations $(+,-,\div,\times,cos,sin,etc.)$. The chain rule can then by applied repeatedly to construct a matrix of the higher derivatives of the results of the individual operations including the left hand side of the state equations.

In order to simplify the following expressions for the higher derivatives, we introduce the following notation for the i$^{\text{th}}$ normalized derivative of the j$^{\text{th}}$ element of w:

$$w_j^{[n]} = \frac{1}{n!}\frac{d^n w_j}{dt^n} \tag{2.21}$$

The following rules can then be employed to derive recursive relations for the higher derivatives.[34] Rules for other elementary operations such as inverse trigonometric functions can be derived if necessary.

$$
\begin{aligned}
a(t) &= b(t) \pm c(t) \\
a^{[n]}(t) &= b^{[n]}(t) \pm c^{[n]}(t)
\end{aligned}
\tag{2.22}
$$

$$
\begin{aligned}
a(t) &= b(t)c(t) \\
a^{[n]}(t) &= \sum_{j=0}^{n} b^{[n-j]}(t)c^{[j]}(t)
\end{aligned}
\tag{2.23}
$$

$$
\begin{aligned}
a(t) &= \tfrac{b(t)}{c(t)} \\
a^{[n]}(t) &= \tfrac{1}{c^{[0]}(t)} \left[b^{[n]}(t) - \sum_{j=0}^{n} c^{[j]}(t)a^{[n-j]}(t) \right]
\end{aligned}
\tag{2.24}
$$

$$
\begin{aligned}
a(t) &= b(t)^{\alpha} \\
a^{[n]}(t) &= \tfrac{1}{nb^{[0]}(t)} \sum_{j=0}^{n} \left(n\alpha - j(\alpha+1)\right) b^{[n-j]}(t)a^{[j]}(t)
\end{aligned}
\tag{2.25}
$$

$$
\begin{aligned}
a(t) &= e^{b(t)} \\
a^{[n]}(t) &= \tfrac{1}{n} \sum_{j=0}^{n-1} (n-j)\, a^{[j]}(t)b^{[n-j]}(t)
\end{aligned}
\tag{2.26}
$$

$$
\begin{aligned}
a(t) &= \ln b(t) \\
a^{[n]}(t) &= \tfrac{1}{b^{[0]}(t)} \left[b^{[n]}(t) - \tfrac{1}{n} \sum_{j=0}^{n-1} (n-j)\, b^{[j]}(t)a^{[n-j]}(t) \right]
\end{aligned}
\tag{2.27}
$$

$$
\begin{aligned}
a(t) &= \cos c(t) \\
b(t) &= \sin c(t) \\
a^{[n]}(t) &= -\tfrac{1}{n} \sum_{j=1}^{n} j b^{[n-j]}(t)c^{[j]}(t) \\
b^{[n]}(t) &= \tfrac{1}{n} \sum_{j=1}^{n} j a^{[n-j]}(t)c^{[j]}(t)
\end{aligned}
\tag{2.28}
$$

2.3.1 Automatic Differentiation Example: Two Body System Motion in Polar Coordinates

In order to illustrate the automatic differentiation method as applied in this work, the two-body equations of motion in polar coordinates will be used as an example:

$$
\begin{aligned}
\dot{r} &= v_r \\
\dot{\theta} &= \tfrac{v_\theta}{r} \\
\dot{v}_r &= \tfrac{v_\theta^2}{r} - \tfrac{1}{r^2} + T_a \sin u \\
\dot{v}_\theta &= \tfrac{v_r v_\theta}{r} + T_a \cos u
\end{aligned}
\tag{2.29}
$$

The equations are decomposed into the following sequence of elementary operations:

$$\begin{aligned}
w_1 &= r \\
w_2 &= r \\
w_3 &= v_r \\
w_4 &= v_\theta \\
w_5 &= u \\
w_6 &= \sin w_5 \\
w_7 &= \cos w_5 \\
w_8 &= T_a w_6 \\
w_9 &= T_a w_7 \\
w_{10} &= \tfrac{w_4}{w_1} \\
w_{11} &= w_4 w_{10} \\
w_{12} &= w_1 w_1 \\
w_{13} &= \tfrac{1}{w_{12}} \\
w_{14} &= w_{11} - w_{13} + w_8 \\
w_{15} &= w_3 w_4 \\
w_{16} &= \tfrac{w_{15}}{w_1} \\
w_{17} &= w_8 - w_{16}
\end{aligned} \tag{2.30}$$

The original equations of motion (2.29) thus become:

$$\begin{aligned}
\dot{r} &= w_3 \\
\dot{\theta} &= w_{10} \\
\dot{v}_r &= w_{14} \\
\dot{v}_\theta &= w_{17}
\end{aligned} \tag{2.31}$$

in terms of the elementary operators. The differentiation rules (2.22-2.28) can then be employed to derive recursive relations for the higher derivatives.[34] This yields the following formulas for the higher-order derivatives of each element of w:

$$
\begin{aligned}
w_1^{[n]} &= r^{[n]} \\
w_2^{[n]} &= \theta^{[n]} \\
w_3^{[n]} &= v_r^{[n]} \\
w_4^{[n]} &= v_\theta^{[n]} \\
w_5^{[n]} &= u^{[n]} \\
w_6^{[n]} &= \tfrac{1}{n} \sum_{j=1}^{n} j w_7^{[n-j]} w_5^{[j]} \\
w_7^{[n]} &= -\tfrac{1}{n} \sum_{j=1}^{n} j w_6^{[n-j]} w_5^{[j]} \\
w_8^{[n]} &= T_a w_6^{[n]} \\
w_9^{[n]} &= T_a w_7^{[n]} \\
w_{10}^{[n]} &= \tfrac{1}{w_1^{[0]}} \left[w_4^{[n]} - \sum_{j=1}^{n} w_1^{[j]} w_{10}^{[n-j]} \right] \\
w_{11}^{[n]} &= \sum_{j=0}^{n} w_4^{[n-j]} w_{10}^{[j]} \\
w_{12}^{[n]} &= \sum_{j=0}^{n} w_1^{[n-j]} w_1^{[j]} \\
w_{13}^{[n]} &= -\tfrac{1}{w_{12}^{[0]}} \sum_{j=1}^{n} w_{12}^{[j]} w_{13}^{[n-j]} \\
w_{14}^{[n]} &= w_{11}^{[n]} - w_{13}^{[n]} + w_8^{[n]} \\
w_{15}^{[n]} &= \sum_{j=0}^{n} w_3^{[n-j]} w_4^{[j]} \\
w_{16}^{[n]} &= \tfrac{1}{w_1^{[0]}} \left[w_{15}^{[n]} - \sum_{j=1}^{n} w_1^{[j]} w_{16}^{[n-j]} \right] \\
w_{17}^{[n]} &= -w_{16}^{[n]} + w_8^{[n]}
\end{aligned}
\tag{2.32}
$$

the higher derivatives of the equations of motion (2.29) thus become:

$$
\begin{aligned}
r^{[n+1]} &= \tfrac{w_3^{[n]}}{(n+1)} \\
\theta^{[n+1]} &= \tfrac{w_{10}^{[n]}}{(n+1)} \\
v_r^{[n+1]} &= \tfrac{w_{14}^{[n]}}{(n+1)} \\
v_\theta^{[n+1]} &= \tfrac{w_{17}^{[n]}}{(n+1)}
\end{aligned}
\tag{2.33}
$$

in terms of the elementary operators and their derivatives.

2.4 Control Parameterizations

In order to compute the higher derivatives of the state equations the higher derivatives of the control variables are also needed. The formula for w_5^n in equation (2.32) is an example of this. The control variables must be specified in such a way that their derivatives can be readily computed.

The ideal control specification would have as few, similarly-scaled coefficients as possible while having many continuous derivatives. The fewer control parameters, the smaller the NLP problem, and consequently the problem becomes easier and faster to solve. NLP solvers also perform better on problems where the variables are similarly scaled. This is why the state variables are normalized.

2.4.1 Fourier Series Parameterization

One method of parameterizing control would be a Fourier series. The entire control history is described by $(2N+2)$ coefficients $(L, a_0, b_0, a_1, \ldots, a_N, b_N)$ where N is chosen so that the Fourier approximation is an adequate approximation of the optimal control history.

$$u(t) = a_0 + \sum_{n=1}^{N} \left[a_n \cos \frac{n\pi t}{L} + b_n \sin \frac{n\pi t}{L} \right] \tag{2.34}$$

In general, the Fourier series will converge to an arbitrary function if enough terms are kept, and it has infinite non-zero derivatives that can be easily computed. However, the coefficients are poorly scaled and certain coefficients, in particular a_0 and L, have a far greater effect on the resulting function $(u(t))$ than the others.

2.4.2 Piecewise Polynomial - Spline Parameterization

Allowing the optimizer to choose the coefficients of a function can result in scaling problems. An alternative is to allow the optimizer to pick the control values at certain points, and a piecewise polynomial is fitted to these control points (knots). The piecewise polynomial has infinitely many derivatives (most of which are zero) that can be easily computed. The derivatives of order n (where n is the degree of the polynomial) are not continuous so care must be taken to ensure that the Taylor series expansion does not span a control knot. The fitted piecewise polynomial can be of any order. Higher-order polynomials are much more numerically expensive to compute and may not better approximate the unknown optimal control function due to Runge's phenomenon.[40] In this work linear and cubic splines were used as it was found that they provided the best tradeoff between flexibility and computation efficiency.

The quality of a spline approximation to a function is heavily dependent on the placement of knots.[40] It is therefore of great benefit to allow the optimizer to pick the placement (in time) of the control knots. However this results in more control parameters. Each knot requires two control parameters to define its position rather than one but allows the control parametrization to better approximate the optimal control. The control is still limited to functions that can be described by a piecewise linear or piecewise cubic curve; a small subset of all functions.

2.4.3 Non-Uniform Rational Basis Spline Parameterization

Non-Uniform Rational Basis Splines (NURBS) are used extensively in computer graphics and computer aided design (CAD) to describe and model curves and surfaces. NURBS are used in automotive,[41] aerospace,[42] medical[43] and maritime industries[44] as they allow complex surfaces such turbine blades,[42] ship hulls[45] and even hearts[46] to be described by a compact, mathematically precise representation.

A NURB is a parametric curve that is a weighted linear combination of normalized B-spline basis functions $B_{j,k}$. The control curve U in $t-u$ space is given by:

$$U(p) = \sum_{i=1}^{n+1} P_i B_{i,k}(p) \quad , p_{min} \leq p \leq p_{max} \quad , 2 \leq k \leq n+1 \tag{2.35}$$

where P_i are the positions (t_i, u_i) of the $n+1$ vertices of the control polygon, $B_{i,k}$ are the normalized B-Spline basis functions of order k (degree $k-1$). B-Splines are defined recursively by the Cox-de Boor formulas.[40]

$$B_{i,1} = \begin{cases} 1 & \text{if } z_i \leq p < z_{i+1} \\ 0 & \text{otherwise} \end{cases} \tag{2.36}$$

and

$$B_{i,k}(p) = \frac{(p - z_i) B_{i,k-1}(p)}{z_{i+k-1} - z_i} + \frac{(z_{i+k} - p) B_{i+1,k-1}(p)}{z_{i+k} - z_{i+1}} \tag{2.37}$$

The values of z_i are elements of a knot vector satisfying the relation $z_i \leq z_{i+1}$. The choice of knot vector has a significant influence on the shape of the resulting curve. In this work open uniform knot vectors were used. Open uniform knot vectors have knots of multiplicity k at each end and evenly spaced knots in between, where k is the order of the B-Spline basis functions.

$$\begin{aligned} x_i &= 0 && \text{for } 1 \leq i \leq k \\ x_i &= i - k && \text{for } k+1 \leq i \leq n+1 \\ x_i &= n - k + 2 && \text{for } n+2 \leq i \leq n+k+1 \end{aligned}$$

Example basis splines of order $k = 4$ and $n = 8$ are shown in Figure 2.5. A open uniform knot vector was used.

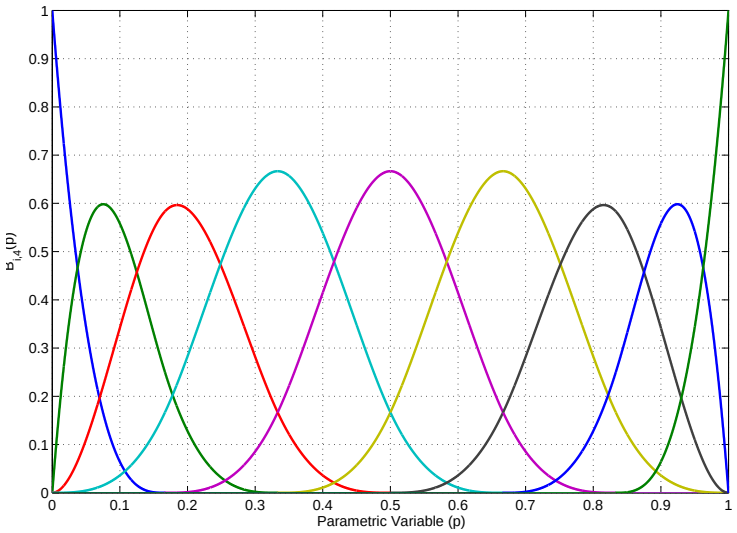

Figure 2.5: Example basis splines $B_{i,4}$ of order 4 with a open uniform knot vector.

Allowing the elements of the knot vector to be optimization parameters would allow greater flexibility in the curves that the NURB could represent, but the basis functions would have to be recalculated every iteration, at great computational cost. Using an open uniform knot vector allows the basis functions to be pre-computed. An example of the fitting of a NURB curve to a control polygon is shown in Figure 2.6.

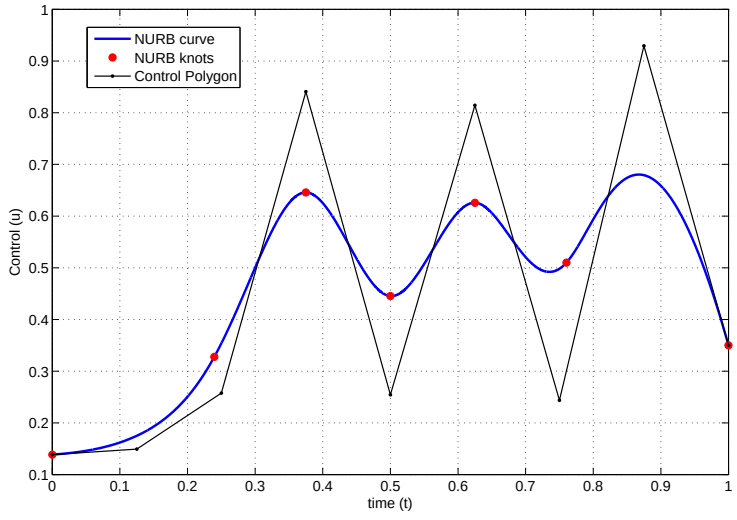

Figure 2.6: Example NURB curve fitted to a control polygon. Basis splines $B_{i,4}$ are of order 4 and use a open uniform knot vector.

The parametric definition of the NURB curve provides greater flexibility in the functions that it can approximate. However, it greatly complicates the computation of its derivatives. The basis splines are functions of parametric variable p, therefore equation (2.35) yields both control $(u(p))$ and time $(t(p))$ as polynomial functions of p of order $(k-1)$. The derivatives of control and time with respect to p are then straightforward to compute. However, to compute the Taylor series expansion at time t^* the value of the control as well as its derivatives with respect to time are required. First the parametric variable p that corresponds to time t^* must be computed. It is calculated by solving;

$$t^* - t(p) = 0 \tag{2.38}$$

With p known, the control value can be computed directly from $u(p)$. The first derivative is computed by using the chain rule to convert the derivative with respect to time to a derivative with respect to p:

$$\frac{du}{dt} = \frac{\frac{du}{dp}}{\frac{dt}{dp}} = \frac{u'}{t'} \tag{2.39}$$

The second and third derivatives are then:

$$\frac{d^2u}{dt^2} = \frac{u''}{(t')^2} - \frac{u't''}{t'} \tag{2.40}$$

$$\frac{d^3u}{dt^3} = \frac{u'''}{(t')^3} + \frac{3u''t''}{(t')^4} + \frac{u't'''}{(t')^4} - \frac{3u'(t'')^2}{(t')^5} \tag{2.41}$$

Unlike the piecewise polynomial the $(k+1)^{th}$ and higher-order derivatives do not vanish. The number of terms in the expressions for the higher-order derivatives grow rapidly, potentially causing numerical difficulties. However, all the terms in the n^{th} derivative are of the form:

$$a\frac{u^{(b)}\prod_{i=1}^{n}\left(t^{(i)}\right)^{d_i}}{(t')^c} \tag{2.42}$$

where a, b, c and $(d_1, d_2, ..., d_n)$ are integer constants.

Therefore the form of the equations for the higher derivatives can be pre-computed and stored in matrix form. This greatly reduces the computational overhead during the optimization. The control NURB-Spline is only C^{k-2} as the derivatives of higher-order are not continuous at the knots. Care must then be taken to ensure that no Taylor approximation step spans a knot in the NURB curve.

2.4.4 Switching Times

It is sometimes known *a priori* that a control variable will only take values at its bounds[22] on the optimal trajectory; as in so called *bang-bang* control. The timings of this instantaneous change in control from one extreme to the other are governed by a switching function. This is prevalent in the control parameters that govern the magnitude of the control acceleration such as throttle parameters. Without a loss of generality we will consider controls that are bounded between zero and one $u \in [0, 1]$. Since we know that the control will only take the values zero or one, and that it instantly switches between them a finite number of times, the control history can be wholly described by a vector of "switching times". That is, the times at which the control switches from one bound to the other.

For switching time vector $\mathbf{t_s}$ the control u at time t is then:

$$u(t) = \begin{cases} 1 & \text{if } \aleph\left\{t_s \leq t\right\} \text{ even} \\ 0 & \text{if } \aleph\left\{t_s \leq t\right\} \text{ odd} \end{cases} \tag{2.43}$$

It is not generally known *a priori* how many times the control variable will switch. While the control parameterization can place two switches at the exact same time, effectively removing a switch, it cannot add switches. Therefore the optimal control found might not be the global optimum as there may exist a control function with more switches than allowed for, which would result in a lower cost.

2.5 Mesh Refinement and Order Control

In general, an equally spaced mesh, while convenient, will not provide the best performance. An intelligent initial selection for the mesh, such as having a higher concentration of nodes where controls or states are expected to vary rapidly, will provide an improvement on a uniform mesh. However, it is not necessarily known *a priori* where states or controls will change rapidly. Therefore we seek a method to automatically refine the mesh without user intervention. Ideally the mesh will equally distribute the numerical error over every segment and keep this error below a certain tolerance.

To get an estimate of the numerical error associated with the mesh, consider the Taylor series expansion of $\mathbf{x}$ about about t_i.

$$\begin{aligned} \mathbf{x}\left(t_{i+1}\right) = \quad & \mathbf{x}\left(t_i\right) + \dot{\mathbf{x}}\left(t_i\right)\left(t_{i+1} - t_i\right) + \tfrac{\ddot{\mathbf{x}}(t_i)}{2!}\left(t_{i+1} - t_i\right)^2 + \ldots \\ & \tfrac{\mathbf{x}^{(3)}(t_i)}{3!}\left(t_{i+1} - t_i\right)^3 + \ldots + \tfrac{\mathbf{x}^{(n)}(t_i)}{n!}\left(t_{i+1} - t_i\right)^N + R_n(x) \end{aligned} \tag{2.44}$$

Since the series is truncated at $n+1$ terms in the formulation of the Taylor series constraints, the error in segment i, E_i is the remainder term $R_n(x)$. The Lagrange form of the remainder states that there exists $\xi \in [t_i, t_{i+1}]$ such that,

$$E_i = R_n(x) = \frac{\mathbf{x}^{(n+1)!}(\xi)}{(n+1)}(t_{i+1} - t_i)^{n+1} \tag{2.45}$$

therefore there is an upper bound on the error given by,

$$E_i \leq (t_{i+1} - t_i)^{n+1} \max_{\xi \in [t_i, t_{i+1}]} \left(\mathbf{x}^{[n+1]}(\xi) \right) \tag{2.46}$$

In order to find the upper bound on the error, the maximum value of the $(n+1)^{th}$ derivative over the segment must be calculated. This is obtained by using the first $(n+1)$ terms of the Taylor series about t_i to estimate the state variables on a much finer mesh within the segment. The $(n+1)^{th}$ derivative can then be calculated on the fine mesh from the state estimate, as well as the control derivatives computed from the control parameterization. Once repeated for every segment this gives the $(n+1)^{th}$ derivatives on a fine mesh along the nominal trajectory.

Therefore an estimate for the maximum derivative value is given by:

$$\max_{j=1,\ldots,M} \left(\boldsymbol{x}^{[n+1]}(\hat{t}_j) \right) \approx \max_{\xi \in [t_i, t_{i+1}]} \left(\boldsymbol{x}^{[n+1]}(\xi) \right) \tag{2.47}$$

where $(\hat{t}_1, \hat{t}_2, ..., \hat{t}_M)$ are the times on the finer mesh between t_i and t_{i-1}.

Mesh refinement can then be posed as an optimization problem with the positions of the segment boundaries (nodes) as optimization parameters. The objective is then to minimize the maximum error in any one segment (equivalent to most equally distributing the error). This yields the objective function:

$$J_n = \max_{i=1,\ldots,N} E_i \tag{2.48}$$

Where N is the number of segments and E_i is the upper bound on the error in the i^{th} segment given by equation (2.46).

The resulting mesh $(t_0, t_1, \ldots, t_N)$ will be the optimal mesh on the nominal trajectory for a Taylor series of order (n). Since the computation of derivatives is expensive, the value of the Taylor series order (n) significantly impacts the runtime of the original optimal control problem. Therefore we wish to minimize the Taylor series order (n). Ideally once the mesh is optimized, (n) will be such that the maximum error is below some user specified error tolerance, but the maximum error for the optimal mesh for $(n-1)$ is not. This is then the minimum order required to keep the error

below a certain tolerance. Find n^* such that:

$$J_{n^*} \leq tol \leq J_{n^*+1} \tag{2.49}$$

This n^* can be found using a binary search. The procedure for this is as follows:

1. Upper (n_U) and lower (n_L) bounds for n are set. In this work we have considered Taylor series truncated at between 10 and 50 terms.

2. Evaluate the optimal mesh by solving an NLP problem to obtain the maximum error at both boundary values for n. Find J_{n_U} and J_{n_L}

3. If $J_{n_U} > tol$ then more segments are required. The original optimal control problem must be rerun with a finer mesh.

4. If $J_{n_L} < tol$ then less segments are required. The original optimal control problem may either be rerun with a coarser mesh or the Taylor series may be set as n_L even though it is not minimal.

5. If $J_{n_L} > tol > J_{n_U}$, then a new test value for n is set at the midpoint of n_U and n_L
   $n_m = (n_L + n_U)/2$

6. Evaluate the optimal mesh and the corresponding maximum error at this new test value J_{n_m}.

7. If $J_{n_m} > tol$ then set test value as new lower bound $n_L = n_m$.

8. If $J_{n_m} < tol$ then set test value as new upper bound $n_U = n_m$.

9. If $n_U - n_L = 1$ then continue to step 10, otherwise return to step 5.

10. The upper bound n_U is now the minimum order required to meet the specified tolerance.

This mesh refinement and order control procedure can be run several times during the coarse of an optimization. The original optimal control NLP problem is run for a fixed number of iterations until the trajectory and control is a reasonable approximation of the optimal solution. The mesh refinement procedure is then performed on this nominal trajectory to generate an optimal mesh. The states and controls are then interpolated on this optimized mesh, and the optimal control problem is restarted. This can be repeated as many times as is necessary.

Chapter 3

Solved Problems

3.1 Motivation

In order to test the performance of the new Taylor series shooting and higher-order collocation constraints, a series of progressively more challenging optimal control problems will be solved in this chapter. The first problem solved is that of periodic orbit generation in the circular restricted three body system. This problem is the least complex of the problems considered as it is a reformulation of a two point boundary value problem and has no costate or control variables. The remaining test problems all have control variables and are made progressively more difficult by using more sophisticated system equations, the addition of terminal constraints, the addition of a throttle parameter, or some combination of these. The example problems will also be solved using the conventional Runge-Kutta constraints so that the results obtained with the new methods may be compared with an efficient extant method.

3.2 Example: Generation of a Periodic Orbit About the L_1 Lagrange Point

3.2.1 Circular Restricted Three Body System Dynamics

The differential equations of the circular restricted three body problem (CR3BP) describe the motion of a point mass P_3 with mass m_3 under the gravitational influence of two massive primaries P_1 and P_2 with masses m_1 and m_2 respectively, where $m_1 > m_2 \gg m_3 \approx 0$. It is assumed that P_3 exerts negligible influence on the primaries. The motion is considered in a non-inertial frame that moves with the two primaries as they rotate about the system barycenter at constant radius, as shown in Figure 3.1.

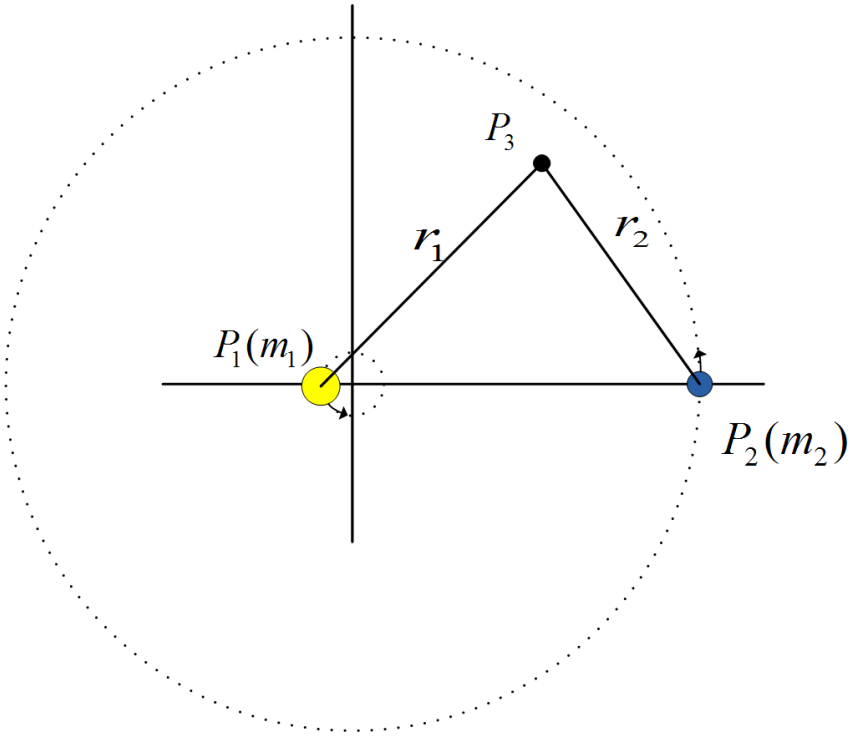

Figure 3.1: Circular restricted three body system geometry.

It is convenient to normalize the system. The constant separation of the two primaries P_1 and P_2 is chosen to be the length unit. The combined mass of the two primaries $m_1 + m_2$ becomes the mass unit. The time unit is then selected to make the orbital period of the two primaries about the system barycenter equal to 2π time units. To further simplify, the universal gravitational constant G becomes unity, therefore the mean motion n of the primaries is also equal to 1. The system can now be solely described by a single parameter; the mass ratio μ.

$$\mu = \frac{m_2}{m_1 + m_2} \tag{3.1}$$

By convention $m_1 \geq m_2$, therefore $\mu \in [0, 0.5]$. The normalized masses of the primaries are then $P_1 = (1 - \mu)$ and $P_2 = \mu$. They orbit the system barycenter at radii μ and $(1 - \mu)$ length units respectively.

The circular restricted three body system equations of motion are:

$$\dot{x} = v_x$$

$$\dot{y} = v_y$$

$$\dot{z} = v_z$$

$$\dot{v}_x = 2v_y + x - \frac{(1-\mu)(x+\mu)}{r_1^3} - \frac{\mu(x-1+\mu)}{r_2^3} \tag{3.2}$$

$$\dot{v}_y = -2v_x + y - \frac{(1-\mu)y}{r_1^3} - \frac{\mu y}{r_2^3}$$

$$\dot{v}_z = \frac{-(1-\mu)z}{r_1^3} - \frac{\mu z}{r_2^3}$$

where,

$$\mathrm{r}_1 = \sqrt{(\mathrm{x}+\mu)^2 + \mathrm{y}^2 + \mathrm{z}^2}$$

$$\mathrm{r}_2 = \sqrt{(\mathrm{x}-1+\mu)^2 + \mathrm{y}^2 + \mathrm{z}^2}$$

Lagrange Points

The system equations for the CR3BP are autonomous, hence there exists the possibility of stationary or equilibrium points in the phase space. For a stationary point (x^*, y^*, z^*), equation (3.2) becomes:

$$-x^* = -\frac{(1-\mu)(x^*+\mu)}{r_1^3} - \frac{\mu\,(x^*-1+\mu)}{r_2^3} \tag{3.3}$$

$$-\,y^* = -\frac{(1-\mu)y^*}{r_1^3} - \frac{\mu y^*}{r_2^3} \tag{3.4}$$

$$0 = -\frac{(1-\mu)z^*}{r_1^3} - \frac{\mu z^*}{r_2^3} \tag{3.5}$$

Clearly from equation (3.5) any equilibrium points must lie in the $x-y$ plane, as $z^* = 0$ is the only solution to equation (3.5). Consider solutions on the x-axis, with $y^* = z^* = 0$. Equation (3.3) becomes:

$$x^* - \frac{(1-\mu)(x+\mu)}{|x^*+\mu|^3} - \frac{\mu\,(x^*-1+\mu)}{|x^*-1+\mu|^3} \tag{3.6}$$

This is equivalent to a quintic polynomial in x^* with three real solutions. These solutions yield the locations of the three collinear Lagrange points L_1, L_2 and L_3.

Lagrange showed that two other equilibria exist with $r_1 = r_2 = 1$. Equations (3.3) and (3.4) are both satisfied, hence there exist equilibria at the two points in the $X - Y$ plane unit distance from both primaries. These are the equilateral Lagrange points L_4 and L_5 where $L_4 = (\frac{1}{2} - \mu, \frac{\sqrt{3}}{2})$ and $L_5 = (\frac{1}{2} - \mu, -\frac{\sqrt{3}}{2})$. All five of the Lagrange points are shown in Figure 3.2.

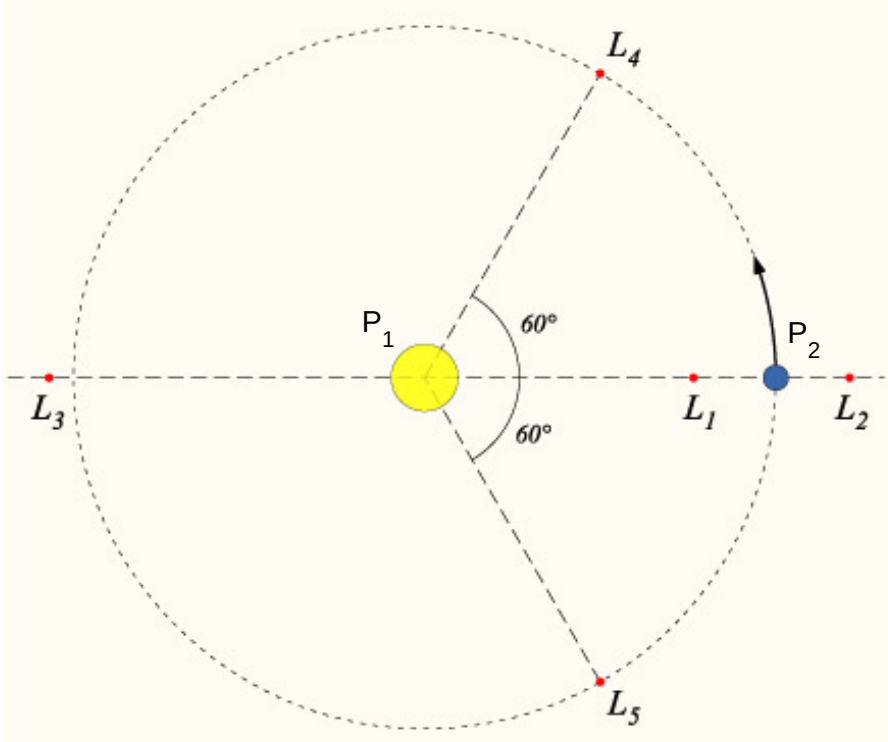

Figure 3.2: Locations of the Lagrange points.

The equilateral Lagrange points (L_4, L_5) are stable but the collinear points (L_1, L_2, L_3) are not. Periodic orbits do however exist about the unstable collinear points.

Periodic Orbits

Periodic solutions to the CR3BP have been sought since Poincaré. Due to the fact that computational power was not readily available, early work focused on analytic approximations. Richardson[9] constructed 1st and 3rd order analytic approximations by linearizing the equations of motion about the L_1 and L_2 points, and Gomez and Marcote[10] extended the analysis to higher orders. More accurate solutions have been obtained through computational means, however, all numerical methods have their disadvantages. Shooting methods such as those used by Howell and Pernicka[13] are

highly sensitive to the quality of the initial guess. Generating functions as used by Scheeres and Guibout[11] have a limited (spatial) range of applicability. In this work an alternative and more robust method for generating periodic orbits is used.

Periodic orbits are trajectories such that $\mathbf{x}(t_0) = \mathbf{x}(t_0 + NT)$ for some integer N and orbital period T. Therefore, the search for periodic solutions to the circular restricted three body problem of specified amplitude or period can be described as an optimal control problem[47] with the objective of minimizing the function:

$$J = |\mathbf{x}(t_o) - \mathbf{x}(t_0 + NT)| \tag{3.7}$$

subject to the system equations (3.2). The problem can be solved using the methods described in Chapter 2.

Periodic orbits are sought about the interior Lagrange point L_1 in the Earth-Moon system but the method would apply equally well to other Lagrange points and/or different three body systems. In normalized units the Earth-Moon system is fully defined by the mass ratio $\mu = m_{\text{moon}}/(m_{\text{earth}} + m_{\text{moon}}) = 0.0122$. The full three-dimensional solution to equations (3.2) was sought. The time histories of the states were discretized into N segments (as shown in Figure 2.1). The values of state variables at the segment boundaries and the final time t_f then constitute the NLP parameter vector $(\mathbf{P})$. No control parameters are necessary.

3.2.2 Terminal Conditions and Constraints

The problem was solved using the conventional Runge Kutta multiple shooting constraints,[25] the new Taylor Series Constraints, and also higher-order collocation. To ensure that the resulting trajectory has the required amplitude, the z position of the first and final nodes is fixed. Without loss of generality it can be assumed that the initial (and final) y-position is zero. In order for the orbit to be periodic the velocity component in both the x and z direction must be zero where the orbit crosses the $y = 0$ plane. The initial and terminal conditions are then

$$\begin{aligned} y_{N+1} &= y_1 = 0 \\ z_{N+1} &= z_1 = A_z \\ v_{x_{N+1}} &= v_{x_1} = 0 \\ v_{z_{N+1}} &= v_{z_1} = 0 \end{aligned} \tag{3.8}$$

For a periodic solution the positions and velocities at the initial and final nodes must also be equal. Since (y, z, v_x, v_z) are ensured to be equal at the first and last nodes by their bounds, only (x, v_y) need to be involved in the objective

(penalty) function:

$$\Phi(\mathbf{x}) = \sqrt{x_i - x_f)^2 + (v_{y_i} - v_{y_f})^2} \tag{3.9}$$

This function has a global minimum $\Phi(x) = 0$ when $x_i = x_f$ and $v_{y_i} = v_{y_f}$, (i.e. when the trajectory is a periodic orbit). Thus, the pure penalty function of equation (3.7) is not required.

3.2.3 Initial Guess

The NLP problem solver requires an initial guess of the optimal solution. For this case Richardson's 1st order analytical approximation[9] is used, in which

$$\begin{aligned} x &= A_x \cos(\lambda t + \Phi) \\ y &= kA_x \sin(\lambda t + \Phi) \\ z &= A_z \cos(\lambda t + \psi) \end{aligned} \tag{3.10}$$

where Φ and ψ are phase angles and:

$$k = \frac{2\lambda}{\lambda^2 + 1 - c_2} \tag{3.11}$$

The linearized frequency λ is found from the solution to:

$$\lambda^4 + (c_2 - 2)\,\lambda^2 - (c_2 - 1)\,(1 + 2c_2) = 0 \tag{3.12}$$

Constant c_2 is defined by:

$$c_2 = \frac{1}{\gamma_L^3}\left[\mu + \frac{(1-\mu)\,\gamma_L^3}{(1 \mp \gamma_L)^3}\right] \tag{3.13}$$

where the upper sign applies for orbits around L_1 and the lower sign for orbits around L_2. γ_L is defined by:

$$\gamma_L = \left(\frac{G\,(m_{moon} + m_{earth})}{a^3}\right)^{\frac{1}{3}} \tag{3.14}$$

3.2.4 Generation of a Periodic Orbit About the L_1 Lagrange Point: Results

Higher-order approximations are available,[9,10] however, this simple initial guess proved to be sufficient and demonstrated the robustness of the solution technique. Figures 3.3 and 3.4 show a single periodic orbit about the Earth-Moon L_1 point with an out-of-plane amplitude (A_z) of 8000 km. It was computed on a uniform mesh with 10 segments and using the Taylor Series shooting method, keeping 40 terms.

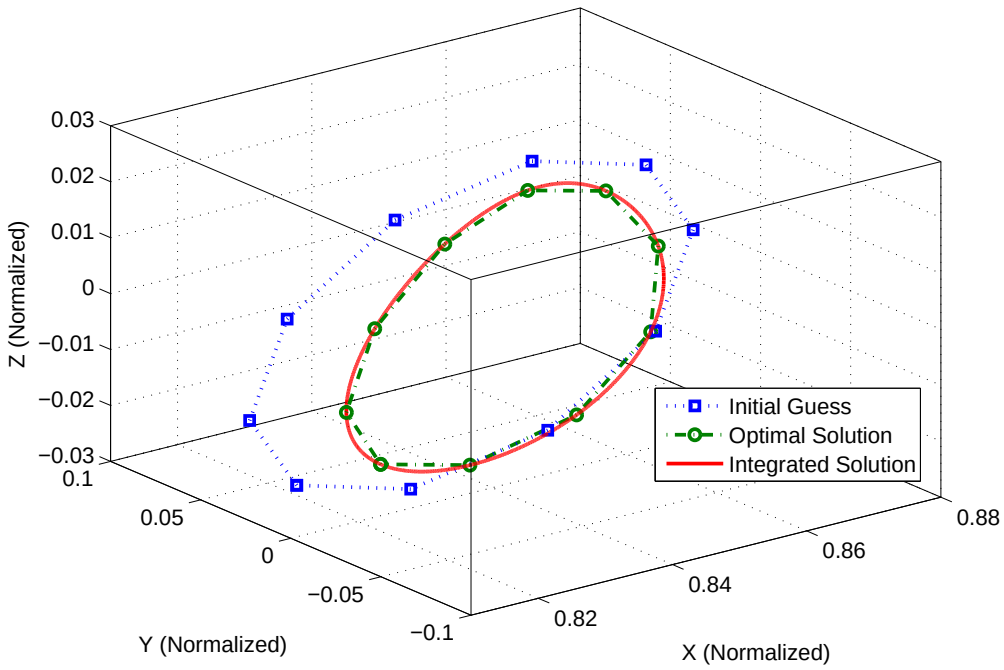

Figure 3.3: Periodic orbit about Earth-Moon L_1 Lagrange point $A_z = 8000$ km.

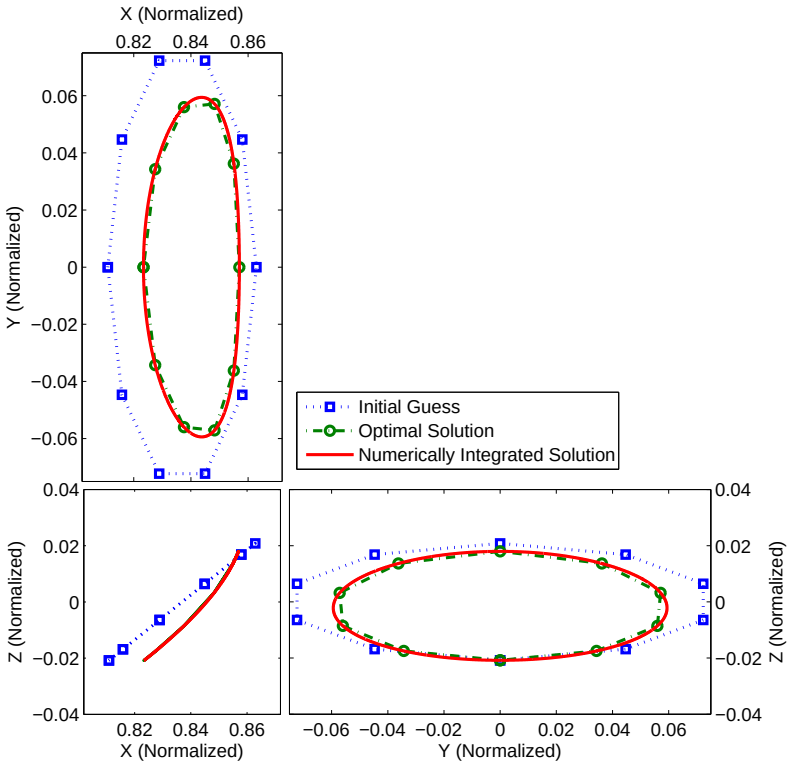

Figure 3.4: Periodic orbit about Earth-Moon L_1 Lagrange point $A_z = 8000$ km.

For calculations of families of periodic orbits homotopy can be employed, i.e. the solution for a periodic orbit of a certain amplitude is used as an initial guess in the calculation of a periodic orbit with a similar amplitude and this process is continued. Figures 3.5, 3.6 and 3.7 show families of halo, vertical and Lyapunov periodic orbits respectively.

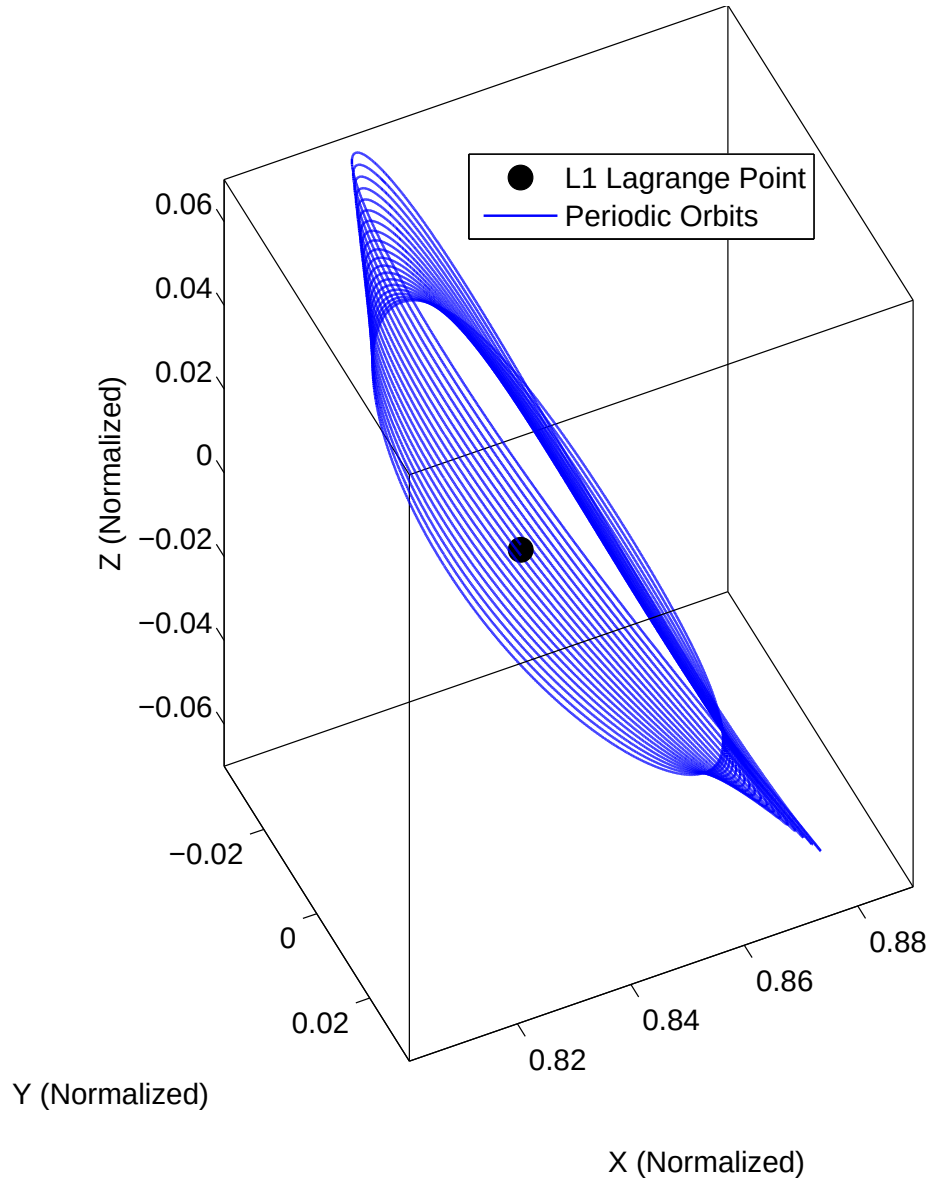

Figure 3.5: Family of Halo orbits about Earth-Moon L_1 Lagrange point $A_z \in [1000, 20000]$ km.

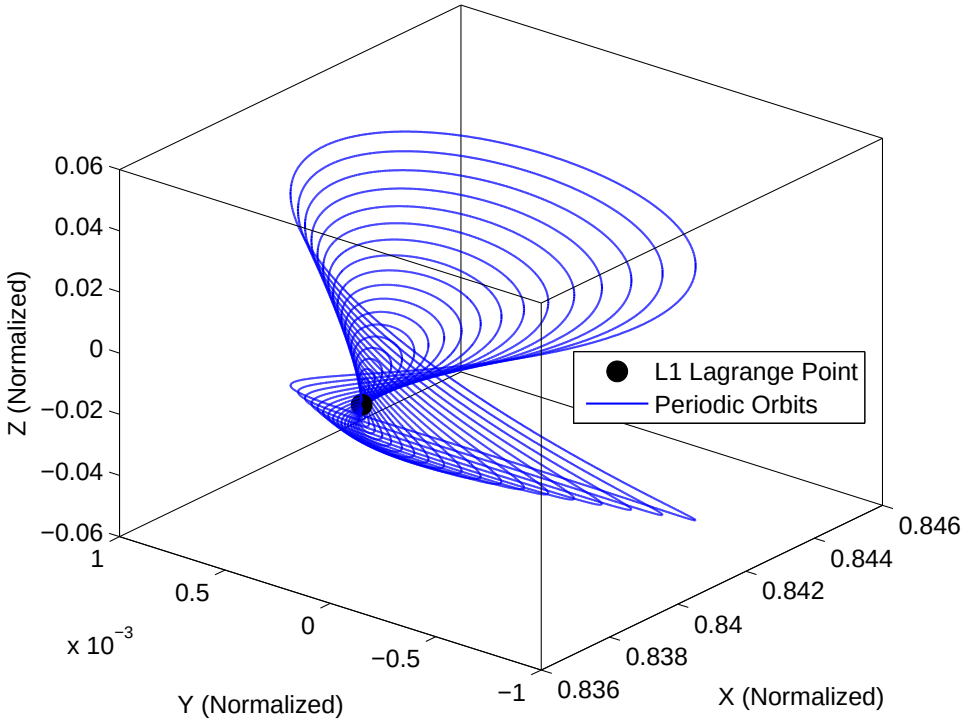

Figure 3.6: Family of vertical periodic orbits about Earth-Moon L_1 Lagrange point $A_z \in [1000, 20000]$ km.

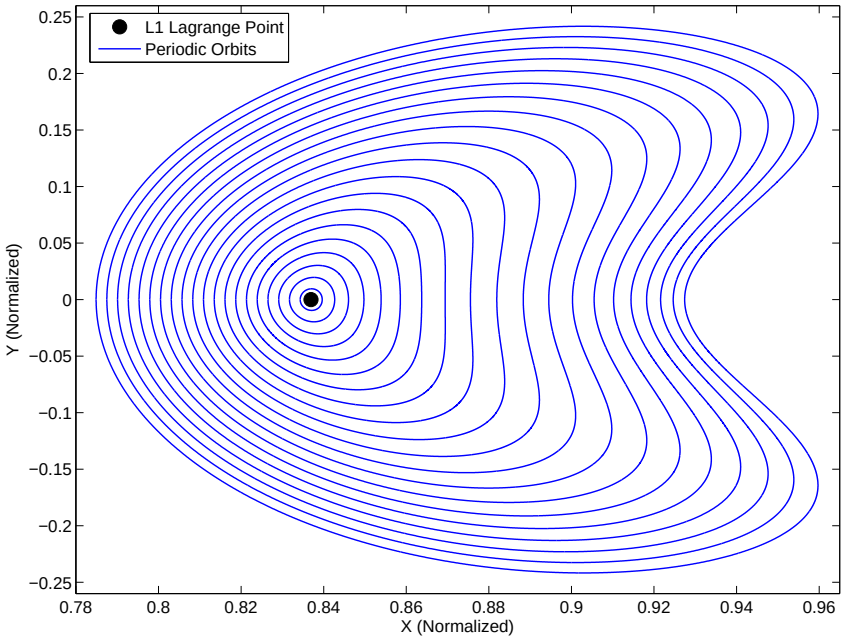

Figure 3.7: Family of Lyapunov periodic orbits about Earth-Moon L_1 Lagrange point $A_x \in [1000, 20000]$ km.

The accuracy of the Runge-Kutta and Taylor series methods depend on the number of segments used to discretize the trajectory. The problem was solved using the native MATLAB NLP solver *fmincon* with feasibility and optimality tolerances of 10^{-12}. The error is taken as the Euclidean norm of the difference between the initial state and the terminal state, that is, after the trajectory has been integrated forward in time for one period. The Matlab routine *ode45* with minimum possible relative tolerance allowed by Matlab ($\approx 2 \times 10^{-14}$) was used for the numerical integration.

The results for the Taylor series shooting method (2.17), (2.19) for various Taylor series lengths are shown in Figure 3.8. To allow for more direct comparison with the Runge-Kutta multiple shooting method, the same number of subsegments (3) were used in both methods. The results show that the later the Taylor series is truncated, the more accurate the periodic orbit obtained. At least up to a certain point, in this instance the higher-order terms (> 30) do not contribute to the Taylor series as the results for 30, 40 and 50 terms are identical. Accurate periodic orbits can be generated with extremely coarse meshes. A periodic orbit with an error of less than the optimality tolerance (10^{-12}) can be generated using only 4 segments if 30 (or more) terms are retained in the Taylor series.

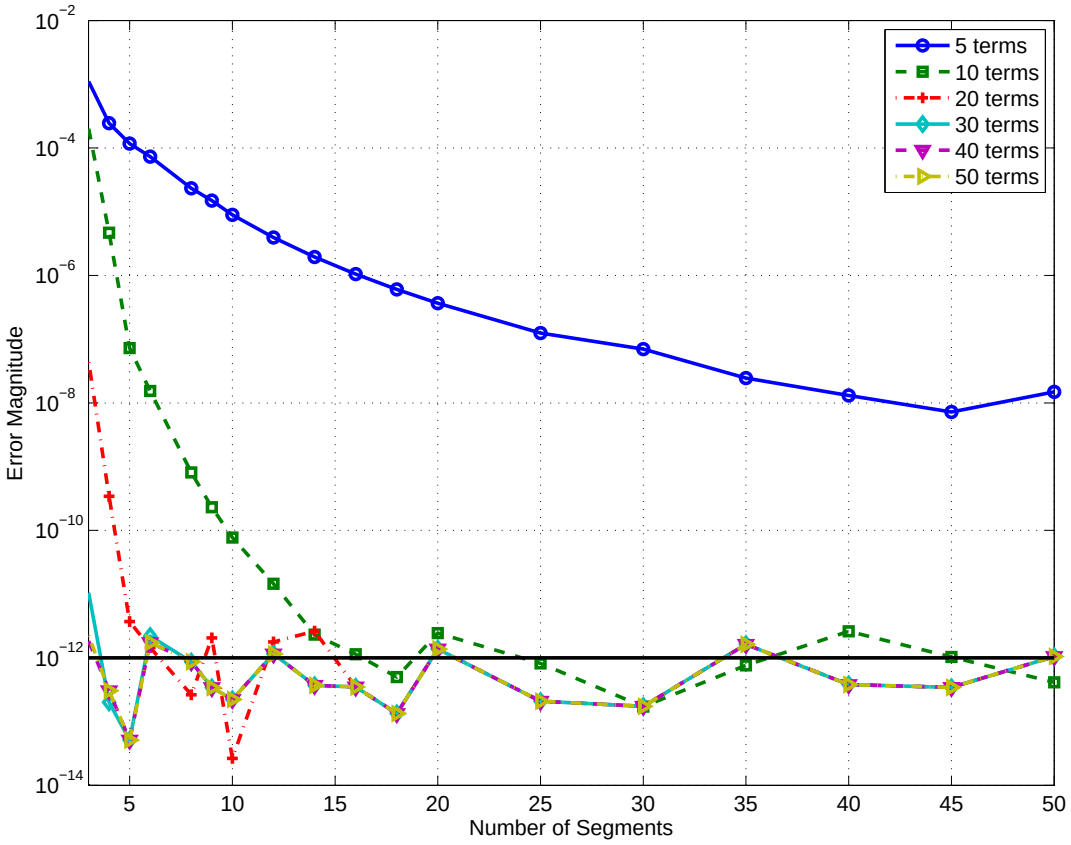

Figure 3.8: Error magnitude for periodic orbit generation with Taylor series multiple shooting constraints.

Periodic orbits were also generated using the higher-order collocation constraints (2.20). The results are shown in Figure 3.9. Interpolating polynomials of odd degree were used to preserve symmetry; so the same number of derivatives are required at each segment boundary. The more derivatives used, and hence the higher-order interpolating polynomial used, the more accurate the results. This was not necessarily expected as high-order polynomials can suffer from Runge's phenomenon[40] where an increase in the polynomial order can actually significantly increase the error associated with the polynomial fit. Runge's phenomenon does not seem to affect this application. A periodic orbit with an error approximately equal to the optimality tolerance (10^{-12}) can be generated using 8 segments and a 19^{th} degree polynomial.

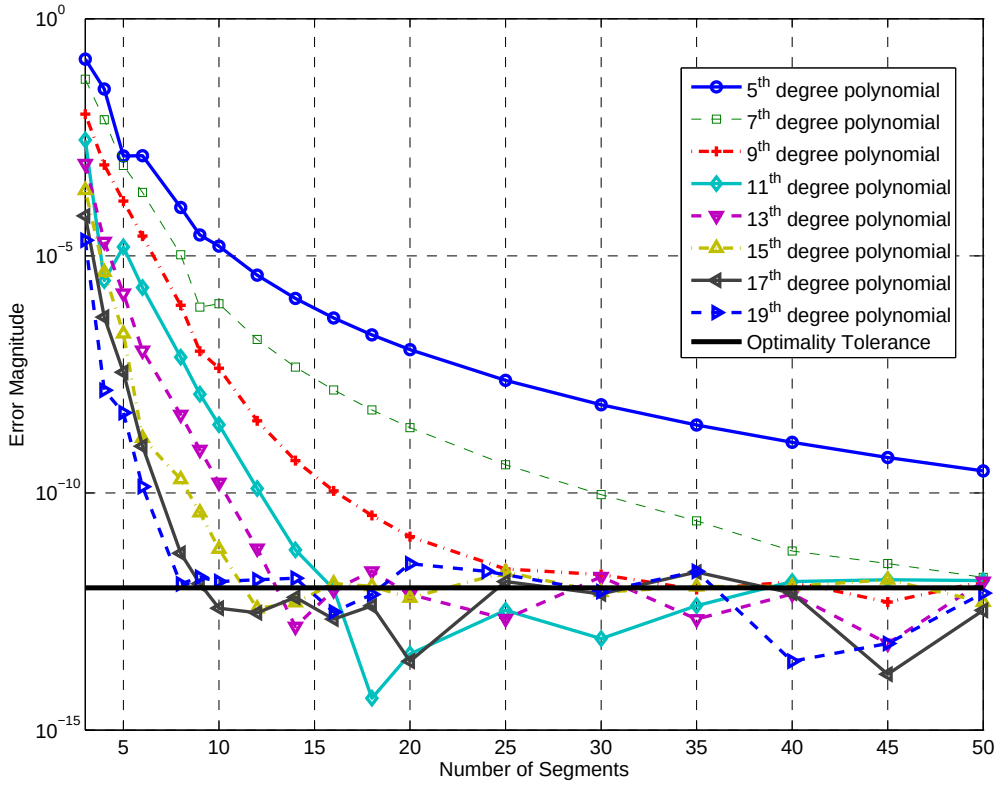

Figure 3.9: Error magnitude for periodic orbit generation with higher-order collocation.

A comparison of the results for Taylor series shooting, Taylor series collocation and Runge-Kutta multiple shooting constraints is shown in Figure 3.10. Results for certain Taylor series lengths and collocation polynomial orders are omitted for clarity. The results show that the two Taylor-series-based methods vastly outperform the Runge-Kutta multiple shooting method, with only the 5^{th} order Taylor collocation method being less accurate than the Runge-Kutta method in any instance, and even then, only for the 3 and 4 segment cases.

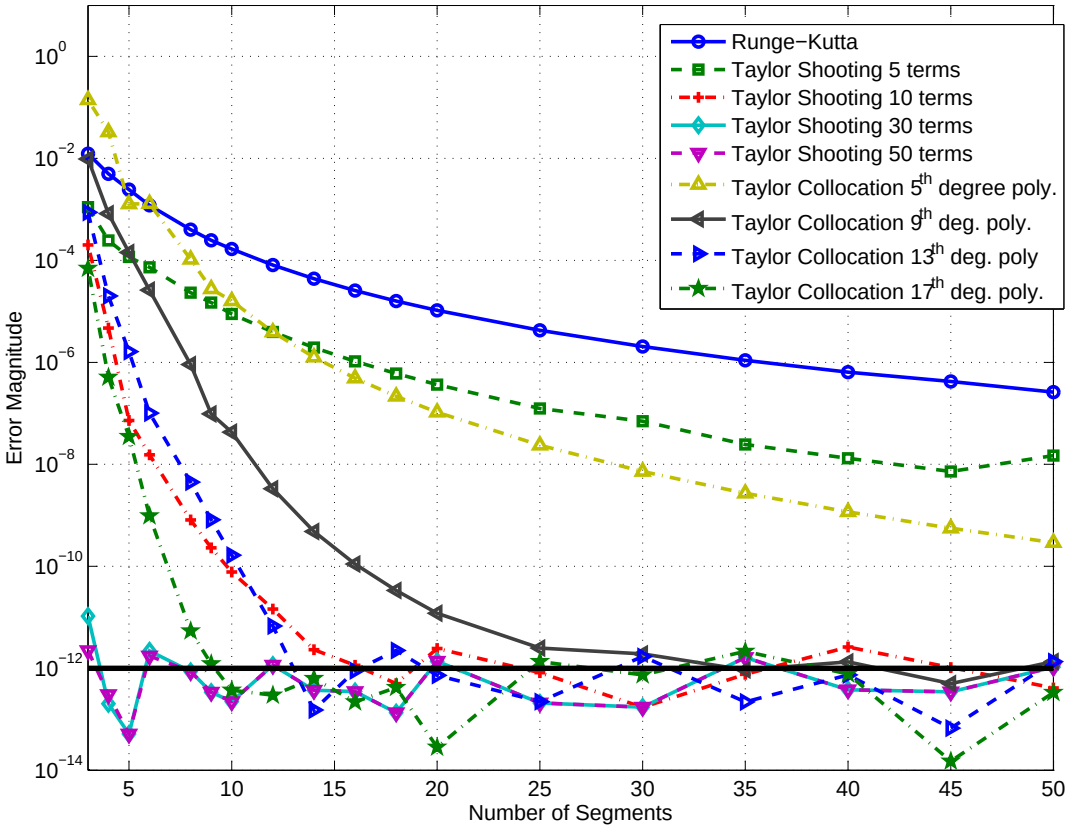

Figure 3.10: Error magnitude for periodic orbit generation with Runge-Kutta multiple shooting, Taylor series multiple shooting and higher-order collocation constraints.

The results so far show that for the same number of segments the Taylor series methods are both more accurate than the Runge-Kutta method. However, the higher derivatives of the states must be computed and as such they require more computation per segment. In order to compare the accuracy obtained with the computational burden for each method we found the minimum number of segments and the CPU time required to ensure the error was below a certain tolerance. The results are shown in Table 3.1. Even with the added burden of computing the higher derivatives, the Taylor series methods are able to produce solutions of similar accuracy faster than the Runge-Kutta method. Additionally, it appears that in this case the more derivatives used (more terms in the Taylor series or a higher-order polynomial approximation) the more accurate the solution.

# Segments CPU time (s)	Runge	Taylor Series Shooting (#terms)						Higher-order Collocation (polynomial order)							
Error	Kutta	5	10	20	30	40	50	5	7	9	11	13	15	17	19
10^{-3}	8 1.26	4 9.47	3 3.08					7 6.47	5 2.44	4 1.03		3 0.86	3 1.11		
10^{-4}	12 19.42	6 11.27						9 9.61	7 3.37	6 2.33		4 1.64		3 1.01	3 2.46
10^{-5}	25 70.47	10 10.00	4 5.94					12 15.74		7 6.63	4 1.2	5 1.90	4 1.37		
10^{-6}	40 94.43	18 18.88						16 28.02	9 9.41	8 7.27	7 10.49	6 7.07	5 1.64	4 4.04	
10^{-7}		30 234.78	5 10.88	3 3.54				25 53.6	14 9.33	9 4.12	8 5.32	7 8.94		5 2.3	4 2.84
10^{-8}		45 234.78						30 124.57	18 15.21	12 6.99	10 5.38	8 5.14	6 7.13		5 3.38
10^{-9}			8 5.12	4 7.56				45 383.72	25 28.75	14 10.54	12 6.34	9 4.63	8 9.87	6 12.57	6 19.62
10^{-10}			10		3				30 48.18	18 16.28			9 4.90	7 5.88	
10^{-11}			14 10.74	5 31.19		3 1.42	3 2.44		40 212.15	25 30.90	14 10.01	12 7.20	10 5.25	8 28.67	8 21.04
10^{-12}			18 9.06	8 13.45	4 11.84	4 9.83	4 8.06			35 111.56	16 13.98	14 10.77	12 7.67	10 5.3	16 17.32

Table 3.1: Number of segments (and CPU time(s)) required to ensure the error magnitude is below a certain threshold.

3.3 Example: Maximum Velocity Transfer to Rectilinear Path

This problem is taken from Bryson and Ho[22] and is attractive for comparing solution methods as it is non-trivial but has an analytic solution. A particle of mass m moves in the $x-y$ plane under a thrust force of constant magnitude ma. The angle of the thrust vector with respect to the x axis is the control variable for the system $\beta(t)$. Equations of motion are then

$$\begin{aligned} \dot{x} &= u \\ \dot{y} &= v \\ \dot{u} &= a\cos\beta \\ \dot{v} &= a\sin\beta \end{aligned} \tag{3.15}$$

where u and v are the components of the velocity vector in the x and y directions respectively. The initial and terminal conditions for this problem are:

$$\begin{aligned} x(0) = y(0) = u(0) = v(0) = 0 \\ y(T) = h \\ v(T) = 0 \end{aligned} \tag{3.16}$$

where final time T and final height h are fixed. Both the final x position $x(T)$ and horizontal velocity $u(T)$ are free. The goal is to maximize final velocity, therefore the objective function is:

$$J = -u(T) \tag{3.17}$$

It can be shown that for constant thrust acceleration this optimal control problem has an analytic solution where the control follows a "linear tangent law".[22]

$$\tan\beta = \tan\beta_0 - ct \tag{3.18}$$

The initial control angle β_0 is obtained by solving:

$$\frac{4h}{aT^2} = \frac{1}{\sin\beta_0} - \frac{\log\frac{\sec\beta_0+\tan\beta_0}{\sec\beta_0-\tan\beta_0}}{2\tan^2\beta_0} \tag{3.19}$$

The control law then becomes:

$$\tan\beta = \tan\beta_0\left(1-\frac{2t}{T}\right) \tag{3.20}$$

Integrating the equations of motion with the control law (3.20) produces the following optimal solution:

$$\begin{aligned}
\hat{x} &= \tfrac{a}{c^2}\left(\sec\beta_0 - \sec\beta - \tan\beta\log\tfrac{\tan\beta_0+\sec\beta_0}{\tan\beta+\sec\beta}\right)\\
\hat{y} &= \tfrac{a}{2c^2}\left((\tan\beta_0-\tan\beta)\sec\beta_0 - (\sec\beta_0-\sec\beta)\tan\beta - \log\tfrac{\tan\beta_0+\sec\beta_0}{\tan\beta+\sec\beta}\right)\\
\hat{u} &= \tfrac{a}{c}\log\tfrac{\tan\beta_0+\sec\beta_0}{\tan\beta+\sec\beta}\\
\hat{v} &= \tfrac{a}{c}\left(\sec\beta_0-\sec\beta\right)
\end{aligned} \tag{3.21}$$

where:

$$c = \frac{2\tan\beta_0}{T} \tag{3.22}$$

3.3.1 Maximum Velocity Transfer to Rectilinear Path: *Direct* Results

The problem was solved using the conventional Runge-Kutta method, the new Taylor series method in multiple shooting form and also higher-order collocation, with parameters (a, h, T) equal to $(1, 1, 3)$ respectively. The initial guess for all cases was:

$$\begin{gathered}
x(t) = y(t) = u(t) = v(t) = \beta(t) = 0\\
0 \le t \le T
\end{gathered} \tag{3.23}$$

An example solution is shown in Figure 3.11. The solution was obtained with the Taylor series constraints on an equally spaced mesh of 6 segments with the Taylor series truncated at 20 terms. The control was specified by a variable knot cubic spline with 13 control knots. The optimal control is shown in Figure 3.12. In both cases the optimal solution obtained using direct transcription agrees very closely with the exact analytic solution.

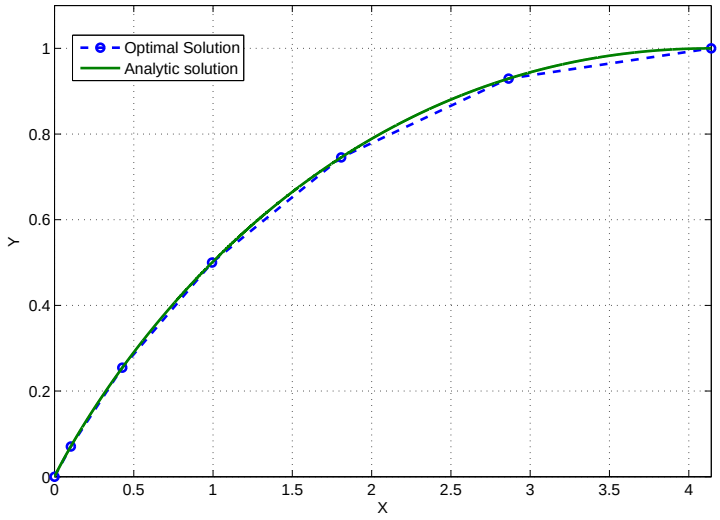

Figure 3.11: Optimal solution solved Taylor series constraints using 6 segments.

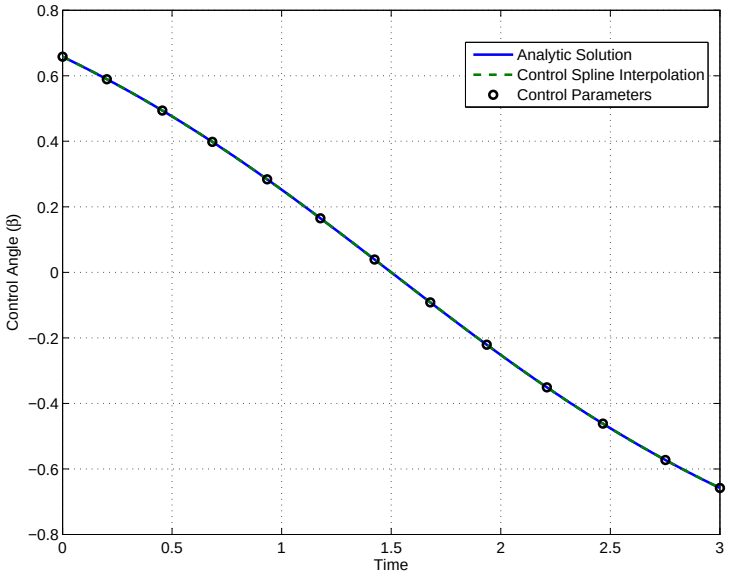

Figure 3.12: Optimal control angle using variable knot spline control parameterizaton with 13 control points.

In order to compare the solutions obtained for various control parameterizations and meshes we consider three error measurements:

1. The maximum difference between the exact analytic control β and the control given particular control parameterization used:

$$\max_{i\in[1,6N+1]} \left|\hat{\beta}\left(t_i\right) - \beta\left(t\right)\right| \tag{3.24}$$

   where N is the number of segments. For direct comparison with the Runge-Kutta method this difference was taken at every point where the control would be specified using the Runge-Kutta method, i.e. at every segment boundary as well as at 5 uniformly spaced interior points.

2. The maximum difference between every state (x, y, u, v) in the solution obtained and the corresponding state in the exact analytic solution (equation (3.21), at any segment boundary:

$$\frac{\sum_{i=1}^{N+1}\left(\left|\hat{x}\left(t_i\right) - x\left(t_i\right)\right| + \left|\hat{y}\left(t_i\right) - y\left(t_i\right)\right| + \left|\hat{u}\left(t_i\right) - u\left(t_i\right)\right| + \left|\hat{v}\left(t_i\right) - v\left(t_i\right)\right|\right)}{N+1} \tag{3.25}$$

3. The difference between the objective value ($J = -u(T)$) in the solution found and that from the exact analytic solution (equation (3.21):

$$|u(T) - \hat{u}(T)| \tag{3.26}$$

More accurate solutions are obtained if more terms in the Taylor series are retained, however, more computation is required to calculate the extra derivatives required. As shown in Table 3.2 any terms retained after the 20th do not contribute to the solution at double precision. The examples shown in Table 3.2 are for piecewise linear control with 6 subsegments. Similar results were obtained for other control parameterizations but were omitted for brevity. All subsequent results for Taylor series shooting constraints in this section will be for Taylor series truncated at 20 terms.

Objective Function Error	Taylor Series					
Segments	5	10	20	30	40	50
2	1.9070348E-07	1.7890538E-07	1.7890538E-07	1.7890538E-07	1.7890538E-07	1.7890538E-07
3	3.6009463E-08	3.4976562E-08	3.4976562E-08	3.4976562E-08	3.4976562E-08	3.4976562E-08
4	1.1210701E-08	1.1027048E-08	1.1027047E-08	1.1027047E-08	1.1027047E-08	1.1027047E-08
5	4.5573572E-09	4.5092348E-09	4.5092365E-09	4.5092365E-09	4.5092365E-09	4.5092365E-09
6	2.1889184E-09	2.1728095E-09	2.1728095E-09	2.1728095E-09	2.1728095E-09	2.1728095E-09
7	1.1784089E-09	1.1720243E-09	1.1720256E-09	1.1720256E-09	1.1720256E-09	1.1720256E-09
8	6.9025408E-10	6.8738659E-10	6.8738615E-10	6.8738615E-10	6.8738615E-10	6.8738615E-10
9	4.3012482E-10	4.2871173E-10	4.2871084E-10	4.2871084E-10	4.2871084E-10	4.2871084E-10
10	2.8261082E-10	2.8186342E-10	2.8186431E-10	2.8186431E-10	2.8186431E-10	2.8186431E-10
12	1.3647172E-10	1.3622303E-10	1.3622170E-10	1.3622170E-10	1.3622170E-10	1.3622170E-10
14	7.4096285E-11	7.3994588E-11	7.3993256E-11	7.3993256E-11	7.3993256E-11	7.3993256E-11
16	4.3892001E-11	4.3852921E-11	4.2961634E-11	4.2961634E-11	4.2961634E-11	4.2961634E-11
18	2.7881697E-11	2.8703706E-11	2.7842173E-11	2.7842173E-11	2.7842173E-11	2.7842173E-11
20	1.7661428E-11	1.7650326E-11	1.7648105E-11	1.7648105E-11	1.7648105E-11	1.7648105E-11

Table 3.2: Objective function error for direct solution using Taylor series shooting and piecewise linear control.

The problem was also solved using higher-order collocation. For the solutions using Taylor series shooting, piecewise linear control with 6 subsegments was used. The same control could not be used with higher-order location as some control points, in particular the 2nd and the 5th, would not affect the state derivatives at the collocation point or at one of the segment boundaries. Therefore these control values would have no effect on the solution and would not change from their initial value. This is why only 3 subsegments were used for piecewise linear control.

The higher-order collocation method converged to the optimal solution for most of the interpolating polynomials tested. However, unlike the periodic orbit generation example it appears that in this case the higher-order polynomials are unstable. In particular the 17th and 19th degree polynomials perform poorly. Additional polynomial orders after the 11th appear not to increase the accuracy enough to justify the extra computation. Therefore 11th degree collocation

was used to obtain the solutions shown in the remainder of this section. The results of various orders for various numbers of segments are shown in Figures 3.13-3.15.

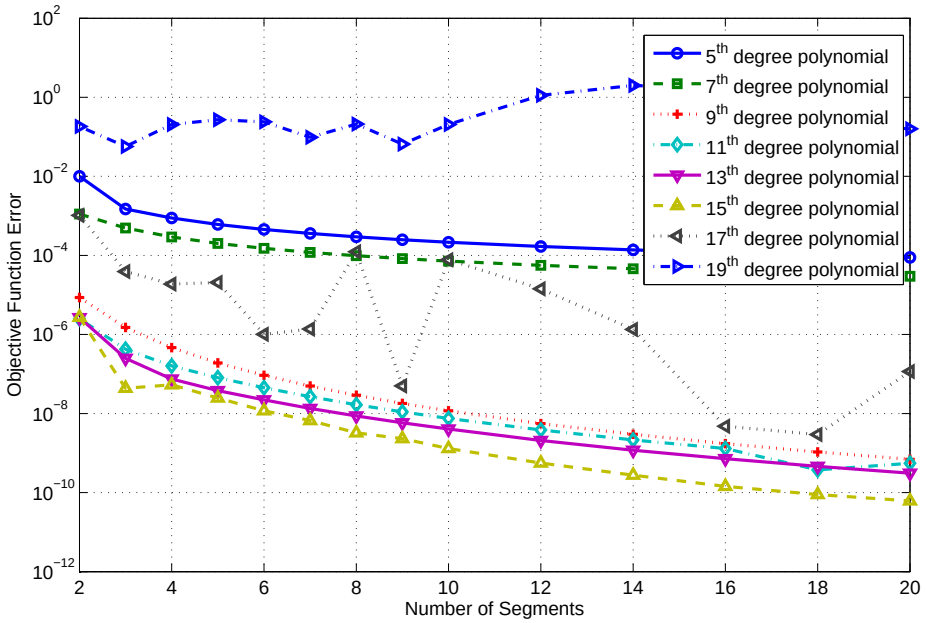

Figure 3.13: Objective function error for direct solution using higher-order collocation and piecewise linear control.

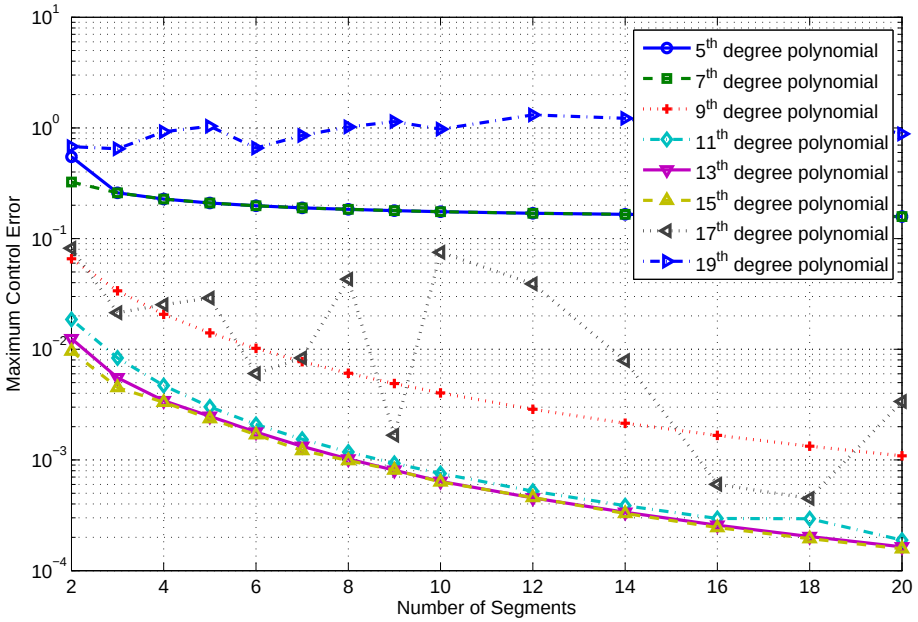

Figure 3.14: Maximum difference in control angle between (exact) analytic solution and direct solution found using higher-order collocation and piecewise linear control.

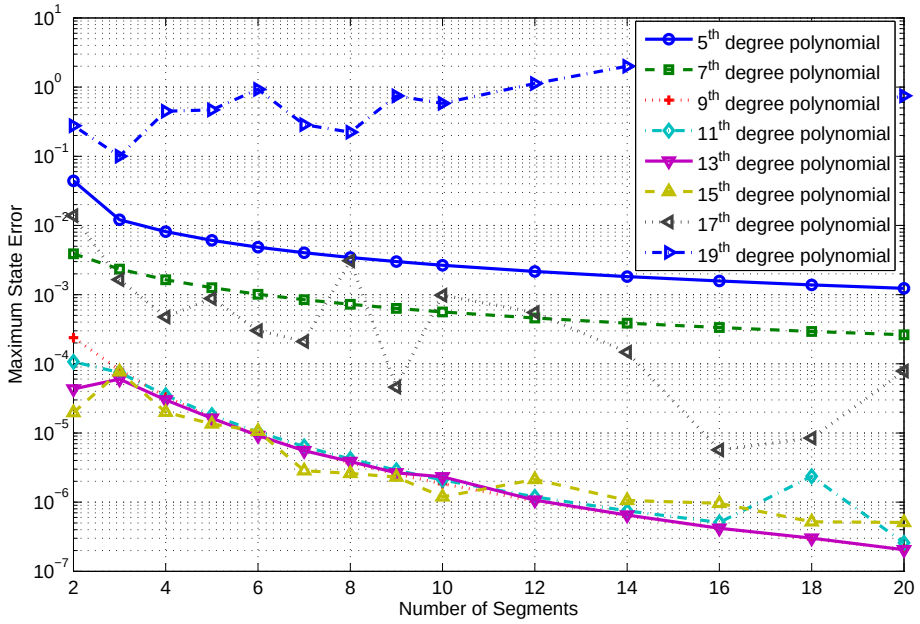

Figure 3.15: Maximum state error for direct solution using higher-order collocation and piecewise linear control.

The problem was also solved using the conventional Runge-Kutta multiple shooting constraints. A comparison of the errors for Taylor series shooting, higher-order collocation and Runge-Kutta multiple shooting constraints for various control parameterizations was performed, the results are shown in Figures 3.16-3.18. For all cases solved using Taylor series shooting constraints, 20 terms of the Taylor series were retained. For all cases solved using higher-order collocation an 11^{th} degree interpolating polynomial was used.

The maximum control error (cf. Figure 3.16) for the Runge-Kutta multiple shooting constraints is relatively constant regardless of the number of segments used. This behavior is not observed in any of the solutions obtained using Taylor series multiple shooting or higher-order collocation, where in general the finer the mesh used, the smaller the maximum control error. For both constraint formulations, Taylor series multiple shooting and higher-order collocation, the control parameterization using BSplines before perform poorly. The best performing control parameterizations are the splines (fixed and variable knot), which can find solutions that have errors in the objective function (cf. Figure 3.18) that are within the optimality tolerance (10^{-12}) for meshes of 8 or more segments.

Despite being one of the best performing methods based on the maximum control error, the Runge-Kutta multiple shooting method is the worst performing method on the measure of objective function error (cf. Figure 3.18). Recall that the control errors where taken at every point the control value is specified in the Runge-Kutta method (segment

boundaries and at 5 equally space interior points), regardless of how (or where) the control value is specified in the particular control parameterization. This may account for the relatively poor performance of most of the control parameterizations in terms of maximum control error despite their objective function error being small.

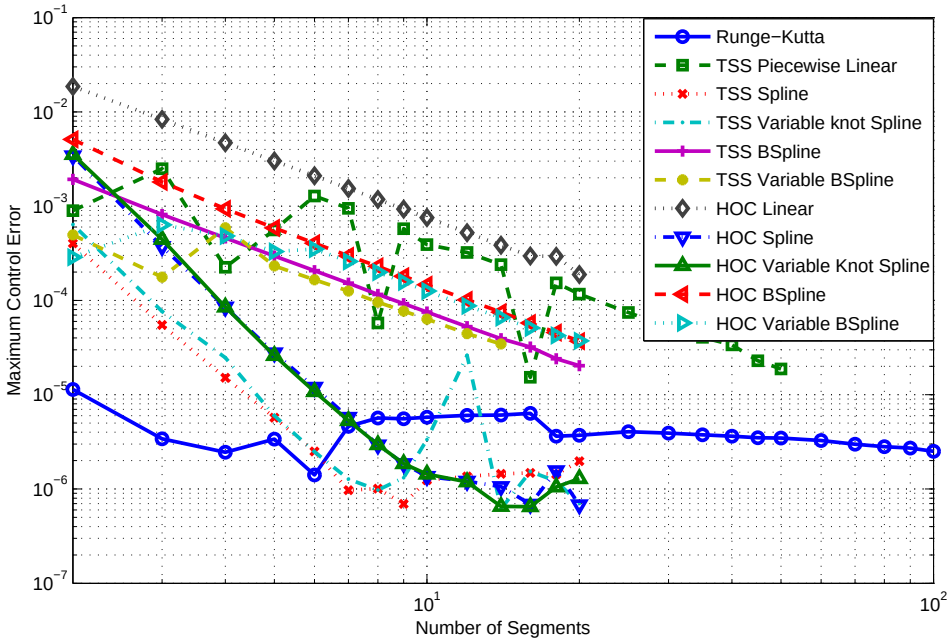

Figure 3.16: Maximum difference in control angle between (exact) analytic solution and direct solution found using Runge-Kutta, Taylor series and higher-order collocation methods for various control parameterizations.

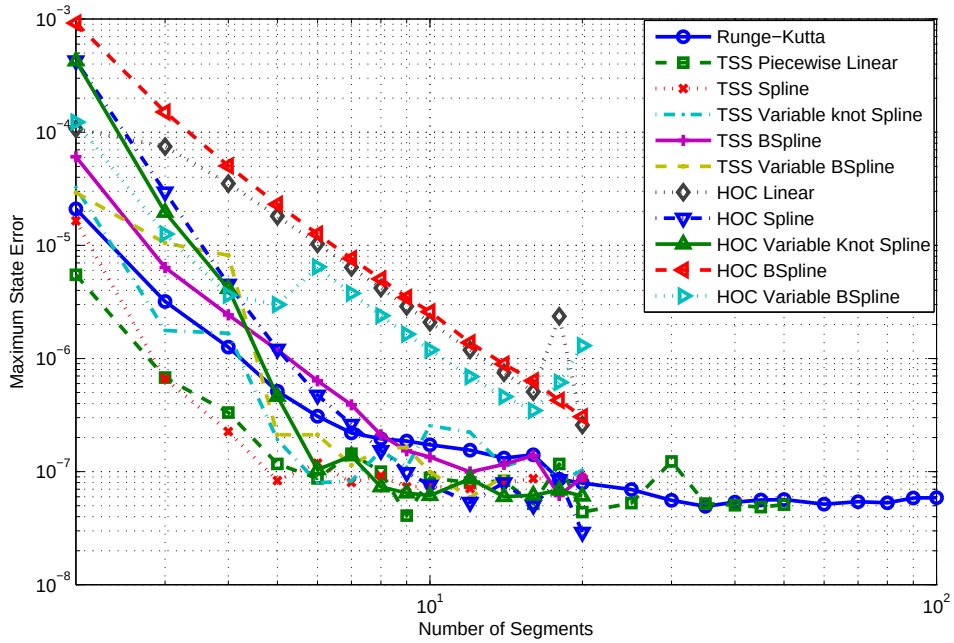

Figure 3.17: Maximum state error in direct solution for Runge-Kutta, Taylor series and higher-order collocation methods for various control parameterizations.

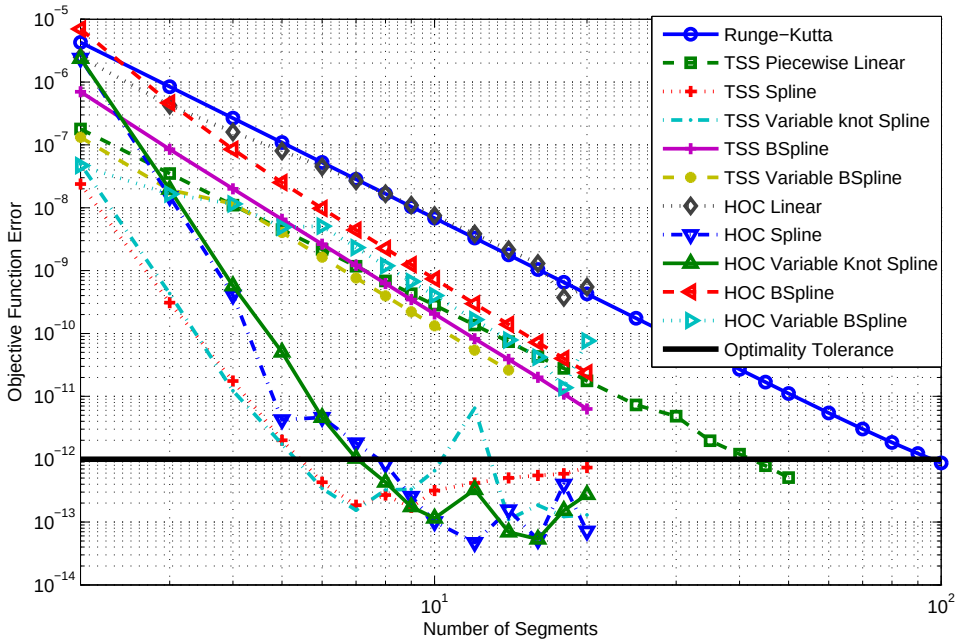

Figure 3.18: Objective function error in direct solution for Runge-Kutta, Taylor series and higher-order collocation methods for various control parameterizations.

The runtime of the NLP problem is related more to the number of parameters in the NLP vector than the number of segments in the mesh (although the two are obviously related). One of the potential benefits of the control parameterizations is being able to describe the control in fewer NLP optimization parameters. Figure 3.19 shows the error in the objective function as a function of the size of the NLP parameter vector.

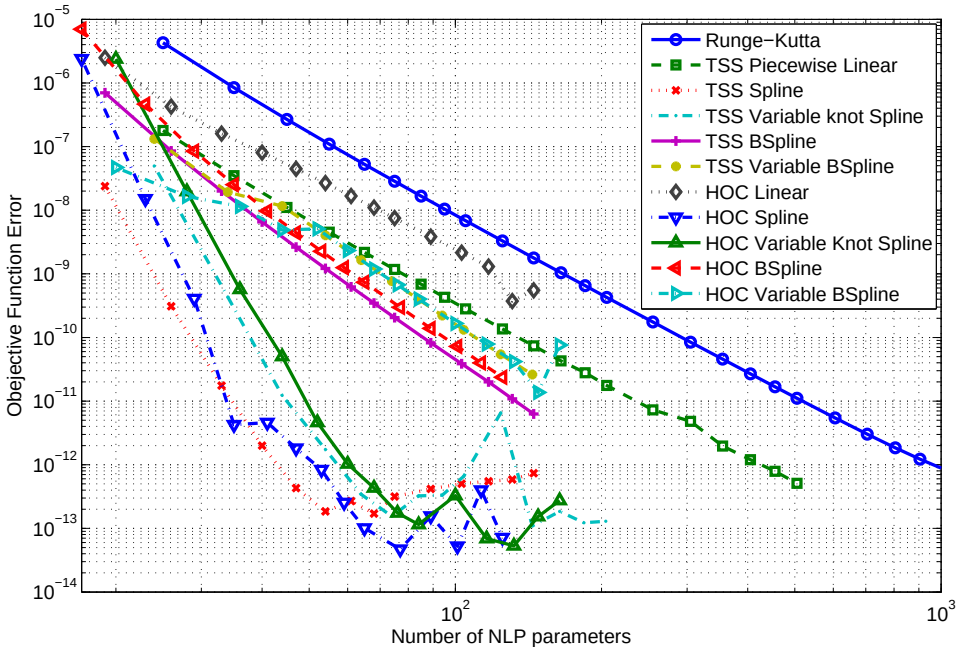

Figure 3.19: Objective function error in direct solution for Runge-Kutta and Taylor series methods for various control parameterizations.

The results for objective function error (shown in Figure 3.19) show that both new methods, the Taylor series multiple shooting and the higher-order collocation, achieve greater accuracy than the Runge-Kutta method for similarly sized NLP vectors. The cubic spline control parameterization produced the best performance for both shooting and collocation. In this case the added flexibility of allowing the spline knots to move in time does not significantly increase the accuracy.

3.3.2 Maximum Velocity Transfer to Rectilinear Path: *Indirect* Results

The indirect solution requires the addition of the costate equations:

$$\begin{aligned} \dot{\lambda}_x &= 0 \\ \dot{\lambda}_y &= 0 \\ \dot{\lambda}_u &= -\lambda_x \\ \dot{\lambda}_v &= -\lambda_y \end{aligned} \tag{3.27}$$

with terminal conditions:

$$\begin{aligned} \lambda_x(T) &= 0 \\ \lambda_y(T) &= \upsilon_y \\ \lambda_u(T) &= 1 \\ \lambda_v(T) &= \upsilon_v \end{aligned} \tag{3.28}$$

The terminal conditions for the state variables (x, y, u, v) are unchanged. The optimal control must be found. The Hamiltonian of the system is:

$$H = a\lambda_u \cos\beta + a\lambda_v \sin\beta + \lambda_x u + \lambda_y v \tag{3.29}$$

Define control unit vector σ:

$$\boldsymbol{\sigma} = \begin{bmatrix} \cos\beta \\ \sin\beta \end{bmatrix} \tag{3.30}$$

and velocity costate vector $\boldsymbol{\lambda_v}$:

$$\boldsymbol{\lambda}_w = \begin{bmatrix} \lambda_u \\ \lambda_v \end{bmatrix} \tag{3.31}$$

The Hamiltonian then becomes:

$$H = a\boldsymbol{\lambda}_w^T\boldsymbol{\sigma} + \lambda_x u + \lambda_y v \tag{3.32}$$

By the Pontryagin minimum principle the optimal control will minimize the Hamiltonian. This is clearly when the unit control vector σ directly opposes the velocity costate vector $\boldsymbol{\lambda_w}$. Therefore:

$$\boldsymbol{\sigma} = \frac{-\boldsymbol{\lambda}_w}{|\boldsymbol{\lambda}_w|} \tag{3.33}$$

The control law is then:

$$\begin{aligned} \cos\beta &= \frac{-\lambda_u}{\sqrt{\lambda_u^2+\lambda_v^2}} \\ \sin\beta &= \frac{-\lambda_v}{\sqrt{\lambda_u^2+\lambda_v^2}} \end{aligned} \tag{3.34}$$

The full state and costate equations become:

$$\begin{aligned}
\dot{x} &= u \\
\dot{y} &= v \\
\dot{u} &= -a\frac{\lambda_u}{\sqrt{\lambda_u^2+\lambda_v^2}} \\
\dot{v} &= -a\frac{\lambda_v}{\sqrt{\lambda_u^2+\lambda_v^2}} \\
\dot{\lambda}_x &= 0 \\
\dot{\lambda}_y &= 0 \\
\dot{\lambda}_u &= -\lambda_x \\
\dot{\lambda}_v &= -\lambda_y
\end{aligned} \tag{3.35}$$

This increases the number of state variables to eight. As for the direct case, the problem was solved using both the Runge-Kutta and the Taylor series methods to form the constraints. The initial guess was:

$$\begin{gathered}
x(t) = y(t) = u(t) = v(t) = \lambda_x(t) = \lambda_y(t) = 0 \\
\lambda_u(t) = \lambda_v(t) = 1 \\
0 \leq t \leq T
\end{gathered} \tag{3.36}$$

An example optimal solution is shown in Figure 3.20 and the corresponding optimal control is shown in Figure 3.21. The example solution was obtained by solving the NLP using the Taylor series constraints (truncated at 30 terms) on an equal mesh with 5 segments and 3 subsegments. The graphs show that the optimal solution obtained using this method very closely agrees with the exact analytic solution.

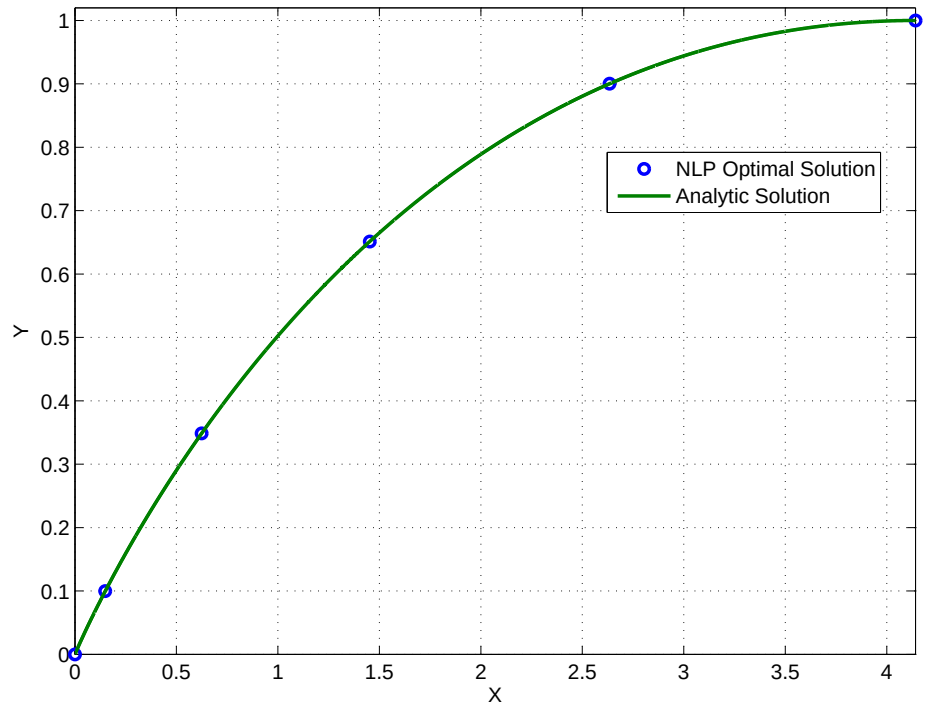

Figure 3.20: Optimal solution for Maximum Velocity Transfer to Rectilinear Path problem.

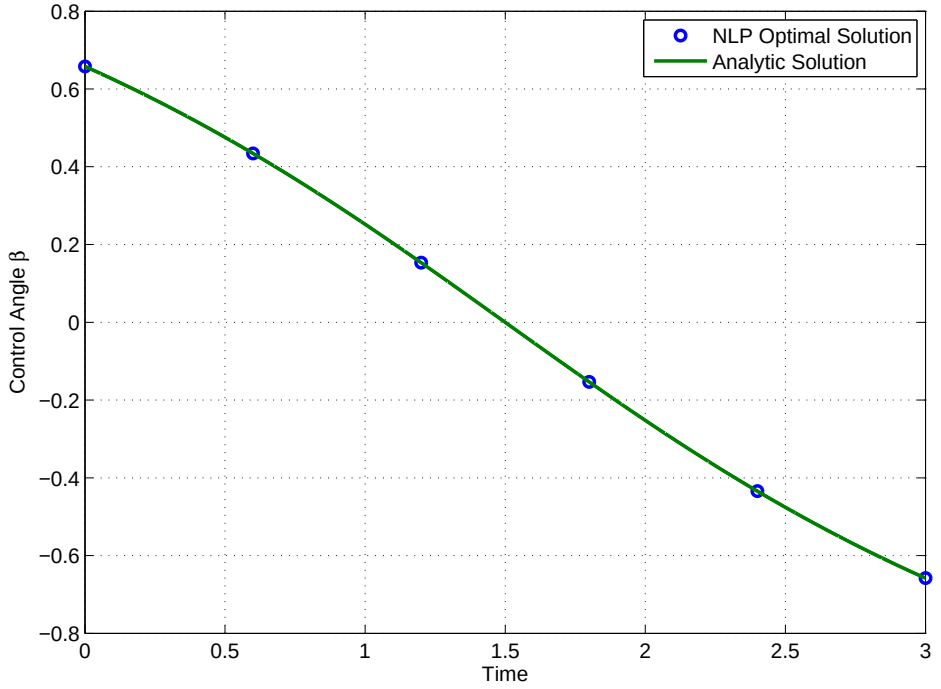

Figure 3.21: Optimal control history for Maximum Velocity Transfer to Rectilinear Path problem.

In order to compare the solutions obtained from various methods we consider five error measurements:

1. The maximum difference between the exact analytic control β and the control given by the control law, equation (3.34), at any segment boundary:

$$\max_{i=1,..,N+1} \left(\tan^{-1} \frac{\lambda_{v_i}}{\lambda_{u_i}} - \beta\left(t_i\right) \right) \tag{3.37}$$

   where N is the number of segments.

2. The mean of the difference between the exact analytic control β and the control given by the control law, equation (3.34), at every segment boundary:

$$\frac{\sum_{i=1}^{N+1} \left(\tan^{-1} \frac{\lambda_{v_i}}{\lambda_{u_i}} - \beta\left(t_i\right) \right)}{N+1} \tag{3.38}$$

3. The maximum difference between any state (x, y, u, v) in the solution found and the corresponding state in the exact analytic solution (equation (3.21), at any segment boundary:

$$\max_{i=1,..,N+1} \left(\max \left(\left| \hat{x}\left(t_i\right) - x\left(t_i\right) \right|, \left| \hat{y}\left(t_i\right) - y\left(t_i\right) \right|, \left| \hat{u}\left(t_i\right) - u\left(t_i\right) \right|, \left| \hat{v}\left(t_i\right) - v\left(t_i\right) \right| \right) \right) \tag{3.39}$$

4. The mean of difference between every state (x, y, u, v) in the solution found and the corresponding state in the exact analytic solution (equation (3.21), at any segment boundary:

$$\frac{\sum_{i=1}^{N+1} \left(\left| \hat{x}\left(t_i\right) - x\left(t_i\right) \right| + \left| \hat{y}\left(t_i\right) - y\left(t_i\right) \right| + \left| \hat{u}\left(t_i\right) - u\left(t_i\right) \right| + \left| \hat{v}\left(t_i\right) - v\left(t_i\right) \right| \right)}{N+1} \tag{3.40}$$

5. The difference between the objective value $(J = -u(T))$ in the solution found and that from the exact analytic solution (equation (3.21):

$$\left| u\left(T\right) - \hat{u}\left(T\right) \right| \tag{3.41}$$

The indirect problem was solved using Taylor series shooting constraints on a uniformly spaced mesh. The results for various meshes and Taylor series lengths are shown in Figures 3.22 - 3.26. In all cases the solution was found using the MATLAB function *fmincon* with the optimality and feasibility tolerances both set to 10^{-12} and 3 subsegments per segment.

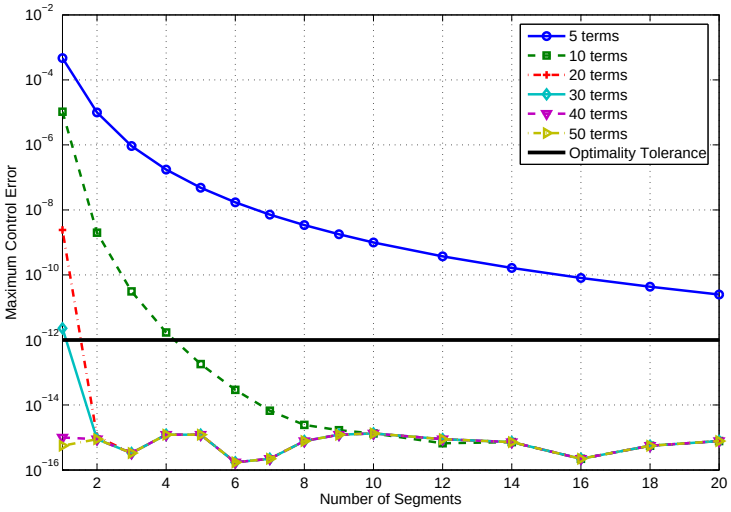

Figure 3.22: Maximum difference in control angle between (exact) analytic solution and indirect solution found using Taylor series shooting method.

The results show that accurate solutions can be obtained for relatively few segments; 5 segments are all that is required to ensure the maximum control error is less than the optimality tolerance if 10 or more terms of the Taylor series are used. In general the addition of more terms in the Taylor series or more segments in the discretization improves the accuracy, however, it is limited by number format used. In this case the double precision floating point representation was used, so the minimum magnitude of the errors is limited by machine precision ($eps = 2.2204 \times 10^{-16}$). The mean of the control error (cf. Figure 3.23) is approximately equal to the maximum (cf. Figure 3.22), therefore the numerical error is well distributed over the time domain. It appears that using a uniform mesh is reasonable for this problem.

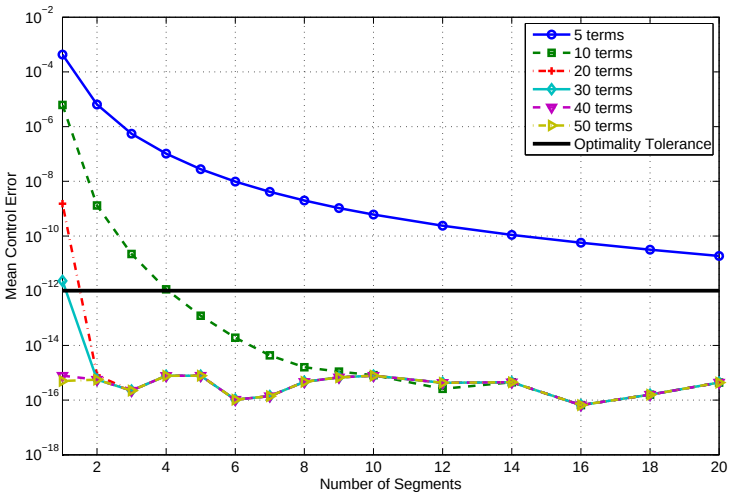

Figure 3.23: Mean control angle deviation from analytic solution in indirect solution for Taylor series shooting method for various orders.

The results for the errors in the state variables, shown in Figures 3.24 and 3.25, and objective function, shown in Figure 3.26, are similar to those seen for the control errors. The errors are less than the optimality tolerance (10^{-12} for all cases with five or more segments and ten or more terms in the Taylor series. The maximum error and mean error are also approximately equal, giving further evidence that a uniform mesh is sufficient for this problem.

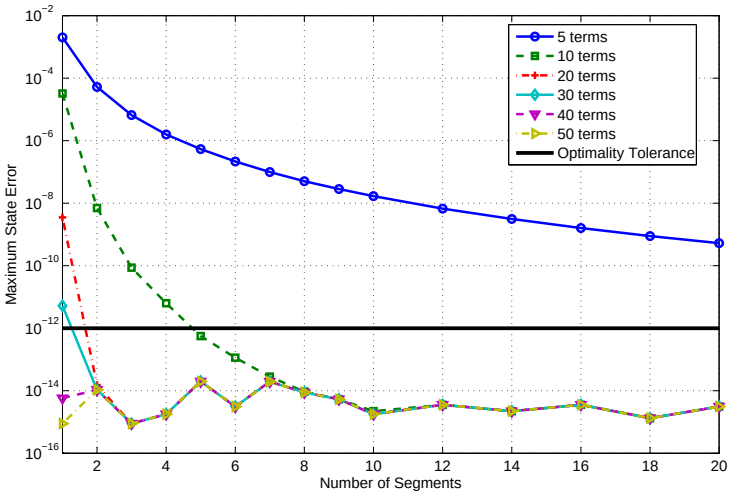

Figure 3.24: Maximum state error in indirect solution for Taylor series shooting method for various orders.

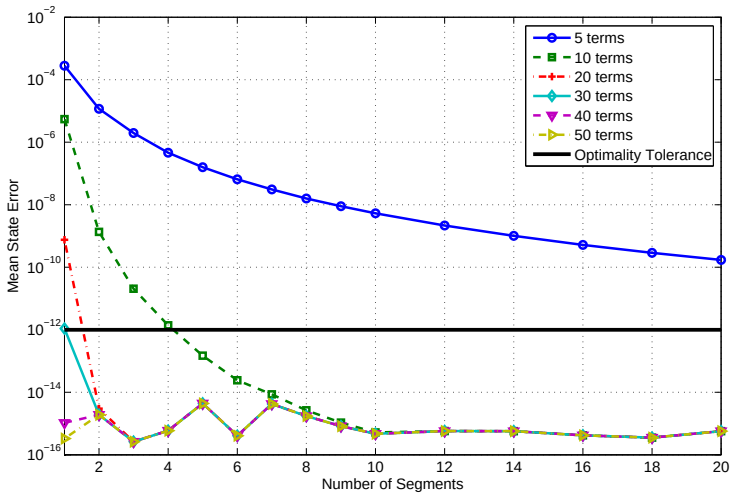

Figure 3.25: Mean state error in indirect solution for Taylor series shooting method for various orders.

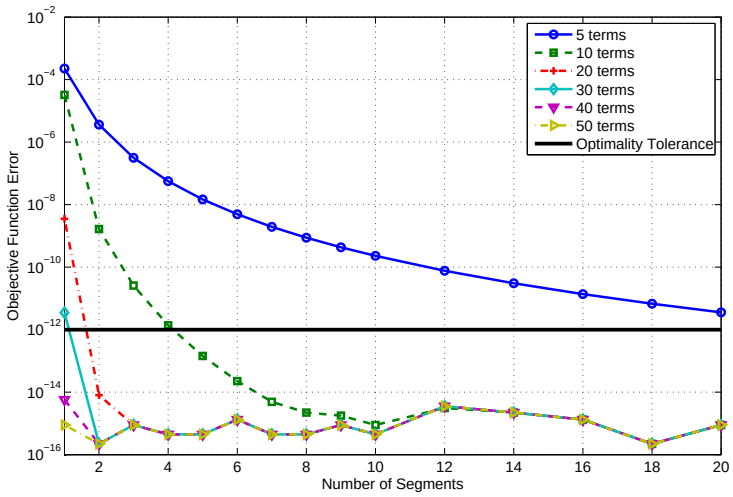

Figure 3.26: Objective function error in indirect solution for Taylor series shooting method for various orders.

The indirect problem was also solved using the Taylor series collocation constraints on a uniformly spaced mesh. The results for various meshes and order of collocation polynomial are shown in Figures 3.27-3.31. In all cases the solution was found using the MATLAB function *fmincon* with the optimality and feasibility tolerances both set to 10^{-12}.

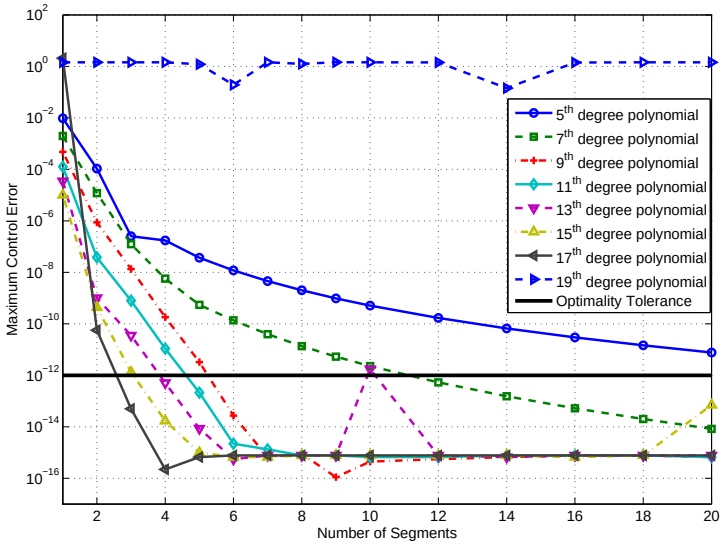

Figure 3.27: Maximum control angle deviation from analytic solution in indirect solutions for various orders of the higher-order collocation method.

Accurate solutions can be obtained using higher-order collocation, however, the 19^{th} degree interpolating polynomial is unstable. It does not converge to the optimal solution for any case attempted. As for the Taylor series shooting method the error is evenly distributed. The maximum (cf. Figure 3.27) and mean control errors (cf. Figure 3.28) are approximately equal.

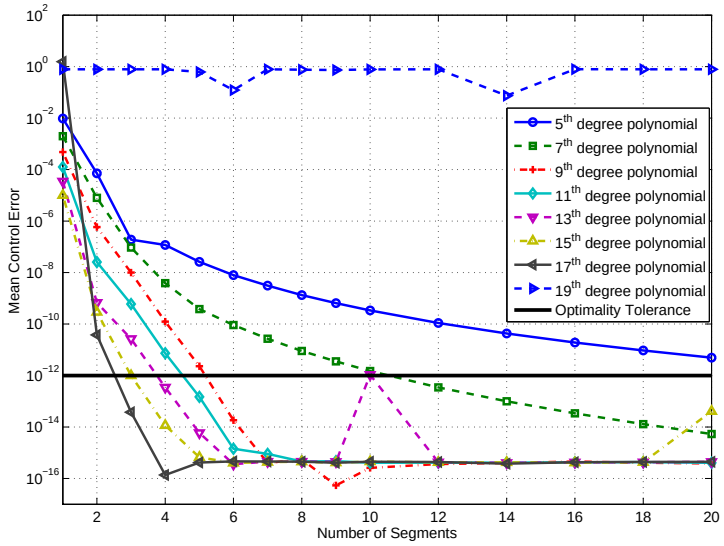

Figure 3.28: Mean control angle deviation from analytic solution in indirect solutions for various orders of the higher-order collocation method.

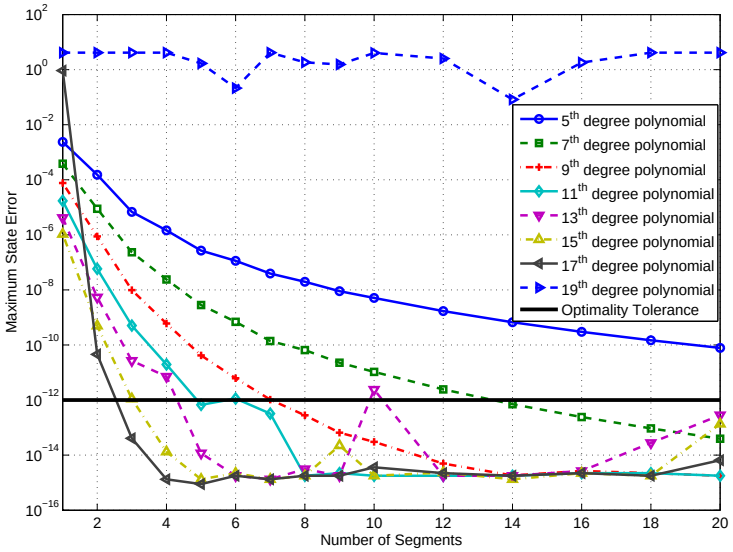

Figure 3.29: Maximum state error in indirect solutions for various orders of the higher-order collocation method.

Similar behavior is seen in the state (cf. Figures 3.29 and 3.30) and objective function errors (cf. Figure 3.31). Accuracy increases with an increase in order of the interpolating polynomial until the 19^{th} degree polynomial where the interpolant becomes unstable and the solution fails to converge. As seen from the large errors in the state variables when using the 19^{th} degree polynomial in Figures 3.29 and 3.30.

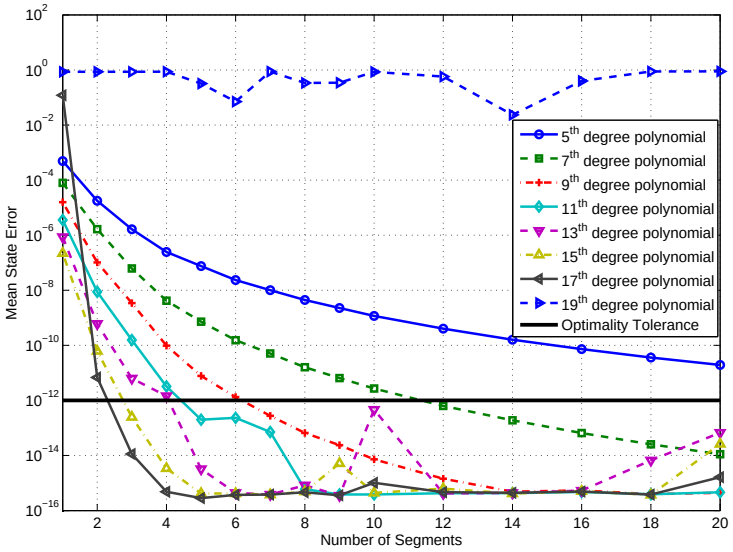

Figure 3.30: Mean state error in indirect solutions for various orders of the higher-order collocation method.

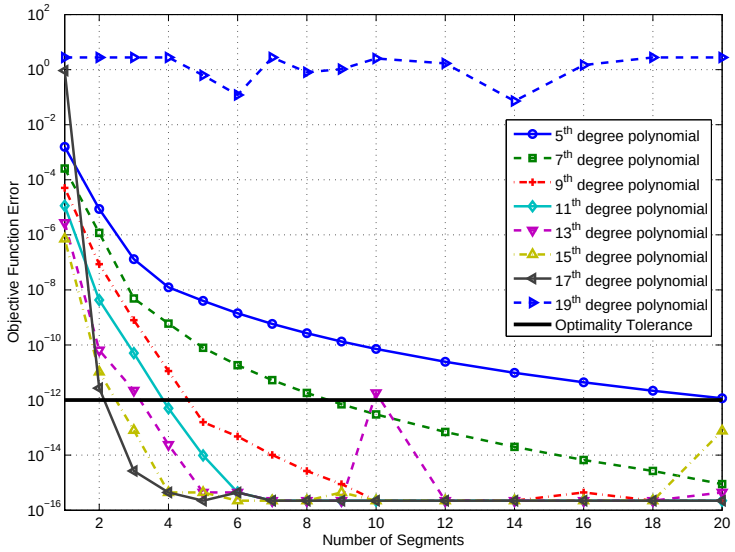

Figure 3.31: Objective function error in indirect solutions for various orders of the higher-order collocation method.

Solutions were also obtained using the conventional Runge-Kutta multiple shooting constraints. Comparisons of the maximum state, maximum control and objective function errors in the solutions obtained using the Runge-Kutta multiple shooting constraints and those obtained with the Taylor series methods are shown in Figures 3.32, 3.33 and 3.34 respectively.

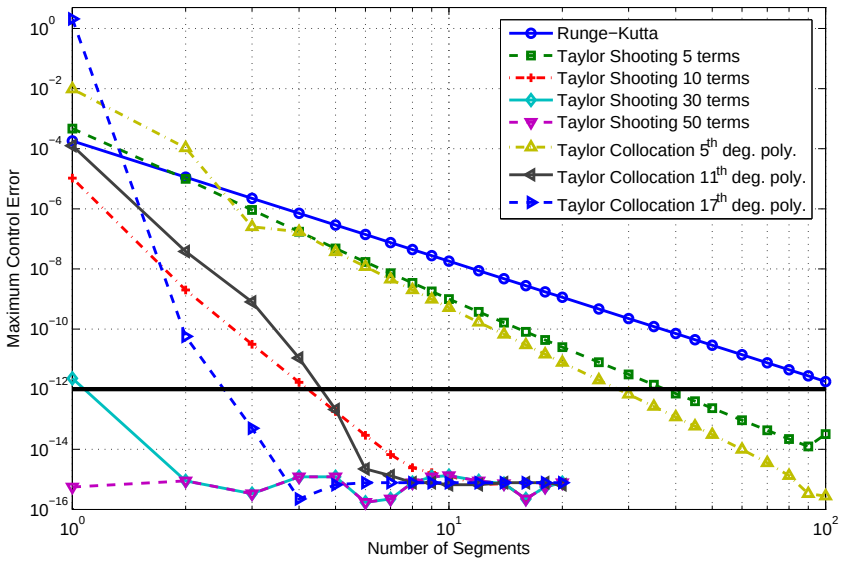

Figure 3.32: Maximum control angle deviation from analytic solution in indirect solution for Runge-Kutta multiple shooting, Taylor series multiple shooting and higher-order collocation constraints.

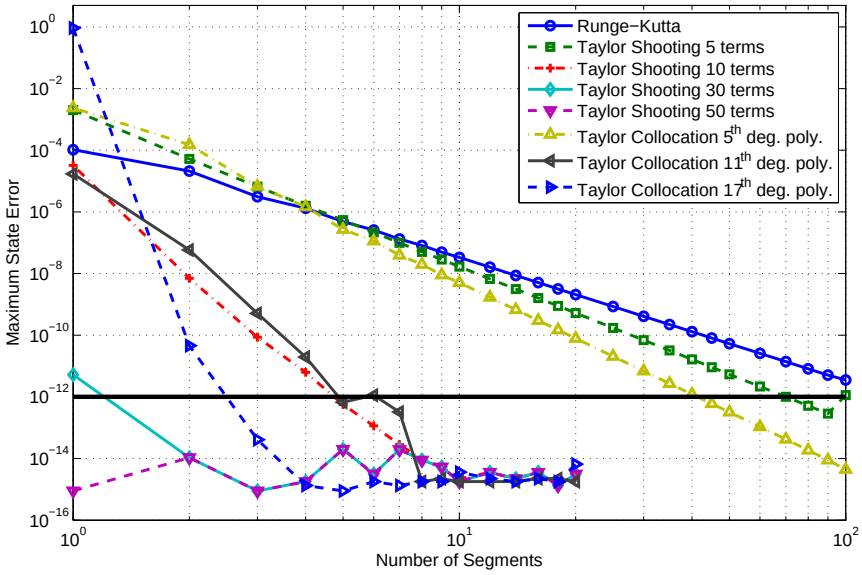

Figure 3.33: Maximum state error in indirect solution for Runge-Kutta multiple shooting, Taylor series multiple shooting and higher-order collocation constraints.

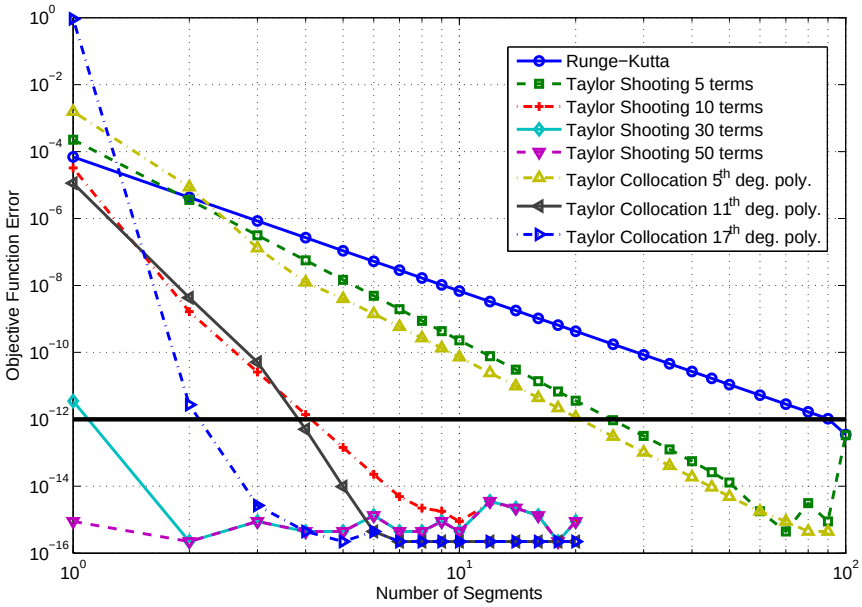

Figure 3.34: Objective function error in indirect solution for Runge-Kutta multiple shooting, Taylor series multiple shooting and higher-order collocation constraints.

For all types of error considered, both of the Taylor series methods outperform the Runge-Kutta method as seen in Figures 3.32-3.34. The Taylor series shooting method is able to reduce errors to near machine precision with only

a single segment if 40 or 50 terms of the Taylor series are retained! Two segments are required to obtain machine precision if 20 or 30 terms are kept, and if 10 terms are kept 10 segments are needed. It is not until the Taylor series is reduced to 5 terms that the performance is comparable to that of the Runge-Kutta method, and even then it is approximately an order of magnitude more accurate. While retaining more terms in the Taylor series results in more accurate solutions, it also requires the calculation of extra derivatives which lengthens the runtime of the optimization, as seen in Figure 3.35. While for the same number of segments the Taylor series solution takes longer to compute, a more apt comparison would be to see how many segments and how much CPU time are required to obtain a solution to a certain accuracy. The results are shown in Table 3.3.2 where the error considered is the maximum control angle error at any segment boundary.

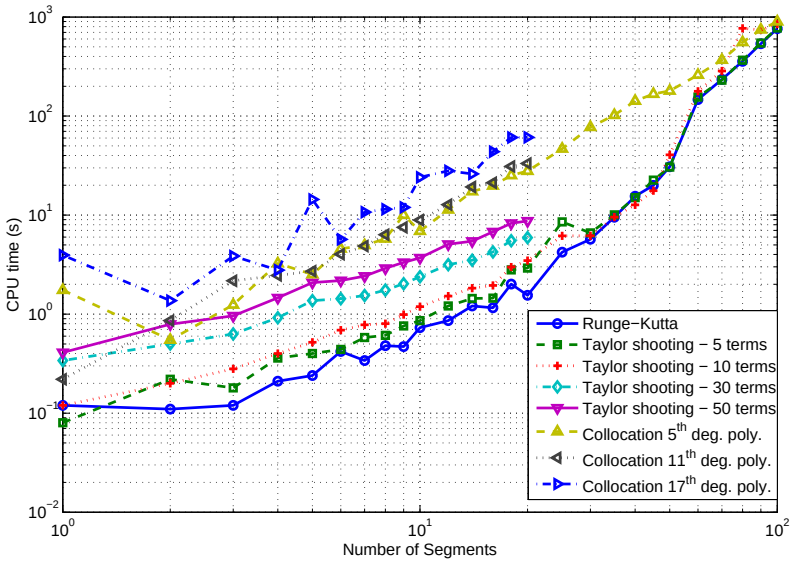

Figure 3.35: CPU time required for indirect solution for Runge-Kutta and Taylor series methods for various orders.

For accuracy tolerances of 10^{-7} or higher, the performance of the Runge-Kutta method and the Taylor series method (5 terms) is similar. The Taylor series method requires fewer segments, but the extra computation involved with calculating the derivatives causes the run times to be approximately equal. However, once a tighter accuracy tolerance is required the Taylor series constraints vastly outperform the Runge-Kutta constraints, requiring many fewer segments and consequently shorter run times. The gap widens as the accuracy tolerance is tightened. At a maximum allowed control error of 10^{-11} a optimization using Taylor series constraints (5 terms) requires 25 segments and runs in ~8s while an optimization using the Runge-Kutta method requires 70 segments and ~235s of CPU time. The difference is even more stark as more terms are retained in the Taylor series. If 40 terms are kept, only 1 segment is required to solve the problem to machine precision and the optimization takes less than one second.

# Segments CPU time (s)	Runge	Taylor Series Shooting (#terms)						Higher-order Collocation (polynomial order)							
Error	Kutta	5	10	20	30	40	50	5	7	9	11	13	15	17	19
10^{-3}	1 0.116	1 0.076						2 0.550		1 0.205	1 0.218				
10^{-4}	1 0.1078		2 0.118						2 0.599			1 0.231	1 0.316		
10^{-5}	3 0.119	2 0.220													
10^{-6}	4 0.215	3 0.180						3 1.239	3 1.045	2 1.523					
10^{-7}	7 0.343	5 0.401						5 2.516		3 0.917	2 0.862				
10^{-8}	12 0.859	7 0.578	2 0.200	1 0.209				7 4.963	4 2.449			2 0.827			
10^{-9}	25 4.225	12 1.211						9 9.998	5 3.833	4 2.349	3 2.171		2 0.827		
10^{-10}	40 15.514	16 1.448	3 0.278					14 17.296	7 4.361		4 2.463	3 2.029		1 1.368	
10^{-11}	70 234.841	25 8.540	4 0.617		1 0.342			20 27.822	9 6.835	5 3.238			3 1.580		
10^{-12}		40 15.026	5 0.523					30 77.310	12 13.504		5 2.719	4 2.363			
10^{-13}		60 155.672	6 0.691					45 166.759	16 20.349	6 3.934			4 2.363	3 3.864	
10^{-14}			7 0.778	2 0.367				60 260.044	20 36.793		6 4.025	5 3.465			
10^{-15}			12 1.523	3 0.516	2 0.497	1 0.364	1 0.413	90 745.058	25 52.906	7 6.823	8 6.341	6 4.766	5 9.186	4 2.775	

3.4 Example: Maximum Energy in Fixed Time

Given a spacecraft with constant thrust acceleration (a_T) that starts in a circular orbit with initial radius ($r_1 = 1.1$), we seek the trajectory that will maximize the final energy after a fixed period of time ($50\ TU$). This problem has been studied before by Herman and Conway.[25] The problem will be considered in geocentric polar coordinates. The equations of motion are:

$$\begin{aligned} \dot{r} &= v_r \\ \dot{\theta} &= \tfrac{v_\theta}{r} \\ \dot{v}_r &= \tfrac{v_\theta^2}{r} - \tfrac{1}{r^2} + a_T \sin u \\ \dot{v}_\theta &= \tfrac{v_r v_\theta}{r} + a_T \cos u \end{aligned} \tag{3.42}$$

The thrust pointing angle u is measured relative to the vector perpendicular to the radius vector, i.e. relative to the direction of $\boldsymbol{v}_\theta$. The objective is to maximize final energy where energy is given by:

$$E = -\frac{\mu}{2a} = \frac{v_r^2 + v_\theta^2}{2} - \frac{\mu}{r} \tag{3.43}$$

3.4.1 Maximum Energy in Fixed Time: *Direct* Problem Formulation

The spacecraft starts in a circular orbit with radius ($r = 1.1$). Without loss of generality we can consider the initial angle to be zero. The initial conditions are then:

$$\begin{aligned} r &= 1.1 \\ \theta &= 0 \\ v_r &= 0 \\ v_\theta &= \tfrac{1}{\sqrt{1.1}} \end{aligned} \tag{3.44}$$

All of the terminal states are free (unspecified). The initial guess is obtained by assuming tangential thrust, that is a thrust pointing angle equal to zero, and integrating the equations of motion forward for the fixed time of flight ($50\ TU$).

3.4.2 Maximum Energy in Fixed Time: *Indirect* Problem Formulation

Since the direct formulation of the problem does not explicitly use the necessary conditions for optimality, there is no guarantee that the solution found is even locally minimal. Therefore, in order to compute the accuracy of the solution of the direct problem, the indirect method, which does use the necessary conditions is used to compute the

solution. The Hamiltonian is:

$$H = v_r\lambda_r + \frac{v_\theta\lambda_\theta}{r} + \left(\frac{v_\theta^2}{r} - \frac{1}{r^2}\right)\lambda_{v_r} - \frac{v_r v_\theta \lambda_{v_\theta}}{r} + \lambda_{v_r} a_T \sin u + \lambda_{v_\theta} a_T \cos u \tag{3.45}$$

Define control unit vector σ:

$$\boldsymbol{\sigma} = \begin{bmatrix} \sin(u) \\ \cos(u) \end{bmatrix} \tag{3.46}$$

and velocity costate vector $\boldsymbol{\lambda_v}$:

$$\boldsymbol{\lambda}_v = \begin{bmatrix} \lambda_{v_r} \\ \lambda_{v_\theta} \end{bmatrix} \tag{3.47}$$

The Hamiltonian then becomes:

$$H = v_r\lambda_r + \frac{v_\theta\lambda_\theta}{r} + \boldsymbol{\lambda}_v^T \begin{bmatrix} \left(\frac{v_\theta^2}{r} - \frac{1}{r^2}\right) \\ -\frac{v_r v_\theta \lambda_{v_\theta}}{r} \end{bmatrix} + a_T \boldsymbol{\lambda}_v^T \boldsymbol{\sigma} \tag{3.48}$$

By the Pontryagin minimum principle the optimal control will minimize the Hamiltonian. This is clearly when the unit control vector σ directly opposes the velocity costate vector $\boldsymbol{\lambda_v}$. Therefore:

$$\boldsymbol{\sigma} = \frac{-\boldsymbol{\lambda}_v}{|\boldsymbol{\lambda}_v|} \tag{3.49}$$

The control law is then:

$$\begin{aligned} \sin u &= \frac{-\lambda_{v_r}}{\sqrt{\lambda_{v_r}^2 + \lambda_{v_\theta}^2}} \\ \cos u &= \frac{-\lambda_{v_\theta}}{\sqrt{\lambda_{v_r}^2 + \lambda_{v_\theta}^2}} \end{aligned} \tag{3.50}$$

The full costate equations are then:

$$\begin{aligned} \dot{r} &= v_r \\ \dot{\theta} &= \tfrac{v_\theta}{r} \\ \dot{v}_r &= \tfrac{v_\theta^2}{r} - \tfrac{1}{r^2} - a_T \tfrac{\lambda_{v_r}}{\sqrt{\lambda_{v_r}^2 + \lambda_{v_\theta}^2}} \\ \dot{v}_\theta &= -\tfrac{v_r v_\theta}{r} - a_T \tfrac{\lambda_{v_\theta}}{\sqrt{\lambda_{v_r}^2 + \lambda_{v_\theta}^2}} \\ \dot{\lambda}_r &= \tfrac{v_\theta\lambda_\theta}{r^2} + \tfrac{v_\theta^2\lambda_{v_r}}{r^2} - \tfrac{2\lambda_{v_r}}{r^3} - \tfrac{v_r v_\theta \lambda_{v_\theta}}{r^2} \\ \dot{\lambda}_\theta &= 0 \\ \dot{\lambda}_{v_r} &= -\lambda_r + \tfrac{v_\theta\lambda_{v_\theta}}{r} \\ \dot{\lambda}_{v_\theta} &= -\tfrac{\lambda_\theta}{r} - \tfrac{2v_\theta\lambda_{v_r}}{r} + \tfrac{v_r\lambda_{v_\theta}}{r} \end{aligned} \tag{3.51}$$

Since the objective function J is only a function of the terminal states:

$$\lambda(T) = \left(\frac{\partial J}{\partial x}\right)_{t=T} \tag{3.52}$$

The terminal conditions for the costates are then:

$$\begin{aligned} \lambda_r(T) &= -\tfrac{\mu}{r(T)^2} \\ \lambda_\theta(T) &= 0 \\ \lambda_{v_r}(T) &= -v_r(T) \\ \lambda_{v_\theta}(T) &= -v_\theta(T) \end{aligned} \tag{3.53}$$

There are no initial conditions for the costates. The initial and final conditions for the state variables remain the same as in the direct case (3.44). The initial conditions for the states were obtained by integrating the equations of motion (3.42) forward for the fixed time of flight $(50\ TU)$. The initial guess for the costates was generated by assuming that the terminal conditions for the costates hold for the entire trajectory. That is, they share the same relationship with the states for the whole trajectory as they do at the terminal point. Therefore:

$$\begin{aligned} \lambda_r(t) &= -\tfrac{\mu}{r(t)^2} \\ \lambda_\theta(t) &= 0 \\ \lambda_{v_r}(t) &= -v_r(t) \\ \lambda_{v_\theta}(t) &= -v_\theta(t) \end{aligned} \tag{3.54}$$

for $0 \leq t \leq T$.

This initial guess is not feasible as it does not satisfy the equations of motion. That is because using this guess of the costates in the control law does not produce the control angle assumed in the calculation of the states, i.e. zero. However, it proved to be sufficient to generate optimal solutions.

3.4.3 Maximum Energy in Fixed Time: *Direct* Results

The optimal solution for the direct problem (Section 3.4.1) is shown in Figure 3.36, and the optimal thrust-pointing angle history is shown in Figure 3.37. The final energy is $E_{final} = -0.091523$. The solution shown was obtained using the Taylor constraints (40 terms) with 10 equal segments, and the control was specified by a cubic spline with 31 equally spaced control knots. The true solution was found by solving the indirect formulation of the problem (see Section 3.4.2) using a very fine mesh of 200 segments.

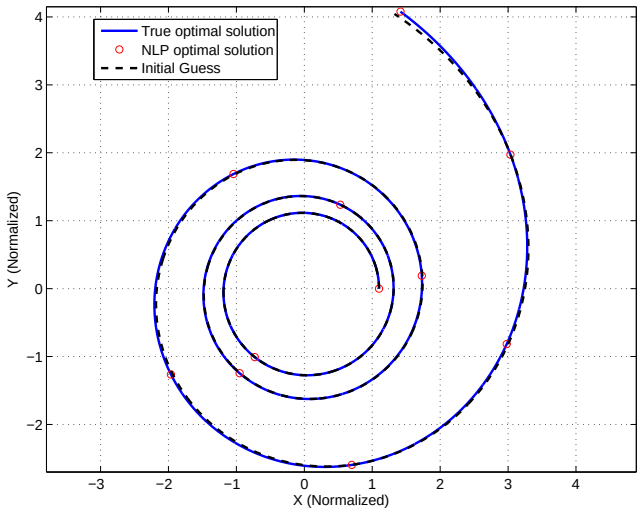

Figure 3.36: Optimal trajectory to maximize energy in fixed time $(50TU)$ from a circular initial orbit (R=1.1). Solved using Taylor series (40 terms) shooting constraints with 10 segments.

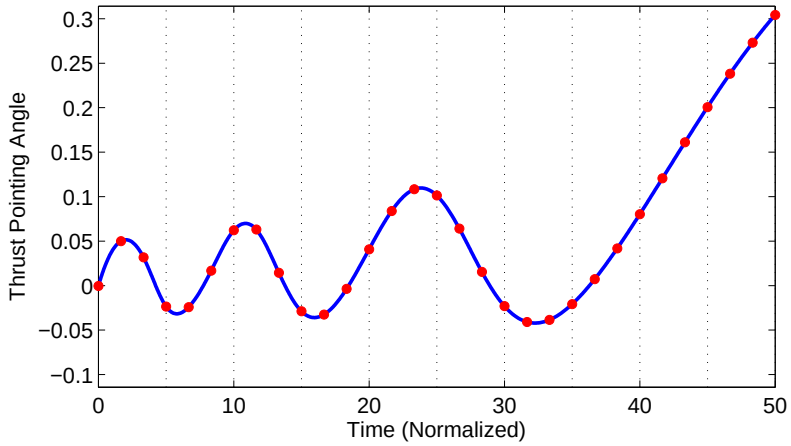

Figure 3.37: Optimal control angle to maximize energy in fixed time $(50TU)$ from a circular initial orbit (R=1.1). Solved using Taylor series (40 terms) shooting constraints with 10 segments.

The optimal trajectory and optimal control angle very closely match the exact solution, which was obtained by solving the indirect (calculus of variations) problem (Section 3.4.2). The error between the optimal control angle and the exact solution is shown in Figure 3.38.

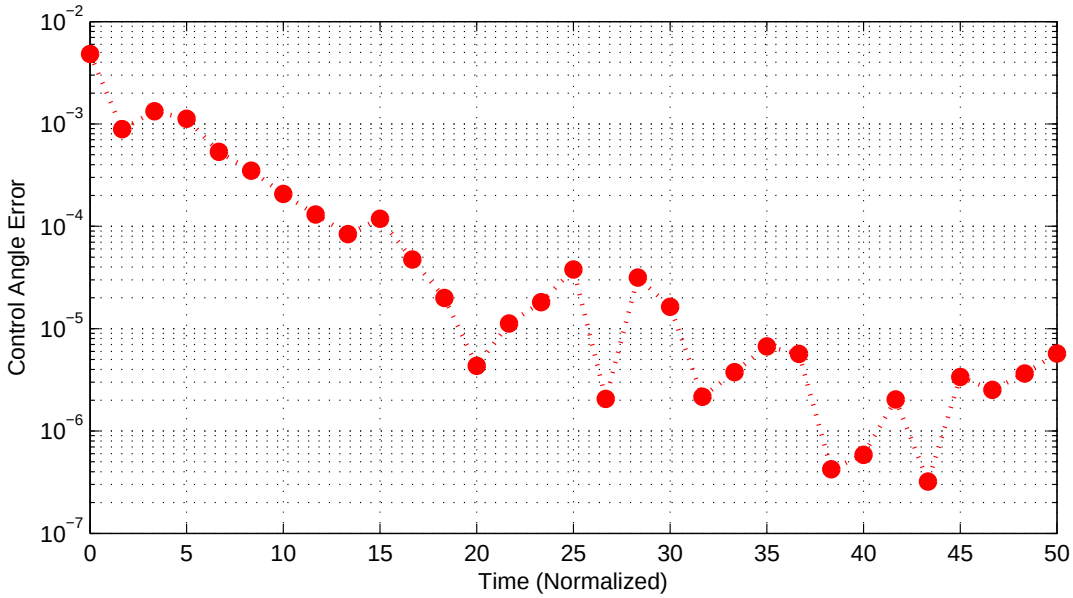

Figure 3.38: Absolute difference between optimal control angle from direct solution (10 segments, 40 term Taylor series shooting constraints) and indirect (exact) solution.

The maximum energy in fixed time problem was solved using the new constraints as well as various control parameterizations and different meshes. The solutions found are compared to the exact solution obtained by solving the indirect problem using a very fine mesh. Figure 3.39 shows the difference between the objective function value and that of the exact solution ($E = -0.095123383$). The maximum difference between the thrust pointing angle and the control determined from the control law (Equation 3.61) in the indirect solution is shown in Figure 3.40. These differences are taken at every point that the control is specified in the Runge-Kutta multiple shooting method. That is, at the segment boundaries and 5 equally spaced interior points, regardless of the positions of the control points in the particular control parameterization considered. Figure 3.41 shows the maximum error in any of the state variables at any node.

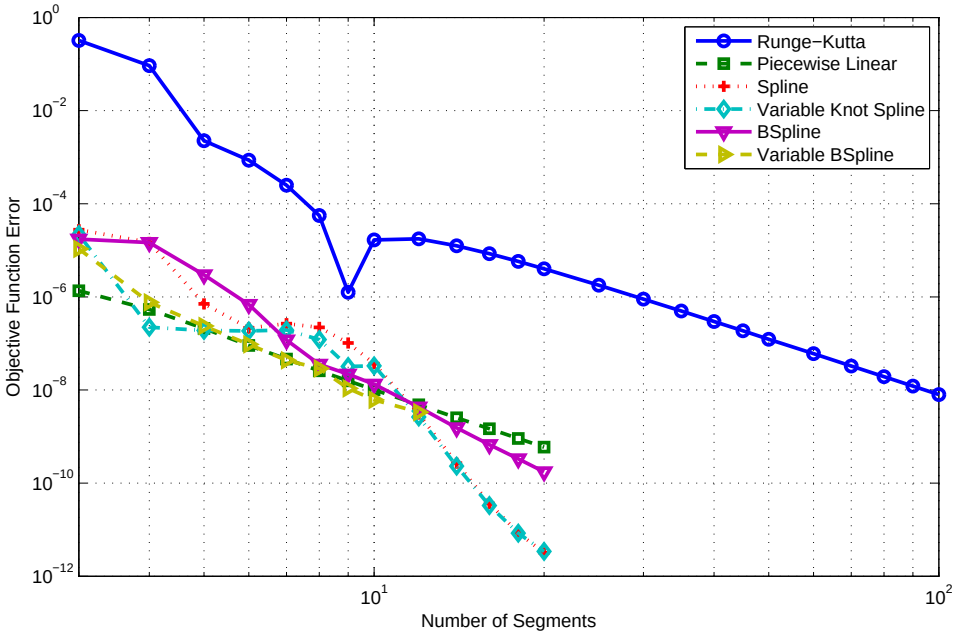

Figure 3.39: Objective function error comparison for direct solution to Maximum Energy in Fixed Time problem for Taylor series shooting method (20 terms) with various control parameterization and Runge-Kutta.

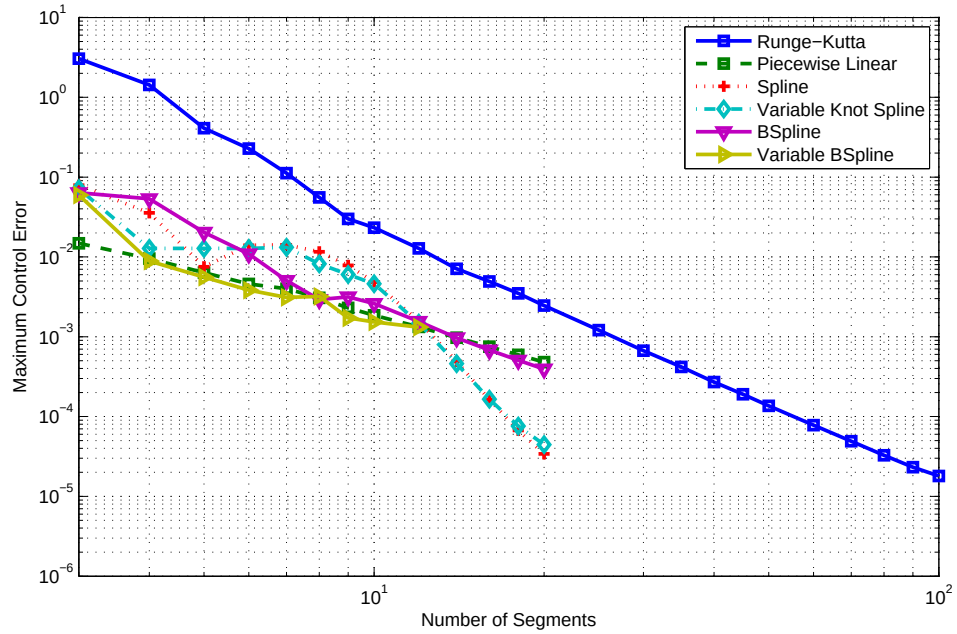

Figure 3.40: Maximum control error comparison for direct solution to Maximum Energy in Fixed Time problem for Taylor series shooting method (20 terms) with various control parameterization and Runge-Kutta.

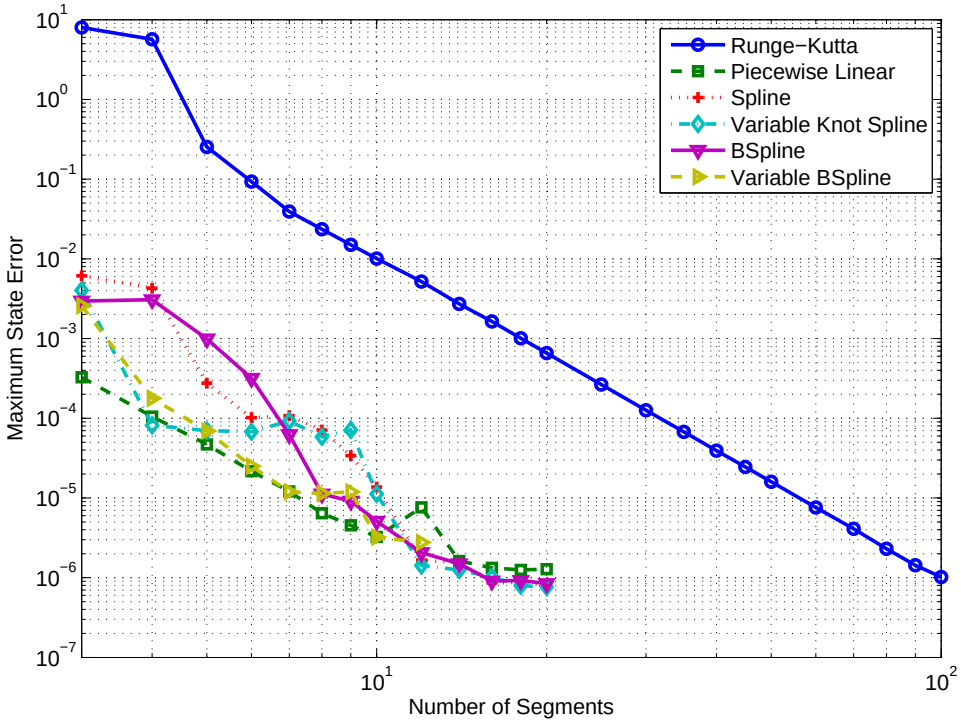

Figure 3.41: Maximum state error comparison for direct solution to Maximum Energy in Fixed Time problem for Taylor series shooting method (20 terms) with various control parameterization and Runge-Kutta.

Figures 3.39-3.41 show that the Taylor series shooting constraints outperform the Runge-Kutta multiple shooting constraints for all three error measures considered. It appears that the spline is the most effective control parameterization and that in this application, allowing the spline knots to be variable in both time and control value does not make a significant difference to the quality of the approximation of the control function.

3.4.4 Maximum Energy in Fixed Time: *Indirect* Results

The example trajectory, shown in Figure 3.42, was generated using the Taylor series method (50 terms) with 10 equal segments. The corresponding control history is shown in 3.43.

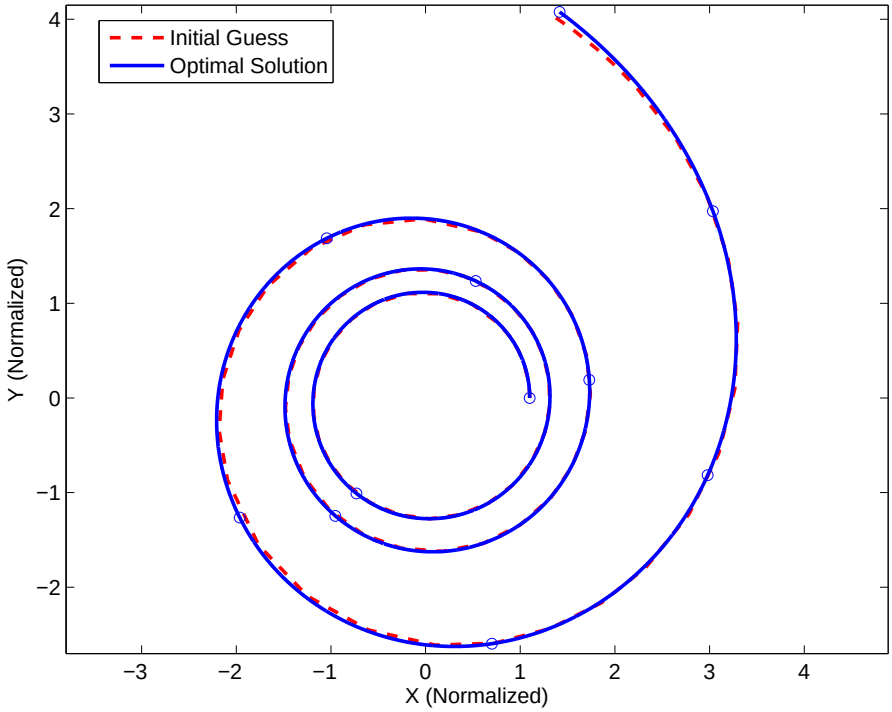

Figure 3.42: Optimal trajectory to maximize energy in fixed time $(50TU)$ from a circular initial orbit (R=1.1). Indirect problem solved using Taylor series (50 terms) constraints with 10 segments.

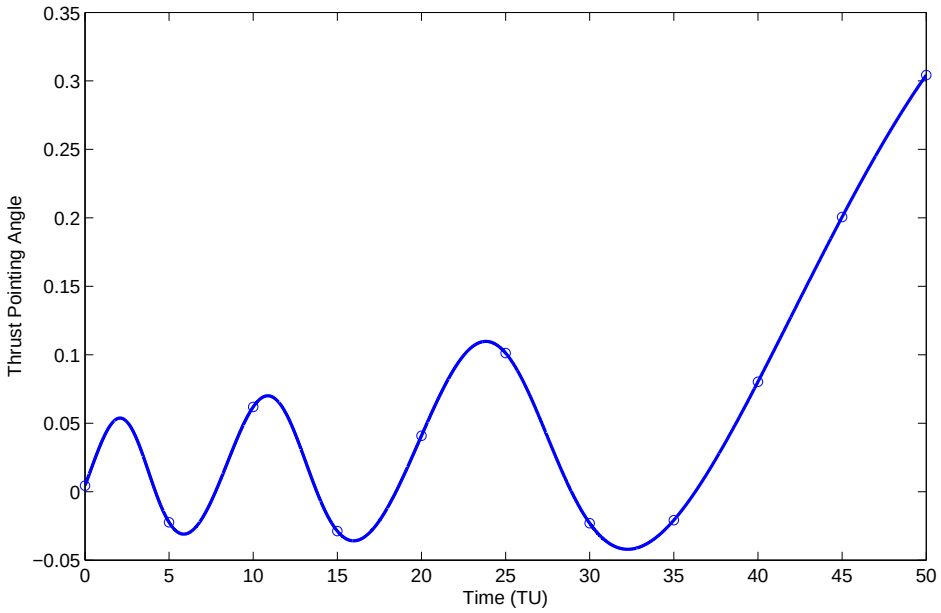

Figure 3.43: Optimal control angle to maximize energy in fixed time $(50TU)$ from a circular initial orbit (R=1.1). Indirect problem solved using Taylor series (50 terms) constraints with 10 segments.

A comparison of the accuracy of the results for the Runge-Kutta multiple shooting and the Taylor series shooting method is shown in Figures 3.44-3.46. The exact solution was taken from a indirect solution obtained using a very fine mesh of 200 segments. It shows that the Taylor series shooting method obtains more accurate results than the Runge-Kutta method for similar meshes, even when only 5 terms are retained in the Taylor series.

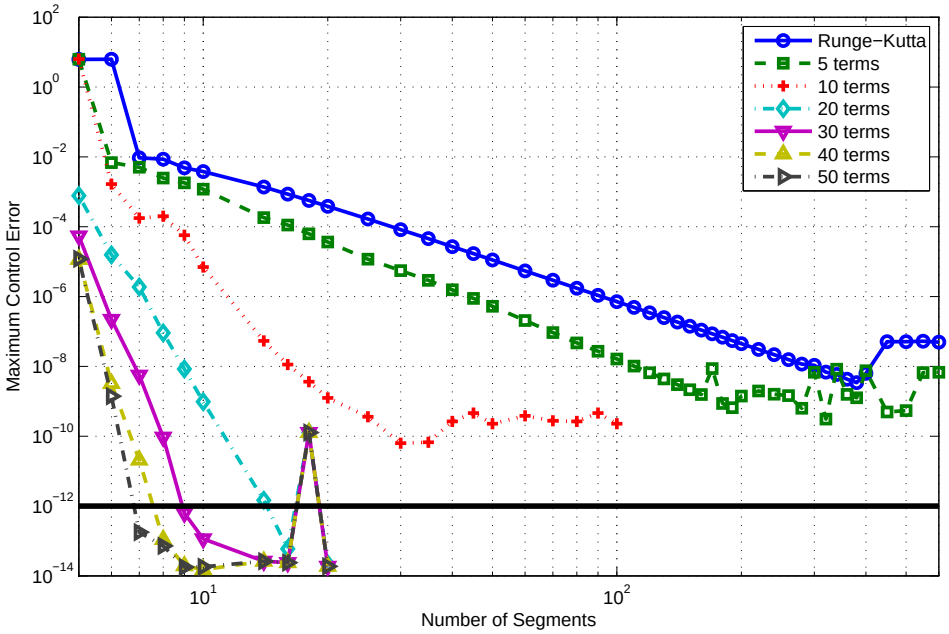

Figure 3.44: Maximum control angle deviation from exact solution in indirect solution for Taylor series shooting method for various Taylor series lengths.

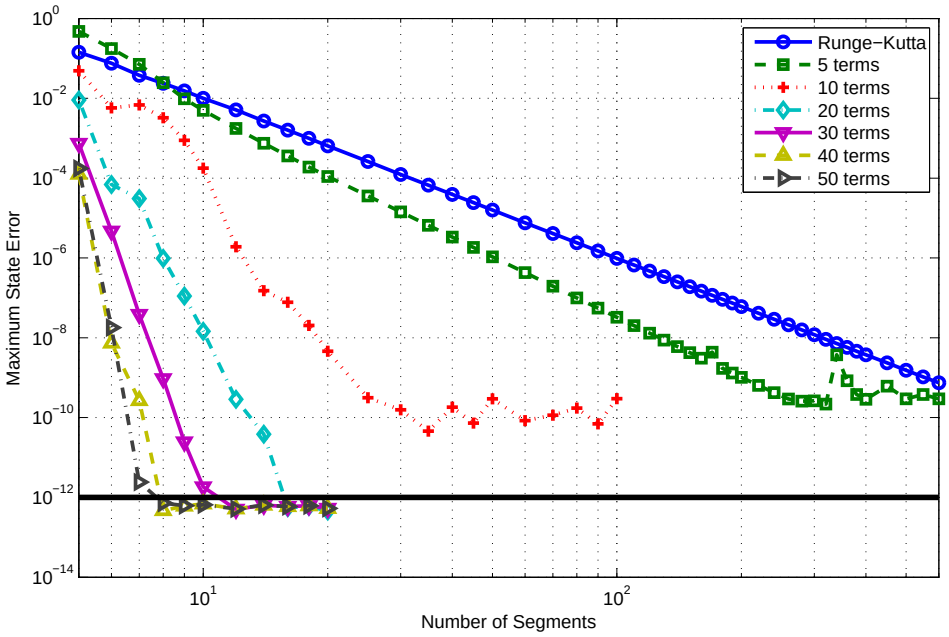

Figure 3.45: Maximum state error in indirect solution for Taylor series shooting method for various Taylor series lengths.

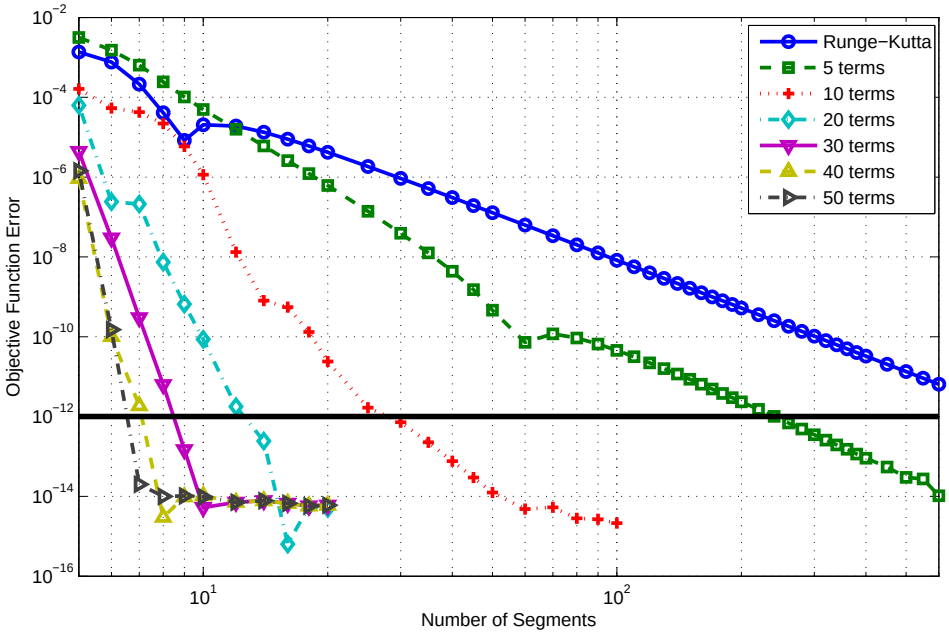

Figure 3.46: Objective function error in indirect solution for Taylor series collocation method for various Taylor series lengths.

3.4.5 Modified Equinoctial Elements

The problems solved so far have all had relatively simple governing equations (3.2), (3.42). To demonstrate that the Taylor series method will work with more sophisticated equations we solve the maximum energy in a fixed time problem using Modified Orbit Elements (p, f, g, h, k, L) rather than $2D$ polar coordinates $(r, \theta, v_r, v_\theta)$. The problem remains the same; given a spacecraft with constant thrust acceleration (a_T) that starts in a circular orbit with initial radius $(r_1 = 1.1)$, we seek the trajectory that will maximize the final energy after a fixed period of time $(50\ TU)$. The modified equinoctial elements are related to the conventional orbit elements $(a, e, i, \Omega, \omega, f)$ by:

$$\begin{aligned} p &= a\left(1 - e^2\right) \\ f &= e\cos\left(\omega + \Omega\right) \\ g &= e\sin\left(\omega + \Omega\right) \\ h &= \tan\left(\tfrac{i}{2}\right)\cos\Omega \\ k &= \tan\left(\tfrac{i}{2}\right)\sin\Omega \\ L &= \Omega + \omega + \theta \end{aligned} \tag{3.55}$$

The variational equations are:

$$\begin{aligned} \dot{p} &= \tfrac{2p}{w}\sqrt{\tfrac{p}{\mu}}T \\ \dot{f} &= \sqrt{\tfrac{p}{\mu}}\left[R\sin L + \left[(w+1)\cos L + f\right]\tfrac{T}{w} - \left(h\sin L - k\cos L\right)\tfrac{gN}{w}\right] \\ \dot{g} &= \sqrt{\tfrac{p}{\mu}}\left[-R\cos L + \left[(w+1)\sin L + g\right]\tfrac{T}{w} - \left(h\sin L - k\cos L\right)\tfrac{gN}{w}\right] \\ \dot{h} &= \sqrt{\tfrac{p}{\mu}}\tfrac{s^2 N}{2w}\cos L \\ \dot{k} &= \sqrt{\tfrac{p}{\mu}}\tfrac{s^2 N}{2w}\sin L \\ \dot{L} &= \sqrt{\mu p}\left(\tfrac{w}{p}\right)^2 + \tfrac{1}{w}\sqrt{\tfrac{p}{\mu}}\left(h\sin L - k\cos L\right)N \end{aligned} \tag{3.56}$$

where:

$$\begin{aligned} w &= 1 + f\cos L + g\sin L \\ s^2 &= 1 + h^2 + k^2; \end{aligned}$$

R, T and N are perturbations in the local body fixed axes. The only perturbation in this problem is due to the engine thrust acceleration a_T. Thus:

$$\begin{aligned} R &= a_T\cos u_2\sin u_1 \\ T &= a_T\cos u_2\cos u_1 \\ N &= a_T\sin u_2 \end{aligned} \tag{3.57}$$

where u_1 and u_2 are the in-plane and out-of-plane thrust pointing angles respectively. This problem is effectively

planar, however in this case it has been solved using the full $3D$ modified equinoctial elements. As a result out-of-plane thrust pointing angle u_2 has been included. The objective is to maximize final energy where energy is given by:

$$E = -\frac{\mu}{2a} = -\frac{\mu\left(1 - f^2 - g^2\right)}{2p} \tag{3.58}$$

The initial conditions are:

$$\begin{aligned} p\left(0\right) &= 1.1 \\ f\left(0\right) = g\left(0\right) = h\left(0\right) = k\left(0\right) = L\left(0\right) &= 0 \end{aligned} \tag{3.59}$$

All of the terminal states are free (unspecified). The initial guess is obtained by assuming tangential thrust, that is both thrust pointing angles equal to zero, and integrating the equations of motion forward for the fixed time $\left(50\ TU\right)$.

The optimal solution is shown in Figure 3.47 and the optimal thrust-pointing angle history is shown in Figure 3.48. The final energy is $E_{final} = -0.091524$. The solution shown was obtained using the Taylor constraints (20 terms) with 10 equal segments and the control was specified by a BSpline with 31 equally spaced control points.

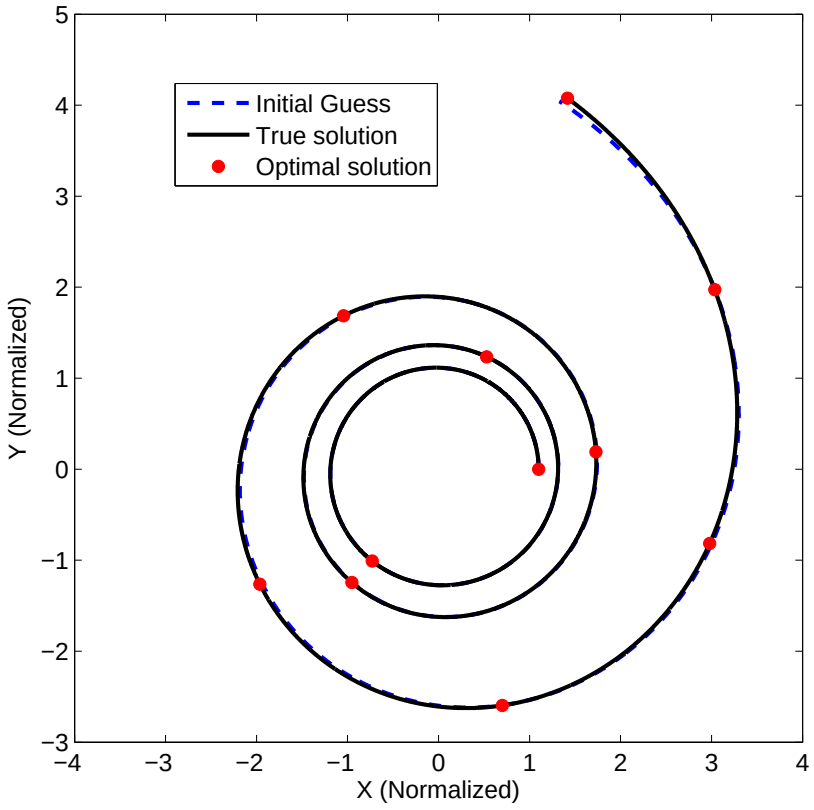

Figure 3.47: Optimal trajectory to maximize energy in fixed time $\left(50TU\right)$ from a circular initial orbit (R=1.1). Solved using Taylor series (20 terms) shooting constraints with 10 segments.

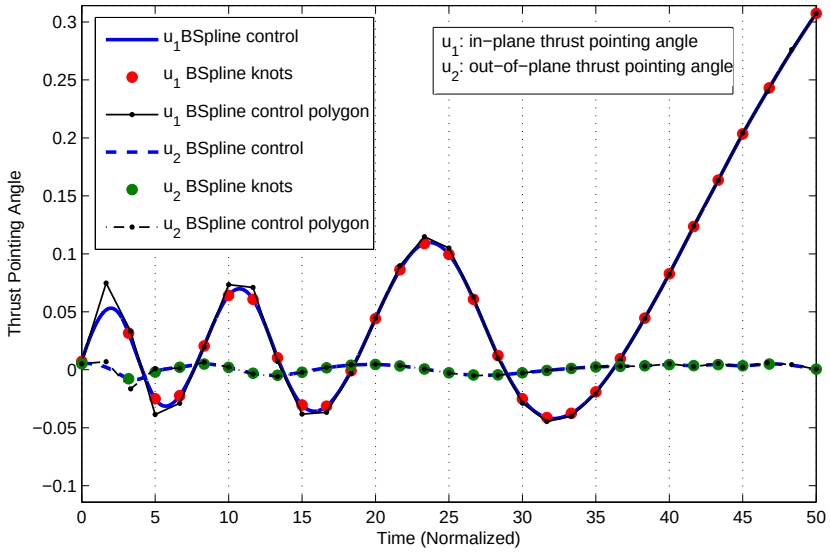

Figure 3.48: Optimal control angle to maximize energy in fixed time $(50TU)$ from a circular initial orbit (R=1.1). Solved using Taylor series (40 terms) shooting constraints with 10 segments.

The optimal trajectory and optimal control angle very closely match the exact solution obtained by solving the indirect problem (Section 3.4.2) using polar coordinates. The error between the optimal control angle and the exact solution is shown in Figure 3.49

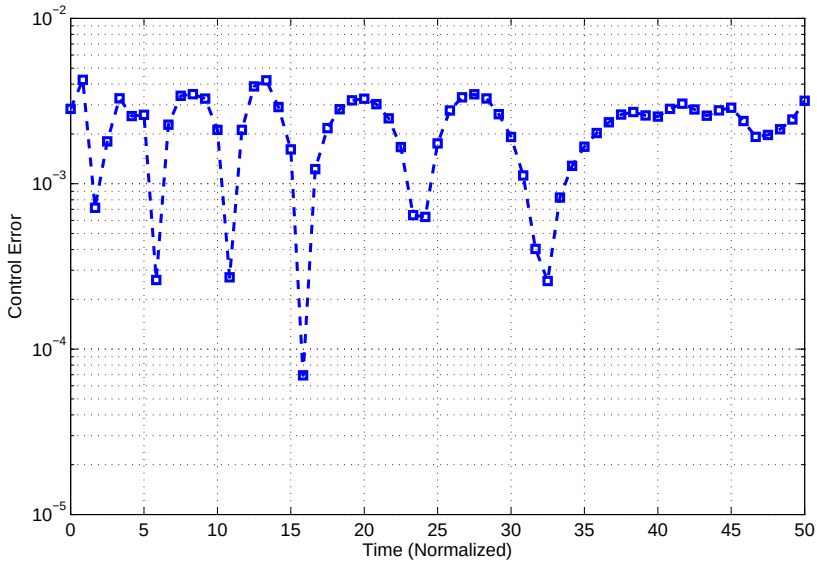

Figure 3.49: Absolute difference between optimal control angle for direct solution (10 segments, 20 term Taylor series shooting constraints) and indirect (exact) solution.

A comparison of the results for various control parameterizations is shown in Figure 3.50. The new Taylor series method again outperforms the conventional Runge-Kutta method for all control parameterizations and the Variable Knot Spline is the best performing control parameterization. The solutions obtained using the modified equinoctial elements are less accurate than those obtained using polar coordinates (cf. Figure 3.39), perhaps due to the added complexity of the system equations and the addition of a control variable (out-of-plane thrust pointing angle (u_2)). However, the difference is minor and the Taylor series method is able to successfully solve optimal control problems with sophisticated equations of motion.

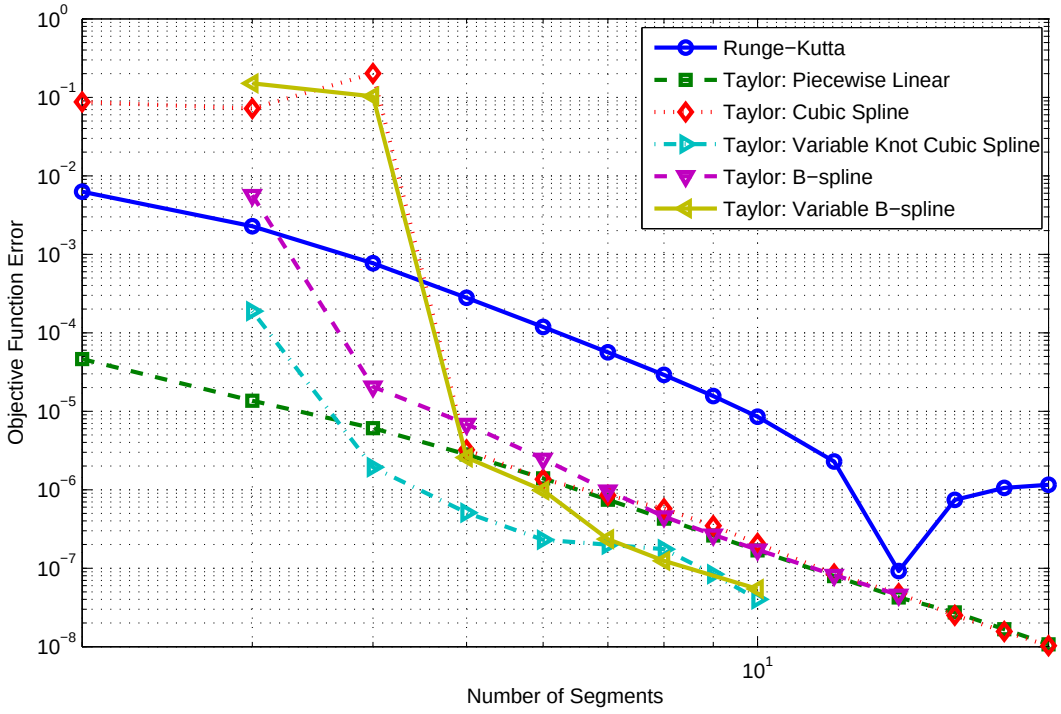

Figure 3.50: Objective function error comparison for direct solution to Maximum Energy in Fixed Time (Modified Equinoctial Elements) problem for Taylor series shooting method (20 terms) with various control parameterization and Runge-Kutta.

3.5 Example: Optimal Low-Thrust Orbit Raising

Given a spacecraft with constant thrust acceleration (T_a), we seek the minimum time transfer from a circular orbit (with initial radius $r_1 = 1$) to a larger circular orbit (with radius $r_2 = 1.523679$). This is equivalent to a transfer from Earth to Mars, ignoring the eccentricity and inclination of their respective orbits. The problem will be considered in heliocentric polar coordinates; the equations of motion are (2.29). The thrust pointing angle u is measured relative to the vector perpendicular to the radius vector, i.e. relative to the direction of $\boldsymbol{v}_\theta$. The initial and final conditions are:

$$\begin{array}{rclrcl} r(0) & = & r_1 & r(T) & = & r_2 \\ \theta(0) & = & 0 & \theta(T) & is & free \\ v_r(0) & = & 0 & v_r(T) & = & 0 \\ v_\theta(0) & = & r_1 & v_\theta(T) & = & \frac{1}{\sqrt{r_2}} \end{array}$$

The initial guess is obtained by assuming a thrust pointing angle of zero, that is thrust aligned with v_θ and integrating the equations of motion forward for a fixed final time.

3.5.1 Direct Solutions

The optimal solution is shown in Figure 3.51 and the optimal thrust-pointing angle history is shown in Figure 3.52. The minimum time of flight is 4.1114270 TU. The solution shown was obtained using the Taylor constraints (40 terms) with 20 equal segments and 6 subsegments per segment. Tangential thrust proved to be a poor guess for the optimal control, therefore the initial guess for the trajectory was vastly different from the optimal solution. However, the method easily converges to the optimal solution regardless of the poor initial guess.

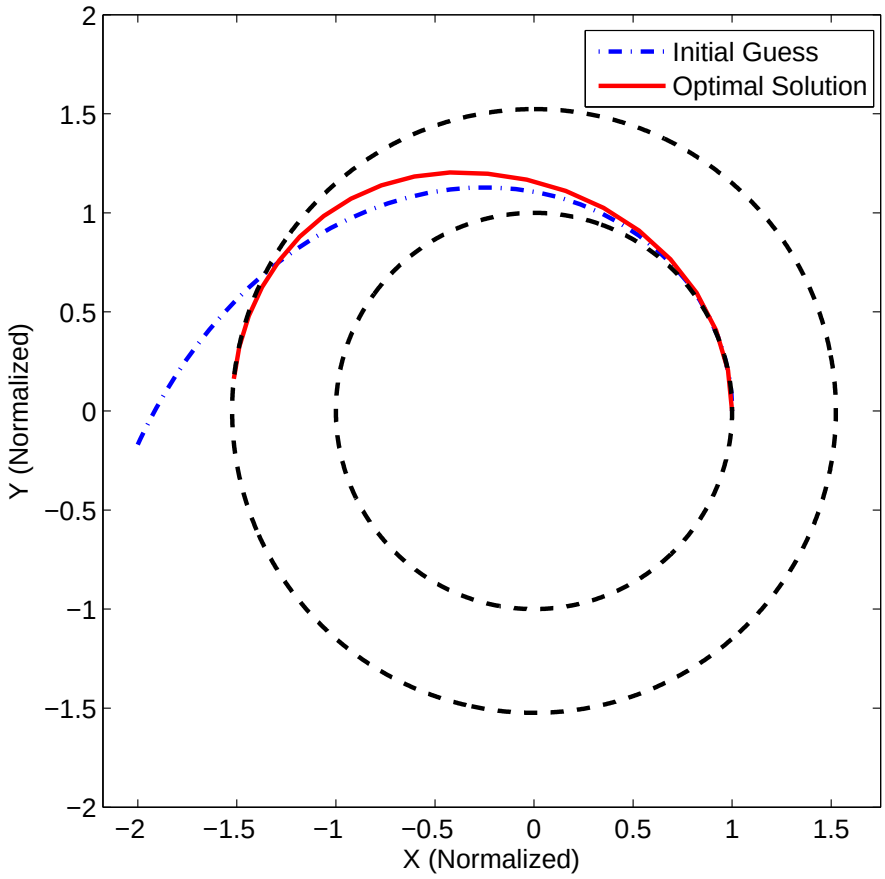

Figure 3.51: Optimal trajectory for transfer from circular orbit (R=1) to circular orbit (R=1.523679) . Solved using Taylor series (40 terms) constraints with 20 segments.

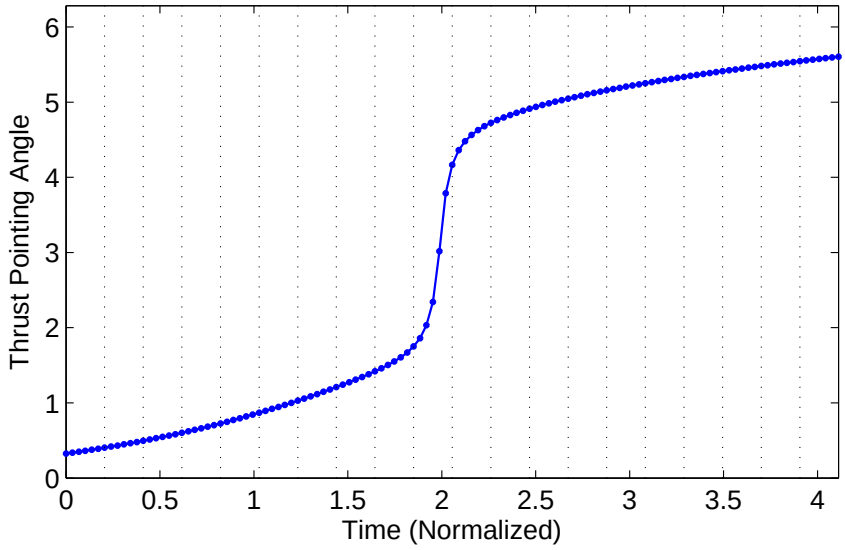

Figure 3.52: Optimal control angle for transfer from circular orbit (R=1) to circular orbit (R=1.523679). Solved using Taylor series (40 terms) constraints with 20 segments.

3.5.2 Optimal Low-Thrust Orbit Raising: *Indirect* Problem Formulation

In order to determine the accuracy of the solutions obtained using direct methods, the indirect method, a solution using the necessary conditions for optimality, is also used to compute the solution. The Hamiltonian is:

$$H = v_r\lambda_r + \frac{v_\theta\lambda_\theta}{r} + \left(\frac{v_\theta^2}{r} - \frac{1}{r^2}\right)\lambda_{v_r} - \frac{v_r v_\theta \lambda_{v_\theta}}{r} + \lambda_{v_r} T_a \sin u + \lambda_{v_\theta} T_a \cos u \tag{3.60}$$

This is equivalent to the Hamiltonian for the maximum energy in fixed time problem solved in section 3.4.2. Therefore by the same arguments the optimal control law is:

$$\begin{aligned} \sin u &= \frac{-\lambda_{v_r}}{\sqrt{\lambda_{v_r}^2+\lambda_{v_\theta}^2}} \\ \cos u &= \frac{-\lambda_{v_\theta}}{\sqrt{\lambda_{v_r}^2+\lambda_{v_\theta}^2}} \end{aligned} \tag{3.61}$$

The complete state and costate equations are then:

$$\begin{aligned} \dot{r} &= v_r \\ \dot{\theta} &= \tfrac{v_\theta}{r} \\ \dot{v}_r &= \tfrac{v_\theta^2}{r} - \tfrac{1}{r^2} - T_a \tfrac{\lambda_{v_r}}{\sqrt{\lambda_{v_r}^2+\lambda_{v_\theta}^2}} \\ \dot{v}_\theta &= -\tfrac{v_r v_\theta}{r} - T_a \tfrac{\lambda_{v_\theta}}{\sqrt{\lambda_{v_r}^2+\lambda_{v_\theta}^2}} \\ \dot{\lambda}_r &= \tfrac{v_\theta\lambda_\theta}{r^2} + \tfrac{v_\theta^2\lambda_{v_r}}{r^2} - \tfrac{2\lambda_{v_r}}{r^3} - \tfrac{v_r v_\theta \lambda_{v_\theta}}{r^2} \\ \dot{\lambda}_\theta &= 0 \\ \dot{\lambda}_{v_r} &= -\lambda_r + \tfrac{v_\theta\lambda_{v_\theta}}{r} \\ \dot{\lambda}_{v_\theta} &= -\tfrac{\lambda_\theta}{r} - \tfrac{2v_\theta\lambda_{v_r}}{r} + \tfrac{v_r\lambda_{v_\theta}}{r} \end{aligned} \tag{3.62}$$

with final conditions:

$$\begin{aligned} \lambda_r(T) &= \upsilon_r \\ \lambda_\theta(T) &= 0 \\ \lambda_{v_r}(T) &= \upsilon_{v_r} \\ \lambda_{v_\theta}(T) &= \upsilon_{v_\theta} \end{aligned} \tag{3.63}$$

and transversality condition:

$$1 - T_a\sqrt{\lambda_{v_r}^2(T) + \lambda_{v_\theta}^2(T)} = 0 \tag{3.64}$$

Since the costate equations are so sensitive in this problem, particularly around $t = 2$ where the control changes rapidly, a good initial guess for the costates is required in order for the indirect problem to converge. An estimate of the costates can be obtained from the Karush-Kuhn-Tucker conditions for the nonlinear programming problem of the

direct solution of the previous section. This gives estimates of the costates at every node except for the first, since there are no constraints at this node. The costates at the first node are estimated by simply integrating the full costate equations (3.62) backward over the first segment. This gives an initial guess that while not necessarily feasible, proved to be adequate for this problem.

3.5.3 Optimal Low-Thrust Orbit Raising: *Indirect* Results

The optimal solution is shown in Figure 3.53 and the optimal thrust-pointing angle history is shown in Figure 3.54. The minimum time of flight is 4.1114267 TU. The solution shown was obtained using the Taylor constraints (40 terms) with 20 equal segments and 6 subsegments per segment. The initial guess for both the states and the costates came from the solution of the direct problem.

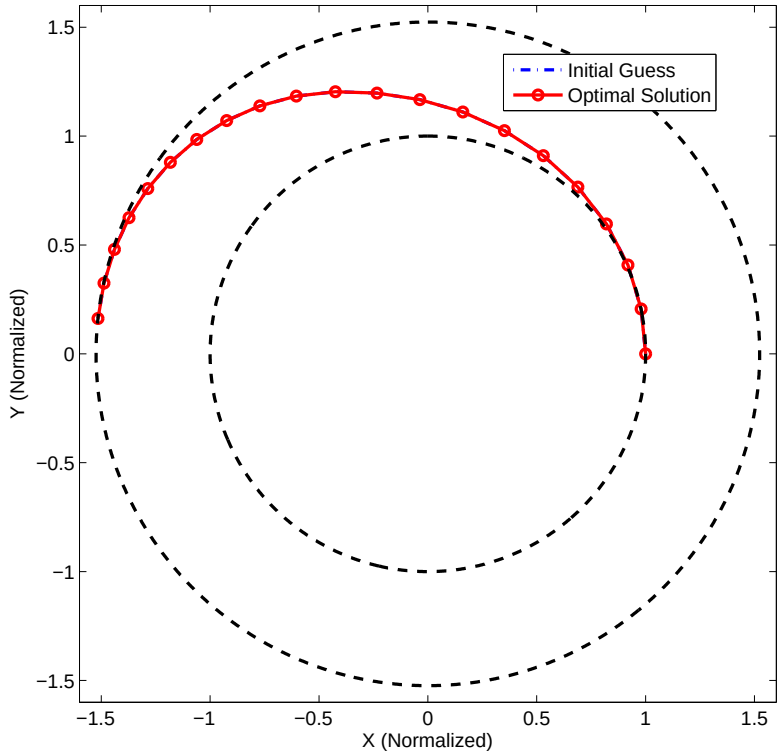

Figure 3.53: Optimal trajectory for transfer from circular orbit (R=1) to circular orbit (R=1.523679) . Solved using Taylor series (40 terms) constraints with 20 segments.

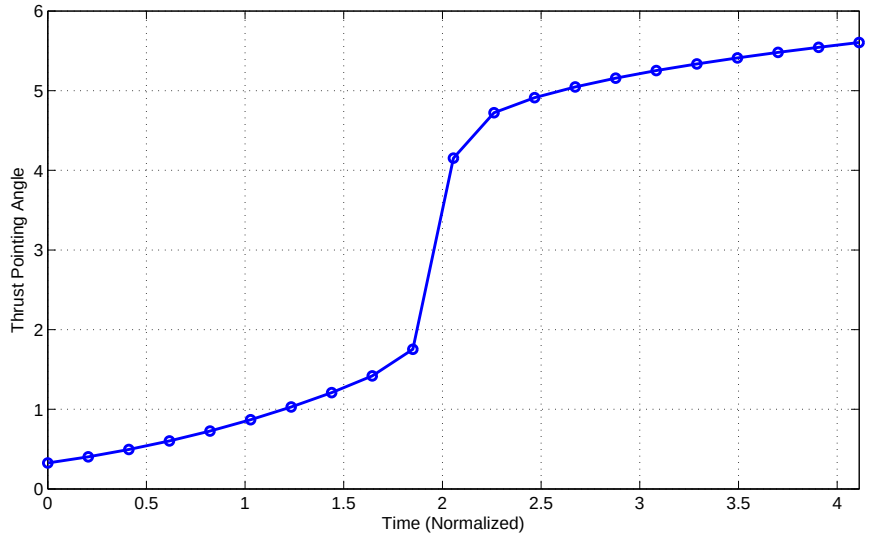

Figure 3.54: Optimal control angle for transfer from circular orbit (R=1) to circular orbit (R=1.523679). Solved using Taylor series (40 terms) constraints with 20 segments.

The solution obtained using 20 segments agrees very closely with the exact solution found using a much finer mesh of 100 segments. The difference between the control angle given and the exact solution is given in Figure 3.55. The control angle error is always below 10^{-8} except for one point around $t = 2\ TU$, this is where the optimal control changes most rapidly (cf. Figure 3.54).

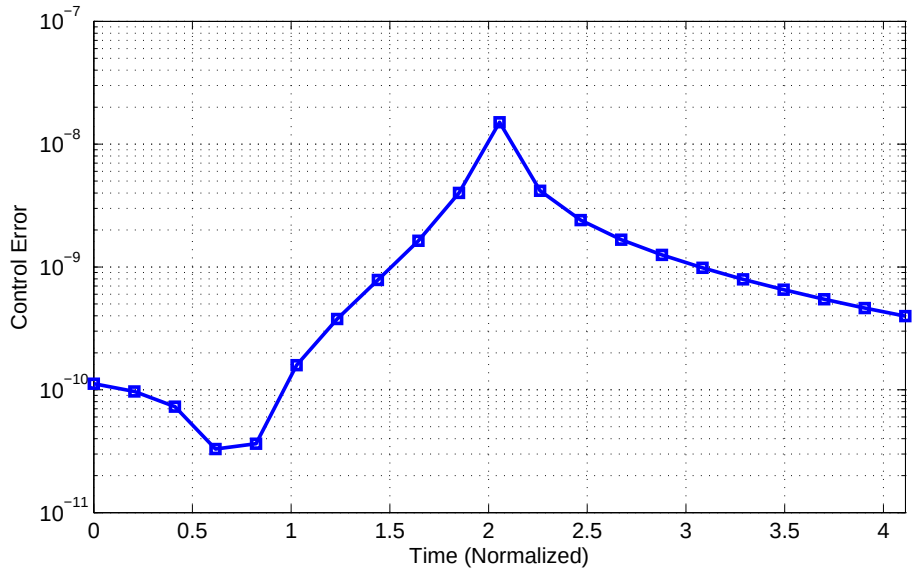

Figure 3.55: Control angle error for transfer from circular orbit (R=1) to circular orbit (R=1.523679). Solved using Taylor series (40 terms) constraints with 20 segments.

The solution was also obtained for the same parameters (20 segments, 6 subsegments) using the mesh refinement scheme outlined in Section 2.5. Figure 3.56 shows the optimal trajectory and the control angle history is shown in Figure 3.57.

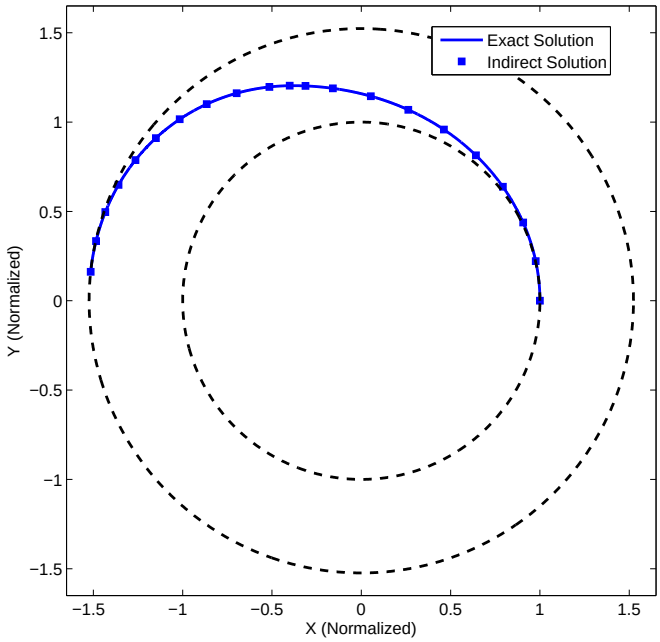

Figure 3.56: Optimal trajectory for transfer from circular orbit (R=1) to circular orbit (R=1.523679) . Solved using Taylor series (18 terms) constraints with 20 segments using an adaptive mesh.

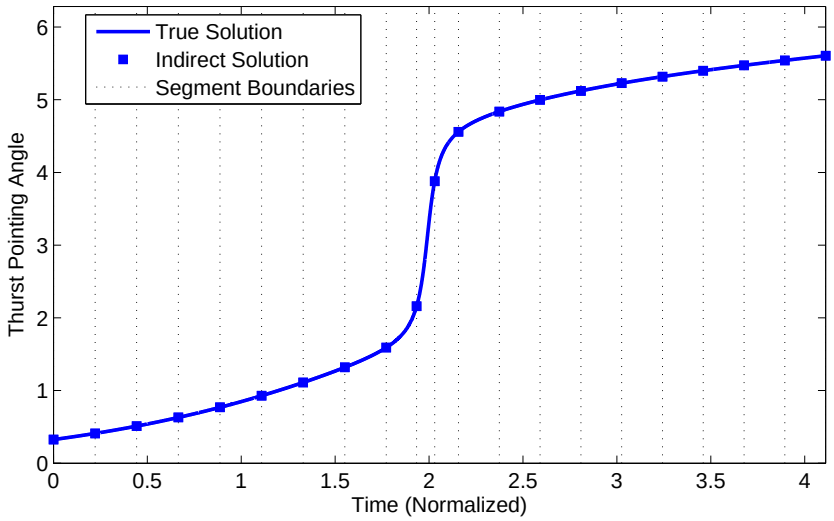

Figure 3.57: Optimal control angle for transfer from circular orbit (R=1) to circular orbit (R=1.523679). Solved using Taylor series (18 terms) constraints with 20 segments using an adaptive mesh.

The difference between the control angle and the exact solution is given in Figure 3.58. The control angle error is lower with the mesh refinement than the similar case solved with a uniform mesh (see Figure 3.55). The error in objective function value is reduced from 6.1366×10^{-11} to 1.1546×10^{-14} even though the number of terms in the Taylor series is reduced from 40 to 18. Smaller reductions are observed in the maximum state and maximum control errors. A comparison of the errors with and without mesh refinement is shown in Table 3.3.

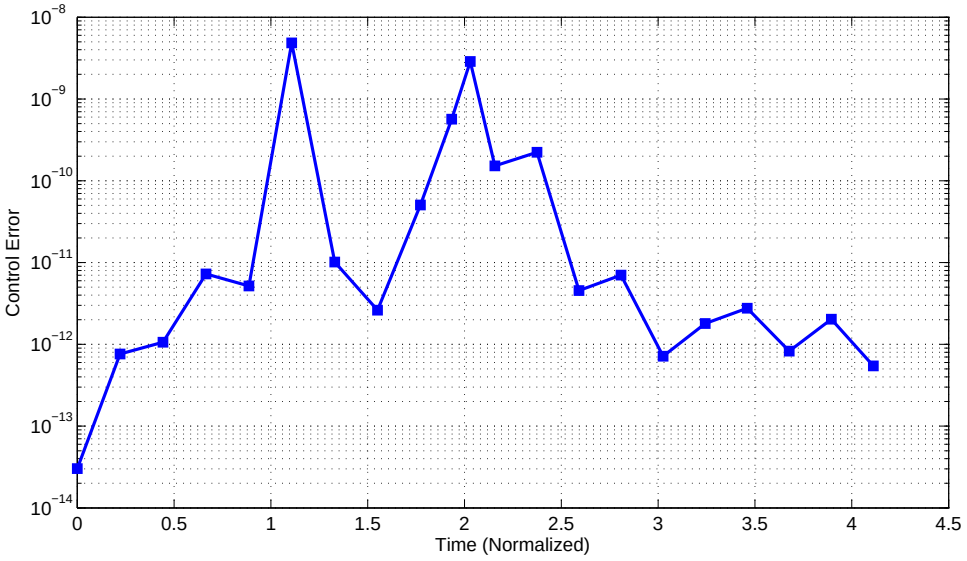

Figure 3.58: Control angle error for transfer from circular orbit (R=1) to circular orbit (R=1.523679). Solved using Taylor series (18 terms) constraints with 20 segments using an adaptive mesh.

	# Terms in Taylor Series	Objective Function Error	Maximum Control Error	Maximum State Error
Uniform Mesh	40	6.1366E-11	1.5065E-08	3.7654E-10
With Mesh Refinement	18	1.1546E-14	4.2973E-09	2.1456E-10
Uniform Mesh	18	2.1817E-08	1.0455E-05	2.1047E-07

Table 3.3: Results for *indirect* formulation of the orbit raising problem using mesh refinement.

3.5.4 Optimal Low-Thrust Orbit Raising: Comparison of Results

For the example direct solution (cf. Figure 3.51), the difference between the control angle (cf. Figure 3.51) and the exact solution is given in Figure 3.59. The exact solution was computed by solving the indirect problem (section 3.5.2) with 100 segments. The time of flight of the exact solution is 4.1114267 TU.

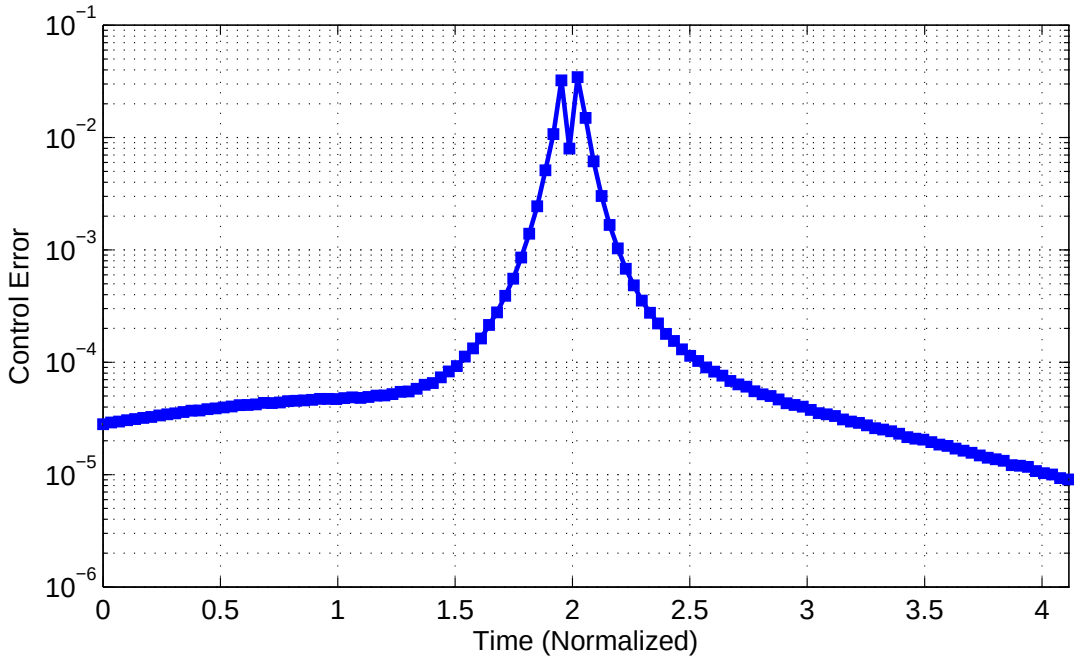

Figure 3.59: Control angle error for transfer from circular orbit (R=1) to circular orbit (R=1.523679). Solved using Taylor series (40 terms) constraints with 20 segments.

In the previous example problems mesh refinement proved to be of little concern as the states and controls all changed relatively uniformly over the time domain. The errors were relatively evenly distributed over the mesh, so the mesh refinement procedure outlined in Section 2.5 would have unnecessarily increased the computational burden. However, that is not the case in this example. The states and control change rapidly near the midpoint of the flight, i.e. near $t = 2\ TU$. The problem was solved using the aforementioned mesh refinement scheme. An example using the Taylor series shooting constraints and spline control with 12 segments and 37 control knots is shown in Figure 3.60. The mesh refinement scheme concentrates the nodes around the rapid change in control near $t = 2TU$, the initial and final node distribution is shown in Figure 3.61. This improved the accuracy of the solution, a comparison between the errors for this example and the similar solution obtained without mesh refinement, is in Table 3.4. The difference in the objective function errors with and without mesh refinement, 2.8008×10^{-6} and 1.4804×10^{-5} respectively , were not as great as those observed for the indirect case (cf. Table 3.3). This suggests the accuracy of the direct solutions

is affected more by the ability of the control parameterization to approximate the optimal control than the accuracy of the state propagation. The maximum state and maximum control errors were reduced 4.6 and 2.5 fold respectively. The runtime increased significantly 117s to 722s as the optimization is restarted several times as the mesh is refined.

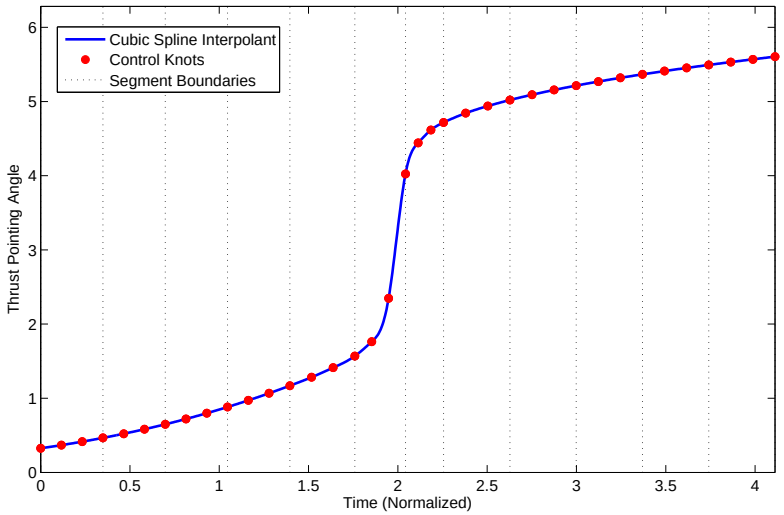

Figure 3.60: Control angle history for transfer from circular orbit (R=1) to circular orbit (R=1.523679). Solved using Taylor series shooting constraints with 12 segments and mesh refinement.

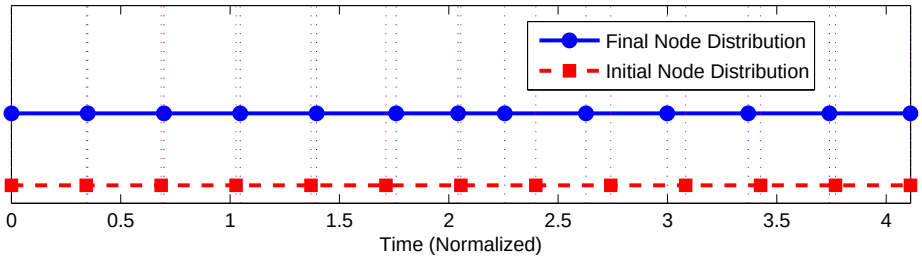

Figure 3.61: Initial and final node distribution for a transfer (R=1) to circular orbit (R=1.523679). Solved using Taylor series shooting constraints with 12 segments and mesh refinement.

	Objective Function Error	Maximum Control Error	Maximum State Error	CPU time (s)
Uniform Mesh	1.4804E-05	6.9136E-02	4.2654E-04	116.7017
With Mesh Refinement	2.8008E-06	2.7617E-02	9.2394E-05	722.0144

Table 3.4: Results for *direct* formulation of the orbit raising problem using mesh refinement.

To investigate the performance of the Taylor series multiple shooting constraints and the various control parameterizations, the direct problem was solved for various combinations of control parameterization and mesh density. In all cases 20 terms were retained in the Taylor series, no mesh refinement was performed and all solutions are on a uniform mesh. The direct problem was also solved using both Runge-Kutta multiple shooting with the same initial/terminal conditions and initial guess. The errors obtained from the various solution methods are compared in Figures 3.62 - 3.64.

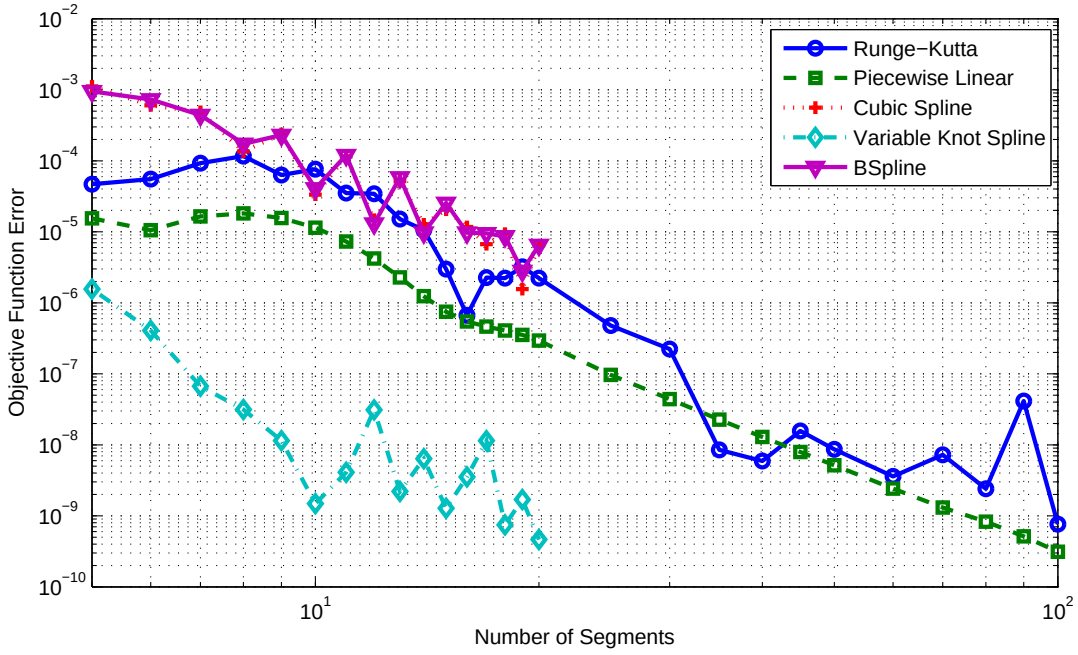

Figure 3.62: Objective function control error for transfer from circular orbit (R=1) to circular orbit (R=1.523679). Solved using Runge-Kutta multiple shooting or Taylor series (20 terms) constraints with various control parameterizations.

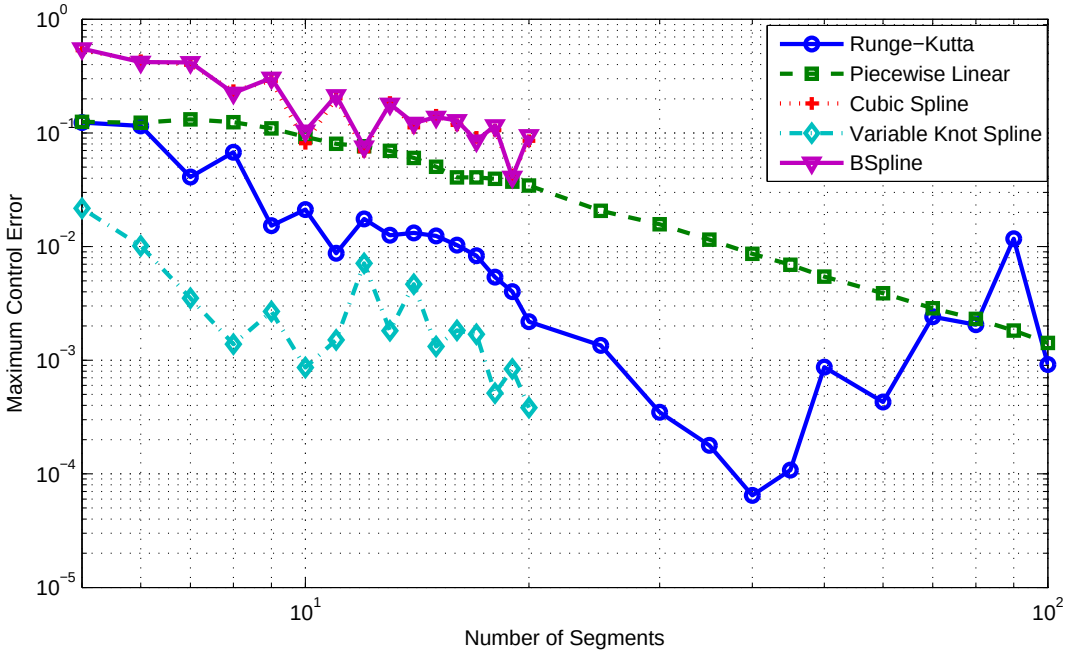

Figure 3.63: Maximum control error for transfer from circular orbit (R=1) to circular orbit (R=1.523679). Solved using Runge-Kutta multiple shooting or Taylor series (20 terms) constraints with various control parameterizations.

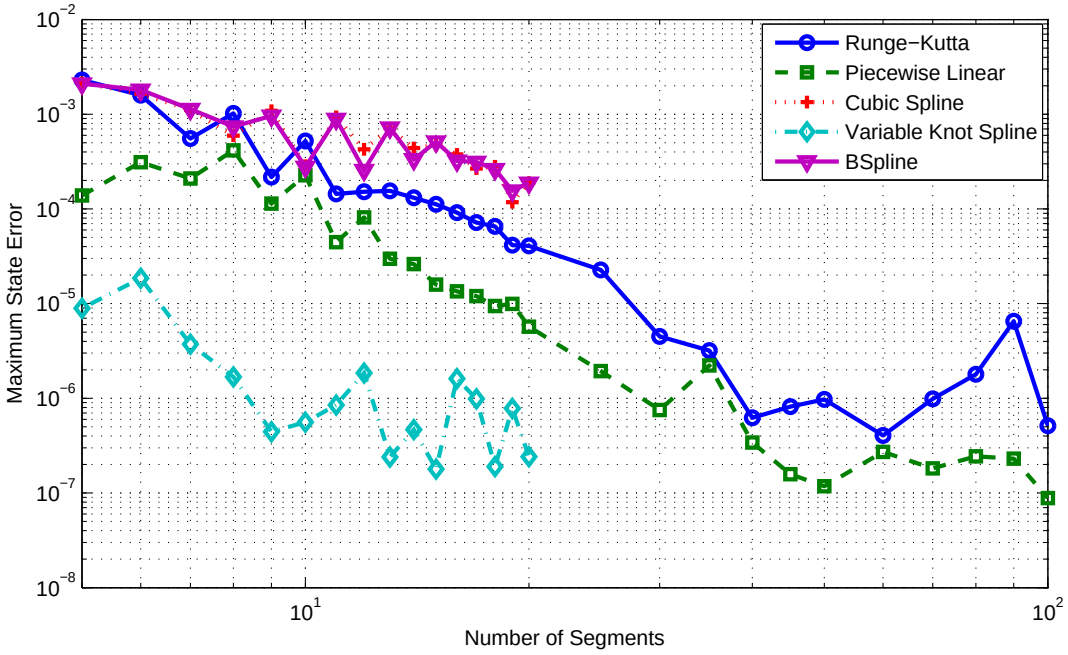

Figure 3.64: Maximum state error for transfer from circular orbit (R=1) to circular orbit (R=1.523679). Solved using Runge-Kutta multiple shooting or Taylor series (20 terms) constraints with various control parameterizations.

As seen in Figures 3.62-3.64 the spline and BSpline control parameterizations did not perform well for this problem. They were unable to adequately capture the rapid change in the thrust pointing angle around the midpoint of trajectory. Consequently the errors associated with Taylor series multiple shooting using those control parameterizations are greater than those of the Runge-Kutta method. The control parameterization that most closely resembles the way control is specified in the Runge-Kutta method is piecewise linear. The Taylor series shooting method with piecewise linear control slightly outperformed the Runge-Kutta method, however, the difference was not substantial despite the much higher-order accuracy of the Taylor series constraints (20 terms, therefore $O(h^{21})$) compared to the Runge-Kutta constraints ($O(h^5)$). This indicates that the most important factor in the accuracy of the solution is the control parameterization. The most accurate solutions are obtained with variable knot splines. In this case the added flexibility of allowing the optimizer to move the control points in time proved beneficial. By concentrating control knots around the rapid change in control, the resulting spline was able to better approximate the exact optimal control.

The same comparison is made for the solutions to the indirect problem (section 3.5.2). Three methods are compared: the Runge-Kutta multiple shooting, the Taylor series shooting method without mesh refinement and the Taylor series shooting method with mesh refinement. In all cases the initial guess came from the direct solution to the problem using the same mesh. The states are taken directly from the direct solution while the costates are computed from the KKT conditions. The results are shown in Figures 3.65-3.67. Both Taylor series based solutions significantly outperform the Runge-Kutta solutions in all three error measurements considered. The mesh refinement has a significant impact on the quality of the solutions. By concentrating nodes around the rapid change in the costates near the midpoint of the trajectory, extremely accurate solutions ($O(10^{-10})$ are able to be obtained for relatively coarse meshes (8 segments).

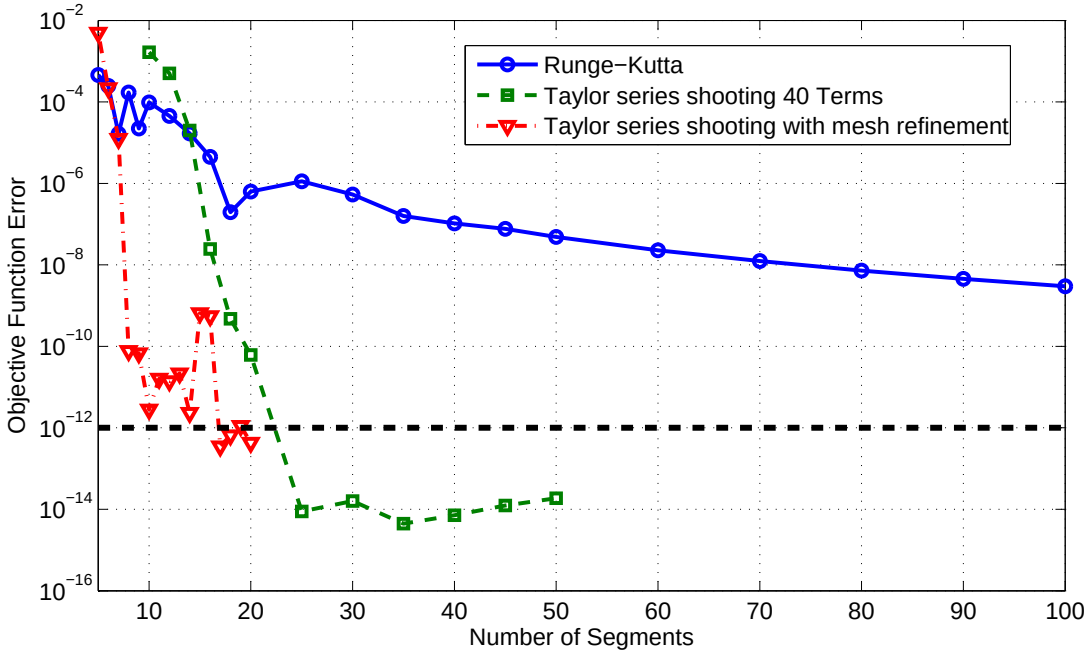

Figure 3.65: Objective function error comparison for indirect solution to orbit raising problem for Taylor series shooting (with and without mesh refinement) and Runge-Kutta multiple shooting methods.

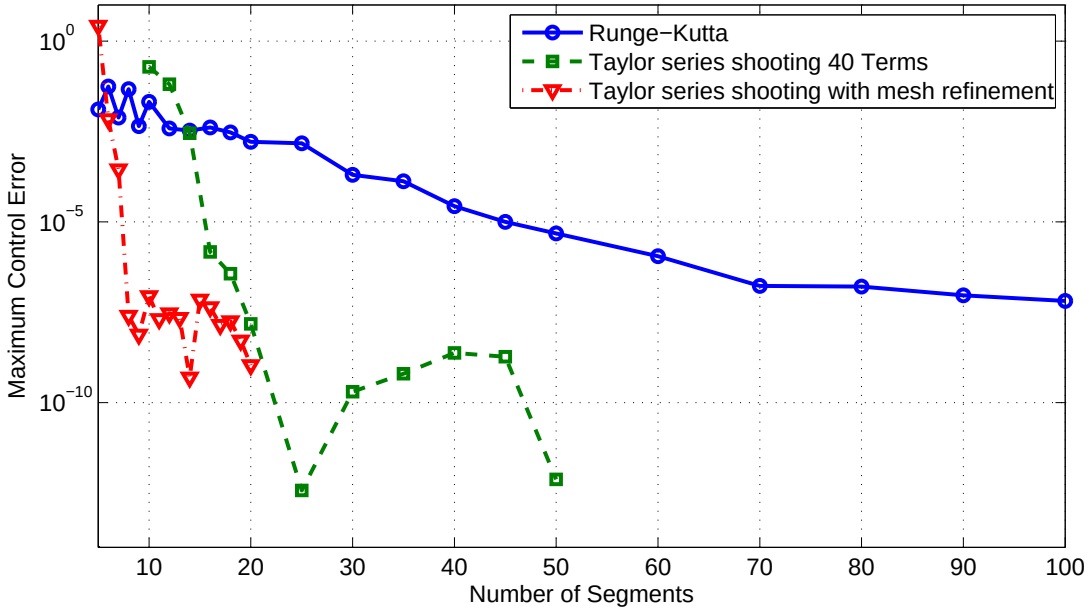

Figure 3.66: Maximum control error comparison for indirect solution to orbit raising problem for Taylor series shooting (with and without mesh refinement) and Runge-Kutta multiple shooting methods.

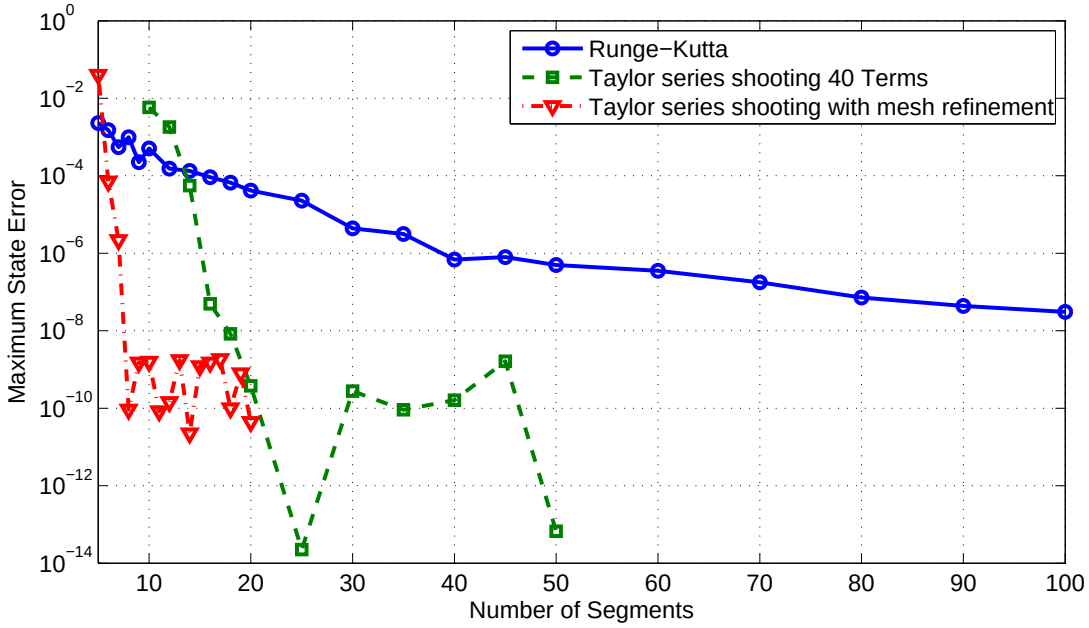

Figure 3.67: Maximum state error comparison for indirect solution to Orbit Raising problem for Taylor series shooting (with and without mesh refinement) and Runge-Kutta multiple shooting methods.

3.5.5 Example: Optimal Low-Thrust Orbit Raising Allowing Variable Thrust

The orbit raising problem is considered with variable thrust in polar coordinates. A throttle parameter u_2 is introduced and the existing control (thrust pointing angle) is renamed u_1. The equations of motion then become:

$$\begin{aligned} \dot{r} &= v_r \\ \dot{\theta} &= \tfrac{v_\theta}{r} \\ \dot{v}_r &= v_\theta^2 - \tfrac{1}{r^2} + u_2 a_T \sin(u_1) \\ \dot{v}_\theta &= \tfrac{v_r v_\theta}{r} + u_2 a_T \cos(u_1) \end{aligned} \tag{3.65}$$

where:

$$0 \leq u_2 \leq 1 \tag{3.66}$$

We seek the trajectory that minimizes fuel consumption. Mass flow rate is given by:

$$\dot{m} = -u_2 \frac{T}{c} \tag{3.67}$$

mass (fuel) consumption is then given by:

$$\Delta m = \int_{t_0}^{t_f} \dot{m} dt = -\frac{T}{c} \int_{t_0}^{t_f} u_2 dt \tag{3.68}$$

where thrust (T) and exhaust velocity (c) are constants. The objective function is then to minimize:

$$J = \int_{t_0}^{t_f} u_2 dt \tag{3.69}$$

The Hamiltonian of the system is therefore:

$$H = u_2 + \lambda_r v_r + \lambda_\theta \frac{v_\theta}{r} + \lambda_{v_r} \left(v_\theta^2 - \frac{1}{r^2} + u_2 a_T \sin(u_1) \right) + \lambda_{v_\theta} \left(\frac{v_r v_\theta}{r} + u_2 a_T \cos(u_1) \right) \tag{3.70}$$

Define control unit vector $\boldsymbol{\sigma}$ and velocity costate vector $\boldsymbol{\lambda_v}$:

$$\begin{aligned} \boldsymbol{\sigma} &= \begin{bmatrix} \sin(u_1) \\ \cos(u_1) \end{bmatrix} \\ \boldsymbol{\lambda}_v &= \begin{bmatrix} \lambda_{v_r} \\ \lambda_{v_\theta} \end{bmatrix} \end{aligned} \tag{3.71}$$

The Hamiltonian then becomes:

$$H = u_2 + v_r \lambda_r + \frac{v_\theta \lambda_\theta}{r} + \lambda_v^T \begin{bmatrix} \left(\frac{v_\theta^2}{r} - \frac{1}{r^2} \right) \\ -\frac{v_r v_\theta \lambda_{v_\theta}}{r} \end{bmatrix} + u_2 a_T \lambda_v^T \sigma \tag{3.72}$$

By the Pontryagin minimum principle the optimal control will minimize the Hamiltonian with respect to u_1. This is clearly when the unit control vector $\boldsymbol{\sigma}$ directly opposes the velocity costate vector $\boldsymbol{\lambda_v}$. Therefore:

$$\boldsymbol{\sigma} = \frac{-\boldsymbol{\lambda}_v}{|\boldsymbol{\lambda}_v|} \tag{3.73}$$

The control law is then:

$$\begin{aligned} \sin u_1 &= \frac{-\lambda_{v_r}}{\sqrt{\lambda_{v_r}^2 + \lambda_{v_\theta}^2}} \\ \cos u_1 &= \frac{-\lambda_{v_\theta}}{\sqrt{\lambda_{v_r}^2 + \lambda_{v_\theta}^2}} \end{aligned} \tag{3.74}$$

The Hamiltonian must also be minimized with respect to throttle parameter u_2. The portion of the Hamiltonian that depends on u_2 is:

$$\hat{H} = u_2 \left(1 + a_T \boldsymbol{\lambda}_v^T \sigma\right) \tag{3.75}$$

The Hamiltonian is therefore minimized by:

$$\arg\min_{u_2} H = \begin{cases} u_2 = 1 & \text{if } 1 + a_T \boldsymbol{\lambda}_v^T \boldsymbol{\sigma} < 0 \\ u_2 = 0 & \text{if } 1 + a_T \boldsymbol{\lambda}_v^T \boldsymbol{\sigma} > 0 \end{cases} \tag{3.76}$$

Define a switching function:

$$S = 1 + a_T \boldsymbol{\lambda}_v^T \boldsymbol{\sigma}$$

Substituting the control law for $\boldsymbol{\sigma}$ (3.74) yields:

$$S = 1 - a_T \sqrt{\lambda_{v_r}^2 + \lambda_{v_\theta}^2} \tag{3.77}$$

We now know that the throttle control will either be 1 or 0, except for any singular arcs where $S = 0$, which we will assume is not optimizing for this problem. Therefore, rather than specifying the throttle at every control node we only need to specify where it switches from 0 to 1 or vice-versa. The orbit raising problem will be solved using the switching times control parametrization (see Section 2.4.4) for the second control variable u_2. Twelve control parameters were used, so up to twelve switches (6 coast arcs and 7 thrust arcs) were possible. Piecewise linear control was chosen for u_1. The solution does not explicitly use the necessary conditions or the costates to govern the timing of the switches. However, the switching function can be computed *a posteriori* from the estimate of the costates given by the output from the NLP solver. This switching function can be used to check that the switches in the throttle given by control u_2 occur at the optimal times. The optimal trajectory is shown in Figure 3.68, with the corresponding control history shown in Figure 3.69. The solution found has a thrust-coast-thrust sequence with a total time of flight of 5.405 TU. The total time of the two thrust arcs is 1.880 TU.

In the solution found, the throttle switches from 1 to 0 at time 1.00345 and back from 0 to 1 at time 4.52846. Figure 3.70 shows the value of the switching function (equation 3.77) over the trajectory. It shows that the switches found numerically in the *direct* solution occur at the same times specified by the necessary conditions, even though the necessary conditions were not explicitly applied.

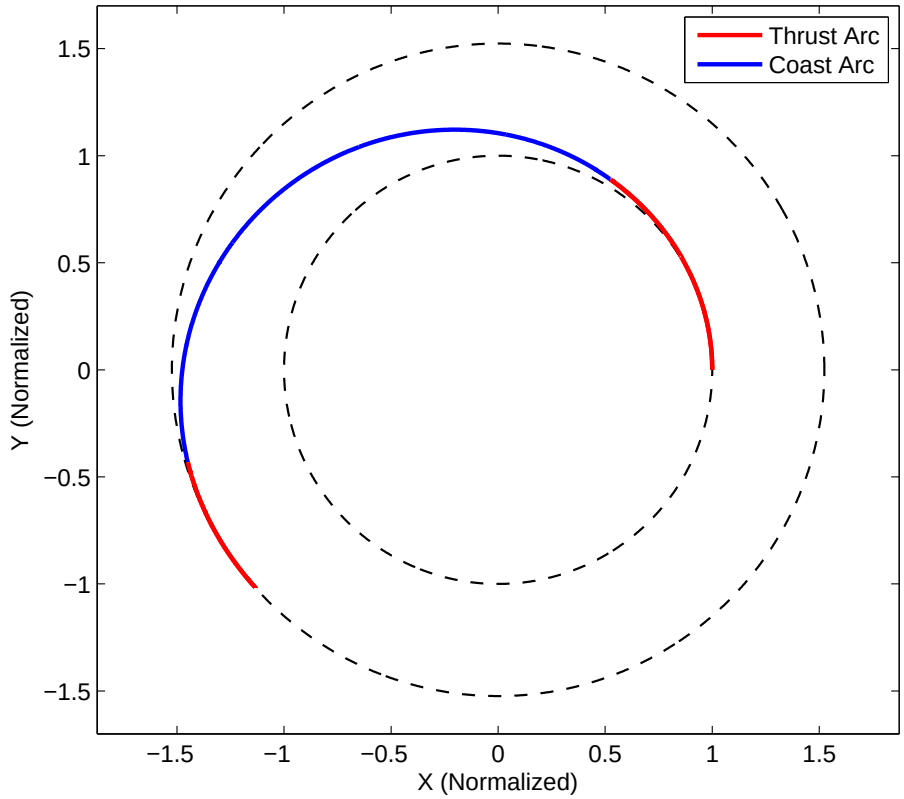

Figure 3.68: Optimal trajectory for transfer from circular orbit (R=1) to circular orbit (R=1.523679) with variable thrust. Solved using Taylor series (40 terms) constraints with 10 segments.

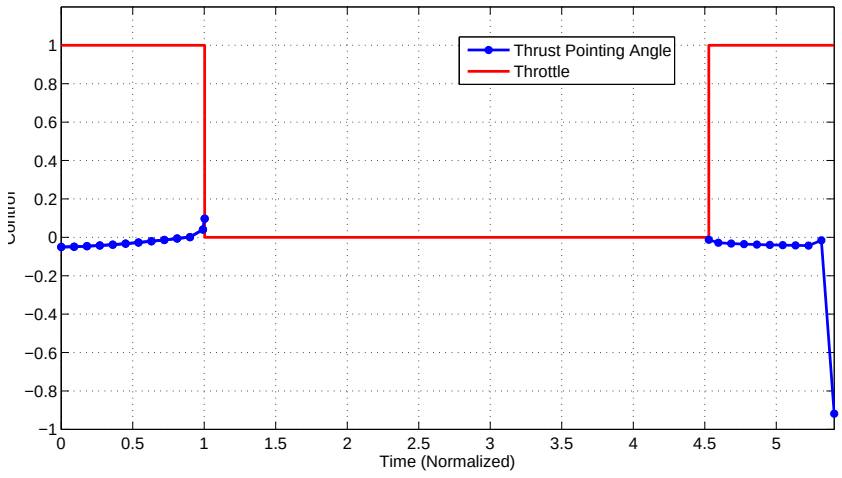

Figure 3.69: Control history for optimal trajectory for transfer from circular orbit (R=1) to circular orbit (R=1.523679) with variable thrust . Solved using Taylor series (40 terms) constraints with 10 segments.

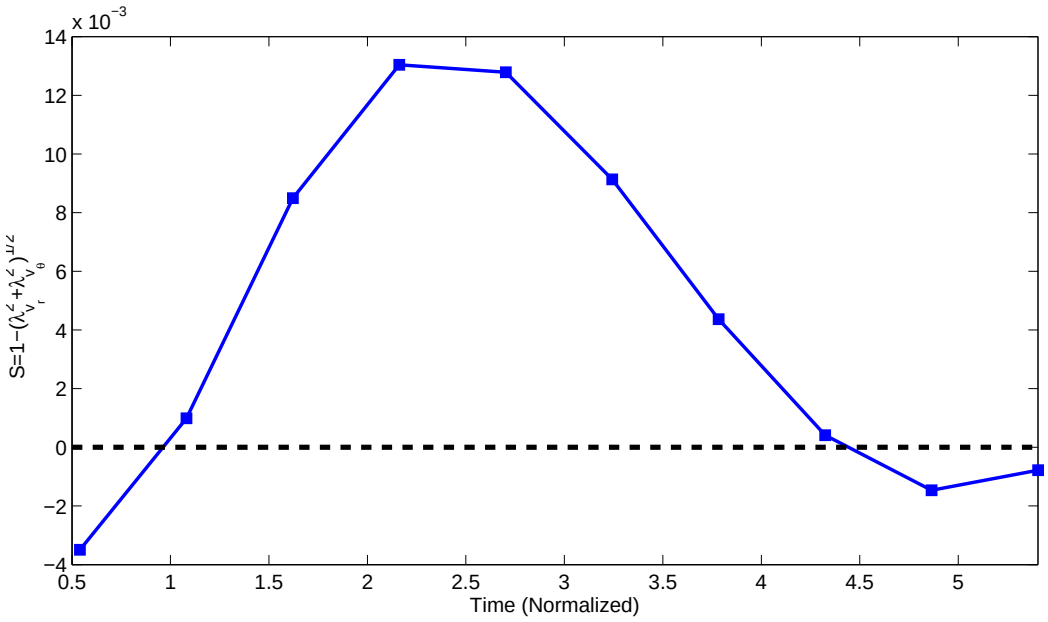

Figure 3.70: Switching function for optimal trajectory for transfer from circular orbit (R=1) to circular orbit (R=1.523679) with variable thrust . Solved using Taylor series (40 terms) constraints with 10 segments.

3.6 Example: Optimal Low-Thrust Orbit Phasing

This problem is similar to the low thrust orbit raising problem of Section 3.5. The goal is now to rendezvous with an object orbiting at unit radius ($r_1 = r_2 = 1$) that begins in the same orbit but on the opposite side of the primary from the spacecraft (i.e. $\theta_0 = \pi$). This is the low-thrust version of the impulsive orbit phasing problem studied by Prussing and Chiu.[48] The equations of motion (3.42) are unchanged. The initial and terminal conditions (3.5) are unchanged except for the rendezvous condition:

$$\theta(T) = \pi + T \tag{3.78}$$

3.6.1 Optimal Low-Thrust Orbit Phasing: *Indirect* Results

The costate equations (3.62) remain the same as for the orbit raising case (Section 3.5). Since this is also a minimum time problem the control law (3.61) is also unchanged. However since the final angle $\theta(T)$ is now constrained the terminal conditions on the costates do change. They are now:

$$\begin{aligned}
\lambda_r(T) &= \upsilon_r \\
\lambda_\theta(T) &= \upsilon_\theta \\
\lambda_{v_r}(T) &= \upsilon_{v_r} \\
\lambda_{v_\theta}(T) &= \upsilon_{v_\theta}
\end{aligned} \tag{3.79}$$

and the transversality condition obtained for this problem is:

$$1 - a_T \sqrt{\lambda_{v_r}^2(T) + \lambda_{v_\theta}^2(T)} = 0 \tag{3.80}$$

The solution for the direct problem provided the initial guess. The solution shown in Figure 3.71 was calculated using Taylor series shooting constraints. An adaptive mesh of 20 segments was used. The corresponding thrust pointing angle is shown in Figure 3.72. The solution obtained agrees very closely with the exact solution. The exact solution was calculated by solving the problem on a very fine mesh (200 Segments).

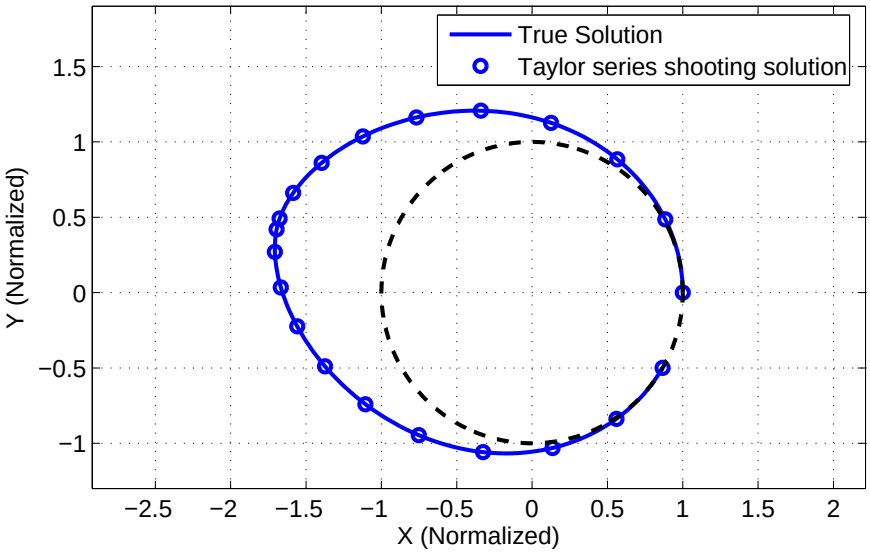

Figure 3.71: Optimal trajectory for transfer from circular orbit (R=1) to circular orbit (R=1) with π phase change. Solved using Taylor series constraints with 20 segments on an adaptive mesh. "True" solution found using same procedure but on a much finer mesh (200 segments).

Figure 3.72: Optimal control history for transfer from circular orbit (R=1) to circular orbit (R=1) with π phase change. Solved using Taylor series constraints with 20 segments on an adaptive mesh. "True" solution found using same procedure but on a much finer mesh (200 segments).

The mesh refinement scheme concentrates nodes around the midpoint of the trajectory where the control changes rapidly. However there is still a spike in control error at this point (see Figure 3.73), even with the optimized mesh. This is because the mesh refinement seeks to evenly distribute errors in the state (and costate) variables, not in the control directly. The error in both of the costates that are in the control law (3.61) is minimized around this point. However, because of the form of the control law and the magnitudes of the costates at this location (near zero) the error in the control angle remains large.

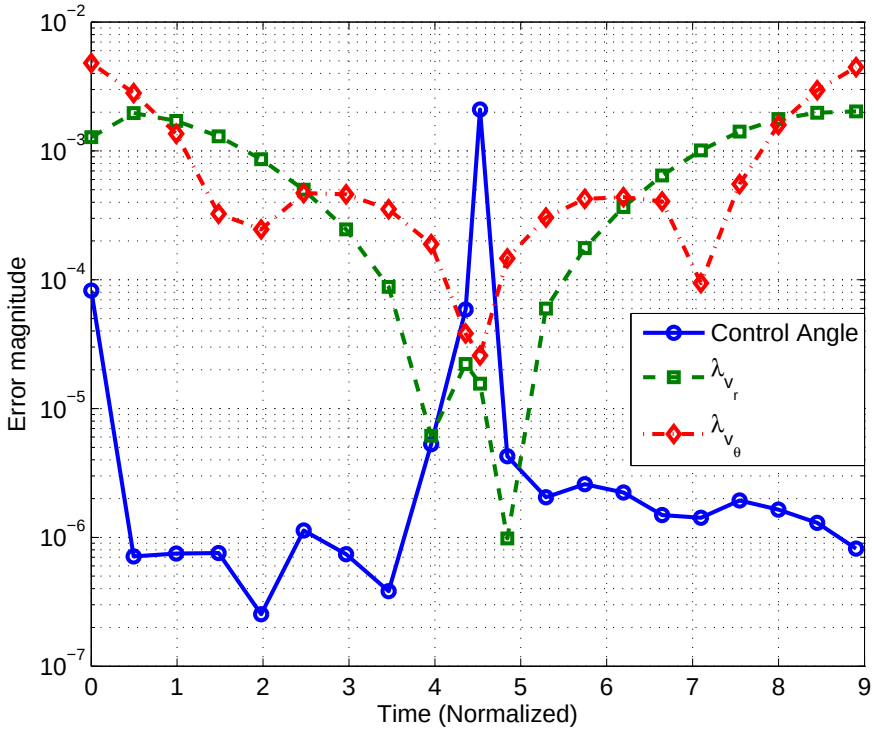

Figure 3.73: Control angle error for transfer from circular orbit (R=1) to circular orbit (R=1) with π phase change. Solved using Taylor series constraints with 20 segments on an adaptive mesh.

3.6.2 Optimal Low-Thrust Orbit Phasing: *Direct* Results

The problem was solved using Taylor series multiple shooting constraints with a uniform mesh of 20 segments with 6 subsegments, 20 terms were retained in the Taylor series. The initial guess was generated by integrating the equations of motion forward for 9 time units assuming tangential thrust (a thrust pointing angle of zero). The optimal trajectory found is shown in Figure 3.74 and the corresponding control history is shown in Figure 3.75.

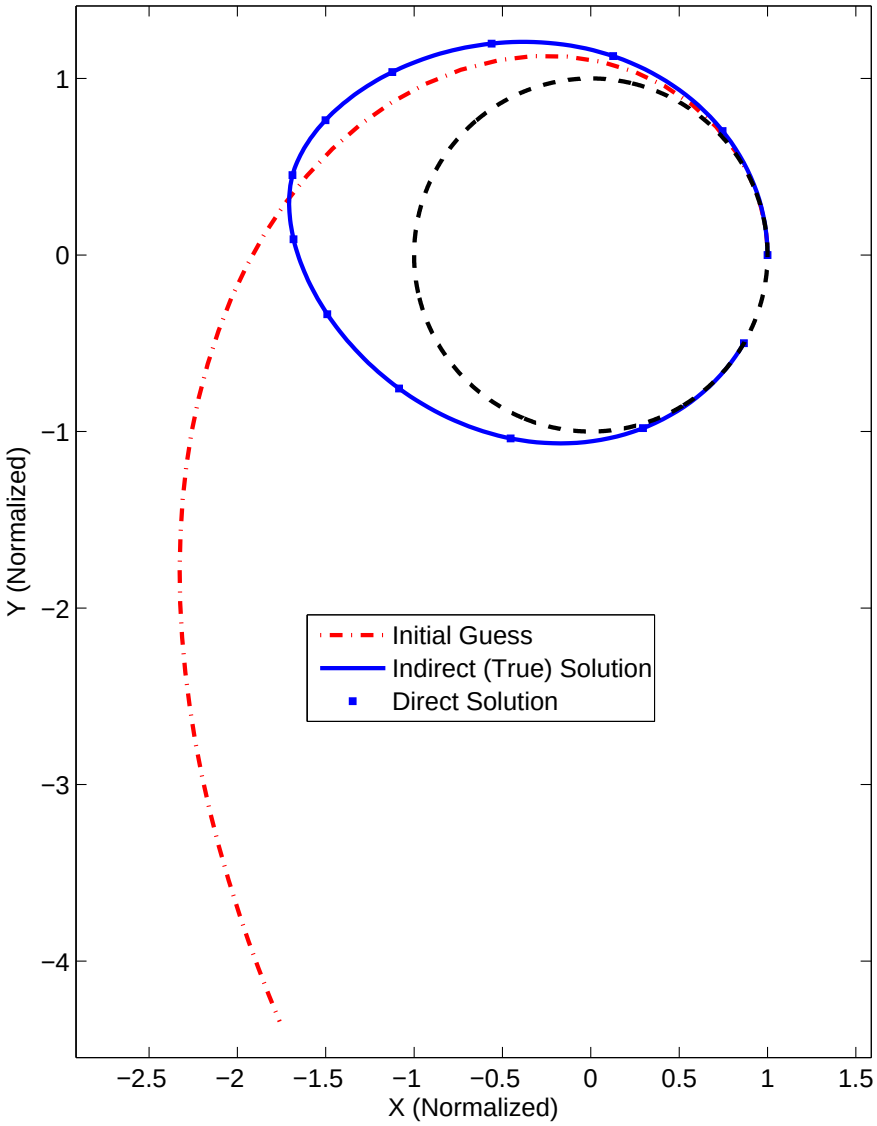

Figure 3.74: Optimal trajectory for transfer from circular orbit (R=1) to circular orbit (R=1) with π phase change . Solved using Taylor series (20 terms) constraints with 20 segments.

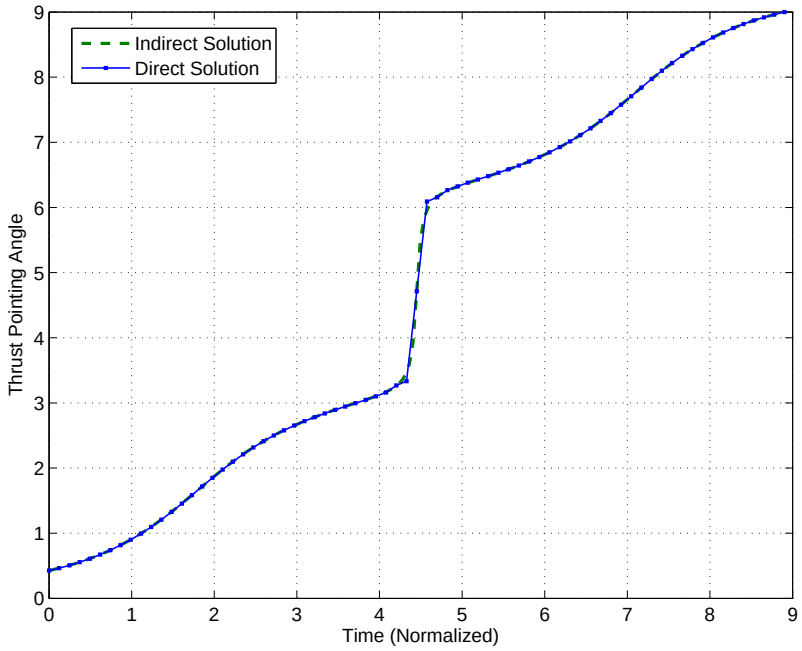

Figure 3.75: Optimal control history for transfer from circular orbit (R=1) to circular orbit (R=1) with π phase change. Solved using Taylor series (20 terms) constraints with 20 segments.

The solution obtained agrees very closely with the exact optimal solution. The exact solution was computed by solving the indirect problem (see Section 3.6.1) using a very fine mesh (200 segments).The deviation of the thrust pointing angle from the exact solution is shown in Figure 3.76.

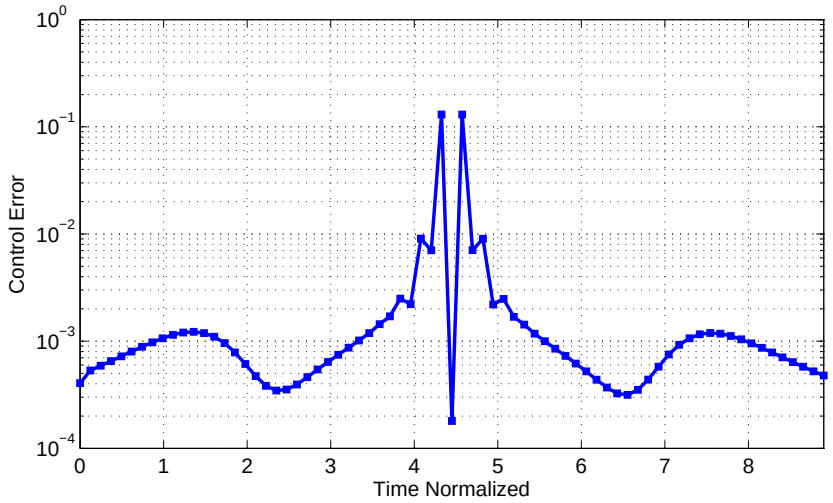

Figure 3.76: Control angle error for transfer from circular orbit (R=1) to circular orbit (R=1) with π phase change. Solved using Taylor series (40 terms) constraints with 20 segments.

3.6.3 Example: Optimal Low-Thrust Orbit Phasing Allowing Variable Thrust

The orbit phasing problem is considered with variable thrust in polar coordinates. As in the orbit raising problem, a throttle parameter u_2 is introduced and the existing control (thrust pointing angle) is renamed u_1. The addition of an extra constraint on final angle does not affect the Hamiltonian (3.70); therefore the arguments outlined in section 3.5.5 with respect to the necessary conditions for the optimality of controls $u_1$and u_2 hold. Hence the throttle parameter u_2 is either zero or one at every point on the optimal trajectory and can be described by its switching times.

The problem is solved with 20 segments and Taylor series shooting constraints (20 terms). Piecewise linear control is used for thrust pointing angle u_1. The throttle parameter u_2 is described by its switching times. Twelve control parameters were used, so up to twelve switches (6 coast arcs and 7 thrust arcs) were possible. The optimal trajectory is shown in Figure 3.77 with the corresponding control history shown in Figure 3.78. The optimal solution obtained has a thrust-coast-thrust sequence. The total time of flight of the trajectory is $9.4248\ TU$ of which $4.2562\ TU$ is spent at full throttle ($u_2 = 1$). The switches occur at 2.1281 and $7.2967\ TU$.

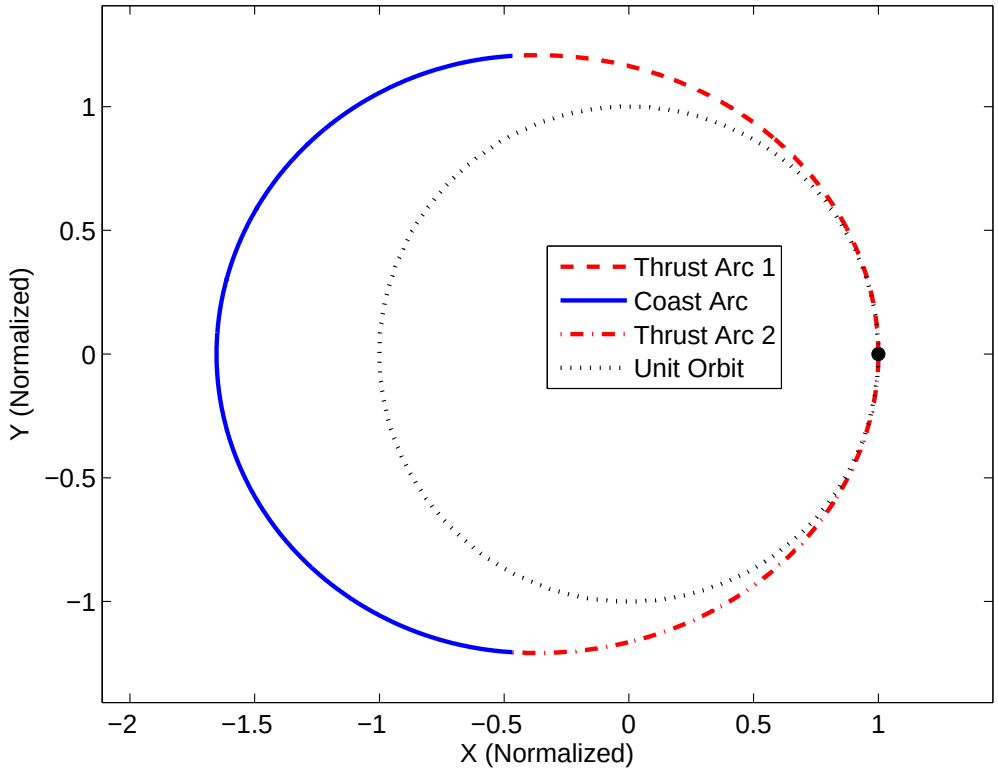

Figure 3.77: Optimal trajectory for transfer from circular orbit (R=1) to circular orbit (R=1) with π phase change and variable thrust. Solved using Taylor series (20 terms) constraints with 20 segments.

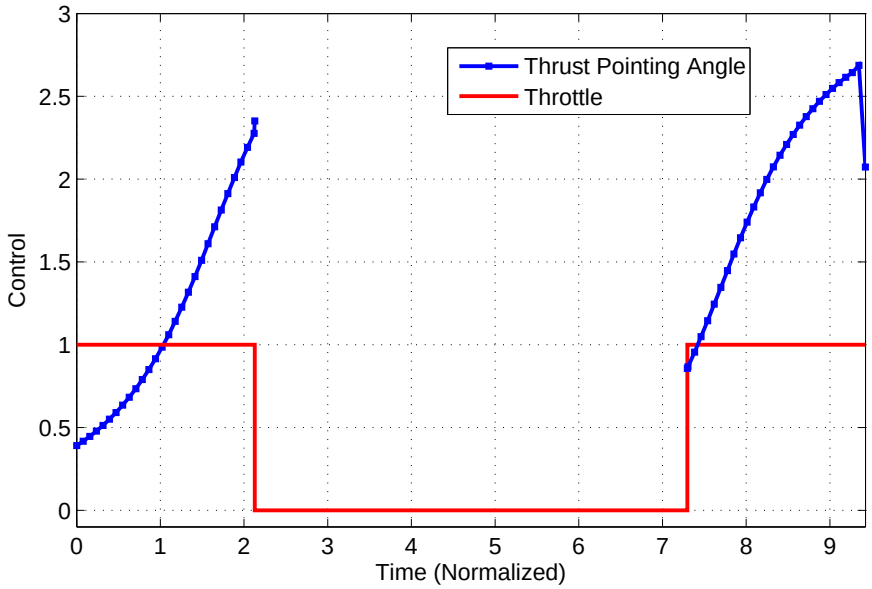

Figure 3.78: Optimal control history for transfer from circular orbit (R=1) to circular orbit (R=1) with π phase change and variable thrust. Solved using Taylor series (20 terms) constraints with 20 segments.

In the solution found, the throttle switches from 1 to 0 at time $2.1281\ TU$ and back from 0 to 1 at time $7.2967\ TU$. Figure 3.79 shows the value of the switching function (equation 3.77) over the trajectory. It shows that the switching times found in the *direct* solution agree with the optimal times specified by the necessary conditions, even though those conditions were not explicitly used.

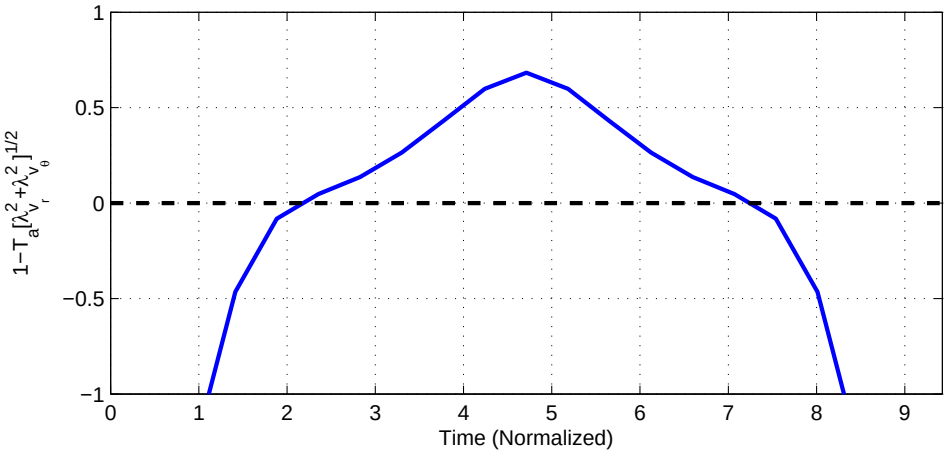

Figure 3.79: Switching function for optimal trajectory for transfer from circular orbit (R=1) to circular orbit (R=1) with π phase change and variable thrust. Solved using Taylor series (20 terms) constraints with 20 segments.

3.7 Conclusion

The new Taylor series shooting constraints performed well, significantly outperforming the conventional Runge-Kutta constraints on a variety of test problems. These problems ranged from a recast two point boundary value problem (periodic orbit generation, Section 3.2) to a 2D orbit transfer with low-thrust, full terminal conditions (including a rendezvous) and *bang-bang* control (low-thrust orbit phasing, Section 3.6). The method was also able to handle sophisticated equations of motion such as the modified equinoctial element variational equations (3.56).

The mesh refinement scheme (Section 2.5) equally distributed the error by concentrating nodes around rapid changes in state and control variables, allowing accurate solutions to be found for relatively few segments. Several control parameterizations were tested, with the variable knot spline producing the most accurate solutions. Piecewise linear control produced only adequate results in terms of accuracy, but it was the most efficient in terms of CPU time. BSplines (fixed and variable knot) produced poor results on both measures, accuracy and computational time.

The performance of the higher-order collocation method was disappointing in comparison. The higher-order interpolating polynomials proved to be unstable, and while collocation using the lower-order polynomials converged, the solutions were not as accurate as those found using the Taylor series shooting method. There was also a reduction in choice of control parameterization that can be used, as control points must be selected such that every control value effects either the state derivative at one of the segment boundaries or the central collocation point. Therefore the more successful Taylor series shooting method will be used to solve the capstone problem of this thesis: the Earth-Moon transfer using halo orbits and their stable and unstable manifolds.

Chapter 4

Earth Moon Transfer

4.1 Problem Description

In this chapter a fuel optimal low-thrust trajectory from Earth orbit to low-Lunar orbit is found using the dynamics of the three-body problem. The differential equations of the circular restricted three body problem (CR3BP) describe the motion of a point mass P_3 with mass m_3 under the gravitational influence of two massive primaries P_1 and P_2 with masses m_1 and m_2 respectively, where $m_1 > m_2 \gg m_3 \approx 0$. It is assumed that P_3 exerts negligible influence on the primaries. The motion is considered in a non-inertial frame that moves with the two primaries as they rotate about the system barycenter at constant radius, as shown in Figure 3.1. The equations of motion (3.2) for the CR3BP admit five equilibrium points, the Lagrange points. The positions of the Lagrange points are shown in Figure 3.2. There exist regions in phase space that asymptote, both towards and away from, these periodic orbits, the stable and unstable manifolds. The stable manifolds are regions in phase space such that once a body is on the stable manifold it will coast to the periodic orbit. The unstable manifolds are regions in phase space that a body will take as it coast away from the periodic orbit.

The Hill's region, that is the region of allowable motion of the 3$^{\text{rd}}$ body (of negligible mass) in the three body system, is a function of energy. At the lowest energy it is merely two small, almost spherical regions around the primaries; this implies that if the small body were to be found within one of these regions it could never escape the vicinity of the nearby primary. As energy increases these regions grow until they touch.[15] The point of contact is the L_1 interior Lagrange point. The energy at which this neck opens up is then the minimum possible energy for an Earth-Moon transfer. Therefore a transfer that is constructed using a halo orbit around this Lagrange point and the stable and unstable manifolds that depart from it, should require less energy than alternative transfers.

In this work the first phase of the transfer is a thrust arc departing a geostationary transfer orbit (GTO) to intersect the stable manifold, followed by a coast along the stable manifold until a transfer to a periodic orbit about L_1 is possible. Due to the low-thrust provided by the engine, many revolutions of the Earth will be required to gather the necessary energy to escape, even from GTO. This initial period of orbit raising will be hereafter referred to as the

escape spiral. The second phase is a coast along the unstable manifold (i.e. the manifold departing L_1) towards the moon followed by a thrust arc to insert into a low lunar orbit. In general, there is no guarantee that the combination of two individually optimal trajectories is optimal. However, in this case the periodic orbit can be considered as a parking orbit which can be traversed with no cost, effectively decoupling the Earth-Halo transfer from the Halo-Moon transfer.

The problem is similar to that studied by Mingotti, Topputo and Bernelli-Zazzera,[49] however, several simplifying assumptions they made were removed in this work. In their work they assumed that: (i) the spacecraft had constant thrust acceleration, (ii) it was optimal to align thrust with the velocity vector during the escape spiral (iii) the initial plane of the geosynchronous transfer orbit (GTO) was in the plane of the Moon's orbit.

In this work: (i) the spacecraft has constant thrust rather than constant thrust *acceleration* (since the thrust acceleration naturally increases as fuel is consumed), (ii) the thrust pointing angle during the escape spiral will be optimized (iii) the initial plane of the geosynchronous transfer orbit (GTO) is equatorial (the usual case) rather than in the plane of the MoonŠs orbit.

For comparison with the work of Mingotti, Topputo and Bernelli-Zazzera, the same spacecraft parameters, will be used, i.e. it the spacecraft has an initial thrust acceleration of $7{\times}10^{-4} m.s^{-2}$ with a specific impulse of 3000s and starts from GTO with semi-major axis of 24510 km and eccentricity 0.72345981. It is assumed that there are no coasting arcs other than the coasting arcs on the stable and unstable manifolds.

4.2 System Dynamics

4.2.1 Circular Restricted Three Body Problem

The idealized low-thrust engine used in this study provides a constant thrust magnitude T. Since there is assumed to be only one thrust arc per phase and the engine is always operating at maximum thrust when it is on, the thrust acceleration is given by:

$$T_a(t) = \frac{T_a(0)\, c}{c - T_a(0)\, t} \tag{4.1}$$

where $t = 0$ corresponds to the time of ignition and c is the exhaust velocity. The thrust pointing angles u_1 and u_2 are defined with respect to the instantaneous velocity vector $\mathbf{v}$ which makes an angle ϕ with the x-y plane. The projection

of **v** to the x-y plane makes an angle γ with the x-axis as shown in Figure 4.1. The equations of motion then become:

$$\begin{aligned}
\dot{x} &= v_x \\
\dot{y} &= v_y \\
\dot{z} &= v_z \\
\dot{v}_x &= 2v_y + x - \frac{(1-\mu)(x+\mu)}{r_1^3} - \frac{\mu(x-1+\mu)}{r_2^3} + T_a \cos(\gamma + u_1)\cos(\phi + u_2) \\
\dot{v}_y &= -2v_x + y - \frac{(1-\mu)y}{r_1^3} - \frac{\mu y}{r_2^3} + T_a \cos(\phi + u_2)\sin(\gamma + u_1) \\
\dot{v}_z &= -\frac{(1-\mu)z}{r_1^3} - \frac{\mu z}{r_2^3} + T_a \sin(\phi + u_2)
\end{aligned} \tag{4.2}$$

where:

$$\gamma = \tan^{-1}\left(\frac{v_y}{v_x}\right) \phi = \tan^{-1}\left(\frac{v_z}{\sqrt{v_x^2 + v_y^2}}\right)$$

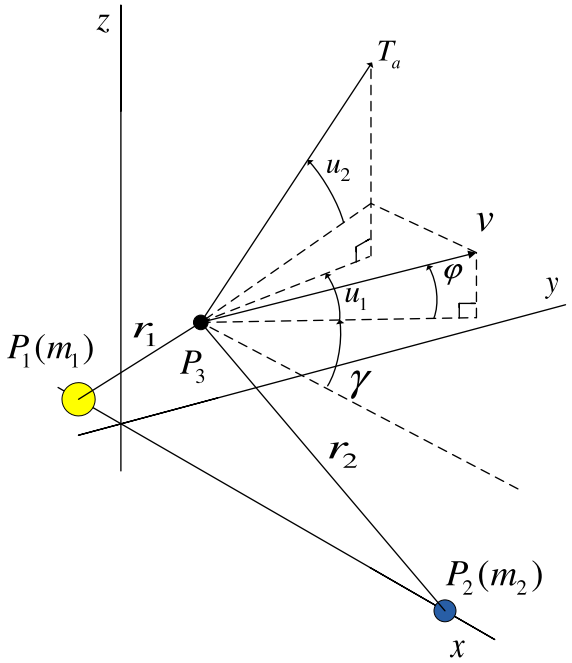

Figure 4.1: Locating the low-thrust spacecraft P_3 in the three body system.

Since only low-thrust engines are used in these cases, significant spiraling about the departure and arrival bodies will be required. It is awkward to describe these spirals in Cartesian coordinates so two alternative coordinate systems will be used: orbit elements $(a, e, i, \omega, \Omega, f)$ and equinoctial elements $(a, P_1, P_2, Q_1, Q_2, L)$.[50] In both cases the

thrust acceleration is described in the local body-fixed axes and modeled as a perturbation. Both coordinate systems, orbit elements and equinoctial elements, describe motion around a central body. To model the three-body system the attraction of the 3rd body (the Earth or the Moon, whichever is not the central body) is included as a perturbation.

Stable and Unstable Manifolds

It will be necessary for the Earth-Moon transfer via a periodic orbit about L_1 to compute the periodic orbit's stable and unstable manifolds (W_s, W_u). The manifolds are tangent to the eigenvectors of the monodromy matrix which is computed by evaluating the variation matrix (4.3) at time equal to one period of the periodic orbit.

$$\left(\frac{\partial x_i}{\partial x_{0j}}\right) = \begin{pmatrix} \frac{\partial x}{\partial x_0} & \frac{\partial x}{\partial y_0} & \frac{\partial x}{\partial z_0} & \frac{\partial x}{\partial v_{x0}} & \frac{\partial x}{\partial v_{y0}} & \frac{\partial x}{\partial v_{z0}} \\ \frac{\partial y}{\partial x_0} & \frac{\partial y}{\partial y_0} & \frac{\partial y}{\partial z_0} & \frac{\partial y}{\partial v_{x0}} & \frac{\partial y}{\partial v_{y0}} & \frac{\partial y}{\partial v_{z0}} \\ \frac{\partial z}{\partial x_0} & \frac{\partial z}{\partial y_0} & \frac{\partial z}{\partial z_0} & \frac{\partial z}{\partial v_{x0}} & \frac{\partial z}{\partial v_{y0}} & \frac{\partial z}{\partial v_{z0}} \\ \frac{\partial v_x}{\partial x_0} & \frac{\partial v_x}{\partial y_0} & \frac{\partial v_x}{\partial z_0} & \frac{\partial v_x}{\partial v_{x0}} & \frac{\partial v_x}{\partial v_{y0}} & \frac{\partial v_x}{\partial v_{z0}} \\ \frac{\partial v_y}{\partial x_0} & \frac{\partial v_y}{\partial y_0} & \frac{\partial v_y}{\partial z_0} & \frac{\partial v_y}{\partial v_{x0}} & \frac{\partial v_y}{\partial v_{y0}} & \frac{\partial v_y}{\partial v_{z0}} \\ \frac{\partial v_z}{\partial x_0} & \frac{\partial v_z}{\partial y_0} & \frac{\partial v_z}{\partial z_0} & \frac{\partial v_z}{\partial v_{x0}} & \frac{\partial v_z}{\partial v_{y0}} & \frac{\partial v_z}{\partial v_{z0}} \end{pmatrix} \tag{4.3}$$

The variation matrix satisfies the differential equation.

$$\frac{d}{dt}\left(\frac{\partial x_i}{\partial x_{0j}}\right) = \sum_{k=1}^{6} \frac{\partial \dot{x}_i}{\partial x_k} \frac{x_k}{x_{0j}} \tag{4.4}$$

where:

$$\left(\frac{\partial \dot{x}_i}{\partial x_k}\right) = \begin{bmatrix} 0 & 0 & 0 & 1 & 0 & 0 \\ 0 & 0 & 0 & 0 & 1 & 0 \\ 0 & 0 & 0 & 0 & 0 & 1 \\ \Omega_{xx} & \Omega_{xy} & \Omega_{xz} & 0 & 2 & 0 \\ \Omega_{yx} & \Omega_{yy} & \Omega_{yz} & -2 & 0 & 0 \\ \Omega_{zx} & \Omega_{zy} & \Omega_{zz} & 0 & 0 & 0 \end{bmatrix} \tag{4.5}$$

and:

$$\Omega(x, y, z) = \frac{x^2 + y^2}{2} + \frac{1-\mu}{r_1} + \frac{\mu}{r_2} + \frac{\mu\,(1-\mu)}{2} \tag{4.6}$$

Combined with the circular restricted three body problem equations (3.2) describing the motion on the periodic orbit there are then 42 simultaneous differential equations that must be solved to give the variation matrix. The 6 eigenvalues

$(\lambda_1, ...\lambda_6)$ of the monodromy matrix are in three pairs:[51]

$$\lambda_1 > 1, \lambda_2 < 1, \lambda_1\lambda_2 = 1$$

$$\lambda_3 = \lambda_4 = 1 \tag{4.7}$$

$$\lambda_5 = \lambda_6^*$$

$$|\lambda_5| = |\lambda_6| = 1$$

The unstable and stable manifolds are approximated near the periodic orbits by the eigenvectors corresponding to λ_1 and λ_2 respectively (V^{W_u}, V^{W_s}). The manifolds are then computed by numerically integrating forward (for unstable manifolds) or backward (for stable manifolds) in time from initial conditions given by displacing the spacecraft a small distance d from the periodic orbit along the eigenvector (or its opposite). The displacement distance d must be small enough to retain the validity of the linear approximation, but also large enough to enable the spacecraft to get far enough away from the periodic orbit in a reasonable time of flight. A value of $d = 5\ km$ was used for this study. The manifolds are computed by combining the trajectories obtained from many initial points on the periodic orbit $(\bar{x}(t_i))$.

$$\mathbf{X}_s = \mathbf{x}(t_i) \pm d.\mathbf{V}^{W_s} \tag{4.8}$$

$$\mathbf{X}_u = \mathbf{x}(t_i) \pm d.\mathbf{V}^{W_u} \tag{4.9}$$

4.2.2 Orbit Elements

The familiar orbital elements $(a, e, i, \Omega, \omega, f)$ are used for the escape spiral from Earth. Since the formula for $\dot{f}$ explicitly depends on time f is replaced by two new variables (χ, ξ) related to the mean anomaly.[52]

$$M = \xi - \chi \tag{4.10}$$

The variational equations become:[52]

$$\begin{aligned}
\dot{a} &= \frac{2a^{\frac{3}{2}}}{\sqrt{\mu_e\left(1-e^2\right)}}\left(Re\sin f + T\left(1+e\cos f\right)\right) \\
\dot{e} &= \sqrt{\frac{a\left(1-e^2\right)}{\mu_e}}\left(R\sin f + T\left(\cos f + \cos E\right)\right) \\
\dot{i} &= \sqrt{\frac{a\left(1-e^2\right)}{\mu_e}}\frac{\cos\theta}{1+e\cos f}N \\
\dot{\Omega} &= \sqrt{\frac{a\left(1-e^2\right)}{\mu_e}}\frac{\sin\theta}{\sin i\left(1+e\cos f\right)}N \\
\dot{\omega} &= -\dot{\Omega}\cos i + \sqrt{\frac{a\left(1-e^2\right)}{\mu_e}}\frac{-R\cos f + T\sin f\left(2+e\cos f\right)}{e\left(1+e\cos f\right)} \\
\dot{\chi} &= \sqrt{\frac{a}{\mu_e}}\frac{\left(1-e^2\right)}{e\left(1+e\cos f\right)}\left(R\left(2e-\cos f - e\cos^2 f\right) + T\sin f\left(2+e\cos f\right)\right) \\
\dot{\xi} &= \sqrt{\frac{\mu_e}{a^3}}
\end{aligned} \tag{4.11}$$

where:

$$\theta = \omega + f$$

The perturbations (R, T, N) are accelerations in the body-fixed radial, tangential and normal directions respectively. These perturbations have two components. The first component is due to the thrust from the engine $(\mathbf{F}_{lt})$ and the second is due to the attraction of the Moon $(\mathbf{F}_m)$. To compute the attraction due to the Moon it is first necessary to get the position vector (in the body fixed frame) of the Moon relative to the spacecraft in terms of the orbit elements:

$$\mathbf{r}_m = r_m \begin{bmatrix} \cos\theta\cos\left(\lambda_m - \Omega\right) + \cos i\sin\theta\sin\left(\lambda_m - \Omega\right) \\ -\sin\theta\cos\left(\lambda_m - \Omega\right) + \cos i\cos\theta\sin\left(\lambda_m - \Omega\right) \\ -\sin i\sin\left(\lambda_m - \Omega\right) \end{bmatrix}$$

where λ_m is the angle between the Moon and the reference axis in the plane of the Moon's orbit. The acceleration due to the Moon is then given by:

$$\mathbf{F}_m = \mu_m\frac{\mathbf{r}_m - \mathbf{r}}{\left|\mathbf{r}_m - \mathbf{r}\right|^3} - \mu_m\frac{\mathbf{r}_m}{\left|\mathbf{r}_m\right|^3}$$

The acceleration due to the low-thrust engine is simply:

$$\mathbf{F}_{lt} = T_A \begin{bmatrix} \sin(u_1)\cos u_2 \\ \cos(u_1)\cos u_2 \\ \sin u_2 \end{bmatrix}$$

where u_1 and u_2 are the in-plane and out-of-plane thrust pointing angle respectively. The total perturbing acceleration is then:

$$\begin{bmatrix} R \\ T \\ N \end{bmatrix} = (\mathbf{F}_m + \mathbf{F}_{lt})$$

It may be the case that extra 3rd body effects are to be considered; for example the effect of the Sun's gravitation.

4.2.3 Equinoctial Elements

The target orbit in the Halo to Moon leg is a circular (e=0) low-lunar orbit in the plane of the Moons orbit about the Earth (i=0). The orbit element variational equations have singularities when eccentricity or inclination are equal to zero, in particular the equations for $\dot{\Omega}$ and $\dot{\omega}$ become undefined. Therefore for the Halo to Moon phase of the transfer an alternative coordinate system that removes these singularities will be used; equinoctial elements $(a, P_1, P_2, Q_1, Q_2, L)$.[50] The thrust acceleration is described in the local body-fixed axes and modeled as a perturbation. The attraction of the 3rd body is also included as a perturbation. The perturbations R, T, N are accelerations in the body-fixed radial, tangential and normal directions respectively. The variational equations for the equinoctial elements are:[50]

$$\begin{aligned}
\dot{a} &= \frac{2a^2}{h}\left(\left(P_2\sin L - P_1\cos L\right)R + \frac{pT}{r}\right) \\
\dot{P}_1 &= \frac{r}{h}\left(-\left(\frac{p}{r}\cos L\right)R + \left(P_1 + \left(1+\frac{p}{r}\right)\sin L\right)T - P_2\left(Q_1\cos L - Q_2\sin L\right)N\right) \\
\dot{P}_2 &= \frac{r}{h}\left(-\left(\frac{p}{r}\sin L\right)R + \left(P_2 + \left(1+\frac{p}{r}\right)\cos L\right)T - P_1\left(Q_1\cos L - Q_2\sin L\right)N\right) \\
\dot{Q}_1 &= \left(\frac{r}{2h}\left(1+Q_1^2+Q_2^2\right)\sin L\right)N \\
\dot{Q}_2 &= \left(\frac{r}{2h}\left(1+Q_1^2+Q_2^2\right)\cos L\right)N \\
\dot{l} &= n - \frac{r}{h}\left(\left(\frac{a}{a+b}\right)\frac{p}{r}\left(P_1\sin L + P_2\cos L\right) + \frac{2b}{a}\right)R \\
&\quad -\frac{r}{h}\left(\left(\frac{a}{a+b}\right)\left(1+\frac{p}{r}\right)\left(P_1\cos L + P_2\sin L\right) + \frac{2b}{a}\right)T \\
&\quad -\frac{r}{h}\left(Q_1\cos L - Q_2\sin L\right)N
\end{aligned} \tag{4.12}$$

where:

$$\begin{aligned}
K &= 1 - P_1 \cos K + P_2 \sin K \\
r &= a\left(1 - P_1 \sin K - P_2 - \sin K\right) \\
b &= \left|a\sqrt{1 - P_1^2 - P_2^2}\right| \\
n &= \sqrt{\frac{\mu}{a^3}} \\
\sin L &= \frac{a}{r}\left(\left(1 - \left(\frac{a}{a+b}\right)P_2^2\right)\sin K + \left(\frac{a}{a+b}\right)P_1 P_2 \cos K - P_1\right) \\
\cos L &= \frac{a}{r}\left(\left(1 - \left(\frac{a}{a+b}\right)P_1^2\right)\cos K + \left(\frac{a}{a+b}\right)P_1 P_2 \sin K - P_2\right) \\
p &= r\left(1 + P_1 \sin L + P_2 \cos L\right) \\
h &= nab
\end{aligned}$$

In this case the Moon is the primary body. As such it is necessary to consider 3rd body perturbations due to the Earth. The position vector of the Earth relative to the spacecraft (in local body axes) in terms of the equinoctial elements is:

$$\mathbf{r}_e = \frac{r_e}{1 + Q_1^2 + Q_2^2}\begin{bmatrix} \frac{r}{r_e} - \cos\left(L - \lambda_e\right) + \left(\frac{r}{r_e} + \cos\left(L - \lambda_e\right)\right)Q_1^2 - 2\sin\left(L + \lambda_e\right)Q_1 Q_2 + ... \\ \left(\frac{r}{r_e} - \cos\left(L + \lambda_e\right)\right)Q_2^2 \\ \sin\left(L - \lambda_e\right) - \sin\left(L + \lambda_e\right)Q_1^2 - 2\cos\left(L + \lambda_e\right)Q_1 Q_2 + \sin\left(L + \lambda_e\right)Q_2^2 \\ 2\left(Q_2 \sin\lambda_e - Q_1 \cos\lambda_e\right) \end{bmatrix}$$

where λ_e is the angle between the Earth and the reference axis in the plane of the Moon's orbit about the Earth. The acceleration due to the Earth is then given by:

$$\mathbf{F}_e = \mu_e \frac{\mathbf{r}_e - \mathbf{r}}{\left|\mathbf{r}_e - \mathbf{r}\right|^3} - \mu_e \frac{\mathbf{r}_e}{\left|\mathbf{r}_e\right|^3}$$

The acceleration due to the low-thrust engine is simply:

$$\mathbf{F}_{lt} = T_A \begin{bmatrix} \sin\left(\gamma + u_1\right)\cos u_2 \\ \cos\left(\gamma + u_1\right)\cos u_2 \\ \sin u_2 \end{bmatrix}$$

The total perturbation acceleration is then:

$$\begin{bmatrix} R \\ T \\ N \end{bmatrix} = (\mathbf{F}_m + \mathbf{F}_{lt})$$

Perturbations from extra bodies such as the Sun, can be included using a similar analysis.

4.3 Optimal Earth-Moon Transfer Found Using (Conventional) Runge-Kutta Multiple Shooting

4.3.1 Terminal Conditions

There exist many modern launch vehicles that can place payloads in geosynchronous transfer orbit (GTO). This is a logical starting orbit for the Earth-Moon transfer. It also has a higher starting energy than LEO, therefore reducing the amount of the low-thrust spiraling required to leave the Earth's sphere of influence. This fixes the semi major axis and eccentricity at 24510 km and 0.72345981 respectively. The virtual spacecraft has an initial thrust acceleration of $7\times10^{-4}m.s^{-2}$. The angle between the plane of the Moon's orbit and the Earth's equatorial plane varies between $18.5°$ and $28.5°$ depending on the positions of the Earth and Moon in their respective orbits. Therefore the initial inclination is limited to the interval $(18.5°, 28.5°)$. The initial longitude of the ascending node (Ω), argument of periapse (ω) and true anomaly (f) are left free (to be optimized). The longitude of the Moon λ_m is alos left free to be chosen optimally. It is assumed that there are no coasting arcs other than the coasting arcs on the stable and unstable manifolds.

If the insertion point on the stable manifold of the target periodic orbit is chosen *a priori* then final position and velocity are known and appropriate constraints can be placed on the states at the final node and an optimal trajectory can be calculated readily. However, if the goal is simply to finish on the periodic orbit, this insertion point can almost certainly be improved upon. This constraint, i.e. simply arriving on the periodic orbit, is problematic as there exists no analytical solution to the periodic orbit or stable manifold generation problems, hence there exists no terminal constraint of the form of equation (2.4).

The solution developed in this work is to express the target periodic orbit in terms of parameters available to the optimizer. To achieve this two additional parameters s and τ are introduced, hereafter referred to as the periodic orbit insertion point parameter and the manifold insertion parameter respectively. The periodic insertion point parameter represents the normalized position around the periodic orbit from some arbitrary starting location ($0 \leq s = t/T \leq 1$

where T is the period of the halo orbit). The manifold insertion parameter represents the time taken to reach the periodic orbit from the manifold insertion point ($\tau \geq 0$). The states are then parameterized in terms of these new parameters.

Target periodic orbits with out-of-plane amplitudes between $0\ km$ and $10000\ km$ ($0 \leq A_z \leq 10000\ km$) were generated by the procedure in Section 3.2. This procedure generates a discretized periodic orbit. For each state (x, y, z, v_x, v_y, v_z) a surface was fitted to create functions of the states in terms of the periodic orbit insertion parameter (s) and the manifold insertion parameter τ. A bicubic spline interpolant was fitted using the MATLAB curve fitting toolbox program *cftool*. These fitted surfaces are continuous and differentiable functions for the terminal states in terms of both insertion parameters (s, τ).

4.3.2 Initial Guess

The quality of the initial guess significantly influences the ability of the NLP problem solver to obtain a convergent solution. It is advantageous to have a feasible trajectory as an initial guess, that is, a trajectory that satisfies the initial and final constraints as well as the Runge-Kutta constraints. This increases the likelihood that the optimizer will converge to a satisfactory solution, however, a valid trajectory that inserts into the target periodic orbit's stable manifold is not known *a priori* and must be computed. The initial guess trajectory was created using a three step process:

1) The equations of motion (4.2) were integrated forward with the assumption that the thrust is always aligned perpendicular to the instantaneous radius vector. The time of flight, the initial angular position of the moon (λ_0) and the initial orbit elements (ω, Ω, f) were selected (by trial and error) such the spacecraft will be in the vicinity of the target periodic orbit at the final time. The trajectory is shown in Figure 4.2

2) The next step was to create a trajectory that terminated at a specified position on the periodic orbit, but with the velocity unconstrained. The initial conditions were the same as step 1 and there were no constraints applied to the final states. The objective function (J) was the difference between the x, y and z states at the final node (x_f, y_f, z_f) and the specified final position (x_s, y_s, z_s). The manifold insertion parameter (τ) was set to zero so that the trajectory produced by this procedure targets the periodic orbit itself; not the stable manifold.

$$J(\boldsymbol{x}) = \sqrt{(x_f - x_s)^2 + (y_f - y_s)^2 + (z_f - z_s)^2} \tag{4.13}$$

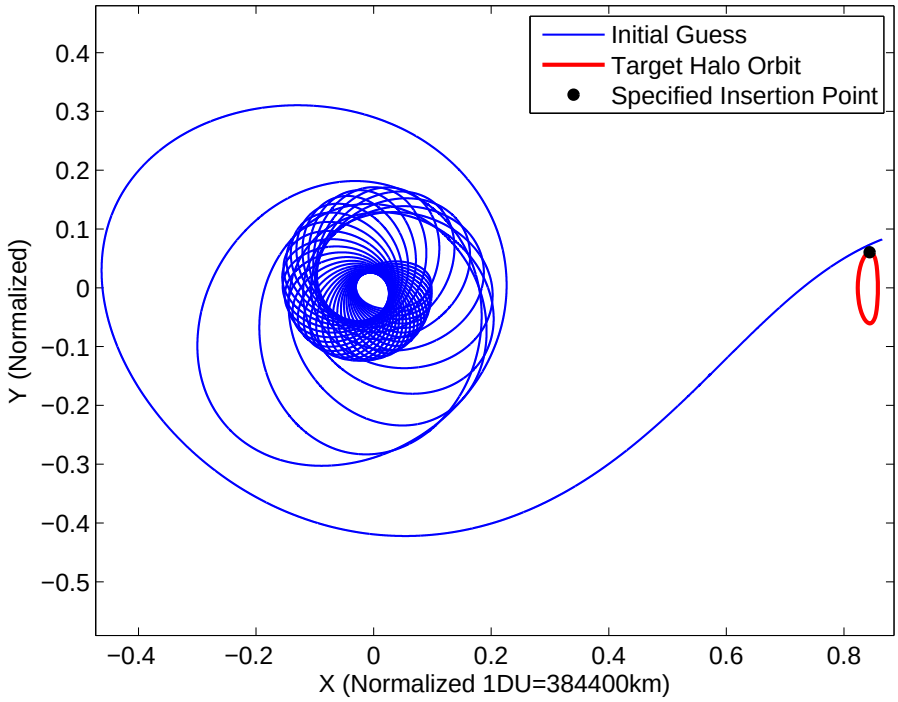

Figure 4.2: Departure trajectory assuming tangential thrust.

The trajectory obtained with tangential thrust is used as the initial guess. A solution with an objective function value of zero, i.e. reaching precisely the specified entry point, was obtained, the trajectory is shown in Figure 4.3. The corresponding thrust pointing angles are shown in Figure 4.4.

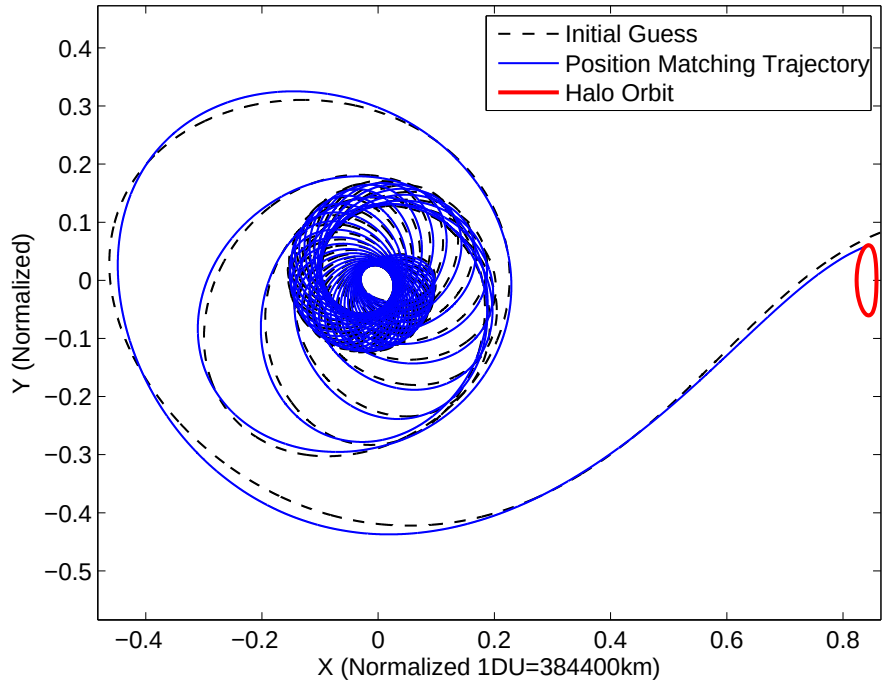

Figure 4.3: Departure trajectory that matches position at a set point on the target halo orbit (velocity is free).

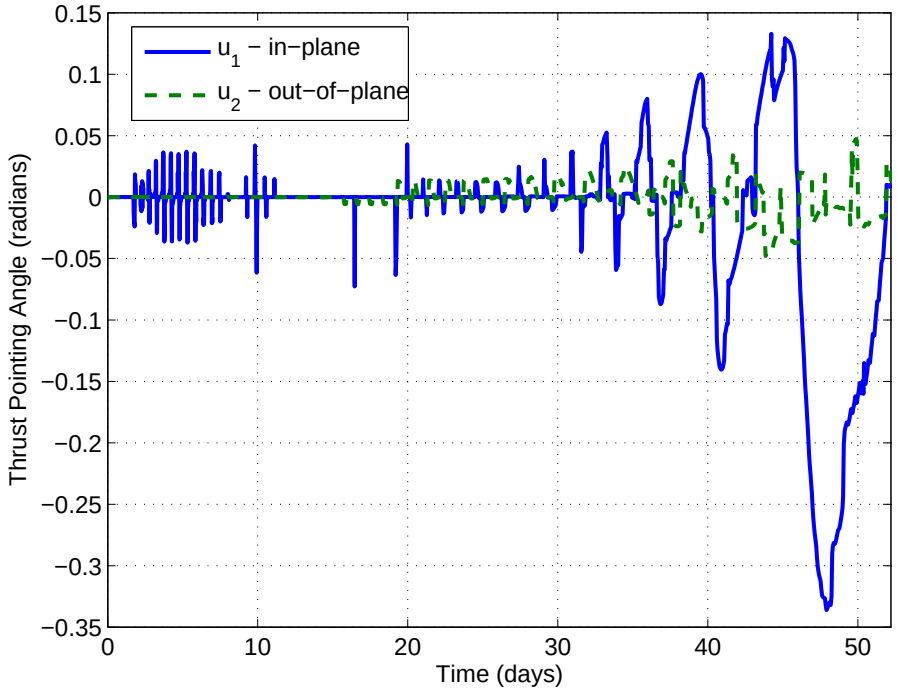

Figure 4.4: Thrust pointing angle for departure trajectory that matches position at a set point on the target halo orbit (velocity is free).

3) The final step is to find a trajectory that not only reached the same position but that also had the velocity required to complete the periodic orbit. The procedure is similar to that of step 2, but the x,y and z states at the final node (x_f, y_f, z_f) are now constrained to the specified final position (x_s, y_s, z_s). The objective then becomes minimization of the difference in the velocities at the final node $(v_{x_f}, v_{y_f}, v_{z_f})$ and the velocity specified at the end point $(v_{x_s}, v_{y_s}, v_{z_s})$. The objective function is then:

$$J(\boldsymbol{x}) = \sqrt{(v_{x_f} - v_{x_s})^2 + (v_{y_f} - v_{y_s})^2 + (v_{z_f} - v_{z_s})^2} \tag{4.14}$$

The resulting trajectory, as shown in Figure 4.5, is a feasible insertion trajectory (with $\tau = 0$) that can be used as an initial guess for the problem of finding a fuel-minimizing trajectory that terminates at some point on the stable manifold. The corresponding thrust pointing angle is shown in Figure 4.6

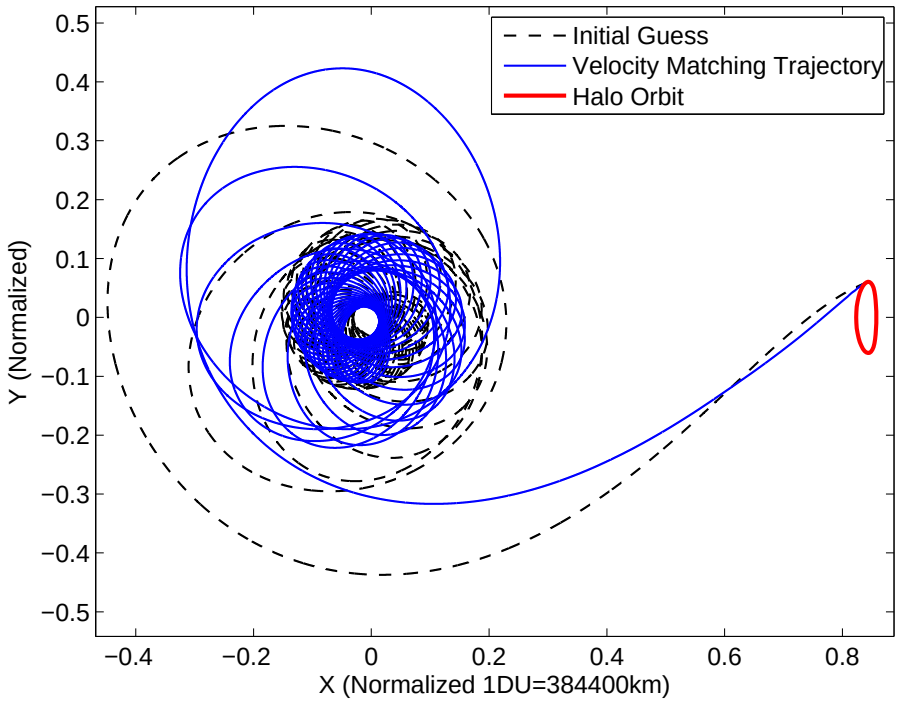

Figure 4.5: Departure trajectory that matches position and velocity at a set point on the target halo orbit.

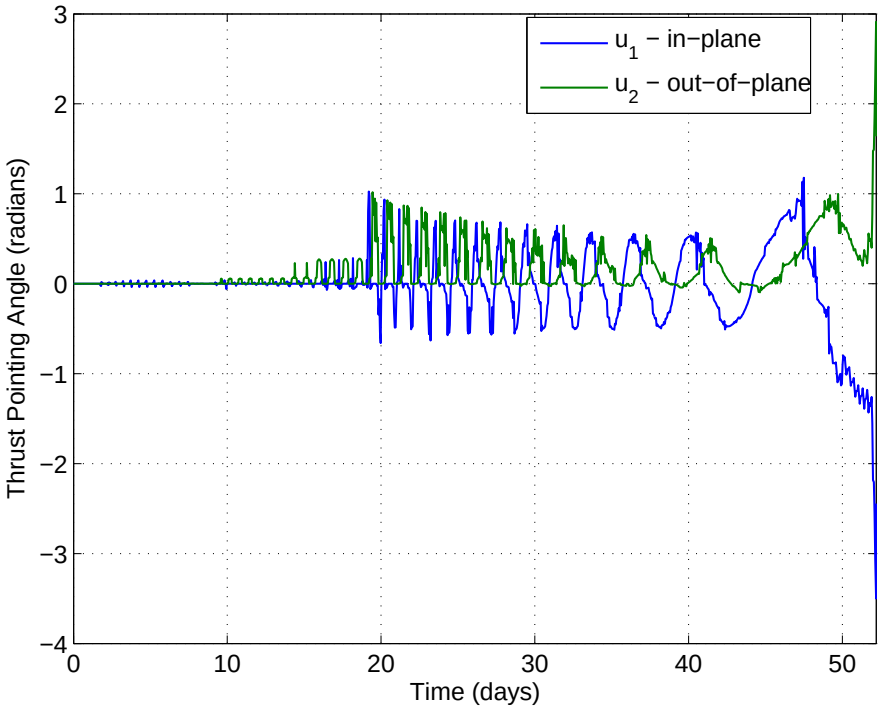

Figure 4.6: Thrust pointing angle for departure trajectory that matches position and velocity at a set point on the target halo orbit.

4.3.3 Optimal Transfer from GTO to L_1 Halo Orbit

The trajectory that terminates on the periodic orbit (cf. Figure 4.6) is used as an initial guess for the optimal transfer from GTO to L_1 halo orbit. The manifold insertion parameter τ is now left free to be optimized. The optimization was performed for various target halo orbit amplitudes. The example trajectory shown in Figures 4.7 and 4.8 is for a target halo orbit with an out-of-plane amplitude of 8000 km. The thrust pointing angles are shown in Figure 4.9. The history of the orbit elements over the thrust arc, i.e. not including the terminal coast on the stable manifold, are shown in Figure 4.10

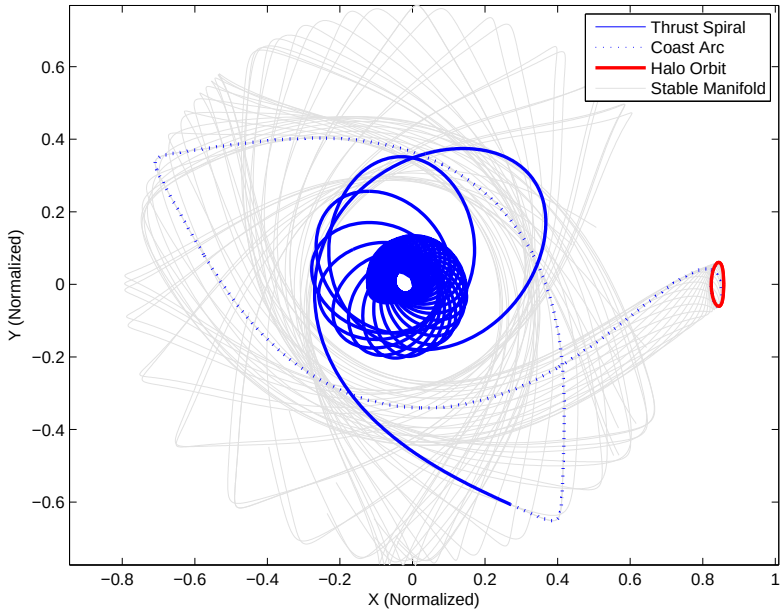

Figure 4.7: Optimal low-thrust trajectory from GTO to a periodic orbit of amplitude $A_z = 8.0 \times 10^3$ km.

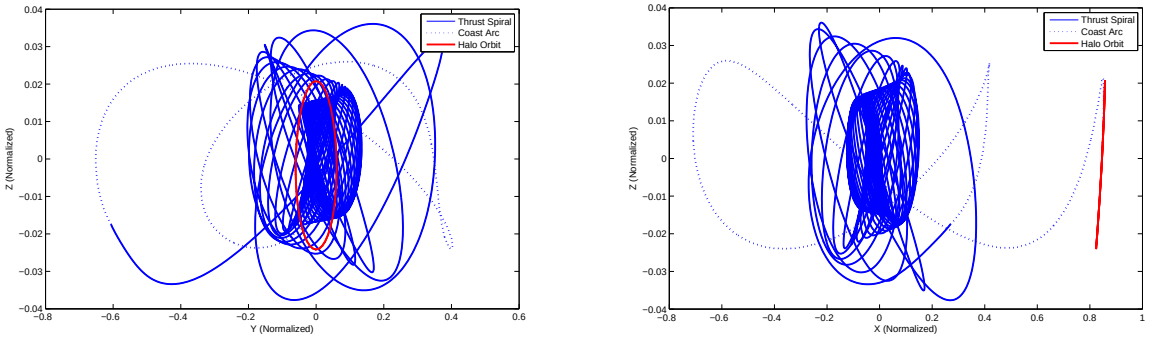

(a) YZ plane

(b) XZ plane

Figure 4.8: Optimal low-thrust trajectory from GTO to a periodic orbit of amplitude $A_z = 8.0 \times 10^3$ km.

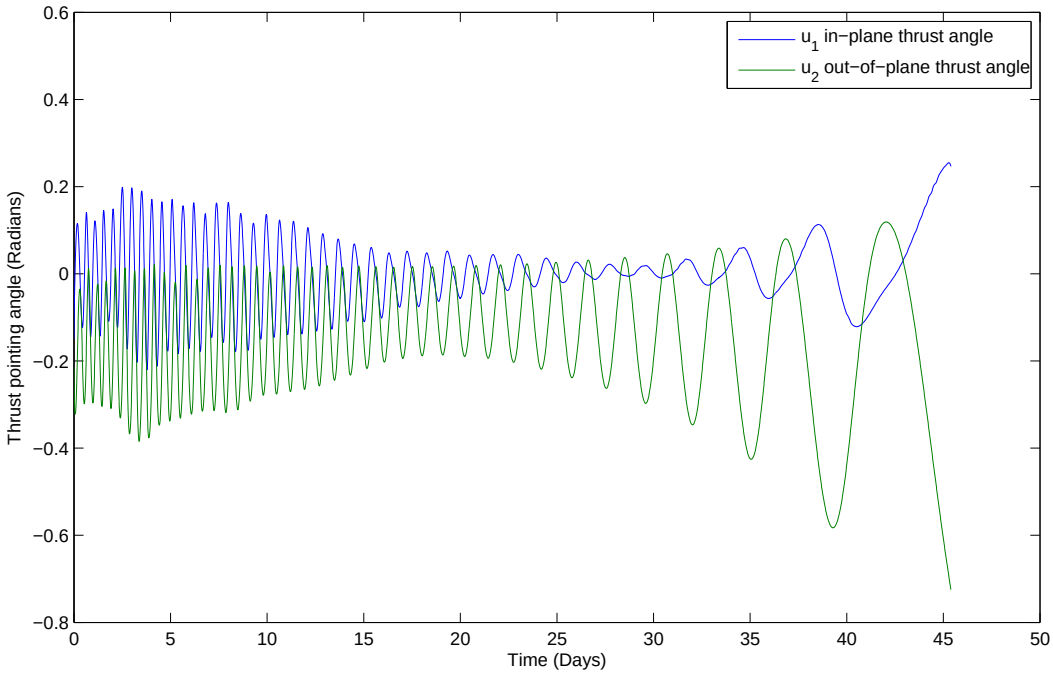

Figure 4.9: Thrust pointing angle time history for an optimal low-thrust trajectory from GTO to a periodic orbit of amplitude $A_z = 8.0 \times 10^3$ km.

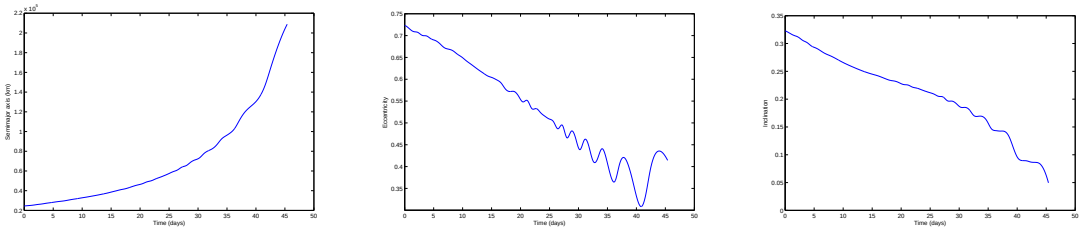

(a) Semimajor axis (b) Eccentricity (c) Inclination

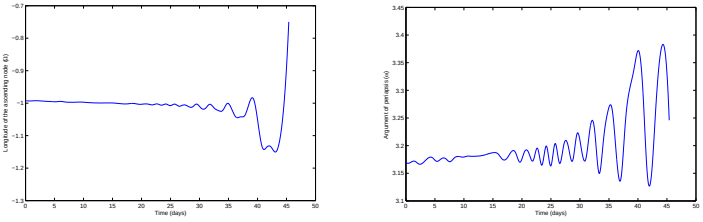

(d) Longitude of Ascending Node (e) Argument of periapsis

Figure 4.10: Time history of orbital elements for an optimal low-thrust trajectory from GTO to a periodic orbit of amplitude $A_z = 8.0 \times 10^3$ km.

The results for target halo orbits with an out of plane amplitude between 0 and 10000 km are shown in Table 4.1. The amplitude of the target halo orbit has a negligible effect on the result, i.e. there is less than 1 % difference between the mass fraction remaining for a trajectory to a target halo orbit with out of plane amplitude (A_z) of 0 km and that for a target halo orbit with out of plane amplitude 10000 km. This implies that you can choose the size of the halo orbit without greatly affecting the optimal trajectory.

Halo Orbit Amplitude (A_z) (km)	Thrust Arc Duration (days)	Coast Arc Duration (days)	Total Time of Flight (days)	Mass fraction of propellant required	Mass fraction Mass fraction $(\frac{m_f}{m_0})$
0	45.582	38.007	83.589	0.906318	0.093682
1000	45.602	38.721	84.323	0.906275	0.093725
2000	45.569	38.745	84.314	0.906343	0.093657
3000	45.559	38.792	84.351	0.906365	0.093635
4000	45.538	38.858	84.395	0.906408	0.093592
5000	45.473	38.933	84.406	0.906542	0.093458
6000	45.440	39.035	84.475	0.906610	0.093390
7000	45.414	39.159	84.572	0.906663	0.093337
8000	45.391	39.306	84.697	0.906709	0.093291
9000	45.372	39.470	84.842	0.906749	0.093251
10000	45.356	39.689	85.045	0.906783	0.093217

Table 4.1: Results for an optimal low-thrust transfer from GTO to halo orbits of various amplitude about the Earth-Moon L_1 Lagrange point.

4.3.4 Optimal Transfer from L_1 Halo Orbit to Low Lunar Orbit

A numerical procedure similar to that used to obtain the optimal Earth to halo trajectory was used to optimize the trajectory departing the halo orbit and entering a circular low-lunar orbit with an altitude of 100 km. Battin's equinoctial elements[50] were used rather than the classical orbit elements due to the singularities in the variational equations for the latter when eccentricity or inclination are equal to zero. The initial guess was formed using a procedure similar to the 3 step process (cf. Section 4.3.2) used to generate the initial guess for the Earth to Halo phase of the transfer, except that in this case the states were integrated backward in time from a position on the final low-lunar orbit. An example transfer from a Halo orbit with an out-of-plane amplitude (A_z) of 8000 km is shown in Figures 4.11 and 4.12. The time histories of the orbital elements are shown in Figure 4.13

As was found for the first leg, the out of plane amplitude of the halo orbit has a minimal effect on the results (see Table 4.2). The best transfer computed is from a halo orbit with an out-of-plane amplitude of 6000 km. The spacecraft coasts along the unstable manifold for 16.6 days before departing the manifold and spiraling into low-lunar orbit over a 15.4 day thrust arc. The entire transfer takes 32 days and consumes 3.76% of the mass of the spacecraft as fuel.

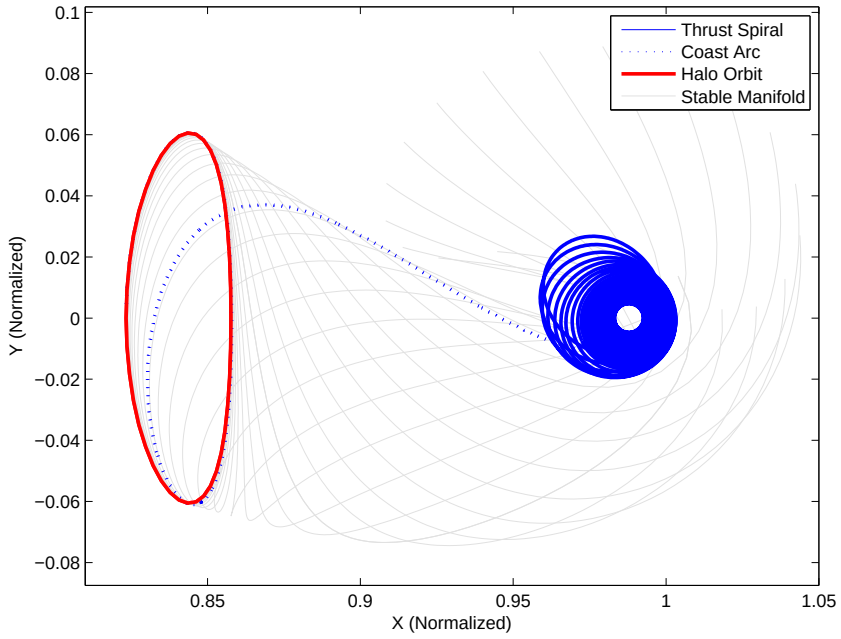

Figure 4.11: Optimal low-thrust trajectory from a periodic orbit of amplitude $A_z = 8.0 \times 10^3$ km to low-lunar orbit.

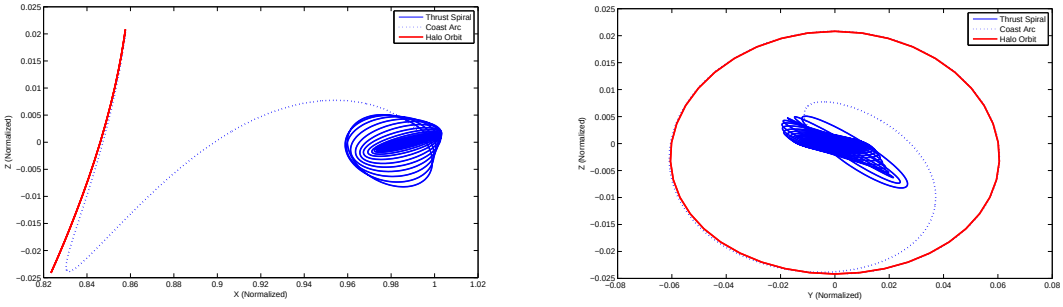

(a) XZ plane

(b) YZ plane

Figure 4.12: Optimal low-thrust trajectory from a periodic orbit of amplitude $A_z = 8.0 \times 10^3$ km to low-lunar orbit.

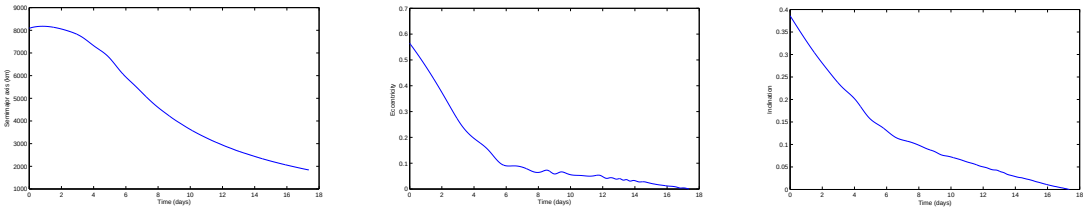

(a) Semimajor axis (b) Eccentricity (c) Inclination

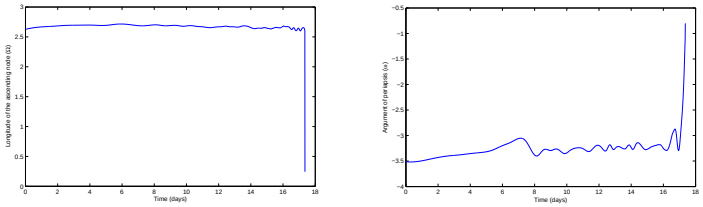

(d) Longitude of Ascending Node (e) Argument of periapsis

Figure 4.13: Time history of orbital elements for an optimal low-thrust trajectory from GTO to a periodic orbit of amplitude $A_z = 8.0 \times 10^3$ km.

Halo Orbit Amplitude (A_z) (km)	Thrust Arc Duration (days)	Coast Arc Duration (days)	Total Time of Flight (days)	Mass fraction of propellant required	Mass fraction Mass fraction $(\frac{m_f}{m_0})$
0	17.2581	15.2736	32.5318	0.960864	0.039136
1000	16.9794	15.0010	31.9804	0.961494	0.038506
2000	17.0466	15.3481	32.3947	0.961345	0.038655
3000	17.2015	15.3794	32.5809	0.960994	0.039006
4000	17.2050	15.3960	32.6011	0.960988	0.039012
5000	16.9835	15.4434	32.4268	0.961496	0.038504
6000	16.5988	15.4387	32.0375	0.962371	0.037629
7000	16.9341	15.4784	32.4125	0.961613	0.038387
8000	17.3606	15.5206	32.8812	0.960648	0.039352
9000	17.6220	15.5654	33.1875	0.960058	0.039942
10000	17.5573	15.6105	33.1678	0.960206	0.039794

Table 4.2: Time of flights and propellant usage for optimal low-thrust transfers from halo orbits of various amplitude about the Earth-Moon L_1 Lagrange point to low-lunar orbit.

4.3.5 Complete Earth-Moon Transfer via Intermediate Halo Orbit

The individually optimal Earth-Halo and Halo-Moon trajectories can be combined to form an optimal trajectory that starts in GTO and arrives in low-lunar orbit with a coast arc along the stable and unstable manifolds of a Halo orbit about the Earth-Moon L_1. This is shown for a halo orbit with amplitude $A_z = 8000\ km$ in Figure 4.14. In general the combination of two individually optimal trajectories, departure to intermediate point and intermediate point to target, is not necessarily optimal for the entire transfer. However, in this case the insertion and departure point from the manifolds are chosen optimally and the halo orbit can be traversed for an arbitrary length of time for no cost, effectively decoupling the two phases.

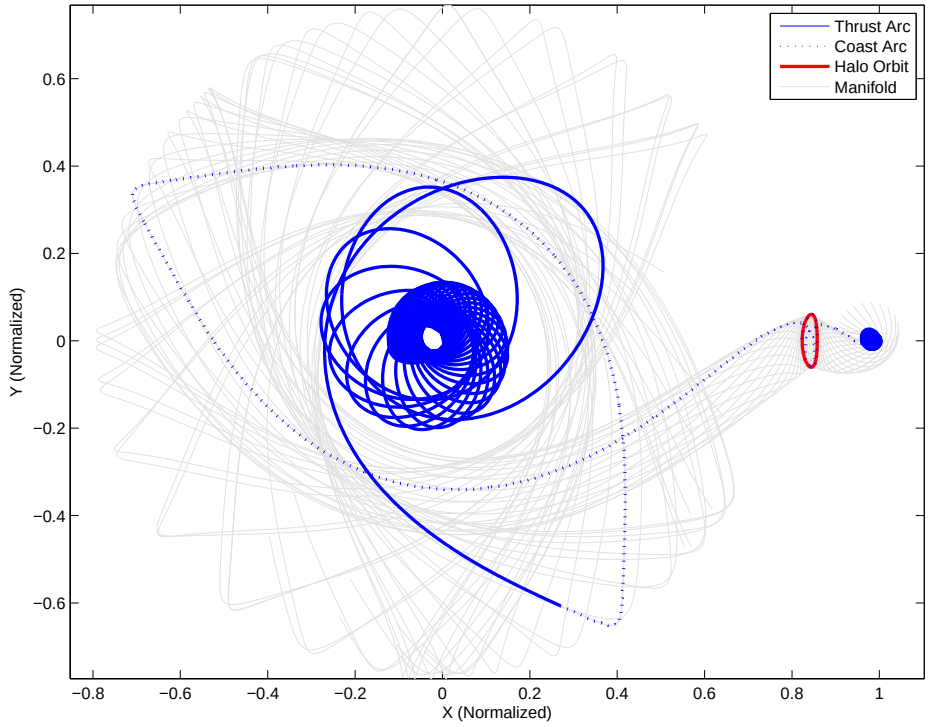

Figure 4.14: Optimal low-thrust trajectory from GTO to LLO of amplitude $A_z = 8.0 \times 10^3$ km to low-lunar orbit via a periodic orbit about L_1 and its manifolds.

The results for the eleven different halo orbits tested are very similar, with only a 1.5% difference between the least and most expensive. However, the best choice for the target halo orbit is one with a 6000 km out of plane amplitude. The resulting trajectory takes a minimum of 122.7 days (depending upon how many revolutions the spacecraft makes around the halo orbit having a period $T \approx 12$ days), of which the engine is on and thrusting at the maximum possible level for 62.0385 days. The mass fraction of propellant required is 0.127505. This is slightly greater than the result

Halo Orbit A_z (km)	Earth Escape Spiral (days)	Stable Manifold Coast (days)	Halo Orbit (min.) (days)	Unstable Manifold Coast (days)	Moon Capture Spiral (days)	Total Time of Flight (days)	Final mass fraction	Propellant mass fraction
0	45.5818	38.0073	1.4166	15.2736	17.2581	117.5375	0.870848	0.129152
1000	45.6025	38.7209	6.3417	15.0010	16.9794	122.6454	0.871378	0.128622
2000	45.5693	38.7447	6.2964	15.3481	17.0466	123.0050	0.871308	0.128692
3000	45.5587	38.7921	5.9702	15.3794	17.2015	122.9019	0.871012	0.128988
4000	45.5378	38.8576	6.2722	15.3960	17.2050	123.2687	0.871047	0.128953
5000	45.4726	38.9335	5.4366	15.4434	16.9835	122.2695	0.871637	0.128363
6000	45.4397	39.0350	6.2126	15.4387	16.5988	122.7248	0.872495	0.127505
7000	45.4136	39.1588	6.1734	15.4784	16.9341	123.1584	0.871860	0.128140
8000	45.3914	39.3057	6.1140	15.5206	17.3606	123.6923	0.871029	0.128971
9000	45.3719	39.4699	6.0691	15.5654	17.6220	124.0984	0.870531	0.129469
10000	45.3556	39.6892	6.0638	15.6105	17.5573	124.2764	0.870698	0.129302

Table 4.3: Time of flights and propellant usage for optimal low-thrust transfers from GTO to low-lunar orbit via halo orbits of various amplitude about the Earth-Moon L_1 Lagrange point.

found by Mingotti, Topputo and Bernelli-Zazzera[49] which was 0.1256. The effect of optimizing thrust pointing angle during the escape spiral and considering the time varying thrust acceleration is overcome by the large change in inclination required by the choice of equatorial GTO for the initial orbit. If this large inclination change was not required it is expected that the solution obtained in this work would have had a lower mass fraction of propellant that the Mingotti et al. solution as the outward thrust spiral was optimized in this work and the increase in thrust acceleration as fuel was expended was considered.

This problem was complex and proved to be difficult to solve using conventional methods. The NLP optimizations required significant CPU time to converge, of the order of days on a desktop computer. Due to its complexity, even with the change of variables, each phase of the trajectory had to be discretized into many segments (60). This results in a large NLP parameter vector, 1153 elements for the first phase and 1091 elements for the second phase, which consequently causes the long simulation time. If the constraints could be formulated in such a way as to alleviate the need for a fine mesh, the number of segments required and hence the number of NLP parameters would be significantly reduced, greatly speeding up simulation time. It was the difficulty encountered in solving this complex problem that motivated the development of the Taylor series numerical optimization methods, presented in Chapter 2, which will now be applied to this Earth-Moon transfer problem.

4.4 Optimal Earth-Moon Transfer Found Using Taylor Series Multiple Shooting

4.4.1 Modified Equinoctial Elements

The variational equations for both the conventional elliptic orbit elements (4.12) and the equinoctial elements (4.13) require zero finding; to solve for eccentric anomaly (E) and eccentric longitude (K) respectively. The Taylor series multiple shooting method requires the derivatives of these quantities. Fortunately the equations for eccentric anomaly (E) and eccentric longitude (K) still only have to be solved once as the higher derivatives can be calculated by differentiating the equation and isolating the derivative of the variable being solved for ($\dot{E}, \dot{K}$). For example when using equinoctial elements the eccentric longitude (K) is found by solving:

$$K = 1 - P_1 \cos K + P_2 \sin K \tag{4.15}$$

Differentiating and isolating $\dot{K}$ yields:

$$\dot{K} = \frac{-\dot{P}_1 \cos K - \dot{P}_2 \sin K}{1 - P_1 \sin K + P_2 \cos K} \tag{4.16}$$

The higher order derivatives of eccentric longitude can then be calculated using automatic differentiation, since the derivatives of P_1 and P_2 are known. However, even though it is only performed once per call, the zero finding adds significant computation to each derivative calculation. It is therefore desirable to use a set of variables that do not require any zero finding to evaluate the variational equations. The modified equinoctial elements[53] are used in this work. The modified equinoctial elements are related to the conventional orbit elements $(a, e, i, \Omega, \omega, f)$ by:

$$\begin{aligned} p &= a\left(1 - e^2\right) \\ f &= e\cos\left(\omega + \Omega\right) \\ g &= e\sin\left(\omega + \Omega\right) \\ h &= \tan\left(\tfrac{i}{2}\right)\cos\Omega \\ k &= \tan\left(\tfrac{i}{2}\right)\sin\Omega \\ L &= \Omega + \omega + \theta \end{aligned} \tag{4.17}$$

The variational equations are:

$$\begin{aligned}
\dot{p} &= \tfrac{2p}{w}\sqrt{\tfrac{p}{\mu}}T \\
\dot{f} &= \sqrt{\tfrac{p}{\mu}}\left[R\sin L + \left[(w+1)\cos L + f\right]\tfrac{T}{w} - \left(h\sin L - k\cos L\right)\tfrac{gN}{w}\right] \\
\dot{g} &= \sqrt{\tfrac{p}{\mu}}\left[-R\cos L + \left[(w+1)\sin L + g\right]\tfrac{T}{w} - \left(h\sin L - k\cos L\right)\tfrac{gN}{w}\right] \\
\dot{h} &= \sqrt{\tfrac{p}{\mu}}\tfrac{s^2 N}{2w}\cos L \\
\dot{k} &= \sqrt{\tfrac{p}{\mu}}\tfrac{s^2 N}{2w}\sin L \\
\dot{L} &= \sqrt{\mu p}\left(\tfrac{w}{p}\right)^2 + \tfrac{1}{w}\sqrt{\tfrac{p}{\mu}}\left(h\sin L - k\cos L\right)N
\end{aligned} \tag{4.18}$$

where:

$$\begin{aligned}
w &= 1 + f\cos L + g\sin L \\
s^2 &= 1 + h^2 + k^2;
\end{aligned}$$

R, T and N are perturbations in the local body fixed axes, as previously defined. The perturbations are from the thrust from the engines as well as the third-body perturbations from the Moon during the Earth-Halo leg and from the Earth during the Halo-Moon leg. The perturbation due to the low-thrust engines is given by:

$$\begin{aligned}
R_{LT} &= a_T \cos u_2 \sin u_1 \\
T_{LT} &= a_T \cos u_2 \cos u_1 \\
N_{LT} &= a_T \sin u_2
\end{aligned} \tag{4.19}$$

where a_T is thrust acceleration of the engine. Since the engine is always on in the thrust arc of each leg, the thrust acceleration is a simple function of time since ignition:

$$a_T(t) = \frac{a_T(0)\,c}{c - a_T(0)\,t} \tag{4.20}$$

where c is the exhaust velocity and $t = 0$ corresponds to the time of ignition. Third body perturbations are given by:

$$\begin{bmatrix} R_{3B} \\ T_{3B} \\ N_{3B} \end{bmatrix} = \boldsymbol{Q}^T \boldsymbol{w} \tag{4.21}$$

where matrix Q is composed of unit vectors in the radial, tangential and normal directions:

$$Q = \left[\hat{i}_r, \hat{i}_t, \hat{i}_n\right] \tag{4.22}$$

The unit vectors $\hat{i}_r$, $\hat{i}_t$ and $\hat{i}_n$ are computed from the position vector ($\boldsymbol{r}$) and velocity vector ($\boldsymbol{v}$):

$$\begin{aligned} \hat{i}_r &= \tfrac{r}{|r|} \\ \hat{i}_t &= \tfrac{(r\times v)\times r}{|(r\times v)\times r|} \\ \hat{i}_n &= \tfrac{r\times v}{|r\times v|} \end{aligned} \tag{4.23}$$

where the position and velocity vectors are relative to the primary body in an inertial frame. They are given by:

$$\boldsymbol{r} = \frac{r}{s^2}\begin{bmatrix} \cos L + \alpha^2 \cos L + 2hk \sin L \\ \sin L - \alpha^2 \sin L + 2hk \cos L \\ 2\left(h \sin L - k \cos L\right) \end{bmatrix} \tag{4.24}$$

$$\boldsymbol{v} = \frac{1}{s^2}\sqrt{\frac{\mu}{p}}\begin{bmatrix} -\left(\sin L + \alpha^2 \sin L - 2hk \cos L + g - 2fhk + \alpha^2 g\right) \\ -\left(-\cos L + \alpha^2 \cos L + 2hk \sin L - f + 2ghk + \alpha^2 f\right) \\ 2\left(h \cos L + k \sin L + fh + gk\right) \end{bmatrix} \tag{4.25}$$

where:

$$\begin{aligned} \alpha^2 &= h^2 - k^2 \\ r &= \tfrac{p}{w} \end{aligned} \tag{4.26}$$

The vector sum of all third-body attractions $\boldsymbol{w}$ is given by:

$$\boldsymbol{w} = -\sum_{j=1}^{n} \mu_j \left[\frac{\boldsymbol{d}_j}{d_j^3} + \frac{\boldsymbol{s}_j}{s_j^3}\right] \tag{4.27}$$

where $\boldsymbol{s}_j$ is the position of third body j with respect to the primary body, and $\boldsymbol{d}_j$ is the position of the particle relative to third body j ($\boldsymbol{d}_j = \boldsymbol{r} - \boldsymbol{s}_j$). The third bodies are assumed to be in coplanar circular orbits about the primary body; therefore:

$$\boldsymbol{s}_j = \begin{bmatrix} r_j \cos\left(n_j t + \lambda_j\right) \\ r_j \sin\left(n_j t + \lambda_j\right) \\ 0 \end{bmatrix} \tag{4.28}$$

where r_j is the constant radial distance from third-body j, to the primary body, n_j is the mean motion and λ_j is the initial angular position.

4.4.2 Initial Guess

The previous Runge-Kutta solutions (cf. Section 4.3.3 and 4.3.4) were used as an initial guess. However, a finer mesh had to be used for the Taylor series multiple shooting method to ensure that no subsegment was larger than the radius of convergence of the Taylor series. Since the radius of convergence of the Taylor series expansion at any point is a function of the controls, as well as the states and time, a conservative mesh had to be chosen to ensure that as the control were altered by the optimizer, the Taylor series expansion remained convergent. A non-uniform mesh of 280 segments was used, with nodes concentrated at the beginning of the transfer when the spacecraft is close to the Earth. An adaptive mesh was not used as the mesh refinement scheme, as described in Section 2.5, proved to be too memory intensive to handle this many segments on a desktop computer with 4GB of RAM.

The spacecraft is originally in a geosynchronous transfer orbit with an inclination between 18.5° and 28.5°. The longitude of the ascending node, the argument of periapsis and the initial true anomaly are all free to be chosen by the optimizers. The initial conditions for the modified orbit elements are then:

$$\begin{bmatrix} a_0\left(1-e_0^2\right) \\ -e_0 \\ -e_0 \\ -\tan\left(\frac{i_{o_{\max}}}{2}\right) \\ -\tan\left(\frac{i_{o_{\max}}}{2}\right) \end{bmatrix} \leq \begin{bmatrix} p_0 \\ f_0 \\ g_0 \\ h_0 \\ k_0 \end{bmatrix} \leq \begin{bmatrix} a_0\left(1-e_0^2\right) \\ e_0 \\ e_0 \\ \tan\left(\frac{i_{o_{\max}}}{2}\right) \\ \tan\left(\frac{i_{o_{\max}}}{2}\right) \end{bmatrix} \tag{4.29}$$

where a_0 and e_0 are the initial semi-major axis and eccentricity that correspond to a geosynchronous transfer orbit, $i_{o_{\max}}$ is the maximum initial inclination (28.5°). Two additional constraints are required to ensure that the initial orbit $(p_0, f_0, g_0, h_0, k_0, L_0)$ has the correct semi-major axis and eccentricity:

$$\begin{aligned} \sqrt{f_0^2+g_0^2} - e_0 &= 0 \\ 2\tan^{-1}\left(\sqrt{h_0^2+k_0^2}\right) - i_0 &= 0 \end{aligned} \tag{4.30}$$

where i_0 is the initial inclination which is included as an event variable. The initial longitude L_0 is left free. The terminal conditions are the same as for the previous solutions.

4.4.3 Optimal Transfer from GTO to L_1 Halo Orbit

The Earth to Halo leg of the transfer was solved using Taylor series constraints (20 terms) with 280 segments and 6 subsegments. The optimal trajectory for a transfer to a target halo orbit with an out-of-plane amplitude of 8000 km is

shown in Figures 4.15 and 4.16. The corresponding control history is shown in Figures 4.17 and 4.18.

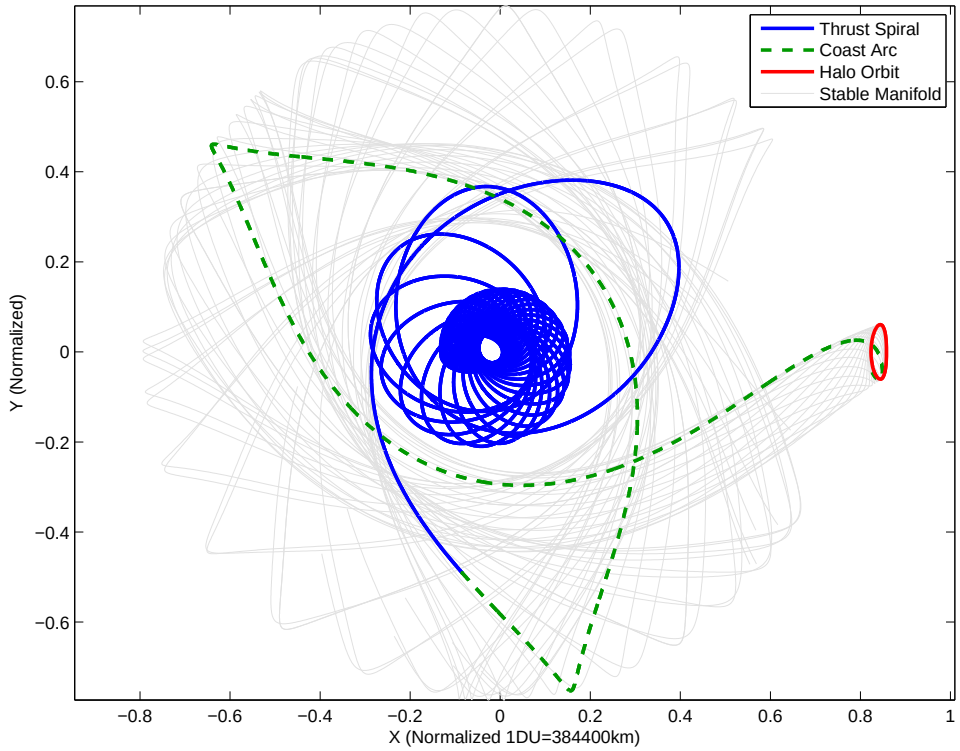

Figure 4.15: Optimal low-thrust trajectory from GTO to a periodic orbit of amplitude $A_z = 8.0 \times 10^3$ km.

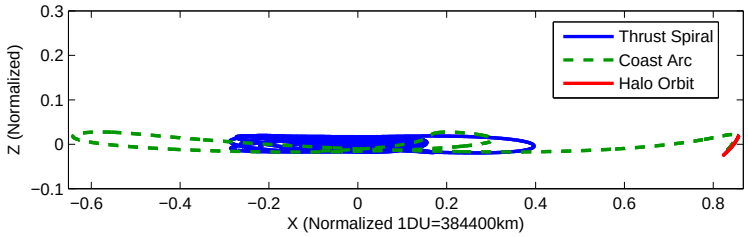

(a) YZ plane

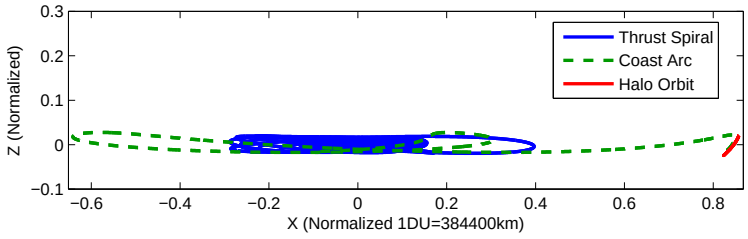

(b) XZ plane

Figure 4.16: Optimal low-thrust trajectory from GTO to a periodic orbit of amplitude $A_z = 8.0 \times 10^3$ km.

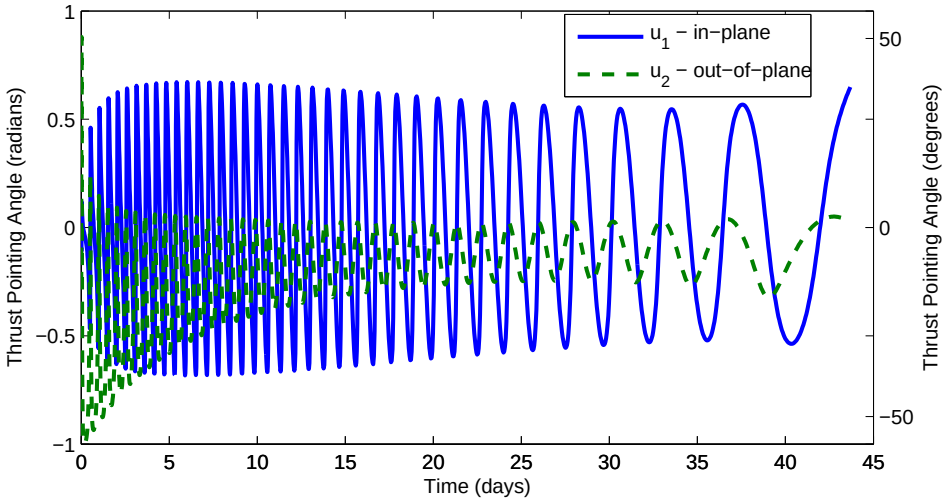

Figure 4.17: Thrust pointing angle time history for an optimal low-thrust trajectory from GTO to a periodic orbit of amplitude $A_z = 8.0 \times 10^3$ km.

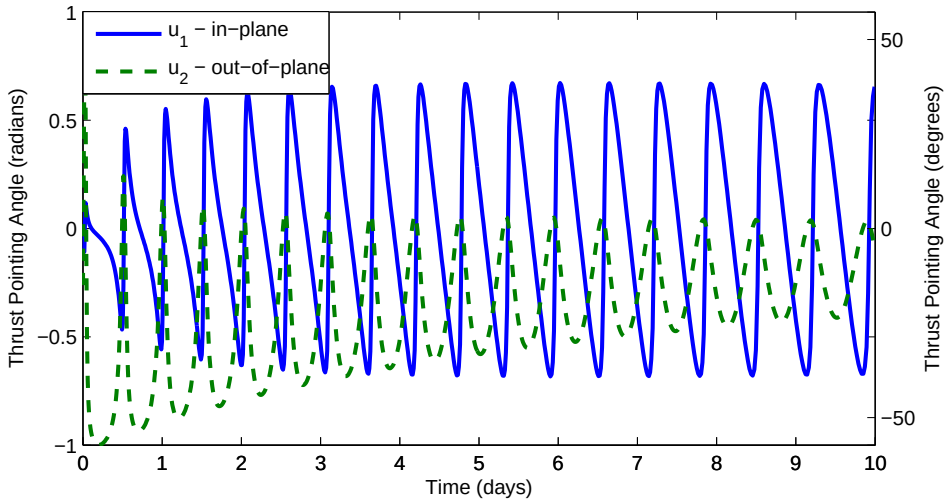

Figure 4.18: Thrust pointing angle time history (first 10 days) for an optimal low-thrust trajectory from GTO to a periodic orbit of amplitude $A_z = 8.0 \times 10^3$ km.

The optimal trajectory has a total time of flight of 83.1066 days of which the engine is on at full throttle for the first 43.6921 days. The remaining 39.4145 days are spent coasting on the stable manifold of the halo orbit. The state time histories are shown in Figure 4.19. The histories of the corresponding classical orbit elements over the trajectory are shown in Figure 4.20.

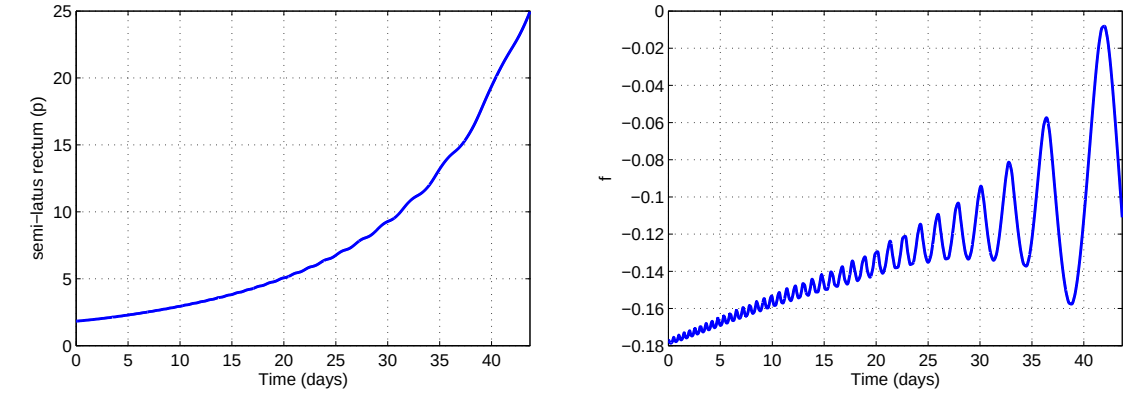

(a) p

(b) f

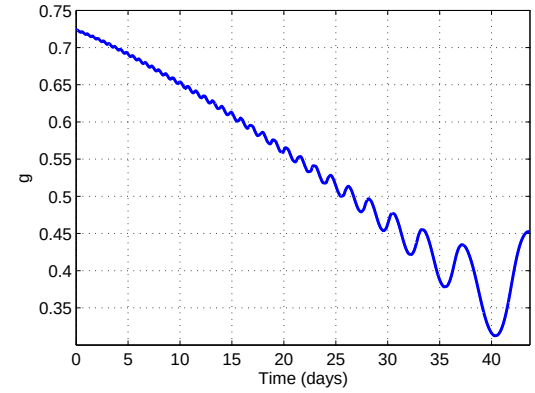

(c) g

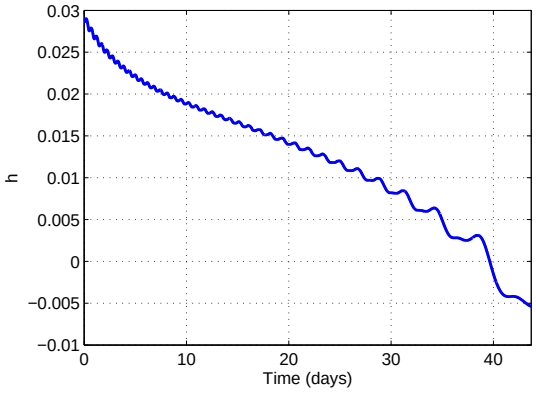

(d) h

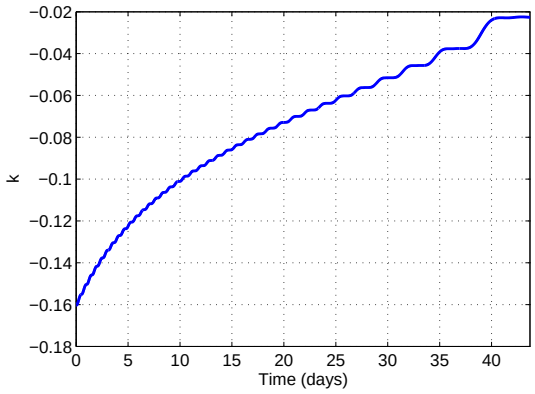

(e) k

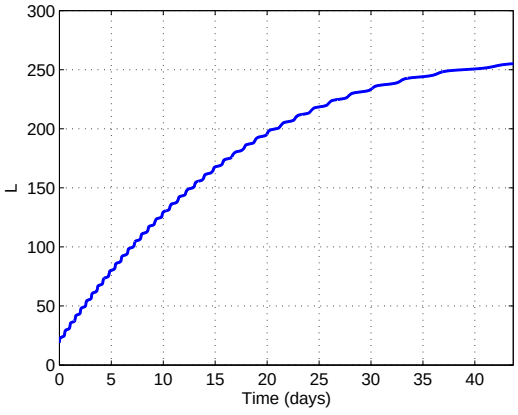

(f) L

Figure 4.19: Time history of modified orbital elements for an optimal low-thrust trajectory from GTO to a periodic orbit of amplitude $A_z = 8.0 \times 10^3$ km.

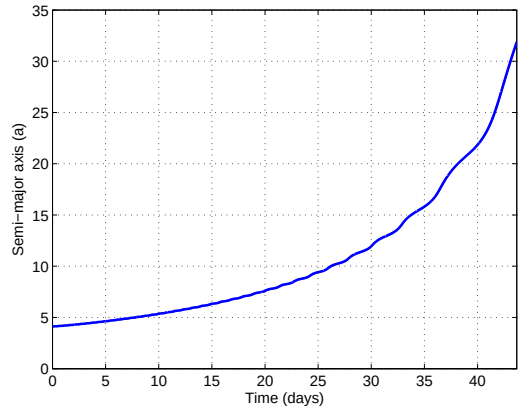

(a) semi-major axis (a)

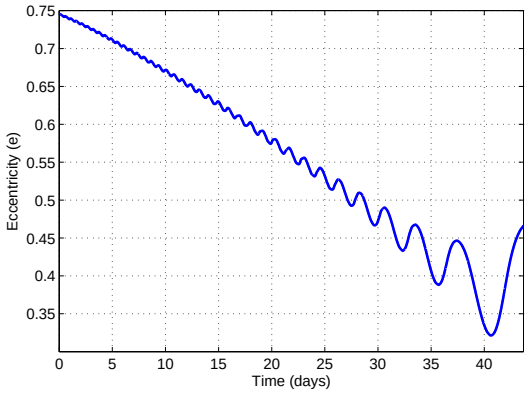

(b) eccentricity (e)

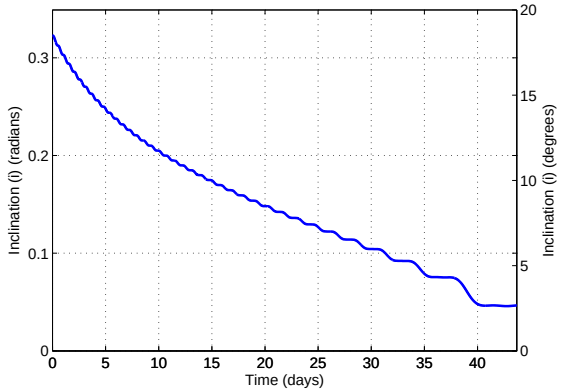

(c) inclination (i)

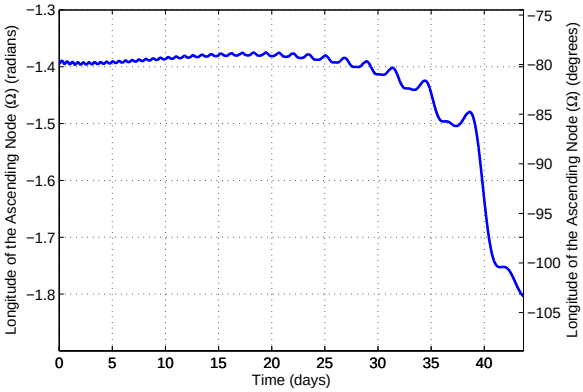

(d) Longitude of Ascending Node (Ω)

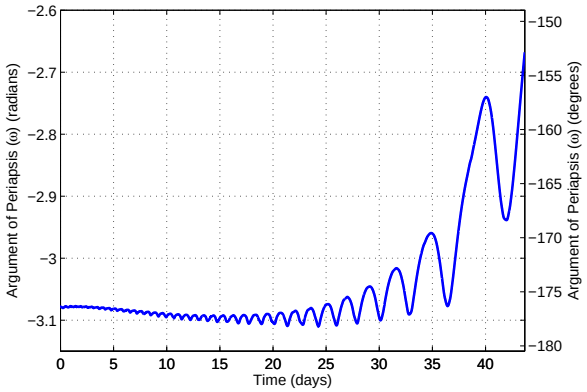

(e) Argument of Periapsis (ω)

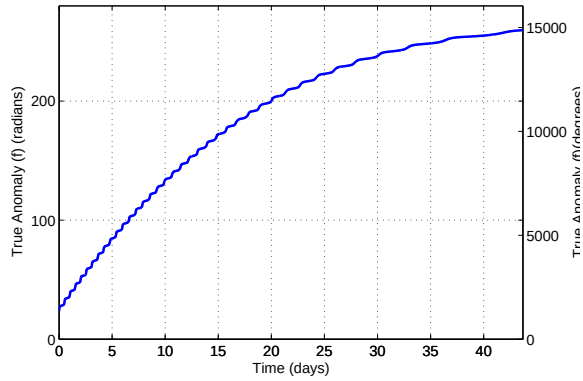

(f) True Anomaly

Figure 4.20: Time history of classical orbital elements for an Optimal low-thrust trajectory from GTO to a periodic orbit of amplitude $A_z = 8.0 \times 10^3$ km.

The optimal trajectory found using the Taylor series constraints has a lower cost than the previous solution obtained using the conventional Runge-Kutta constraints. A comparison is shown in Table 4.4. An optimal Earth to Halo trajectory was also produced using the Runge-Kutta constraints on the finer mesh used for the Taylor series solution, to determine whether the improved result was due to the solution method or the mesh.

Constraints	Numbers of Segments	Thrust Arc Duration (days)	Coast Arc Duration (days)	Total Time of Flight (days)	Mass fraction of propellant required	Mass fraction Mass fraction ($\frac{m_f}{m_0}$)
Runge-Kutta	60	45.391	39.306	84.697	0.093291	0.906709
Taylor-Series	280	43.692	39.415	83.107	0.089798	0.910202
Runge-Kutta	280	43.717	39.434	83.150	0.089849	0.910151

Table 4.4: Results for an optimal low-thrust transfer from GTO to a halo orbits with out-of-plane amplitude 8000 km.

The results on the fine mesh for Taylor series constraints and the Runge-Kutta constraints are very similar in terms of cost; using a mass fraction of propellant of 0.089798 and 0.089849 respectively. This is a difference of only 0.06%. The errors in the states for the Taylor series and Runge-Kutta methods are shown in Figure 4.21 and 4.22 respectively. The error was computed by using the MATLAB numerical integration routine *ode45* to propagate the states over a segment using the optimal control found. The error is then the difference between the propagated states and those stored in the parameter vector. It is seen from Figures 4.21-4.23 that the errors in the solution computed using the Taylor series multiple shooting are several orders of magnitude lower than those in the solution found using the Runge-Kutta multiple shooting.

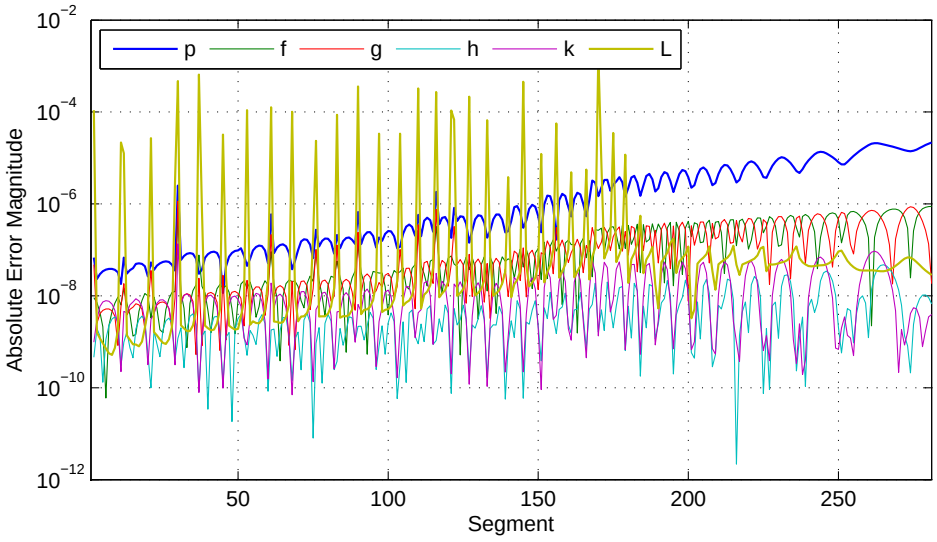

Figure 4.21: State errors for an optimal low-thrust trajectory from GTO to a periodic orbit of amplitude $A_z = 8.0 \times 10^3$ km calculated with Taylor series constraints.

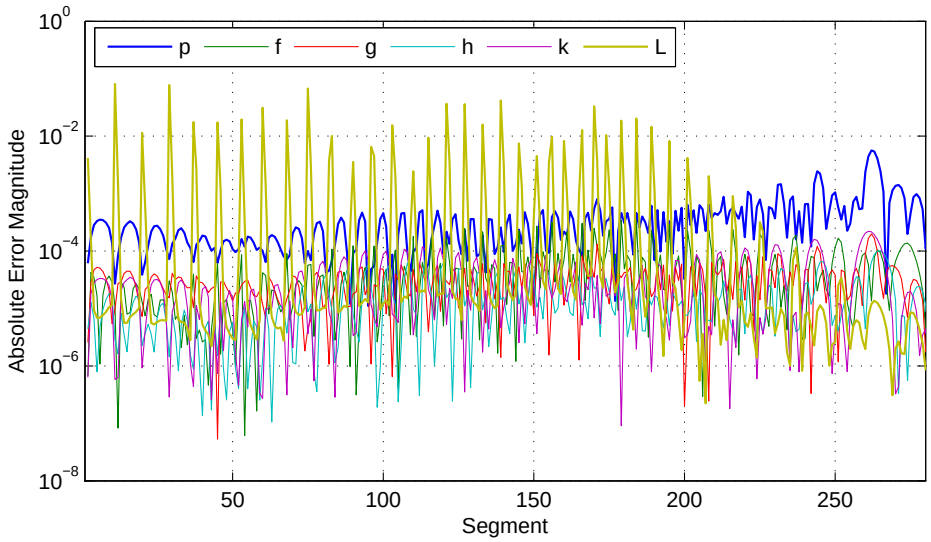

Figure 4.22: State errors for an optimal low-thrust trajectory from GTO to a periodic orbit of amplitude $A_z = 8.0 \times 10^3$ km calculated with Runge-Kutta constraints.

The norm of the state error at each node for both methods is shown in Figure 4.23. Since the norm of the absolute error is dominated by errors in the fast changing variable L, the norms of the errors are shown with and without L.

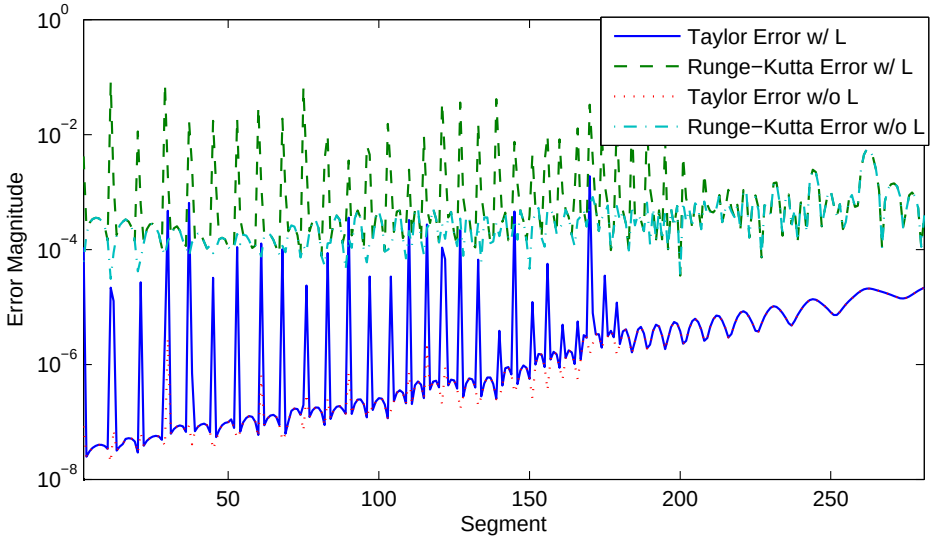

Figure 4.23: Comparison of the state errors for optimal low-thrust trajectories from GTO to a periodic orbit of amplitude $A_z = 8.0 \times 10^3$ km calculated using Taylor series and Runge-Kutta constraints.

4.4.4 Optimal Transfer from L_1 Halo Orbit to Low Lunar Orbit

The Halo to Moon leg of the transfer was also solved using Taylor series constraints (20 terms) and with 138 segments and 6 subsegments. As it was for the Earth to Halo leg, the previous Runge-Kutta solution (see Section 4.3.4) was used as the initial guess. The optimal trajectory is shown in Figures 4.24 and 4.25 with the corresponding control history shown in Figure 4.26.

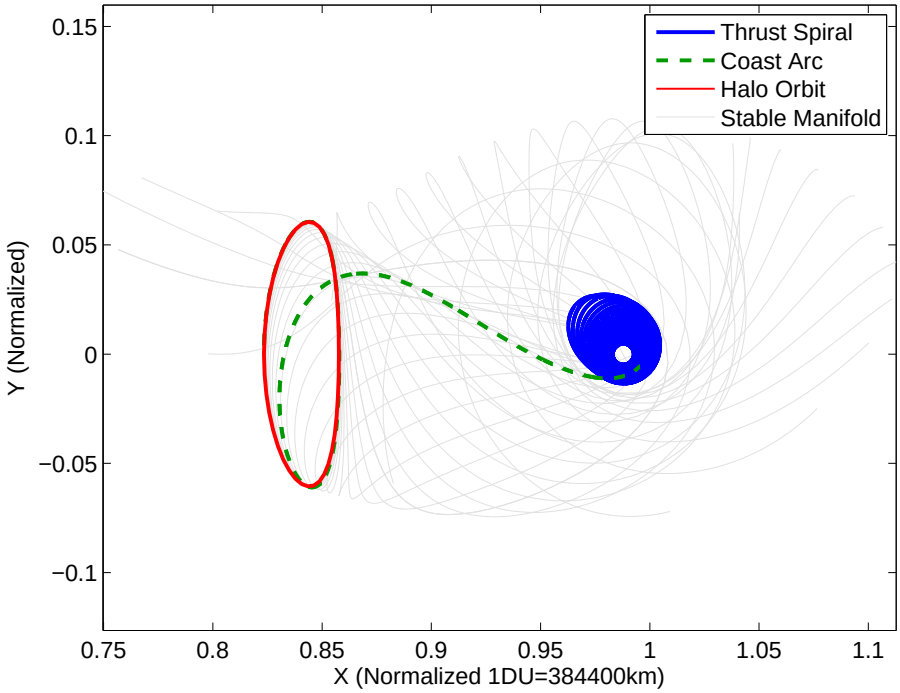

Figure 4.24: Optimal low-thrust trajectory from periodic orbit of amplitude $A_z = 8.0 \times 10^3$ km to low-lunar orbit.

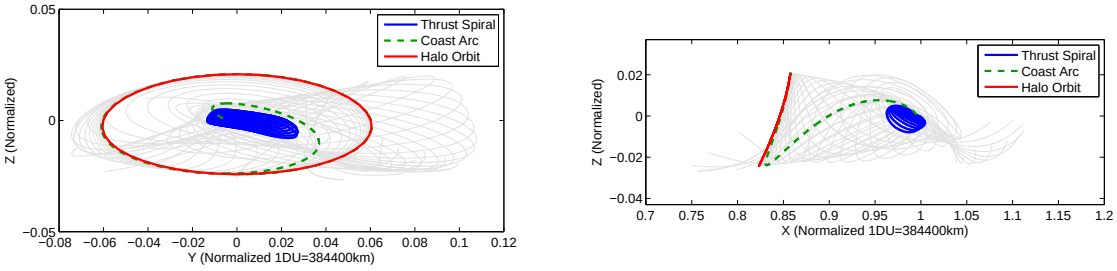

(a) YZ plane

(b) XZ plane

Figure 4.25: Optimal low-thrust trajectory from periodic orbit of amplitude $A_z = 8.0 \times 10^3$ km to low-lunar orbit.

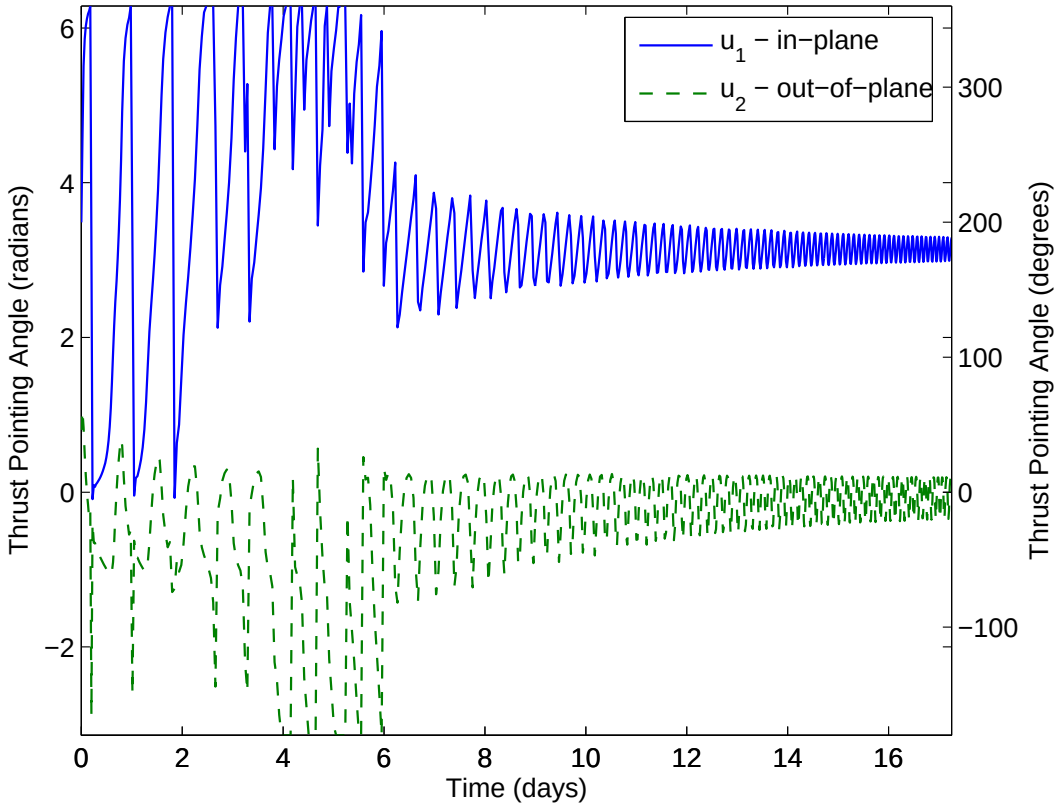

Figure 4.26: Thrust pointing angle time history for an optimal low-thrust trajectory from periodic orbit of amplitude $A_z = 8.0 \times 10^3$ km to low-lunar orbit.

The optimal trajectory has an initial 15.5197 day coast along the unstable manifold. It departs the manifold close to the Moon and enters a highly eccentric lunar orbit ($e = 0.55$). The semi-major axis and eccentricity are decreased over the 17.2488 day thrust spiral until it enters a circular low-lunar orbit at an altitude of 100 km. The total time of flight is 32.7685 days. The solution found using the Taylor series constraints is very similar to that found previously using the Runge-Kutta constraints (section 4.3.4) in both time of flight and propellant cost. The problem was also solved using Runge-Kutta multiple shooting constraints on the finer (138 Segment) mesh. The Runge-Kutta method, when applied on the finer mesh, was able to find a slightly lower cost solution, with similar errors (cf. Figure 4.27), indicating that the solution obtained using the Taylor series constraints may be a local minimum. This solution was then used as an initial guess for an optimization using the Taylor series constraints. A lower coast solution was found, however, the errors in the state variables were too great (maximum state error = 1.1478), and that solution was discarded. A comparison is shown in Table 4.5. The state histories are shown in Figure 4.28. The histories of the classical orbit elements over the trajectory are shown in Figure 4.29.

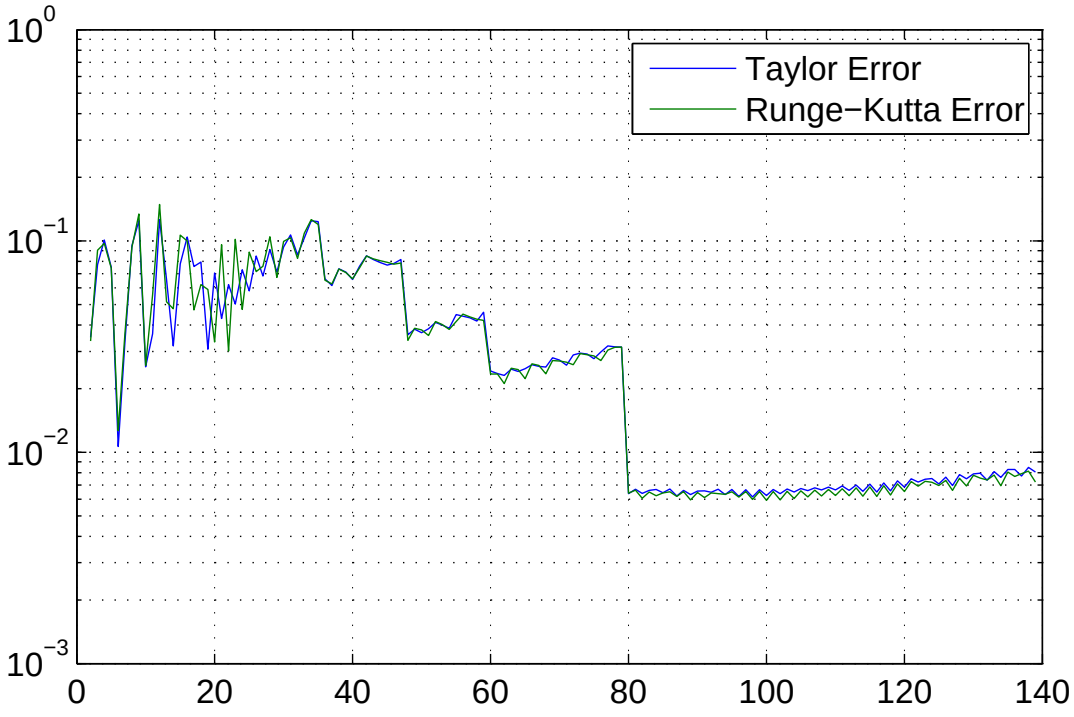

Figure 4.27: State errors for an optimal low-thrust trajectory from a periodic orbit of amplitude $A_z = 8.0 \times 10^3$ km to low-lunar orbit, calculated on a mesh with 138 segments.

Constraints	Numbers of Segments	Coast Arc Duration (days)	Thrust Arc Duration (days)	Total Time of Flight (days)	Mass fraction of propellant required	Mass fraction Remaining ($\frac{m_f}{m_0}$)
Runge-Kutta	60	15.5206	17.3606	32.8812	0.039352	0.960648
Taylor-Series	138	15.5197	17.2488	32.7685	0.038948	0.961052
Runge-Kutta	138	15.5198	17.0387	32.5585	0.038474	0.961526

Table 4.5: Results for an optimal low-thrust transfer from a halo orbit about the Earth-Moon L_1 Lagrange point with an out-of-plane amplitude of 8000 km to low-lunar orbit.

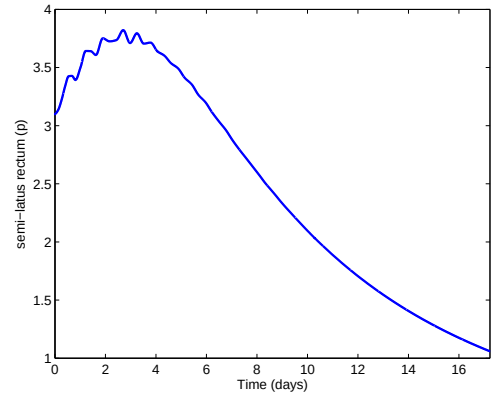

(a) p

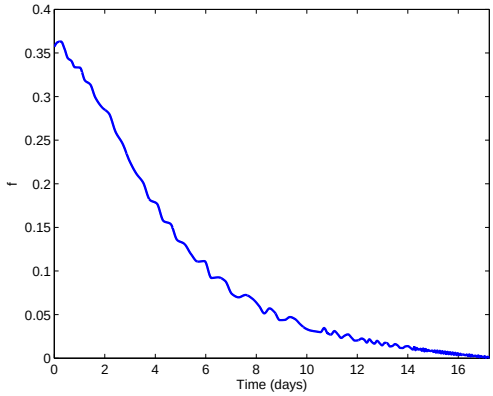

(b) f

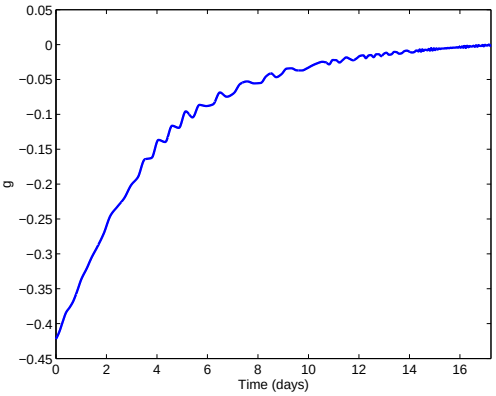

(c) g

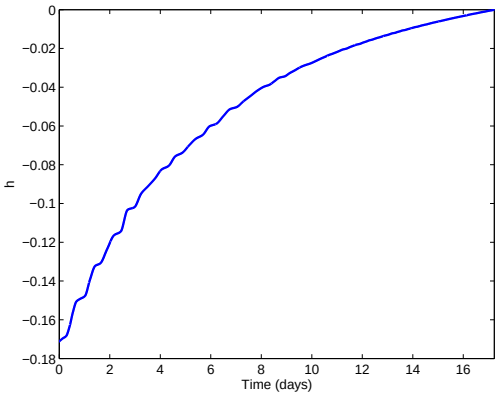

(d) h

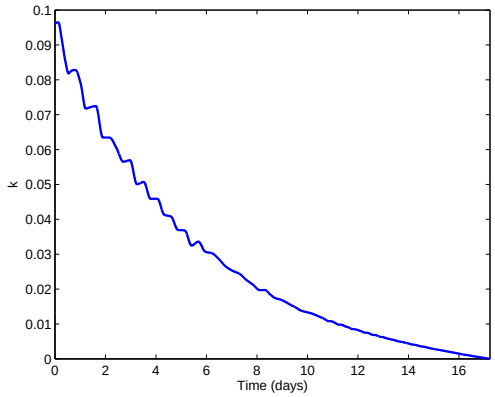

(e) k

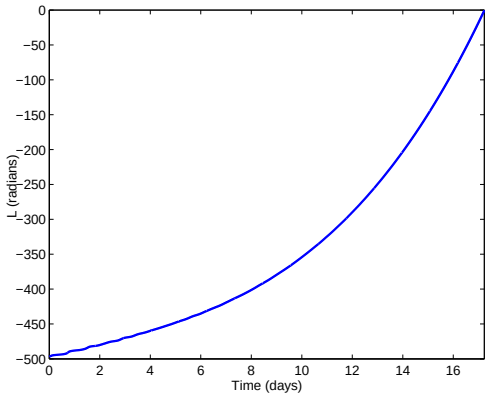

(f) L

Figure 4.28: Time histories of modified orbital elements for an optimal low-thrust trajectory from periodic orbit of amplitude $A_z = 8.0 \times 10^3$ km to low-lunar orbit.

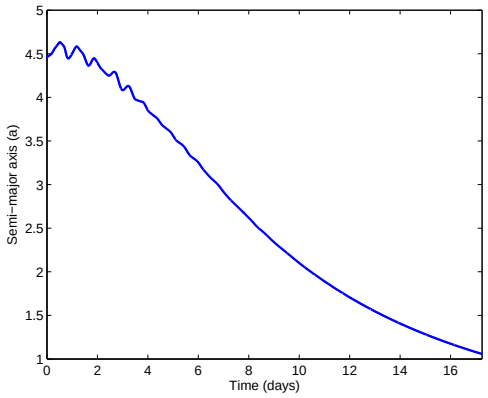

(a) semi-major axis (a)

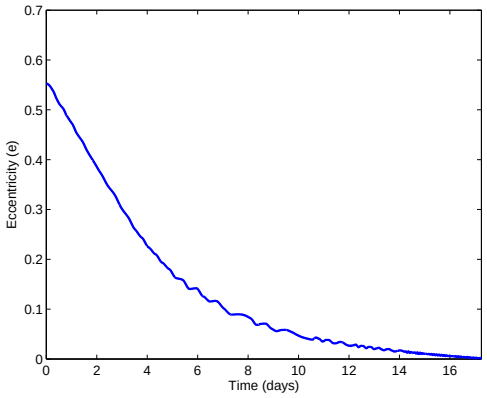

(b) eccentricity (e)

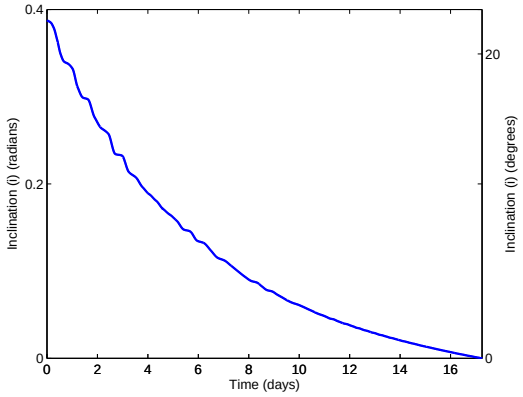

(c) inclination (i)

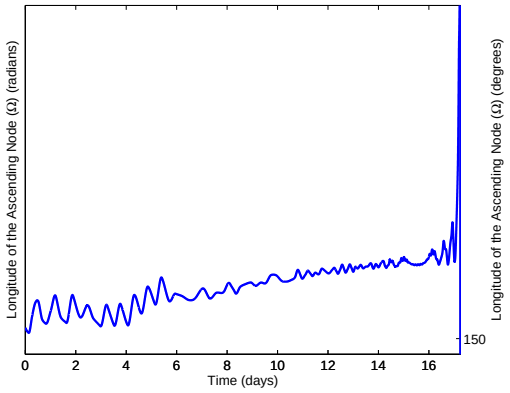

(d) Longitude of Ascending Node (Ω)

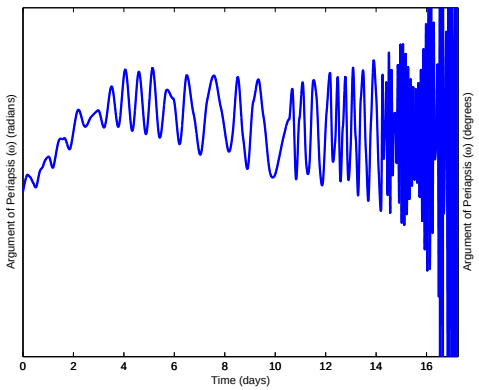

(e) Argument of Periapsis (ω)

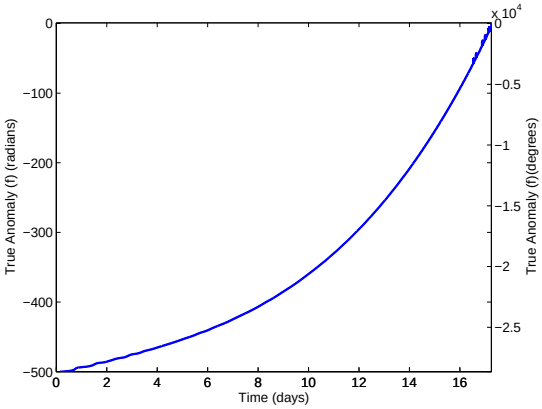

(f) True Anomaly

Figure 4.29: Time history of conventional elliptic orbital elements for an optimal low-thrust trajectory from periodic orbit of amplitude $A_z = 8.0 \times 10^3$ km to low-lunar orbit.

4.4.5 Complete Earth-Moon Transfer via Intermediate Halo Orbit

The individually optimal Earth-Halo and Halo-Moon trajectories can be combined to form an optimal trajectory that starts in GTO and arrives in low-lunar orbit with a coast arc along the stable and unstable manifolds of a Halo orbit about the Earth-Moon L_1, as shown in for a halo orbit with $A_z = 8000\ km$ in Figure 4.30. A comparison of the solution found using the new Taylor series constraints and that found using the conventional Runge-Kutta constraints is shown in Table 4.6

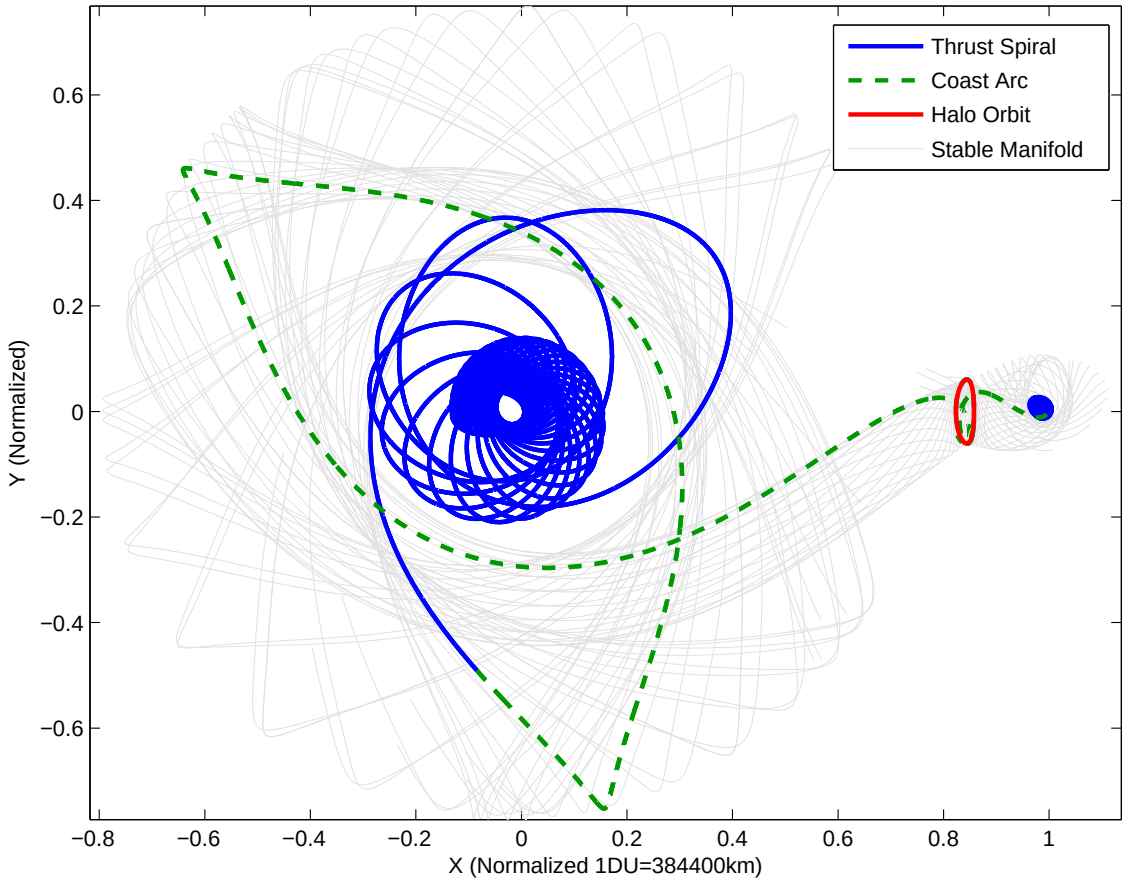

Figure 4.30: Optimal low-thrust trajectory from GTO to low-lunar orbit via a periodic orbit of amplitude $A_z = 8.0 \times 10^3$ km and its stable and unstable manifolds.

	Number of Segments Earth-Halo Leg	Number of Segments Halo-Moon Leg	Earth Escape Spiral (days)	Stable Manifold Coast (days)	Halo Orbit (min.) (days)	Unstable Manifold Coast (days)	Moon Capture Spiral (days)	Total Time of Flight (days)	Final mass fraction	Propellant mass fraction
Runge-Kutta	60	60	45.3914	39.3057	6.1140	15.5206	17.3606	123.6923	0.871029	0.128971
Taylor series	280	138	43.6921	39.4145	5.0734	15.5197	17.2488	120.9484	0.874751	0.125249
Runge-Kutta	280	138	43.7168	39.4336	5.1087	15.5198	17.0387	120.8176	0.875134	0.124866

Table 4.6: Results for an optimal low-thrust transfer from GTO to low-lunar orbit via a halo orbits of amplitude $A_z = 8000\ km$ about the Earth-Moon L_1 Lagrange point.

The trajectory found using the Taylor series constraints takes a minimum of 120.95 days (depending upon how many revolutions the spacecraft makes around the halo orbit having a period $T \approx 12$ days), of which the engine is on and thrusting at the maximum possible level for 60.9409 days. The results found using the Taylor series multiple shooting constraints are similar to those found using the Runge-Kutta constraints on the same mesh, with a total mass fraction of propellant required of 0.125249 and 0.124866 respectively. However the errors associated with the Taylor series solution are lower (cf. Figure 4.23). The mass fraction of propellant required for both the trajectories found using the finer (280 segment) mesh are lower than that for the original solution found using Runge-Kutta constraints on a coarse mesh of 60 segments (cf. Section 4.3). However, since both solutions on the fines mesh are similar this indicates that the decrease in cost of the solution is more a function of mesh rather than the formulation of the constraints.

The main goal of formulating the Taylor series constraints was to reduce the number nodes required in the mesh and hence the number of NLP parameters required to describe the trajectory. Unfortunately this proved not to be the case, 280 segments were required for the Earth-Halo phase and 138 segments were required for the Halo-Moon phase, resulting in NLP parameters vectors of 5053 and 2495 elements respectively. These are much larger than those required (1153 and 1091) for the original solution found using Runge-Kutta constraints. Such a fine mesh was required for the Taylor series multiple shooting constraints because the Taylor series has a radius of convergence, outside of which the Taylor series estimate rapidly tends to $\pm\infty$. The radius of convergence of the Taylor series expansion is a function of the states, time and the control. These are not known *a priori*, therefore a conservative choice must be made for mesh so that the Taylor series estimates remain finite while the trajectory is being altered by the optimizer. So while a valid, more accurate (cf. Figure 4.23) solution was found using the Taylor series multiple shooting constraints, the primarily goal of devising a method that allowed the problem to be solved using a coarser mesh was not achieved.

Chapter 5

Conclusions

In this work the problem of interest is the solution of optimal control problems using direct transcription. In direct transcription the trajectory of each state and control (if there are any) are discretized, so that the trajectory is wholly described by the states and controls on a mesh consisting of a finite number of nodes. The continuous optimal control problem is then a discrete parameter optimization problem that can be solved using non-linear programming techniques. To ensure the trajectory is valid the system governing equations are converted into algebraic constraints.

Two new methods for transcribing the equations of motion in algebraic constraints were developed, the Taylor series multiple shooting method and higher-order collocation. Both methods use higher-order (2^{nd} and above) derivatives of the states and these derivatives are calculated using automatic differentiation. To compute these derivatives, the control must be specified in such a way that its time derivatives can be readily calculated. Several control parameterizations were developed to accomplish this. The ability to compute derivatives to arbitrary order allows an accurate estimate of the error in the Taylor series expansion to be computed. A mesh refinement scheme that uses this error estimate to evenly distribute the error over the mesh was developed. The new methods were tested on a succession of progressively more difficult optimal control problems.

The Taylor series multiple shooting method significantly outperformed the existing Runge-Kutta method on the test problems. It was able to produce more accurate solutions using fewer segments (and hence smaller NLP parameter vectors). In particular it performed extremely well on problems without explicit controls, e.g. the periodic orbit generation problem and the *indirect* formulation of the other test problems. For example, to generate a periodic orbit with an error (the Euclidean norm of the difference between an initial point in phase space on the periodic orbit and the same point after integrating forward in time for one period) of less than 10^{-6} requires 40 segments and 94.43s of CPU time using the Runge-Kutta multiple shooting constraints but only 3 segments and 2.44s using the Taylor series multiple shooting constraints.

For other problems without explicit controls the Taylor series multiple shooting method was able to produce solutions accurate to within the optimality tolerances using far fewer segments than required for the Runge-Kutta method.

For the *direct* formulation of the test problems where the control was parameterized, the best results were obtained using the variable knot spline. That is, a cubic spline where the optimizer was free to place the control knots anywhere in $t - u$ space, where t is time and u is the control. The mesh refinement scheme moved nodes to where the states or control where changing rapidly, equally distributing the numerical error over the mesh, enabling problems to be solved using fewer segments than would be required for a uniform mesh.

The higher-order collocation method produced accurate solutions for the problems it was tested on. However, care must be taken to ensure the interpolating polynomial is stable. The range of control parameterizations possible is also limited as every control point must affect the state derivatives at either the segment boundaries or the interior collocation point. Hence, the Taylor series shooting method was deemed more promising and further testing of the higher-order collocation was not performed.

The capstone problem was a low-thrust transfer from geosynchronous transfer orbit about the Earth to low-lunar orbit using three-body dynamics, in particular the stable and unstable manifolds of a periodic orbit about the interior (L_1) Lagrange point. The transfer was split into two phases, the first phase is a thrust arc to intersect the stable manifold, followed by a coast along the stable manifold until a transfer to a periodic orbit about L_1 is possible. The second phase is a coast along the unstable manifold (i.e. the manifold departing L_1) towards the moon followed by a thrust arc to transfer into a low lunar orbit.

A similar problem was solved by Mingotti, Topputo and Bernelli-Zazzera,[49] however, in this work several simplifying assumptions they made were removed. For example, in this work: (i) the spacecraft has constant thrust rather than constant thrust *acceleration*, (ii) it is not assumed that aligning thrust with the velocity vector is optimal during the escape spiral and (iii) the initial plane of the geosynchronous transfer orbit (GTO) is equatorial (the usual case) rather than in the plane of the Moon's orbit. The problem was solved using both the conventional Runge-Kutta multiple shooting constraints as well as the Taylor series multiple shooting constraints.

The Taylor series multiple shooting method was developed in an effort to reduce the number of NLP parameters required to accurately describe a trajectory. The test optimal control problems solved in Chapter 3 were able to be solved much more accurately by the Taylor series multiple shooting method using fewer NLP parameters. However, this proved not to be the case for the much more complicated Earth-Moon transfer. Many more segments (280) were required for Taylor series solution than for the Runge-Kutta solution (60), due to limited radius of convergence of the Taylor series expansions.

While the Taylor series method for converting the system governing equations to algebraic constraints proved to work in many example problems and its performance was very promising, its development is still in its infancy and there is much room from improvement. In particular, the method can be sensitive to the size of the timestep. If the mesh is made so coarse that size of a propagation step within a segment is larger than the radius of convergence of the Taylor series, the Taylor series estimate can tend to $\pm\infty$, causing the method to fail.

Chapter 6

Future Work

Automatic Differentiation for Jacobian and Hessian

The techniques of automatic differentiation are used to compute the higher-order state derivatives that are required to calculate the later terms in the Taylor series that are used in the constraint formulation. However, they were not used to calculate the derivatives required for the core nonlinear programming calculations such as the gradient of the objective function, the Jacobian of the constraints or the Hessian. These are computed, usually inside the NLP solver (*fmincon* or *SNOPT*), by finite differences or in the case of the Hessian, a Quasi-Newton approximation. Finite differences have a limited accuracy due to cancellation errors caused by the subtraction operation. Using automatic or complex step differentiation would enable these derivatives to be computed much more accurately, resulting in a more accurate solution and possibly positively impacting convergence of NLP problem as well.

Automatic Equation Decomposition

The equations of motion for all the problems solved in this thesis were decomposed into their constitute elementary operations by hand. This decomposition was then used to create a function that returned the state derivatives to any order as required for the Taylor series expansion. While this decomposition and subsequent coding is not difficult, it can be tedious and is prone (as all human calculations are) to error. Jorba[34] created a program that parsed the code for the equations of motion and produced the derivative computation function automatically. A Matlab equivalent to their (C or Fortran) code greatly sped up the initial problem setup time when faced with a new set of governing equations.

Adaptive Control Parameterization

For all problems solved the number of control points was chosen *a priori* and remained constant throughout the runtime of the NLP solver. Ideally there would be an automated adaptive process to add or remove control points depending on how well the current set were approximating the desired control. This should increase efficiency as there would be no control points that are not essential. The deletion of non-essential control points would then decrease

the size of the NLP vector parameter. A similar approach could be taken for the mesh of the state nodes. The current mesh refinement scheme has the ability to change the size of segments by moving the boundary nodes in time, but it cannot change the total number of segments. The optimization must be restarted to solve with a different number of segments.

Improved Mesh Refinement

The mesh refinement scheme considers the accuracy of the state estimations, however, when solving problems using the indirect formulation the control is specified by a function of one or more states or co-states. Errors in the control function may be many orders of magnitude higher than the errors in the constituent elements. This phenomenon was observed in both the Orbit Raising (Section 3.5) and Orbit Phasing (Section 3.6) problems. More efficient meshes could be produced if the mesh refinement scheme was able to take this into account.

Nonuniform Rational BSplines

The performance of the non-uniform basis splines (NURBs) in this study was disappointing. It was anticipated that because of the extra non-zero derivatives, and hence more flexibility, the NURBs would be able to better approximate the control function. However, the NURBs provided no increase in performance over variable knot splines. The NURBs used for this study had uniform knot vectors and a fixed order. This was done to limit the computational cost, however, it might be the case that allowing the optimizer to change the knot vector and the spline order adaptively is worth the added computational cost.

More Realistic Earth-Moon Model

The Earth-Moon transfer trajectory presented in this thesis is computed using an idealized model of the Earth-Moon system and the low thrust engine. While this makes the equations of motion simpler to handle, it is not necessary that the Taylor series method be able to handle extremely complicated equations of motion. In order to compute a trajectory that could one day be flown, more realistic perturbations would have to be included; including but not limited to: the Earth's oblateness ($J2$,etc), more realistic 3rd body calculations (not assuming circular orbits), effects from external bodies such as the Sun, and a more realistic engine model.

Chapter 7

References

[1] M. Guelman, "Earth-to-Moon Transfer with a Limited Power Engine," *Journal Of Guidance Control and Dynamics*, Vol. 18, Sep-Oct 1995, pp. 1133–1138.

[2] H. Pernicka, D. Scarberry, S. Marsh, and T. Sweetser, "A Search for Low Delta-v Earth-to-Moon Trajectories," *Journal of the Astronautical Sciences*, Vol. 43, Jan-Mar 1995, pp. 77–88.

[3] W. Koon, M. Lo, J. Marsden, and S. Ross, "Low energy transfer to the Moon," *Celestial Mechanics & Dynamical Astronomy*, Vol. 81, No. 1-2, 2001, pp. 63–73.

[4] J. S. Parker and G. H. Born, "Modeling a Low-Energy Ballistic Lunar Transfer Using Dynamical Systems Theory," *Journal of Spacecraft and Rockets*, Vol. 45, Nov-Dec 2008, pp. 1269–1281.

[5] E. Belbruno and J. Miller, "Sun-Perturbed Earth-to-Moon Transfers with Ballistic Capture," *Journal of Guidance Control and Dynamics*, Vol. 16, Jul-Aug 1993, pp. 770–775.

[6] N. Assadian and S. H. Pourtakdoust, "Multiobjective genetic optimization of Earth-Moon trajectories in the restricted four-body problem," *Advances in Space Research*, Vol. 45, Feb 2010, pp. 398–409.

[7] K. Yagasaki, "Sun-perturbed earth-to-moon transfers with low energy and moderate flight time," *Celestial Mechanics & Dynamical Astronomy*, Vol. 90, Sep 2004, pp. 197–212.

[8] H. Poincare, *New Methods of Celestial Mechanics. Volume II - Methods of Newcomb, Gylden, Lindstedt, and Bohlin.* United States: NTIS, 1967. Translation.

[9] D. Richardson, "Analytic construction of periodic orbits about the collinear points," *Celestial Mechanics*, Vol. 22, No. 3, 1980, pp. 241 – 253.

[10] G. Gomez and M. Marcote, "High-order analytical solutions of Hill's equations," *Celestial Mechanics and Dynamical Astronomy*, Vol. 94, No. 2, 2006, pp. 197 – 211.

[11] V. Guibout and D. Scheeres, "Periodic orbits from generating functions," *Advances in the Astronautical Sciences*, Vol. 116, No. 2, 2004, pp. 1029–1048.

[12] G. Gomez, J. Masdemont, and C. Simo, "Quasihalo orbits associated with libration points," *Journal of the Astronautical Sciences*, Vol. 46, No. 2, 1998, pp. 135 – 176.

[13] K. Howell and H. Pernicka, "Numerical determination of Lissajous trajectories in the restricted three-body problem," *Celestial Mechanics*, Vol. 41, No. 2, 1988, pp. 107 – 124.

[14] K. Uesugi, H. Matsuo, J. Kawaguchi, and T. Hayashi, "Japanese 1st Double Lunar Swingby Mission Hiten," *Acta Astronautica*, Vol. 25, Jul 1991, pp. 347–355.

[15] S. Ross, *Cylindrical manifolds and tube dynamics in the restricted three-body problem.* PhD thesis, California Institute of Technology, 2004.

[16] W. S. Koon, J. E. Marsden, M. W. Lo, and S. D. Ross, "Constructing a low energy transfer between Jovian moons," *Contemporary Mathematics*, Vol. 292, 2002, p. 2002.

[17] A. Sims, Jon, "Jupiter Icy Moons Orbiter Mission Design Overview," *Paper AAS 06-185, AAS/AIAA Space Flight Mechanics Meeting, Tampa, FL*, Jan 2006.

[18] R. L. Anderson, *Low thrust trajectory design for resonant flybys and captures using invariant manifolds*. PhD thesis, University of Colorado at Boulder, 2005.

[19] G. L. Pilbratt, "Herschel Space Observatory mission overview," *IR Space Telescopes and Instruments*, Vol. 4850, No. 1, 2003, pp. 586–597.

[20] S. Triqueneaux, L. Sentis, P. Camus, A. Benoit, and G. Guyot, "Design and performance of the dilution cooler system for the Planck mission," *Cryogenics*, Vol. 46, No. 4, 2006, pp. 288 – 297.

[21] M. Lo, B. Williams, B. W.E., H. Dongsuk, H. Yungsun, J. Bell, H. E.A., R. Corwin, P. Hong, K. Howell, B. Barden, and R. Wilson, "Genesis mission design," *The Journal of the astronautical sciences*, Vol. 49, No. 1, 2001, pp. 169–184.

[22] Bryson and Ho, *Applied Optimal Control: Optimization, Estimation and Control*. Hemisphere Publishing Corporation, 1975.

[23] O. v. Stryk and R. Bulirsch, "Direct and indirect methods for trajectory optimization," *Annals of Operations Research*, Vol. 37, No. 1-4, 1992, pp. p357 – 373.

[24] D. Dickmanns, F. and H. Wells, K., "Approximate Solution of Optimal Control Problems Using Third Order Hermite Polynomial Function," *Proceedings of the 6th Technical Conference on Optimization Techniques, Springer-Verlag, New York*, 1975.

[25] A. L. Herman and B. A. Conway, "Direct optimization using collocation based on high-order Gauss-Lobatto quadrature rules," *Journal of Guidance, Control, and Dynamics*, Vol. 19, No. 3, 1996, pp. 592 – 599.

[26] B. Bialecki and A. Karageorghis, "Legendre Gauss spectral collocation for the Helmholtz equation on a rectangle," *Numerical Algorithms*, Vol. 36, Jul 2004, pp. 203–227.

[27] S. Kameswaran and L. T. Biegler, "Convergence rates for direct transcription of optimal control problems using collocation at Radau points," *Computational Optimization and Applications*, Vol. 41, Sep 2008, pp. 81–126.

[28] G. Elnagar, M. Kazemi, and M. Razzaghi, "The Pseudospectral Legendre Method for Discretizing Optimal-Control Problems," *IEEE Transactions on Automatic Control*, Vol. 40, Oct 1995, pp. 1793–1796.

[29] G. Elnagar, "Pseudospectral chebyshev optimal control of constrained nonlinear dynamical systems," *Computational Optimization and Applications*, Vol. 11, Nov 1998, pp. 195–217.

[30] D. Benson, *A Gauss pseudospectral transcription for optimal control*. PhD thesis, Massachusetts Institute of Technology, 2005.

[31] J. Enright, Paul. and A. Conway, B., "Discrete Approximations to Optimal Trajectories Using Direct Taanscription and Nonlinear Programming," *Journal of Guidance, Control, and Dynamics*, Vol. 15, No. 4, 1992, pp. 994–1002.

[32] J. A. Sims and S. N. Flanagan, "Preliminary Design of Low-Thrust Interplanetary Missions," *AAS/AIAA Astrodynamics Specialist Conference, AAS Paper 99-338, Girdwood, Alaska*, 1999.

[33] A. Farin, *Evaluating derivatives: principles and techniques of algorithmic differentiation*. Philadelphia, PA, USA: SIAM, 1st ed., 2000.

[34] A. Jorba and M. Zou, "A Software Package for the Numerical Integration of ODEs by Means of High-Order Taylor Methods," *Experimental Mathematics*, Vol. 14, No. 1, 2005, pp. 99–116.

[35] P. Enright and B. Conway, "Discrete Approximations to Optimal Trajectories Using Collocation and Nonlinear Programming," *Journal of Guidance, Control, and Dynamics*, Vol. 15, No. 4, 1992, pp. 994 – 1002.

[36] I. M. Ross and F. Fahroo, "Legendre Pseudospectral Approximations of Optimal Control," *Problems,Ť Lecture Notes in Control and Information Sciences*, Springer-Verlag, 2003, pp. 327–342.

[37] C. R. Hargraves and P. S. W., "Direct trajectory optimization using nonlinear programming and collocation," *Journal of Guidance, Control, and Dynamics*, Vol. 10, No. 4, 19878, pp. 338 – 342.

[38] J. R. R. A. Martins, P. Sturdza, and J. J. Alonso, "The complex-step derivative approximation," *ACM Trans. Math. Softw.*, Vol. 29, No. 3, 2003, pp. 245–262.

[39] C. Lantoine, Gregory, P. Russell, Ryan, and T. Dargent, "Using Multicomplex Variables for Automatic Computation of High-Order Derivatives," *Paper AAS 10-218, AAS/AIAA Space Flight Mechanics Meeting, San Diego, CA*, Feb 2010.

[40] C. d. Boor, *A practical Guide to Splines*. New York, NY, USA: Springler-Verlag, 1978.

[41] G. E. Farin, *NURBS: From Projective Geometry to Practical Use*. Natick, MA, USA: A. K. Peters, Ltd., 2nd ed., 1999.

[42] A. Keane and P. Nair, *Computational Approaches for Aerospace Design: The Pursuit of Excellence*. Wiley, Aug. 2005.

[43] A. Ateshian, G., "A B-spline least-squares surface-fitting method for articular surfaces of diarthrodial joints," *Journal of Biomech Engineering*, Vol. 115, No. 54A, 1993, pp. 366–73.

[44] D. E. Calkins, R. D. Schachter, and L. T. Oliveira, "An automated computational method for planing hull form definition in concept design," *Ocean Engineering*, Vol. 28, No. 3, 2001, pp. 297 – 327.

[45] D. F. Rogers and S. G. Satterfield, "B-spline surfaces for ship hull design," *SIGGRAPH Comput. Graph.*, Vol. 14, July 1980, pp. 211–217.

[46] W. Segars, D. Lalush, E. Frey, D. Manocha, M. King, and B. Tsui, "Improved Dynamic Cardiac Phantom Based on 4D NURBS and Tagged MRI," *Nuclear Science, IEEE Transactions on*, Vol. 56, 10 2009, pp. 2728 –2738.

[47] P. Tarragó, "Study and Assessment of Low-Energy Earth-Moon Transfer Trajectories," Master's thesis, Université de Liége, 2007.

[48] J. E. Prussing and J. H. Chiu, "Optimal Multiple-Impulse TimeFixed Rendezvous Between Circular Orbits," *Journal of Guidance, Control, and Dynamics*, No. 9, 1986, pp. 17–22.

[49] G. Mingotti, F. Topputo, and F. Bernelli-Zazzera, "Combined Optimal Low-Thrust and Stable-Manifold Trajectories to the Earth-Moon Halo Orbits," *New Trends in Astrodynamics and Applications III*, Vol. 886, No. 1, 2007, pp. 100–112.

[50] R. H. Battin, "An Introduction to the Mathematics and Methods of Astrodynamics," *AIAA Education Series, AIAA*, 1987.

[51] K. Howell, B. Barden, and M. Lo, "Application of dynamical systems theory to trajectory design for a libration point mission," *Journal of the Astronautical Sciences*, Vol. 45, No. 2, 1997, pp. 161 – 178.

[52] J. Prussing and B. Conway, *Orbital Mechanics*. Oxford University Press, New York, 1993.

[53] M. J. H. Walker, B. Ireland, and J. Owens, "A set modified equinoctial orbit elements," *Celestial Mechanics and Dynamical Astronomy*, Vol. 36, 1985, pp. 409–419. 10.1007/BF01227493.